PROTONATION OF BIOLOGICALLY REVELANT SULFUR LIGANDS: KINETIC AND MECHANISTIC STUDIES ON SYNTHETIC Fe-S-BASED CLUSTERS AND Ni-THIOLATE COMPLEXES

PROTONATION OF BIOLOGICALLY REVELANT SULFUR LIGANDS: KINETIC AND MECHANISTIC STUDIES ON SYNTHETIC Fe-S-BASED CLUSTERS AND Ni-THIOLATE COMPLEXES

BY

THAER MAHDI MADLOOL AL-RAMMAHI

A thesis submitted in partial fulfilment of the requirements for the degree of

Doctor of Philosophy

University of Newcastle

School of Chemistry

2017

I certify that the work contained in this thesis submitted by me for the degree of PhD is my own original work; except where due reference is made to other authors; and has not been previously submitted for a degree at this or any other university.

Signed

Thaer Al-Rammahi

2017

Acknowledgements

Firstly, I would like to thank Prof. Richard A. Henderson for his helpness, support, guidance, encouragement during my study and patience have been invaluable.

Thank you to my sponsor the Higher Committee for Education Development in Iraq (HCED) and Iraqi Ministry of Higher Education and Scientific Research (MOHE) for a studentship.

Thanks for all the members' staff in school of chemistry: Dr. Kieth Izod, Dr. Simon Doherty, Dr. John Errington. Dr. Paul Waddel and Dr. Michael Probert for the X-ray crystallography. Prof. William McFarlane and Dr. Corinne Wills for the NMR.

Thanks for all my colleagues the PhD students in School of Chemistry.

Thanks for all my friends in the Collage of Science / University of Kerbala – Iraq.

Finally, I would like to thank my wife and my family back home and all my friends for their support and encouragement.

Publications:

The work has been published in:

Full Details
1. X-ray crystal structure of $[NHR_3]_2[Fe_4S_4X_4]$(X = PhS, R = Et or ^{n}Bu; X = Cl, R = ^{n}Bu): Implications for Sites of Protonation in Fe-S clusters. T. M. M. Al-Rammahi, R. A. Henderson and P. G. Waddell. *Trans. Met. Chem.*, 2016, *41*, 555. http://link.springer.com/article/10.1007/s11243-016-0052-5
2. Binding Small Molecules and Ions to $[Fe_4S_4Cl_4]^{2-}$ Modulates the Rate of Protonation of Cluster. T. M. M. Al-Rammahi and R. A. Henderson. *Dalton Trans.*, 2016, *45*, 1373. http://pubs.rsc.org/en/content/articlelanding/2016/dt/c5dt04523a#!divAbstract
3. Exploring the Acid-Catalyzed Substitution Mechanism of $[Fe_4S_4Cl_4]^{2-}$. T. M. M. Al-Rammahi and R. A. Henderson. *Dalton Trans.*, 2016, *45*, 307. http://pubs.rsc.org/en/content/articlelanding/2016/dt/c5dt04008f#!divAbstract
4. X-Ray Crystal Structure of 4-Methylpyridin-l-ium 4-Methylpyridine Tetraphenyl -borate. T. M. M. Al-Rammahi, R. A. Henderson and P. G. Waddell, Web CSD Private Communication, 2015, KUSMIW. https://www.ccdc.cam.ac.uk/structuresbeta/Search?pid=csd:KUSMIW&sid=CCDC Manual

Conferences:

The work has been presented in the following conferences:

Full Details
1. 42nd International Conference on Coordination Chemistry, 2016, 3rd – 8th July, Brest, France.
2. Wynne-Jones Postgraduate Research Day, 2016, 23rd May, Newcastle University, Newcastle upon Tyne, England, United Kingdom.
3. Royal Society of Chemistry, Dalton Meeting, 2016, 29th-31st March, The University of Warwick, Coventry, England, United Kingdom.
4. The Universities of Scotland Inorganic Chemistry Conference (USIC), 2015, 2nd – 3rd July, Heriot-Watt University, Edinburgh, Scotland, United Kingdom.
5. 1st HCED Iraq Scholars Conference, 2015, 29th May, London, England, United Kingdom.
6. Wynne-Jones Postgraduate Research Day, 2015, 19th May, Newcastle University, Newcastle upon Tyne, England, United Kingdom.

ABSTRACT

Protonation of Biologically Relevant Sulfur Ligands: Kinetic and Mechanistic Studies on Synthetic Fe-S-Based Clusters and Ni-thiolate Complexes

A variety of metalloenzymes contain iron-sulfur clusters (*e.g.* nitrogenases, aconitase and carbon monoxide dehydrogenase) or nickel-thiolate components (*e.g.* urease, hydrogenase, CO-dehydrogenase (CODH), methyl coenzyme M reductase, Ni-superoxide dismutase, and glyoxalase I) as the catalytic site where substrates are bound and transformed. The ways in which substrates bind and are transformed at these natural iron and nickel sites remain poorly defined. Studying the natural metalloenzymes is inherently difficult because the complexity of the biological systems, but studies of the protonation on synthetic iron-sulfur and nickel-thiolate complexes allow us to establish possible mechanisms of these natural catalysts. This thesis describes the kinetics and mechanisms of the protonation of synthetic Fe-S clusters and simple Ni-thiolate complexes.

The first part of the thesis describes the protonation and binding of substrates to synthetic Fe-S-based clusters. The $[NBu^n_4]_2[Fe_4S_4X_4]$ (X= SPh or Cl) were synthesised and characterised by ^{1}H NMR spectroscopy. The kinetics of the acid-catalyzed substitution reactions of the teminal chloro-ligands in $[Fe_4S_4Cl_4]^{2-}$ by PhS^- to form $[Fe_4S_4(SPh)_4]^{2-}$ in the presence of the acids NHR_3^+ (R = Me, Pr^n or Bu^n) in MeCN have been studied. Although these acids have very similar pK_as (17.6–18.4) the reactions show a variety of different kinetics, some of which are inconsistent with a mechanism involving simple protonation of the cluster followed by substitution of a terminal ligand. The observed behaviour is more consistent with the recently proposed mechanism in which a Fe–(μ_3-SH) bond elongation/cleavage occurs upon protonation of a μ_3-S, and suggests that both the acidity and bulk of the acid is important in the protonation step. Other studies have determined the activation parameters ($\Delta H^‡$ and $\Delta S^‡$) for both the protonation and substitution steps of the acid-catalyzed substitution reactions of $[Fe_4S_4X_4]^{2-}$ (X = Cl or SEt). A significantly negative $\Delta S^‡$ is observed for the substitution steps of both clusters indicating associative pathways. This is inconsistent with earlier interpretation of the kinetics of these reactions (based exclusively on the dependence of the rate on the concentration of nucleophile) and indicates that there is no dissociative substitution mechanism and the pathway

associated with a zero-order dependence on the concentration of PhS^- involves associative substitution with the solvent (MeCN) being the nucleophile.

The mechanism of the acid-catalyzed substitution reaction of the terminal chloro-ligands in $[NBu^n_4]_2[Fe_4S_4Cl_4]$ by PhS^- in the presence of $NHBu^n_3{}^+$ involves rate-limiting proton transfer from $NHBu^n_3{}^+$ to the cluster (k_0 = 490 ± 20 $dm^3\ mol^{-1}\ s^{-1}$). A variety of small molecules and ions (L = substrate = Cl^-, Br^-, I^-, $RNHNH_2$ (R = Me or Ph), Me_2NNH_2, HCN, NCS^-, N_3^-, Bu^tNC or pyridine) bind to $[Fe_4S_4Cl_4]^{2-}$ and this affects the rate of subsequent protonation of $[Fe_4S_4Cl_4(L)]^{n-}$. Where the kinetics allow, the equilibrium constants for the substrates binding to $[Fe_4S_4Cl_4]^{2-}$ (K^L) and the rates of proton transfer from $NHBu^n_3{}^+$ to $[Fe_4S_4Cl_4(L)]^{n-}$ (k^L_0) have been determined. The results indicate the following general features. (i) Bound substrates increase the rate of protonation of the cluster, but the rate increase is modest (k^L_0/k_0 = 1.6 to ≥72). (ii)When K^L is small, so is k^L_0/k_0. (iii) Binding substrates which are good σ-donors or good π-acceptors lead to the largest k^L_0/k_0. This behaviour is discussed in terms of the recent proposal that protonation of $[Fe_4S_4Cl_4]^{2-}$ at a μ_3-S, is coupled to concomitant Fe–(μ_3-SH) bond elongation/cleavage.

The clusters $[NHR_3]_2[Fe_4S_4X_4]$ (X= PhS, R= Et or Bu^n; X= Cl, R= Bu^n) were synthesised and characterised by ^1H NMR spectroscopy and X-ray crystallography. The crystallography shows NH…X interactions between the cation and the cubanoid cluster. Comparison of the cluster dimensions in $[NHR_3]_2[Fe_4S_4X_4]$ with those reported earlier for $[NR'_4]_2[Fe_4S_4X_4]$ (R′ = Me, X = PhS; R′ = Et, X = Cl) indicates that N–H…X interactions have a negligible effect on the dimensions of the cluster. The relevance of these structures to understanding where on $[Fe_4S_4X_4]^{2-}$ protonation labilises the cluster to substitution is discussed.

The second part of the thesis describes the protonation of $[Ni(SAr)\{PhP(CH_2CH_2PPh_2)_2\}]^+$ complexes. The complexes of $[Ni(SC_6H_4R\text{-}2)(triphos)]BPh_4$ (R= Me, MeO or Cl; triphos = $PhP(CH_2CH_2PPh_2)_2$) and $[Ni(SC_6H_3Me_2\text{-}2,6)(triphos)]BPh_4$ were synthesised and structurally characterised by X-ray crystallography. The crystallography of $[Ni(SC_6H_4R\text{-}2)(triphos)]BPh_4$ (R= Me or MeO) and $[Ni(SC_6H_3Me_2\text{-}2,6)(triphos)]BPh_4$ shows that the geometry at Ni is square planar and Ni is 4-coordinate; but the geometry for $[Ni(SC_6H_4Cl\text{-}2)(triphos)]BPh_4$ is a square-based pyramid with the chloro-group occupying the apical position and Ni is 5-coordinate. The protonation of all synthesised complexes with both $lutH^+$ (lut= 2,6-dimethylpyridine) and $picH^+$ (pic= 4-methylpyridine) in MeCN were studied using stopped-flow spectrophotometry. These studies show that proton transfer reactions are slow and, in many cases, the hydrogen bonded

precursor intermediate {[Ni(thiolate)(triphos)]…Hlut}$^{2+}$ can be detected. For [Ni(SC_6H_4Cl-2)(triphos)]BPh_4, the rates of protonation with $lutH^+$ and $picH^+$ are significantly different (k^{pic}/k^{lut} = 2 x 10^3). However, for [Ni(SC_6H_4R-2)(triphos)]BPh_4 (R= H, Me or MeO) and [Ni($SC_6H_3Me_2$-2,6)(triphos)]BPh_4 complexes, the differences in the rates with $lutH^+$ and $picH^+$ are much less marked (k^{pic}/k^{lut} = 2 - 15) because the thiolate ligand can undergo relatively unhindered Ni-S rotation, allowing protonation from either side of the square plane. Protonation by $picH^+$ is substantially faster than with (the more sterically-demanding) $lutH^+$ because proton transfer in this complex must occur through a cavity in the surrounding phenyl substituents of triphos which is too small for $lutH^+$ to penetrate. DFT calculations support this proposal and allow further exploration of the effects that steric interactions between the phenyl groups for triphos and $lutH^+$ have on the rates of proton transfer to [Ni(thiolate)(triphos)]$^+$.

Table of Contents

PART I

PROTONATION AND BINDING OF SUBSTRATES TO SYNTHETIC Fe-S-BASED CLUSTERS

Chapter 1: Protonation and Binding Substrates to Fe-S-Based Clusters

1.1 Introduction.

In nature, the reduction of (N_2) into two (NH_3) molecules, is essential to all life, and this occurs biologically, by the action of microbial nitrogenase enzymes. These enzymes have been structurally characterised from the bacteria *Azotobacter vinelandii (Av)*, *Klebsiella pneumoniae (Kp)* and *Clostridium pasteurianum (Cp)*. There are three nitrogenases: Mo-nitrogenase (the most studied and the only one characterised by X-ray crystallography); V-nitrogenase and Fe-only-nitrogenase. All three nitrogenases comprise two essential proteins: the Fe-protein and the MFe-protein (M = Mo, V or Fe). The Fe-protein (Mol. Wt. ~ 65,000) is the smaller of the two proteins and contains a single $\{Fe_4S_4\}$ cuboidal cluster which mediates electron transfer from the external reductant (flavodoxin or ferredoxin) to the larger MFe-protein (Mol. Wt. ~ 220,000 for Mo-nitrogenase)[1]. The MFe-protein contains two unique Fe-S-based clusters: P-cluster which has a $\{Fe_8S_7\}$ core and FeM-cofactor with a composition of $\{MFe_7S_9C(R\text{-homocitrate})\}$[2], as shown in (Figure 1.1).

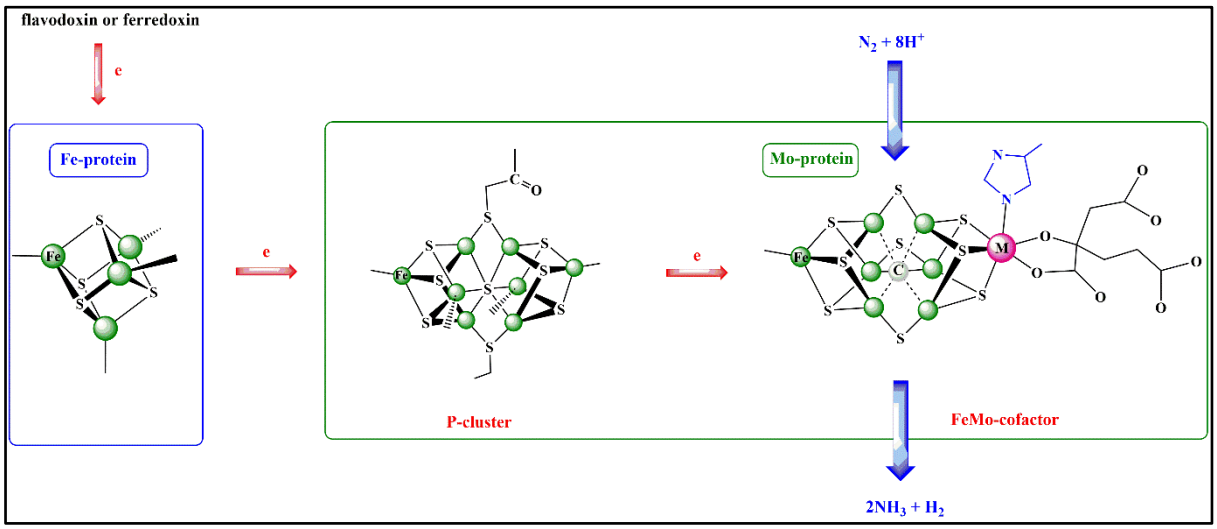

Figure 1.1. Composition of nitrogenases and structures of Fe-S-based clusters associated with each protein.

The P-cluster appears to be a capacitor which transfers electrons to the FeM-cofactor where N_2 is bound and transformed[3]. *In vitro* the enzyme is able to transform a variety of other small molecules and ions, known as alternate substrates (*e.g.* CN^-, N_3^-, RNC, RCN, NO_2^-, C_2H_2 …etc.), as shown in (Table 1.1).

Table 1.1. Transformation of various ions and molecules by the enzyme nitrogenase[4-12].

Substrates	Products	Equations
N_2	NH_3	$N_2 + 6H^+ + 6e^- \longrightarrow 2NH_3$
CN^-/HCN	HCHO, CH_4, NH_3, CH_3NH_2	$HCN + 6H^+ + 6e^- \longrightarrow CH_4 + NH_3$
CH_3NC	CH_3NH_2, $(CH_3)_2NH$, CH_4	$CH_3CN + 6H^+ + 6e^- \longrightarrow CH_3NH_2 + CH_4$
RCN	RCH_3, NH_3	$RCN + 6H^+ + 6e^- \longrightarrow RCH_3 + NH_3$
CH_2=CH-CN	CH_2=$CHCH_3$, C_3H_8, NH_3	CH_2=CH-CN + $8H^+ + 8e^- \longrightarrow C_3H_8 + NH_3$
NC-NH_2	CH_3NH_2, CH_4, NH_3	NC-$NH_2 + 8H^+ + 8e^- \longrightarrow CH_4 + 2NH_3$
CH_3N=NCH_3	CH_3NH_2, CH_4, NH_3	CH_3N=$NCH_3 + 6H^+ + 6e^- \longrightarrow CH_3NH_2 + CH_4 + NH_3$
N_3^-/HN_3	NH_3, N_2H_4	$N_3^- + 9H^+ + 8e^- \longrightarrow 3NH_3$
NO_2^-	NH_3, H_2O	$NO_2^- + 7H^+ + 6e^- \longrightarrow NH_3 + 2H_2O$
C_2H_2	C_2H_4, C_2H_6	$C_2H_2 + 2H^+ + 2e^- \longrightarrow C_2H_4$ $C_2H_2 + 4H^+ + 4e^- \longrightarrow C_2H_6$

Sulfide-based ligands are found in a significant number of metalloenzymes (*e.g.* carbon monoxide dehydrogenase CODH, aconitase, and Mo-based nitrogenase). The operation of these enzymes usually occurs in a protic environment and sometimes involve the transformation of the substrates by sequences of electron and proton transfer reactions. Some 25 years ago, the X-ray crystal structure of FeMo-cofactor (Figure 1.2) was reported[13]. This Fe-S-based cluster is the active site of the enzyme nitrogenase, where substrates are transformed by sequential addition of electrons and protons.

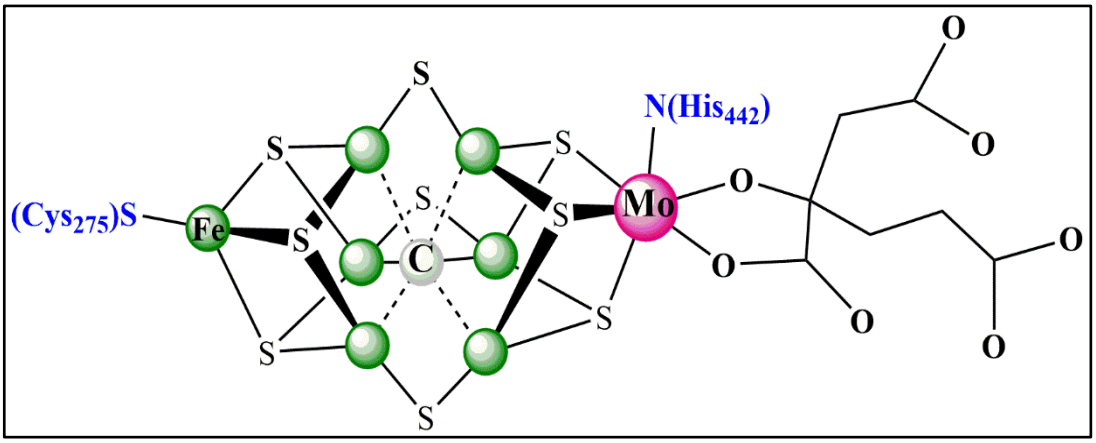

Figure 1.2. Structure of FeMo-cofactor.

Many Fe-S-based clusters have been synthesised in the laboratory and some of these clusters have some of the structural characteristics of FeMo-cofactor (Figure 1.2)[14-19]. Moreover, the research on the synthetic Fe-S-based clusters have established the general reactivity features of this type of cluster that are probably also characteristic of the reactions of the natural Fe-based clusters such as FeMo-cofactor. In this chapter, the reactivity features of the synthetic Fe-S-based clusters will be outlined, particularly involving binding of substrates that have been established through interpretation of kinetic studies. Furthermore, the protonation of the clusters will be presented, and its possible involvement in the substitution of ligands on the synthetic clusters.

1.2 Protonation of coordinated sulfides.

1.2.1 The sulfide ligands in biology.

Cuboidal Fe-S-based clusters are widespread in biology and they constitute the active sites for various proteins and enzymes which have been isolated and structurally characterised since the 1960s[20-25]. The structures of these clusters formally contain sulfide (S^{2-}) ligands. Most of these Fe-S-based clusters are redox centres and participate in the transfer of electron either within the protein (*e.g.* hydrogenase) or as mediators between two other proteins (*e.g.* transfer of electrons between the Fe protein and MoFe protein of nitrogenase). Earlier studies on a select number of enzymes[22, 24] indicate that the Fe-based cluster is a part of the active site (the site where substrate is bound and transformed). These enzymes include some of the most economically and environmentally important metalloenzymes (*e.g.* hydrogenases, nitrogenases, sulfite reductase and carbon monoxide dehydrogenase). Because the action of these enzymes includes the transfer of electrons as part of the substrate transformation, it is understandable why nature has chosen the active site to be a Fe-S-based cluster. However, the enzyme aconitase (and related

hydrolases) also use a Fe-based cluster as the active site. In this enzyme, the cluster is a non-redox centre and it only equilibrates citric and isocitric acid[23]. Apparently, the reason Fe-S-based clusters are chosen as active sites in an enzyme is attributable to more than their activity as electron transfer mediators. There are three types of Fe-S active sites in proteins all of which have been structurally characterised by X-ray crystallography (Figure 1.3). Rubredoxin is the simplest type, it comprises of coordination of a single Fe to the polypeptide by four cysteinate residues. The second type is plant ferredoxins which has the active site including a binuclear unit of two tetrahedral Fe atoms, bridged by two sulfurs (S^{2-}) and bound to the polypeptide by two cysteine residues bound to each Fe. Finally, in bacterial ferredoxins, the cuboidal cluster operates as the active site. The structure of this cluster contains, at each corner, alternating Fe and sulfur atoms and each Fe is coordinated to the polypeptide by a cysteine residue. Although all these structures of clusters represent the simplest of the natural Fe-S-clusters, more complex structures are known. For instance, the Reiske protein which includes the voided cuboidal Fe_3S_4 cluster and the Fe_2S_2 unit. In the Fe_2S_2 cluster, one of the two Fe atoms is coordinated by two histidine residues instead of two cysteine residues.

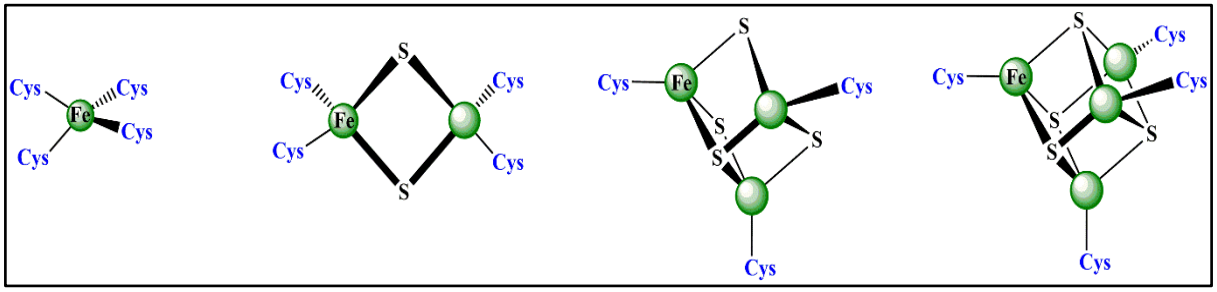

Figure 1.3. Common Fe-S geometries found in biology.

In some enzymes which utilize Fe-S-based clusters on the periphery of the active site, the Fe_4S_4 cuboidal clusters are coordinated to another metal-containing unit *via* a cysteinate residue [26] as in $[Fe_2(CO)_2(CN)_2(\mu\text{-OH})]$ (Fe-only hydrogenase); [Ni(Cys-Gly-Cys)] (CODH A-cluster) and siroheme (sulfite reductase) (Figure 1.4).

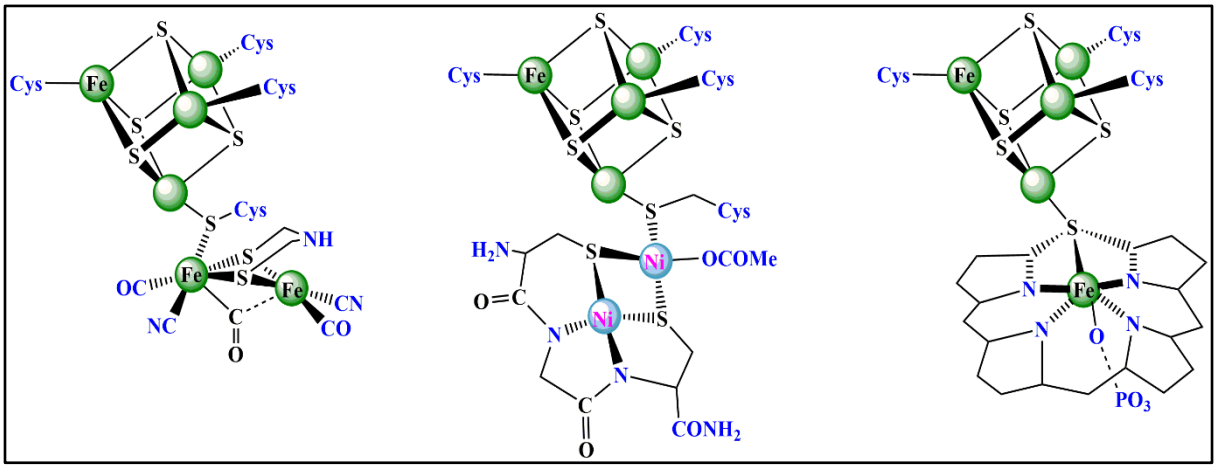

Figure 1.4. Active site structure for (left) Fe-only hydrogenase, (centre) ACS (A-cluster) and (right) sulfite reductase.

Furthermore, other unique clusters have been structurally identified in (i) Mo-based nitrogenase, which includes both the $\{Fe_8S_7\}$ P-cluster (probably electron storage) and the $\{MoFe_7S_9\}$ FeMo-cofactor (active site), and (ii) CODH (C-cluster), where it is a $\{Fe_4NiS_5\}$ cluster (Figure 1.5).

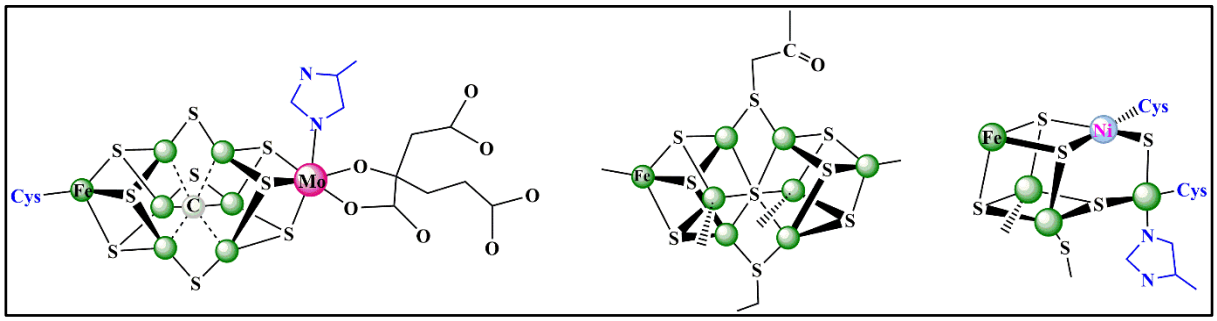

Figure 1.5. Active site structures in (left) FeMo-cofactor of nitrogenase, (centre) P-clusters of nitrogenase and (right) CODH (C-cluster).

1.2.2 Synthetic Fe-S-based clusters.

Efforts to develop synthetic Fe-S-based clusters, whose structures are accurate structural mimics for the natural clusters, was started in the early1970s[26]. An extensive range of Fe-S-based synthetic clusters, which are very close mimics of many of the natural clusters shown in Figure (1.4) and Figure (1.5), have been prepared. The spectroscopic and electrochemical properties of these synthetic clusters were compared with the natural sites. An unexpected feature of the synthesis of these synthetic clusters is that the formation of the dimeric and cuboidal structures does not require any exotic or protracted syntheses. The clusters form spontaneously when the reactants are mixed in the correct proportions (iron salt, thiolate and elemental sulfur). This has been named ‘spontaneous self-assembly’, and this term has stuck

despite studies that have described that there is nothing spontaneous about the assembly and that the cluster formation process involves a series of iron-containing intermediates of various nuclearities[27, 28].

Apparently, the types of synthetic clusters that can be prepared in the laboratory are larger than those found in nature. However, one of the main aims of research on synthetic clusters is to better understand the reactivity of natural Fe-S-based clusters. In the laboratory, a variety of synthetic clusters have been isolated and structurally characterised, with the most well-studied involving the cuboidal $\{Fe_4S_4\}^{2+}$ or $\{MFe_3S_4\}^{n+}$ (M= Mo, V, Nb, Re, W, Ni, Co, etc.) sub-cluster. Since the 1990s, the majority of studies have focused on the fundamental reactions of synthetic Fe-S-based clusters: substitution, protonation, binding of small molecules and ions and cluster assembly reactions[29, 30].

1.2.3 Protonation of Fe-S-based clusters.

Protonation of Fe-S-based clusters is important because protons are transformed into dihydrogen by both the FeMo-cofactor of nitrogenase and reduced synthetic Fe-S-based clusters. As well as protonation of the Fe-S-based clusters being (presumably) an essential prerequisite to produce dihydrogen, protons also play a major role as important reactants in the transformation of the substrates. Consequently, protons play two fundamental roles in the reactions of substrates with Fe-S-based clusters: (i) they are substrates which bind to the cluster prior to forming dihydrogen and (ii) they are reactants which bind to other coordinated substrates during the transformation of the substrate to product.

In 1975, Dukes and Holm reported[31] the first study of the substitution reactions of synthetic Fe-S-based clusters. They studied the kinetics of the reaction of the cuboidal $[Fe_4S_4(SBu^t)_4]^{2-}$ with a series of substituted arylthiols (RC_6H_4SH) when R = 4-NO_2, 2-NO_2, 4-NH_2 and 4-CH_3 in acetonitrile (MeCN) as the solvent. This reaction exhibited a first-order dependence on the concentrations of both the cluster and the thiol; and the rate of the reaction increased with the acidity of the thiol. The proposed mechanism of the reaction involved rate-limiting proton transfer as shown in (Figure 1.6). This proposal requires to be tested because there are lone pair electrons on the sulfurs of both the core of cluster and the thiolate ligands so the protonation of these sites might be expected to be faster than the act of substitution. It is important to study this fundamental type of reaction, when the protons transfer were slow, to understand the reactions of natural Fe-S-based clusters with protons. Although the straightforward way to do this would be to study the simple proton transfer from an acid to the cluster, the problem is that such a

simple reaction is difficult to follow spectroscopically. In general, the clusters have paramagnetic properties, so their nuclear magnetic resonance (NMR) spectra comprise broad and paramagnetically shifted peaks, and the electron paramagnetic resonance (EPR) spectra are complicated by the multiple spin states associated with the clusters. Moreover, the infra-red (IR) spectrum does not contain sufficiently diagnostic peaks associated with the protonated cluster. Finally, the electronic (UV-visible) spectra of the protonated clusters are indistinguishable from that of the parent clusters. Consequently, the best approach to monitor the protonation of cluster is observing the effect that acids have on the rate of substitution of the terminal ligands. This is because the substitution reactions are associated with relatively large UV-visible spectroscopic changes.

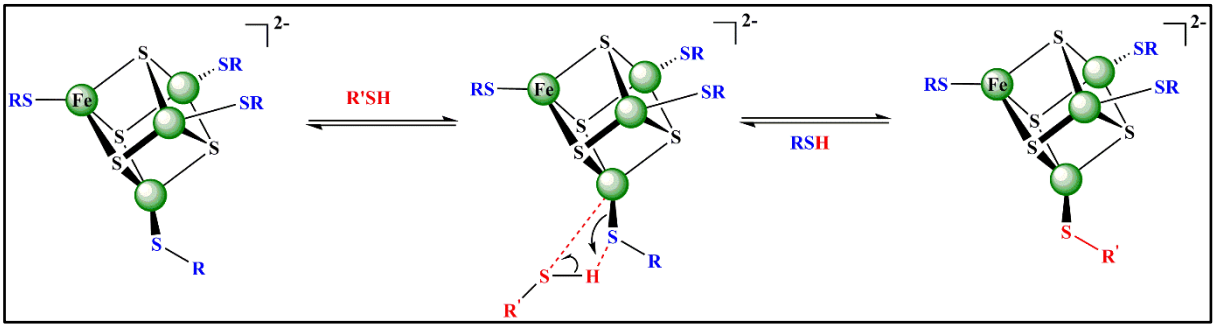

Figure 1.6. Mechanism proposed by Dukes and Holm for the reaction between $[Fe_4S_4(SR)_4]^{2-}$ and R′SH.

The earliest studies on the substitution reactions of the terminal ligands of synthetic Fe-S-based clusters by a nucleophile, in the presence of varying concentrations of acid ($NHEt_3^+$) and conjugate base (NEt_3), employed the system shown in (Figure 1.7)[32-36]. Although $NHEt_3^+$ is a sufficiently strong acid (pK_a = 18.4 in MeCN)[37] to protonate the cluster, it is not strong enough to decompose the cluster. In these substitution reactions, all reactants are present in a large excess over that of the cluster ([reactant]/ [cluster] ≥ 10). A significant point is that the substitution of terminal alkylthiolate ligands of $[Fe_4S_4(SR)_4]^{2-}$ cluster should be replaced by arylthiolates in order that there is a significant UV-visible spectroscopic change. However, if an alkylthiolate is substituted by another alkylthiolate (or arylthiolate by another arylthiolate) there is little appreciable spectroscopic changes.

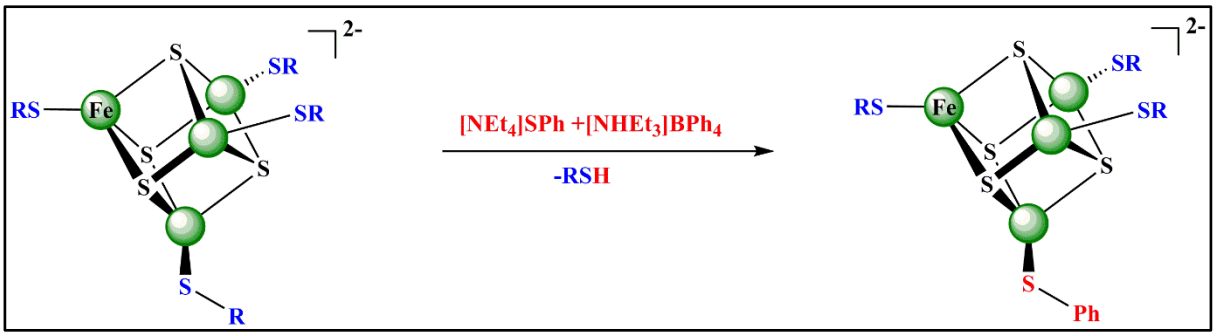

Figure 1.7. Components used to study the acid-catalysed substitution reactions of synthetic Fe-S-based clusters.

In acetonitrile (MeCN), the acid ($NHEt_3^+$) rapidly reacts with nucleophile (PhS^-) according to the protolytic equilibrium shown in Equation (1.1). Because the pK_a of PhSH is > 21[38], any solution containing mixtures of $[NHEt_3^+]_0$ and $[PhS^-]_0$, which are the total concentrations of the respective reagents, the equilibrium concentration of compounds $[NHEt_3^+]_{free}$ and $[PhS^-]_{free}$ can be readily calculated (provided $[NHEt_3^+]_0 > [PhS^-]_0$) utilizing the expressions: $[NHEt_3^+]_{free} = [NHEt_3^+]_0 - [PhS^-]_0$ and $[PhSH]_{free} = [NEt_3]_{free} = [NHEt_3^+]_{free} - [PhS^-]_0$. Therefore, it is possible to independently control the concentrations of acid, base, and nucleophile and then determine the effect each has on the kinetics of the reaction. There are two different limiting conditions in the solution mixtures of $[NHEt_3^+]_0$ and $[PhS^-]_0$. In the first limiting condition, when $[NHEt_3^+]_0 \geq [PhS^-]_0$, and under this condition PhSH is the nucleophile present since there is no PhS^- present. In the second limiting condition, $[NHEt_3^+]_0 < [PhS^-]_0$, there are mixtures of both PhS^- and PhSH present in solution and hence interpretation of the kinetics is complicated because of the presence of the two nucleophiles. For simplicity, all kinetics were studied in the presence of an excess of $NHEt_3^+$.

$$NHEt_3^+ + PhS^- \rightleftharpoons NEt_3 + PhSH \qquad (1.1)$$

The kinetics of the substitution reaction of $[Fe_4S_4(SEt)_4]^{2-}$ with PhSH in the presence of $NHEt_3^+$ and NEt_3 show that the rate of the reaction is independent of [PhSH], but it exhibits a non-linear dependence on the ratio ($[NHEt_3^+]_{free}/[NEt_3]_{free}$). It is notable that the rate of reaction depends only on this ratio and not on the absolute concentrations of $NHEt_3^+$ or NEt_3. Thus, at low values of $[NHEt_3^+]_{free}/[NEt_3]_{free}$, the rate of reaction exhibits a first order dependence on the ratio, and at high values of $[NHEt_3^+]_{free}/[NEt_3]_{free}$, the rate is independent of the ratio as shown in (Figure 1.8).

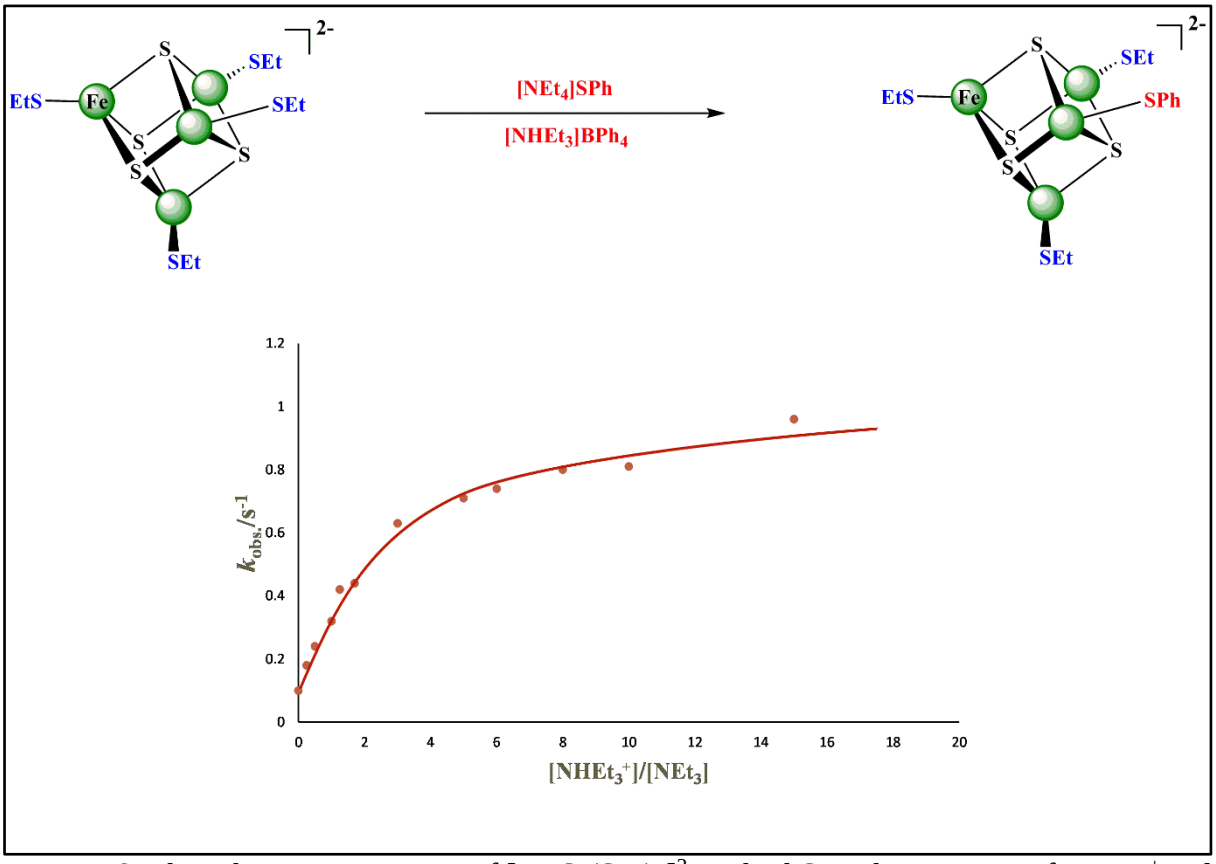

Figure 1.8. The substitution reaction of $[Fe_4S_4(SEt)_4]^{2-}$ with PhS^- in the presence of $NHEt_3^+$ and NEt_3, dependence of the reaction rate on the ratio $[NHEt_3^+]/[NEt_3]$. This behaviour is typical of all synthetic Fe-S-based clusters.

The rate law in Equation (1.2) is consistent with the mechanism shown in (Figure 1.9). The top line of this mechanism shows a non-catalysed pathway (k_0) which involves the rate limiting unimolecular dissociation of an ethanthiolate ligand from Fe site prior to binding of the PhS^-. The other pathway is consistent with an acid-catalysed dissociative substitution reaction in which a single proton rapidly binds to a μ_3-S (K_1) and this labilises the cluster to substitution of the terminal ethanthiolate ligands (k_2). After protonation step an ethanthiolate ligand dissociates to produce a vacant site on the Fe and then the PhSH nucleophile attacks this vacant site to complete the substitution. The derivation of Equation (1.2) assumes the substitution step is rate-limiting. The rate law in Equation (1.2) is presented in Appendix A (***section A.1***).

$$\frac{-\mathrm{d}[\mathrm{cluster}]}{\mathrm{dt}} = \frac{(k_0 + K_1 k_2 [\mathrm{NHEt_3^+}]/[\mathrm{NEt_3}])[\mathrm{cluster}]}{1 + K_1 [\mathrm{NHEt_3^+}]/[\mathrm{NEt_3}]} \qquad (1.2)$$

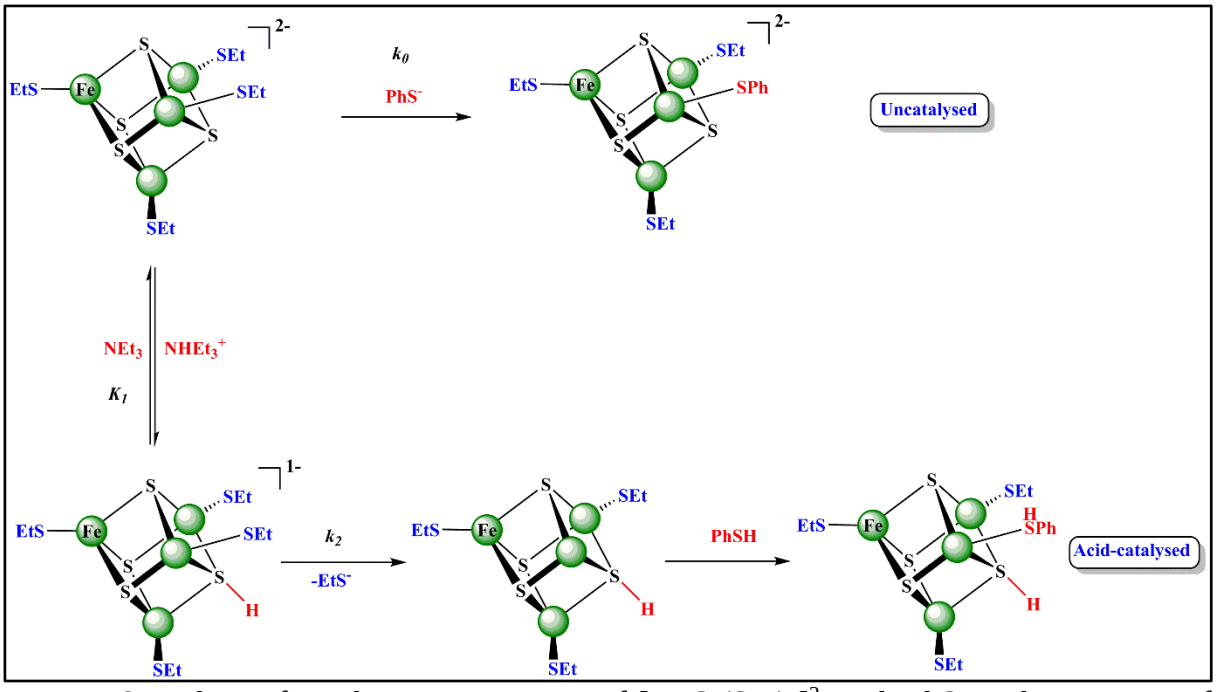

Figure 1.9. Pathway for substitution reaction of $[Fe_4S_4(SEt)_4]^{2-}$ with PhS^- in the presence of $NHEt_3^+$ and NEt_3.

1.2.4 Features of the protonation step.

The kinetics of the acid-catalyzed substitution reactions of synthetic Fe-S-based clusters, particularly the dependence on the ratio ($[NHEt_3^+]_{free}/[NEt_3]_{free}$), indicate that a single proton rapidly binds to the cluster and labilises the terminal ligand of the cluster to substitution. This step involves an equilibrium step when the proton transfers from $NHEt_3^+$ acid to the cluster in the forward reaction and the protonated cluster is deprotonated by NEt_3 base in the back reaction. The dependence on ($[NHEt_3^+]_{free}/[NEt_3]_{free}$) is not consistent with $NHEt_3^+$ just hydrogen bonding to the Fe-S-based cluster. Studies on the substitution reactions of $[FeCl_4]^-$ with PhS^- demonstrate that $NHEt_3^+$ binds to the complex through hydrogen bonding and this interaction modulates the rate of the substitution reaction[39]. In this situation the rate of substitution reaction will be accelerated not due to protonation but by formation of the ion-pair $\{[NHEt_3^+].[FeCl_4^-]\}$ which is more labile to substitution than the parent $[FeCl_4]^-$. The proton in this ion-pair $\{[NHEt_3^+].[FeCl_4^-]\}$ may not transfer completely but it probably involve hydrogen bonding between the acidic N-H and the chloro-ligands. The formation of this ion-pair increases the rate of substitution reaction but significantly less than the effect of proton transfer.

Returning to the mechanism shown in (Figure 1.9), the values of K_1 (protonation equilibrium constant of the cluster) and k_2 (rate constant for substitution) can be calculated using Equation (1.2). Moreover, the apparent value of the pK_a of the cluster can be determined knowing the value of K_1 and the pK_a of $NHEt_3^+$ in MeCN (pK_a = 18.4). Further analogous studies on other

synthetic Fe-S-based clusters have been performed, and the results are presented in Table (1.2)[40]. It can be seen that the values of the apparent pK_a of all different clusters fall on the limited range of 17.9-18.9 (in MeCN)[30, 40, 41], in spite of change in either the composition of cluster or terminal ligands. Because of this insensitivity of the pK_a to the composition and structure of the cluster, it has been suggested that the protonation site is the bridging core sulfur of cluster, and not the terminal ligands. This suggestion has been supported through studies of the protonation for both $[Fe_4S_4(SR)_4]^{2-}$ and $[Fe_4S_4Cl_4]^{2-}$ clusters with the same acid ($NHEt_3^+$). These studies show that the calculated pK_as of these two clusters are very similar notwithstanding that the pK_as of the corresponding protonated ligands are very different (pK_a of PhSH > 21[38] and pK_a of HCl = 10.4[42] in MeCN), so this is a strong evidence that the detected protonation is not on the terminal thiolate.

Table 1.2. The pK_as of synthetic Fe-S-based clusters determined from the kinetics of the acid-catalysed substitution reactions in MeCN[30,40,41].

	Cluster	**pK_a**
Fe-Cl clusters:	$[Cl_2FeS_2VS_2FeCl_2]^{3-}$	17.9
	$[S_2MoS_2FeCl_2]^{2-}$	17.9
	$[Fe_4S_4Cl_4]^{2-}$	18.8
	$[\{MoFe_3S_4Cl_3\}_2(\mu\text{-}SEt)_3]^{3-}$	18.6
	$[\{WFe_3S_4Cl_3\}_2(\mu\text{-}SEt)_3]^{3-}$	18.2
	$[\{WFe_3S_4Cl_3)_2(\mu\text{-}OMe)_3]^{3-}$	18.4
	$[Fe_2S_2Cl_3(NCMe)]^-$	18.1
	$[Fe_6S_6Cl_2(PEt_3)_4]$	18.0
Fe-SR clusters:	$[Fe_4S_4(SPh)_4]^{2-}$	18.6
	$[Fe_4S_4(SEt)_4]^{2-}$	18.0
	$[\{MoFe_3S_4(SEt)_3\}_2(\mu\text{-}SEt)_3]^{3-}$	18.1
	$[\{WFe_3S_4(SEt)_3\}_2(\mu\text{-}SEt)_3]^{3-}$	18.3
	$[Fe_6S_9(SEt)_2]^{4-}$	17.9

In most kinetic studies, the reactions of the synthetic Fe-S-based clusters are investigated in the aprotic solvent MeCN, not in a protic solvent. This is in contrast to the natural Fe-S-clusters which are in the protic solvent water. For comparison with the natural Fe-S-based cluster, it

would be appropriate to observe the acid-catalyzed substitution reaction of the synthetic cluster in water. The substitution reaction of $[Fe_4S_4(SCH_2CH(OH)Me)_4]^{2-}$ with PhS^- has been studied in the presence of $NHEt_3^+$ as acid, in methanol (MeOH) as protic solvent[43]. This study shows that the protonation labilises the terminal substituent by a dissociative mechanism, and the kinetics and mechanism are similar to that observed for the other synthetic Fe-S-based clusters reacting in the aprotic solvent (MeCN). The calculated pK_a of the cluster $[Fe_4S_4(SCH_2CH(OH)Me)_4]^{2-}$ is 8.5 (in methanol). Further studies on $[Fe_4S_4(SCH_2CH_2CO_2)_4]^{6-}$ show pK_a = 7.4 for this cluster in water[44].

General investigation indicates that the structure of cuboidal $\{Fe_4S_4\}^{2+}$ has four potential protonation sites, which are core sulfur, Fe, terminal ligand and above a $\{Fe_2S_2\}$ face, and the structure of cuboidal $\{MFe_3S_4\}^{n+}$ has eight potential protonation sites, which are core sulfur bound to only Fe, core sulfur bound to M and Fe, terminal ligand bond to Fe, terminal ligand bound to M, above a $\{Fe_2S_2\}$ face or above a $\{MFeS_2\}$ face. Nevertheless, the kinetic observations indicated that the protonation occurs on bridging sulfur and this seems reasonable based on the expected relative basicities of the cluster components. The studies measuring the binding affinities of 4-YC_6H_4COCl (Y = MeO, H or Cl) to $[Fe_4S_4(SR)_4]^{2-}$ (R = Ph, Et or Bu^t) suggest that the acid chlorides probably bind to the cluster in a multi-site interaction, as shown in Figure (1.10). These studies focused on observation of maximum binding affinity of the acid chloride (which contained the most electron-withdrawing 4-Y-substituents). An analogous type of interaction, where the proton was proposed to bind above a Fe_2S_2 face, has been suggested[44-46]. Figure 1.10 shows how the acid chlorides binding to the cluster with both the acyl oxygen binding to the Fe and the carbonyl carbon interacting with the sulfur of the terminal thiolate.

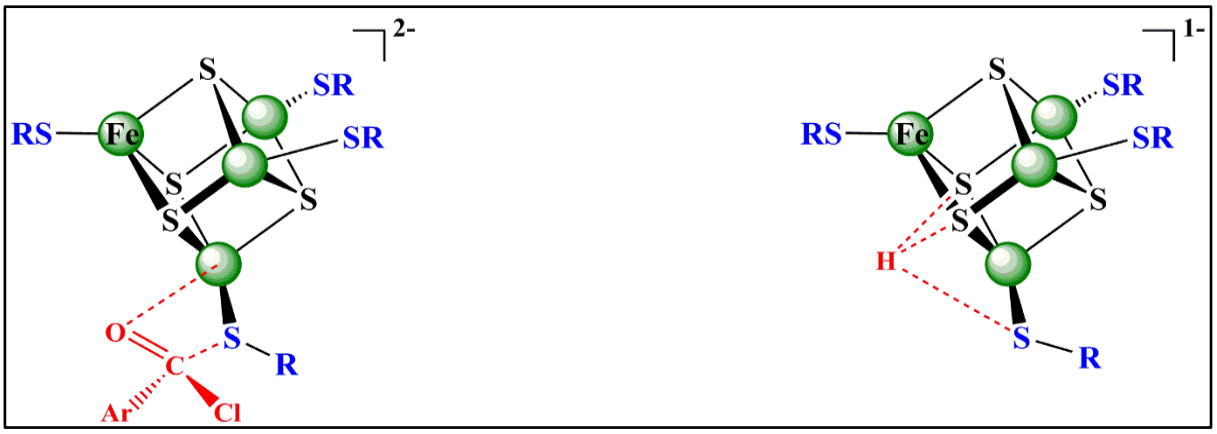

Figure 1.10. Suggested binding of acid chloride to $[Fe_4S_4(SR)_4]^{2-}$, on the left showing involvement of terminal thiolate ligand and on the right, is a possible structure for proton binding to the cluster involving a similar interaction with the terminal thiolate and core sulphides.

In acid-catalysed substitution reactions of synthetic Fe-S-based clusters, the stereochemical relationship between the site of protonation and the site of substitution has been investigated [47]. In Fe-S-based clusters, there are several sites of protonation as well as several sites of substitution, so the problem of matching up a particular protonation site with a particular substitution site is complicated. However, the study on $[Cl_2FeS_2VS_2FeCl_2]^{3-}$, indicates that the site of protonation should be adjacent to the site of substitution[47].

The metal sites in most Fe-S-based clusters are magnetically coupled and hence communicate with one another. However, in the linear trinuclear cluster $[Cl_2FeS_2VS_2FeCl_2]^{3-}$, it is notable that the two Fe sites are chemically equivalent but the two Fe atoms are magnetically isolated by the central V atom[48]. Studies on the substitution reaction of the terminal chloro-ligands in $[Cl_2FeS_2VS_2FeCl_2]^{3-}$ with PhSH in the presence of $NHEt_3^+$ and NEt_3 indicate that the Fe sites undergo both uncatalysed and acid-catalysed substitution reactions. The uncatalysed substitution reaction is slow and dissociative. However, the acid-catalysed substitution reaction, which displays a first-order dependence on the concentration of PhSH, is fast and associative. The species $[Cl_2FeS_2VS(SH)FeCl_2]^{2-}$ is produced after the initial protonation step and then this species undergoes substitution. The associative substitution step can happen either on the Fe atom next to SH and this substitution is fast. Alternatively, the substitution can occur on the Fe centre the other side of the V atom. In this case, the V shields the labilising effect of the SH group and hence, the substitution at the remote Fe is little perturbed by the protonation, as shown in Figure (1.11).

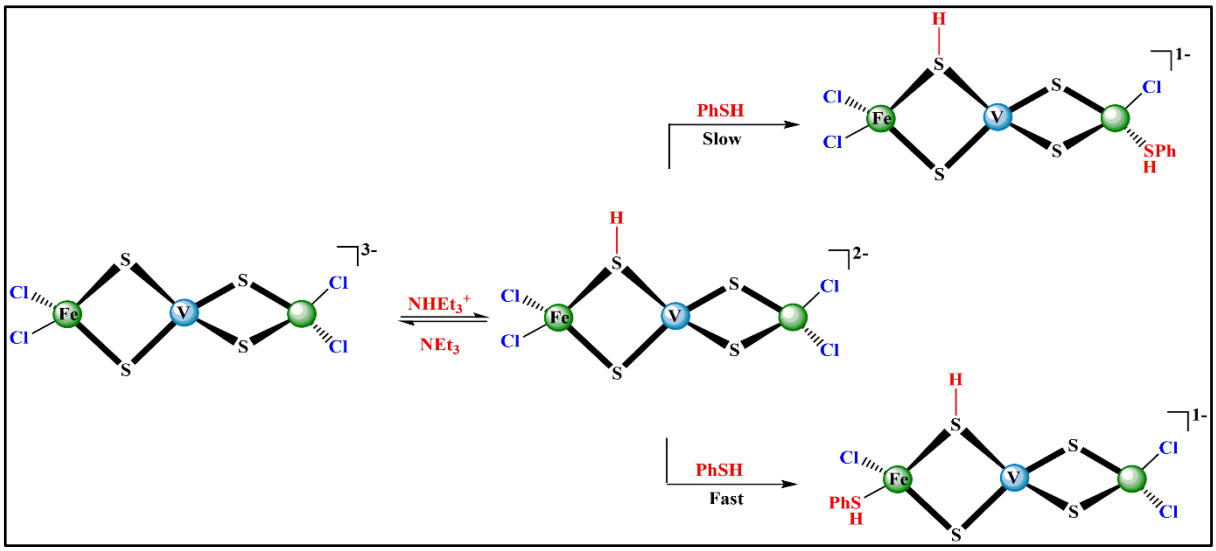

Figure 1.11. Alternative pathways for the acid-catalysed substitution reaction of $[Cl_2FeS_2VS_2FeCl_2]^{3-}$ with PhSH in presence of $NHEt_3^+$ and NEt_3. The top pathway involves protonation and substitution at sites remote from one another. The bottom pathway involves protonation and substitution at adjacent sites.

In the acid catalysed substitution reactions of the Fe-S-based clusters, if the nucleophile-binding site must be adjacent to the protonation site, it is worth considering the corresponding reactions of cuboidal clusters as shown in Figure (1.12). It can be noted that all Fe atoms are equivalent in cuboidal $[Fe_4S_4X_4]^{2-}$, but after the protonation step three of these Fe atoms are adjacent to SH whilst one Fe is remote from the protonated site. Hence, it could be expected that the substitution reaction on the three equivalent Fe atoms is faster than protonation at the single remote Fe. In the cuboidal $[MFe_3S_4X_3]^{n-}$ (M=Mo, V, W, Nb or Re), despite all three Fe sites are equivalent, the S sites are differentiated: three sulfurs are bound to M, but the fourth sulfur is bound only to Fe. In addition, in cuboidal $[MFe_3S_4X_3]^{n-}$, if the protonation occurs at any of the μ_3-S sites bound to M that means just two Fe sites will be adjacent to protonated site and consequently the substitution is facilitated at these sites. In contrast, all three Fe sites are labilised when protonation occurs at the unique μ_3-S as shown in Figure (1.12).

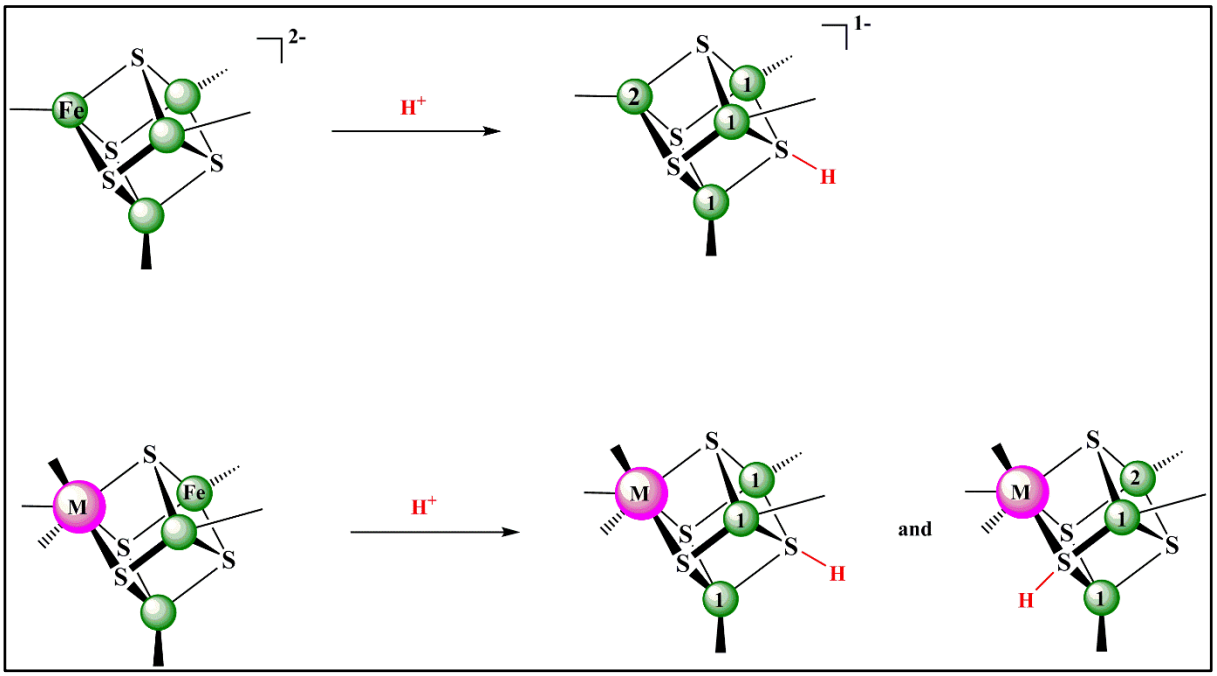

Figure 1.12. Fe site discrimination in cuboidal Fe-S-based clusters after protonation of core S.

The kinetic studies of the substitution reaction of Fe-S-based clusters, for both associative and dissociative mechanisms, indicate that the substitution step is facilitated by prior protonation. Here will be considered the electronic factors that can occur upon protonation. It would be anticipated that protonation would distort the electron density of the parent cluster, and the electron density will be pulled towards the protonation site and that will lead to decrease the electron density at the site of substitution (particularly Fe sites adjacent to the SH). Thus, the protonation will facilitate attack of the nucleophile in an associative substitution step[3].

A broader understanding of the electronic effects on the lability of the clusters, and particularly the rate of dissociation of the terminal chloro-ligands in the reactions of $[Fe_4S_4Cl_4]^{2-}$, was revealed in reactions using the series of 4-$RC_6H_4S^-$ nucleophile (R = H, Me, MeO, Cl or CF_3)[49]. The substitution reactions of $[Fe_4S_4Cl_4]^{2-}$ with 4-$RC_6H_4S^-$ to produce $[Fe_4S_4(SC_6H_4R\text{-}4)Cl_3]^{2-}$ occurs by an associative mechanism where the thiolate ion binds to the cluster and then the chloro-group dissociates. The effect of the 4-R-thiolate substituent on the lability of the Fe-Cl bond can be observed by analysis of the kinetics data which allows calculation of the rate constant for dissociation of the chloro-ligand from the intermediate $[Fe_4S_4(SC_6H_4R\text{-}4)Cl_4]^{3-}$. The surprising observation is that the lability of the chloro-group increases when the 4-R-substituent becomes more electron-withdrawing. From the mechanism, it would have been expected that electron-withdrawing 4-R-substituents would increase Fe-Cl bond strength and hence decrease the rate of dissociation. This result suggests that the electron-withdrawing substituents reduce the anion-anion repulsion felt in the transition state as the thiolate approaches the cluster and this is an important factor in facilitating the reaction.

1.2.5 The rate of proton transfer to Fe-S-based clusters.

The earlier studies on the acid-catalyzed substitution reactions of synthetic Fe-S-based clusters (described in ***section 1.2.4***) showed that the protonation of Fe-S-based clusters by $NHEt_3^+$ occurred prior to the act of substitution, and it is faster than the act of substitution. This behaviour allow determination of the apparent pK_a values of the protonated cluster, but it does not allow measurement of how rapidly protons are transferred. Henderson and Oglieve established a limit for the rate constant of proton transfer from $NHEt_3^+$ to core of cluster ($K \geq 2$ x 10^5 dm^3 mol^{-1} s^{-1}), this study indicates that the proton transfer is complete within the dead time of the stopped-flow apparatus, 1-2 ms, even when $[NHEt_3^+]$ = 1.0 mM[38]. To make proton transfer rate-limiting, a much weaker acid than $NHEt_3^+$ was used, such as the pyrrolidinium ion ($pyrrH^+$, pK_a = 21.5 in MeCN)[37]. As shown in Table (1.2), all pK_as of synthetic Fe-S-based clusters fall in the limited range of 17.9 - 18.9, furthermore this study indicates that the rate of proton transfer from $pyrrH^+$ to core of cluster is 10^4-10^5 times slower than the diffusion-controlled limit, so the protonation of a cluster in presence of $pyrrH^+$ acid is thermodynamically unfavourable with the associated equilibrium constants determined to be in the range of K_H =10^{-3}-10^{-4} [37] (K_H = the homoconjugation constant for the equilibrium shown in Equation 1.3).

$$\overline{[NH_2(CH_2)_3CH_2]}^{+} + \overline{NH(CH_2)_3CH_2} \underset{}{\overset{K_H}{\rightleftharpoons}} \overline{[NH(CH_2)_3CH_2]_2H^+} \qquad (1.3)$$

As a result, the rates of proton transfer to synthetic clusters from $pyrrH^+$ are slower than those in presence of $NHEt_3^+$. Parenthetically, in the substitution reactions of Fe-S-based cluster with PhS^- in presence of both $pyrrH^+$ and $NHEt_3^+$, there are two steps (protonation and substitution). Which step is rate-limiting in the acid-catalyzed substitution reactions of any synthetic Fe-S-based cluster will depend on the concentration of either the acid or the nucleophile[50]. The $pyrrH^+$ is too weak an acid to protonate free PhS^- to produce free PhSH, so the solution mixtures contain only $pyrrH^+$ and PhS^-. Consequently, in the reactions with $pyrrH^+$ the nucleophile is always PhS^-. For the substitution reactions of cluster in the presence of $pyrrH^+$, we will consider the two specified cases, the binding of nucleophile before the proton transfer and the binding of nucleophile after the proton transfer.

1.2.6 Kinetics of the binding of nucleophile before the proton transfer.

In the substitution reaction of the chloro-ligand of $[Fe_4S_4Cl_4]^{2-}$ by PhS^- in presence of $pyrrH^+$, the PhS^- directly binds to the cluster before the proton transfer. In this mechanism, the kinetics show a first order dependence on the concentration of PhS^- and a non-linear dependence on the concentration of $pyrrH^+$ as an acid. These kinetics are consistent with the mechanism shown in Figure (1.13). The mechanism of the reaction of $[Fe_4S_4Cl_4]^{2-}$ with PhS^- and $pyrrH^+$ includes: the initial step involves binding of PhS^- to the cluster to produce $[Fe_4S_4Cl_4(SPh)]^{3-}$ as intermediate and after that this intermediate converts to the product $[Fe_4S_4(SPh)Cl_3]^{2-}$ as substituted cluster after dissociation of a terminal chloro-ligand. This is the dominate pathway of the normal associative substitution mechanism between $[Fe_4S_4Cl_4]^{2-}$ and it operates at low concentration of acid ($pyrrH^+$). In contrast, at high concentration of acid ($pyrrH^+$), the rate of protonation of $[Fe_4S_4Cl_4(SPh)]^{3-}$ by $pyrrH^+$ will exceed the rate of dissociation of the chloro-ligand from $[Fe_4S_4Cl_4(SPh)]^{3-}$, and this becomes the dominate pathway in the reaction. The rate law in Equation (1.4) was used[38, 50, 51] to calculate the rate constant values (k_3, k_{-3}, k_4^{PhS} and k_5) for the substitution reaction of $[Fe_4S_4Cl_4]^{2-}$ with PhS^- in the presence of $pyrrH^+$ or absence of $pyrrH^+$.

$$\frac{-d[\text{cluster}]}{dt} = \frac{\left(k_3k_5 + k_3k_4^{\text{PhS}}[\text{pyrrH}^+]\right)[\text{PhS}^-][\text{cluster}]}{k_{-3} + k_5 + k_4^{\text{PhS}}[\text{pyrrH}^+]} \qquad (1.4)$$

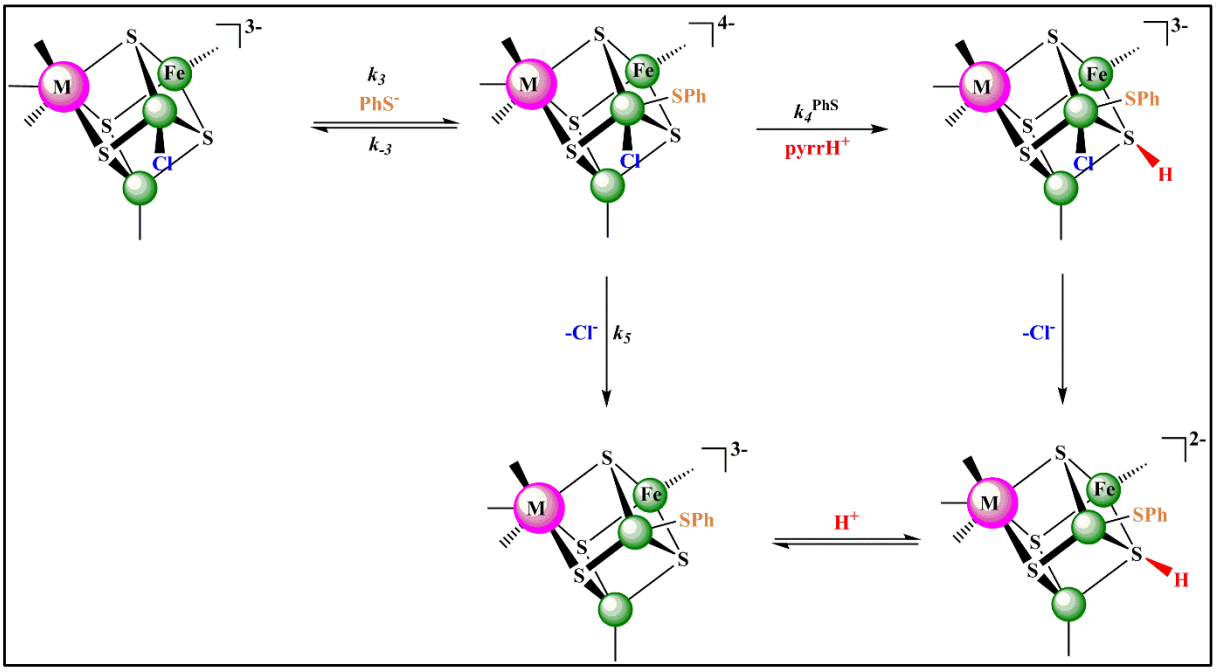

Figure 1.13. Mechanism for the reaction of the Fe-S-based clusters with PhS^- in the presence of $pyrrH^+$, where the nucleophile binds before the protonation.

1.2.7 Kinetics of the binding of nucleophile after the proton transfer.

In the substitution reaction of Fe-S-based cluster in presence of acid, the proton transfer occurs before the nucleophile binds to cluster when the nucleophile is weak (binds slowly to cluster). This behaviour is clearly observed when the nucleophile is (Br^- or I^-)[51]. For example, the kinetics of the reaction of $[Fe_4S_4Cl_4]^{2-}$ with Br^- in presence of $pyrrH^+$ shows a first order dependence on the concentrations of the cluster and $pyrrH^+$, but are independent of the concentration of nucleophile (Br^-) as shown in Equation (1.5). Figure (1.14) shows the mechanism of this reaction which involves the protonation of the cluster by $pyrrH^+$ in the initial step and the next step is the substitution of the terminal ligand by the nucleophile, which can be an associative or dissociative substitution mechanism.

$$\text{Rate} = k_6[\text{pyrrH}^+][\text{cluster}] \qquad (1.5)$$

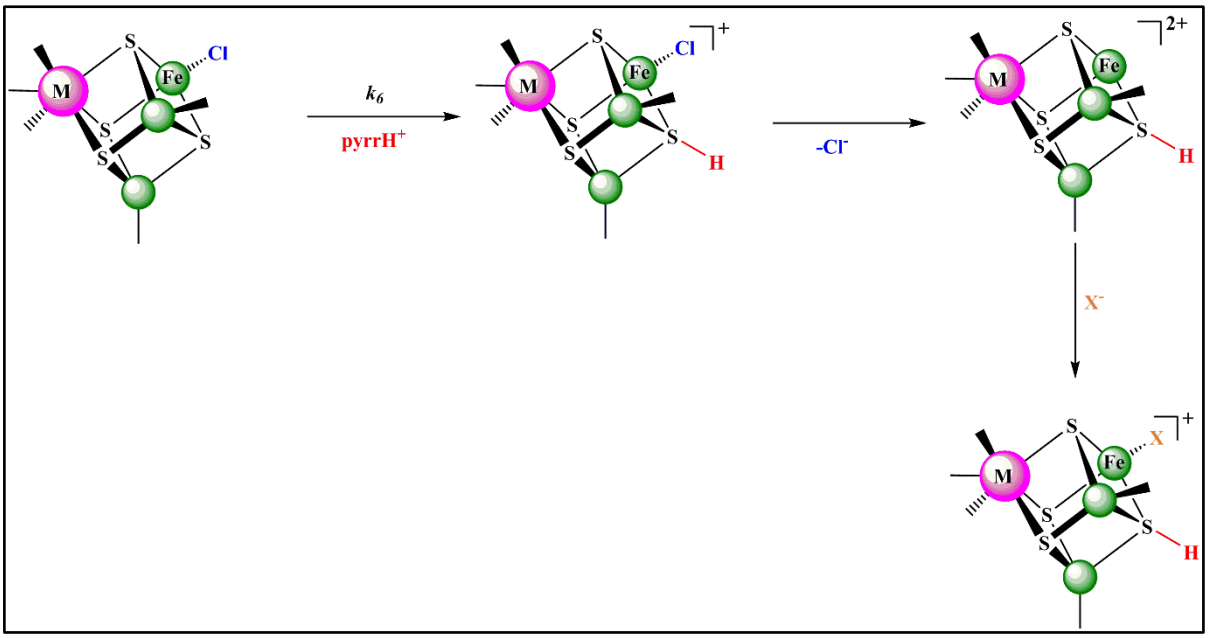

Figure 1.14. Mechanism for the reaction of the Fe-S-based clusters with X^- (X^- = halide) in the presence of $pyrrH^+$, where the nucleophile binds after the protonation.

1.2.8 Rate constant for proton transfer to Fe-S-based clusters.

From the two types of mechanisms described in Figure 1.13 and Figure 1.14, analysis of the kinetics allows determination of the rate constants for the proton transfer from the acid ($pyrrH^+$) to the clusters in both cases (before and after) binding of nucleophile (PhS^-)[38, 50, 51]. Table (1.3) presents the rate constants for proton transfer to the various clusters.

Table 1.3. The rate constants for proton transfer to various synthetic Fe-S-based clusters (k_6) and the same clusters containing an additional bound PhS^- (k_4^{PhS}).

Rate constants for proton transfer			
Cluster	**ΔpK_a**	**k_6 /dm^3 mol^{-1} s^{-1}**	**k_4^{SPh} /dm^3 mol^{-1} s^{-1}**
$[Fe_4S_4Cl_4]^{2-}$	2.7	2.4×10^4	1.8×10^6
$[\{MoFe_3S_4Cl_3\}_2(\mu\text{-SEt})_3]^{3-}$	2.9	2.5×10^2	6.0×10^6
$[\{MoFe_3S_4Cl_3\}_2(\mu\text{-SPh})_3]^{3-}$		5.0×10^2	1.6×10^6
$[\{WFe_3S_4Cl_3\}_2(\mu\text{-SEt})_3]^{3-}$	3.3	8.5×10^2	2.5×10^3
$[\{WFe_3S_4Cl_3\}_2(\mu\text{-OMe})_3]^{3-}$	3.1		7.2×10^3
$[Fe_2S_2Cl_4]^{2-}$	3.4	1.9×10^3	8.8×10^3
$[S_2MoS_2FeCl_2]^{2-}$	3.6	1.0×10^5	
$[S_2WS_2FeCl_2]^{2-}$	3.4	2.0×10^5	

A further feature of the data in Table (1.3), is that the rates of proton transfer to the clusters do not correlate with the apparent thermodynamic driving force of the reactions. As shown in Table (1.2), there is little change in the pK_as associated with change in the composition of Fe-S-based clusters, so the differences in the thermodynamic driving forces for the reactions of the various clusters ($\Delta pK_a = pK_a^{pyrrH} - pK_a^{cluster}$) are small. It is clear that the thermodynamic driving force is not a main factor controlling the rates of protonation as is indicated by only the following two observations. (i) For the cuboidal Fe-S-based clusters, the rate of proton transfer from the acid ($pyrrH^+$) to the cluster $[Fe_4S_4Cl_4]^{2-}$ ($\Delta pK_a = 2.7$) is $k = 2.4 \times 10^4$ dm^3 mol^{-1} s^{-1}, however the rate of proton transfer from $pyrrH^+$ to $[\{WFe_3S_4Cl_3\}_2(\mu\text{-}SEt)_3]^{3-}$ ($\Delta pK_a = 3.3$) is $k = 8.5 \times 10^2$ dm^3 mol^{-1} s^{-1}. (ii) For the reaction of both $[Fe_2S_2Cl_4]^{2-}$ and $[S_2WS_2FeCl_2]^{2-}$ with $pyrrH^+$, although the thermodynamic driving force is the same ($\Delta pK_a = 3.3$), the rates of protonation are appreciably different (for $[Fe_2S_2Cl_4]^{2-}$, $k = 1.9 \times 10^3$ dm^3 mol^{-1} s^{-1}; for $[S_2WS_2FeCl_2]^{2-}$, $k = 2.0 \times 10^5$ dm^3 mol^{-1} s^{-1}).

Further studies applied on the broad range of synthetic cuboidal clusters of the type $[\{MFe_3S_4Cl_3\}_2(\mu\text{-}L)_3]^{3-}$ (M = Mo, W, V, Nb, Ta or Re; L = thiolate or alkoxide)[22, 26, 52]. The comparison for reactivities of these clusters allows delineation of the effects of changing one of the metals (M) in the cluster core, and the effect of changing the bridging ligands (L) which are bonded to M and hence remote from the substitution sites (on the Fe). The protonation reactions of isostructural clusters $[\{MFe_3S_4Cl_3\}_2(\mu\text{-}SEt)_3]^{3-}$ (M = Mo or W) have been investigated in presence of either $NHEt_3^+$ or $pyrrH^+$. In the presence of $NHEt_3^+$, the study shows that the protonation facilitates the substitution step in both clusters (M= Mo or W), and the mechanism of substitution reaction is associative. Analysis of the kinetic data of both clusters showed that the pK_a values fall in the normal range (17.9-18.9). The substitution reactions of both clusters with PhS^- in the presence of $pyrrH^+$ undergo the mechanism in Figure (1.13). The results are presented in Table (1.4). By comparison of these results, it can be determined the impact that changing M from Mo to W has on the rate of proton transfer and rate of binding of PhS^- [39, 50, 53].

Table 1.4. The effect of changing bridging ligands (L) and metal composition (M) on the rates of proton transfer from $pyrrH^+$.

Effect of the metal composition		
Cluster	k_3 / $dm^3\ mol^{-1}\ s^{-1}$	k_4^R / $dm^3\ mol^{-1}\ s^{-1}$
$[\{MoFe_3S_4Cl_3\}_2(\mu\text{-}SEt)_3]^{3-}$	3.3×10^5	6.0×10^6
$[\{WFe_3S_4Cl_3\}_2(\mu\text{-}SEt)_3]^{3-}$	1.0×10^3	2.5×10^3
Effect of Non-Participating ligands		
Cluster	k_3 / $dm^3\ mol^{-1}\ s^{-1}$	k_3^R / $dm^3\ mol^{-1}\ s^{-1}$
$[\{WFe_3S_4Cl_3\}_2(\mu\text{-}SEt)_3]^{3-}$	1.0×10^3	2.5×10^3
$[\{WFe_3S_4Cl_3\}_2(\mu\text{-}OMe)_3]^{3-}$	3.0×10^3	7.2×10^3

The observations show that the rates of the substitution and protonation for the Mo-containing cluster are faster than W-containing cluster. This behaviour for Mo cluster cannot be an electronic impact since electronic factors, which favour binding of anions, would disfavour binding of cations. In addition, it has been proposed that this is further evidence about the main role of bond reorganization on the rate of reaction.

Using stopped flow spectroscopy technique, the synthetic isostructural clusters $[\{WFe_3S_4Cl_3\}_2(\mu\text{-}L)_3]^{3-}$ (L = SEt or OMe) have been studied. These studies allow to investigate the effect of changing the bridging ligands on the reactivity of the Fe-Cl groups[39, 50]. The investigation of the reactions of $[\{WFe_3S_4Cl_3\}_2(\mu\text{-}L)_3]^{3-}$ with PhS^- in the presence of $pyrrH^+$ showed that the both the rate of proton transfer and the rate of thiolate binding are faster when the ligand is OMe derivative. One more time, this is inconsistent with the effect of the bridging ligands on reactivity being an electronic effect. The same change in the cluster describes that bond reorganisation is the dominant barrier to both processes, and that will facilitate the binding of both the anion and the cation. Because the Mo or W is part of the cluster core, the impact of the bridging L ligands is smaller than the impact of changing the metal content of the cluster core.

From the data in Table (1.3) and Table (1.4), it can be noted that the rate constants for proton transfer are variable and depend on the main three factors: (i) The metal composition of the

cluster. In the cuboidal clusters, the $\{Fe_4S_4\}^{2+}$ cluster protonates about 100 times faster than $\{MFe_3S_4\}$ (M= Mo or W) clusters. (ii) The nuclearity of the cluster. For the binuclear clusters of core composition $\{MS_2Fe\}^{n+}$, the rate of protonation of $\{MS_2Fe\}^{4+}$ (M = Mo or W) clusters are 100 times faster than for the $\{FeS_2Fe\}^{2+}$ cluster . (iii) The ligation of the cluster. It is clear that the initial binding of PhS^- to the cluster has an important impact on the rate of the subsequent proton transfer. What is more, comparison of the rates of proton transfer to $[\{WFe_3S_4Cl_3\}_2(\mu\text{-}L)_3]^{3-}$ (L = SEt or OMe) shows that changing the bridging ligands has only a slight effect on the rate of proton transfer.

1.2.9 Proton transfer and bond reorganisation in Fe-S-based clusters

The slow rates of proton transfer involving Fe-S-based clusters and the effects of cluster composition, nuclearity and thermodynamic driving force on the rates of proton transfer can be rationalised if the bond length and angle reorganisation within the cluster core is the predominant factor controlling the rates of protonation. Furthermore, a study on the protonation reactions of $[Fe_4S_4Cl_4]^{2-}$ cluster with $pyrrD^+$ shows no significant primary isotope effect[54]. This behaviour is also consistent with reorganisation of the cluster being a key factor to barrier of proton transfer.

The impact of electronic factors on the proton transfer to the Fe-S-based cluster has been observed in the reactions of $[Fe_4S_4Cl_4]^{2-}$ with $4\text{-}RC_6H_4S^-$ (R = H, MeO, Me, Cl and CF_3) in the presence of $pyrrH^+$ as acid [55]. The mechanism of this reaction involves proton transfer after the binding of thiolate, as shown in Figure (1.15).

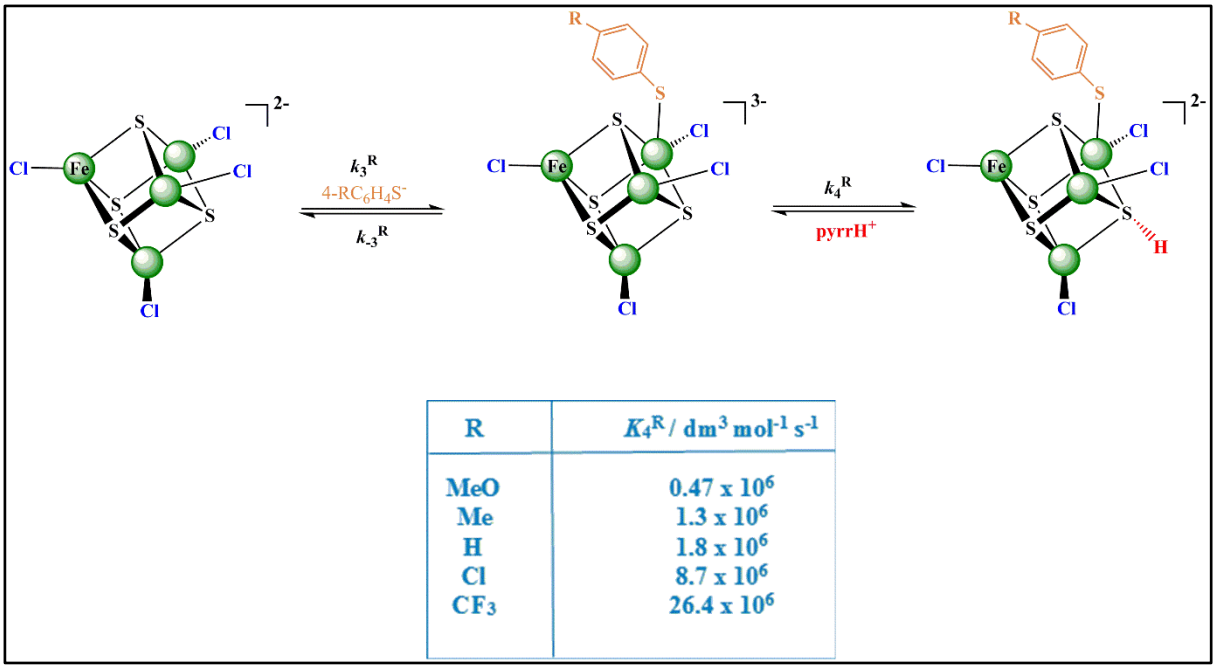

R	K_4^R / dm^3 mol^{-1} s^{-1}
MeO	0.47 x 10^6
Me	1.3 x 10^6
H	1.8 x 10^6
Cl	8.7 x 10^6
CF_3	26.4 x 10^6

Figure 1.15. Effect of 4-R-substantes in $[Fe_4S_4Cl_4(SC_6H_4R\text{-}4)]^{3-}$ on the rate of proton transfer from $pyrrH^+$.

If the 4-R-substituent is electron-withdrawing, the rate constant for proton transfer (k_4^R) is faster than if R is electron-donating, as described in data in Figure (1.15). This observation is understandable if the effect of the 4-R-substituent is to modulate the bond dimensions within the cluster. Electron-withdrawing 4-R-substituents leads to shortening of the bond lengths around the protonation site, hence it will facilitate the proton transfer to clusters. Consequently, if the proton transfers, the energetics associated with bond reorganisation have been (at least partially) overcome.

Further study[46] of the substitution reaction of terminal Cl^- of $[Fe_4S_4Cl_4]^{2-}$ by I^- in presence of $pyrrH^+$ showed that at constant concentration of $pyrrH^+$ and high concentrations of I^- in solution all of the clusters in solution is present in the form $[Fe_4S_4Cl_4(I)]^{3-}$, so the observation will be for only protonation of this species. In addition, the rate of proton transfer is constant and unaffected when the concentration of I^- is changed, but generally the rate of proton transfer to $[Fe_4S_4Cl_4(I)]^{3-}$ cluster is appreciably slower than the proton transfer to the $[Fe_4S_4Cl_4]^{2-}$ cluster. Although the proton transfer from $pyrrH^+$ to the three core μ_3-S bound to the Fe containing the coordinated iodide could be affected by the bulky iodo-ligand, there is no reasonable explanation about the effect of the bulk of the iodo-ligand on proton transfer to the unique μ_3-S not bound to the Fe(Cl)I site. Consequently, it seems more likely that the flexibility of the cluster and its ability to adjust the bond lengths and angles when the proton transfers will be impacted by the binding of I^- to the cluster.

1.3 Structural changes upon protonation of Fe-S-based clusters.

All discussion in this chapter has focused on the acid-catalysed substitution reactions of synthetic Fe-S-based clusters and the mechanism shown in Figure (1.16).

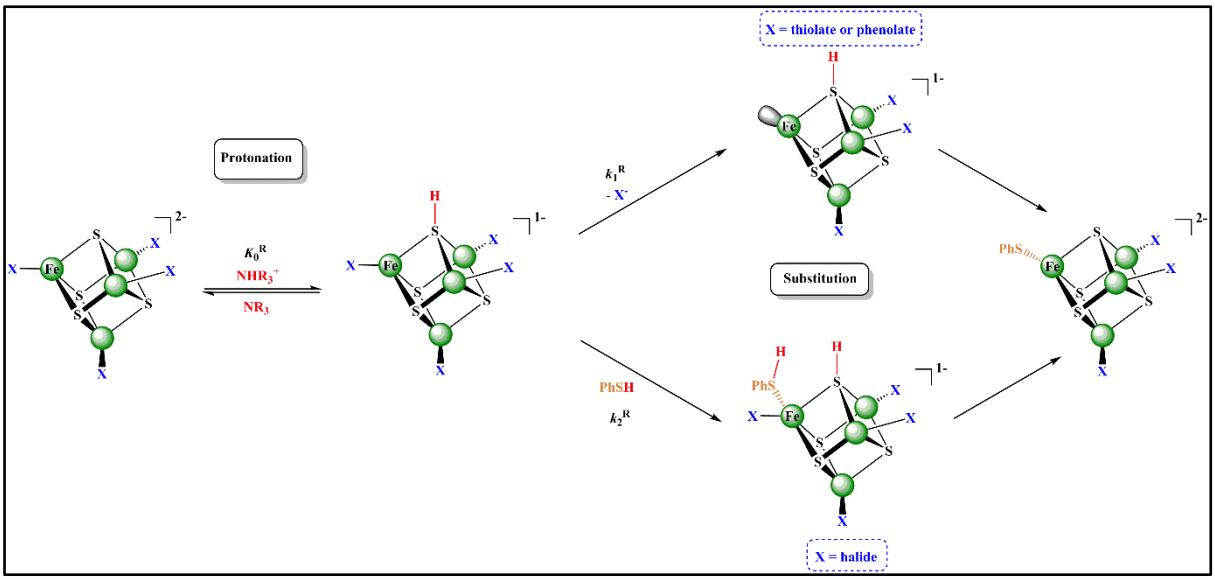

Figure 1.16. The acid catalyzed substitution reaction of the terminal X-ligands in $[Fe_4S_4X_4]^{2-}$ by PhS^- in presence of the acid NHR_3^+.

This mechanism involves initial cluster protonation by acid, followed by substitution. Kinetic studies indicate that the sites of protonation are the core μ_3-S and early work on $[Fe_4S_4X_4]^{2-}$ proposed that the substitution step involves either dissociative, when X= thiolate or phenolate; or associative mechanisms, when X is halide[30, 31, 33, 34, 40, 41, 56]. However, this interpretation of the mechanism of the substitution step is based purely on the dependence of the rate on the concentration of nucleophile.

There are several features of the protonation which are difficult to understand in terms of the mechanism in Figure 1.16. The following intrinsic features (concerning the reactivity of the protonated cluster) remain unclear. (i) That protonation catalyses the substitution of $[Fe_4S_4X_4]^{2-}$ irrespective of the nature of X (X = thiolate, phenolate or halide), (ii) The protonation of μ_3-S is slower than the diffusion-controlled limit. (iii) There is no isotope effect for the proton transfer step. (iv) The measured pK_a values of Fe-S-based clusters are very similar. From these observations, it is clear that the protonation of these clusters is not fully understood

Recent theoretical studies[57-59] indicate that the Fe-S-based clusters undergo unexpected structural changes after protonation of a μ_3-S. The DFT calculations on cubanoid $[Fe_4S_4X_4]^{2-}$ (X= thiolate, phenolate and halide) show that protonation of μ_3-S is coupled to elongation/cleavage of a Fe-(μ_3-SH) bond. These studies suggest a new mechanism to interpret the results of kinetics of acid-catalysed substitution reactions of Fe-S-based clusters as shown in Figure (1.17).

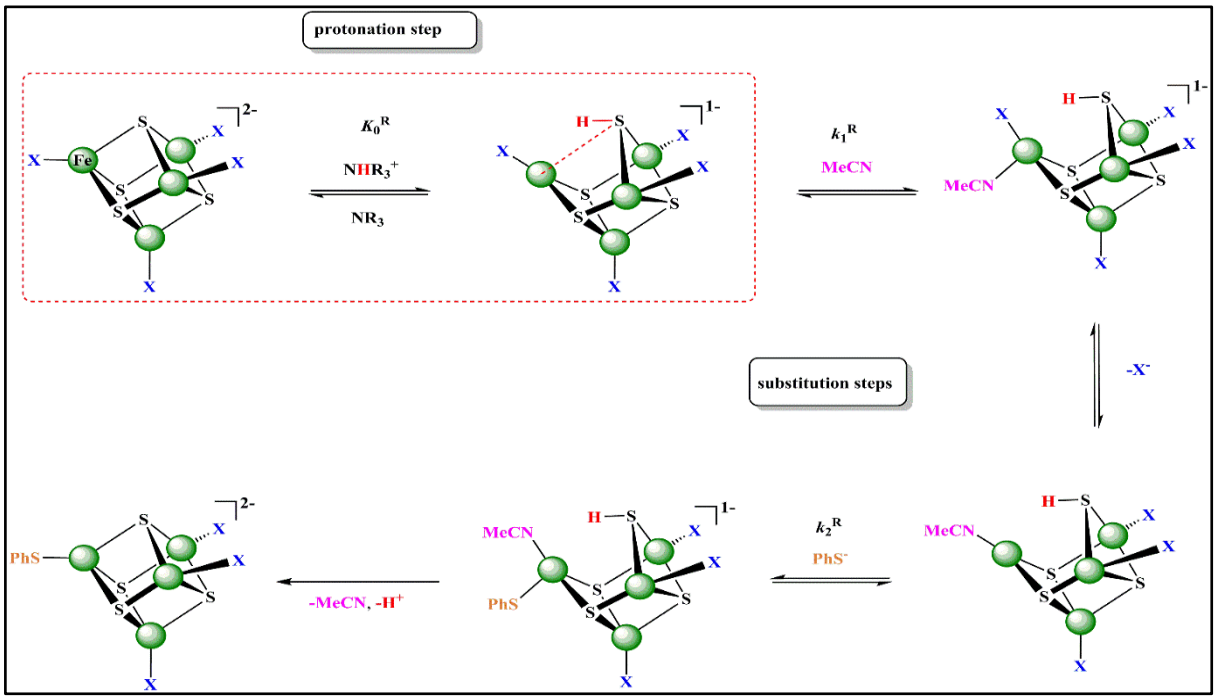

Figure 1.17. Mechanism proposal for acid-catalysed substitution.

This revised mechanism includes the following key steps: initial protonation of a μ_3-S and concomitant Fe-(μ_3-SH) bond cleavage generates a unique 3-coordinate Fe, which would appear to be primed as the site of substitution by an associative mechanism; binding of solvent (MeCN) to the under-coordinated Fe, followed by dissociation of X. Subsequently, the bound MeCN is displaced by the nucleophile (PhS^-). In addition, this mechanism allows to supply reasonable interpretations for most of the protonation features mentioned above. This recent proposed mechanism will be discussed in more details in the later chapters.

1.4 Protonation involving natural Fe-S-based cluster.

Biochemical studies have shown that, in certain enzymes, the Fe-S-based cluster is the active site, where substrates are transformed by sequential addition of electrons and protons. In particular, the nitrogenases are a family of metalloenzymes, which convert dinitrogen into ammonia. Depending on the metal composition of the active site cluster, nitrogenases can be classified into three types: Mo-nitrogenase, V-nitrogenase and Fe-only-nitrogenase[60]. The available X-ray structures of the proteins containing Fe-S-based clusters exhibits that an extensive hydrogen bonding between the cluster and polypeptide is the predominant feature of these natural clusters, as shown in Figure (1.18).

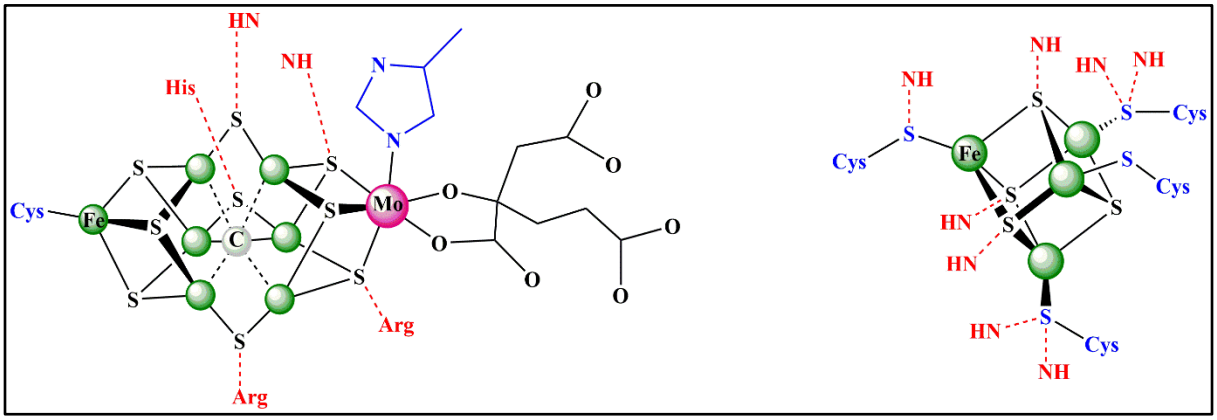

Figure 1.18. Hydrogen bonding from polypeptide to (left) FeMo-cofactor in nitrogenase and (right) $\{Fe_4S_4\}$ ferredoxin cuboidal cluster in *Peptococcus aerogenes*.

Earlier studies[1, 3] showed the cluster Fe_7S_9MoC is the active site of Mo-nitrogenase (FeMo-cofactor). The polypeptide binds to the cofactor at two positions: (i) a cysteinate residue coordinated to the terminal Fe, and (ii) a histidine residue coordinated to the Mo. In Figure (1.18), it can be noted that all Fe sites are tetrahedral whilst the Mo is octahedral with the coordination sphere comprising 3 cluster sulphides, the homocitrate coordinated as a bidentate ligand to Mo through the alkoxy and a carboxylate group and imidazole of a histidine. Recently, both experimental[61] and computational[62, 63] studies on the portion of the FeMo-cofactor indicate that the sequence of proton and electron transfer reactions produce a state of the enzyme, which is capable of binding and transforming dinitrogen, as shown in Figure (1.19).

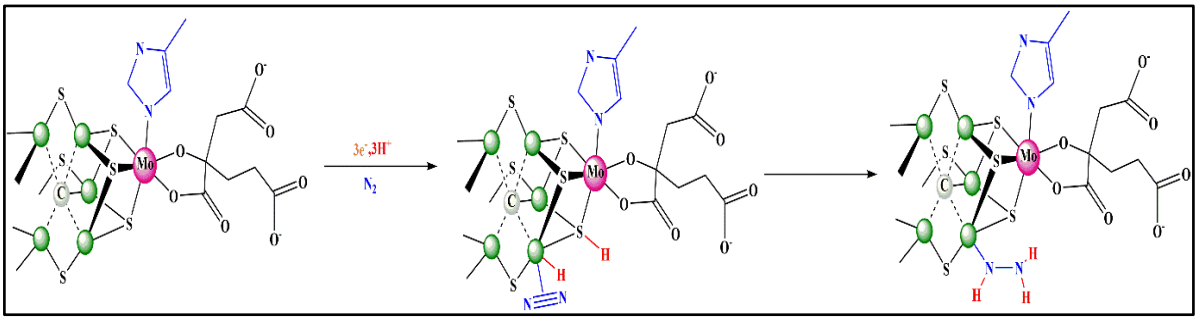

Figure 1.19. Mechanism proposed for the initial stages in the binding and transformation of dinitrogen at the FeMo-cofactor.

The mechanism in Figure (1.19) shows that the conversion of dinitrogen into ammonia occurs at a highly reduced Fe-S-based cluster (three electrons reduced from the resting state) and in the presence of proton as a necessary requirement for this transformation.

1.5 References.

1. J. B. Howard and D. C. Rees, *Chem. Rev.*, 1996, **96**, 2965-2982.

2. T. Spatzal, M. Aksoyoglu, L. M. Zhang, S. L. A. Andrade, E. Schleicher, S. Weber, D. C. Rees and O. Einsle, *Science*, 2011, **334**, 940-940.

3. B. K. Burgess and D. J. Lowe, *Chem. Rev.*, 1996, **96**, 2983-3011.

4. J. G. Li, B. K. Burgess and J. L. Corbin, *Biochemistry-Us*, 1982, **21**, 4393-4402.

5. J. F. Rubinson, J. L. Corbin and B. K. Burgess, *Biochemistry-Us*, 1983, **22**, 6260-6268.

6. R. W. Miller and R. R. Eady, *Biochem. Biophys. Acta*, 1988, **952**, 290-296.

7. D. J. Lowe, K. Fisher, R. N. F. Thorneley, S. A. Vaughn and B. K. Burgess, *Biochemistry-Us*, 1989, **28**, 8460-8466.

8. S. A. Vaughn and B. K. Burgess, *Biochemistry-Us*, 1989, **28**, 419-424.

9. D. J. Lowe, K. Fisher and R. N. F. Thorneley, *Biochem. J.*, 1990, **272**, 621-625.

10. C. E. McKenna, A. M. Simeonov, H. Eran and M. BravoLeerabhandh, *Biochemistry-Us*, 1996, **35**, 4502-4514.

11. K. Fisher, M. J. Dilworth, C. H. Kim and W. E. Newton, *Biochemistry-Us*, 2000, **39**, 2970-2979.

12. K. Fisher, M. J. Dilworth and W. E. Newton, *Biochemistry-Us*, 2006, **45**, 4190-4198.

13. J. S. Kim and D. C. Rees, *Science*, 1992, **257**, 1677-1682.

14. K. D. Demadis, S. M. Malinak and and D. Coucouvanis, *Inorg. Chem.*, 1996, **35**, 4038-4046.

15. S. M. Malinak, K. D. Demadis and D. Coucouvanis, *J. Am. Chem. Soc.*, 1995, **117**, 3126-3133.

16. S. M. Malinak, A. M. Simeonov, P. E. Mosier, C. E. McKenna and D. Coucouvanis, *J. Am. Chem. Soc.*, 1997, **119**, 1662-1667.

17. R. E. Palermo, R. Singh, J. K. Bashkin and R. H. Holm, *J. Am. Chem. Soc.*, 1984, **106**, 2600-2612.

18. S. Ciurli, P. K. Ross, M. J. Scott, Shi-Bao Yu and R. H. Holm, *J. Am. Chem. Soc.* , 1992, **114**, 5415-5423.

19. J. A. Weigel and R. H. Holm, *J. Am. Chem. Soc.* , 1991, **113**, 4184-4191.

20. I. Bertini, S. Ciurli and C. Luchinat, *Struct. Bond.*, 1995, **83**, 1-53.

21. P. J. Stephens, D. R. Jollie and A. Warshel, *Chem. Rev.*, 1996, **96**, 2491-2513.

22. R. H. Holm, P. Kennepohl and E. I. Solomon, *Chem. Rev.*, 1996, **96**, 2239-2314.

23. H. Beinert, M. C. Kennedy and C. D. Stout, *Chem. Rev.*, 1996, **96**, 2335-2373.

24. S. C. Lee and R. H. Holm, *Chem. Rev.*, 2004, **104**, 1135-1157.

25. M. Can, F. A. Armstrong and S. W. Ragsdale, *Chem. Rev.*, 2014, **114**, 4149-4174.

26. P. V. Rao and R. H. Holm, *Chem. Rev.*, 2004, **104**, 527-559.

27. K. S. Hagen, J. G. Reynolds and R. H. Holm, *J. Am. Chem. Soc.*, 1981, **103**, 4054-4063.

28. Z. Cui and R. A. Henderson, *Transit. Metal Chem.*, 2006, **31**, 530-540.

29. R. A. Henderson, *Coordination Chemistry Reviews*, 2005, **249**, 1841-1856.

30. R. A. Henderson, *Chem. Rev.*, 2005, **105**, 2365-2437.

31. G. R. Dukes and R. H. Holm, *J. Am. Chem. Soc.*, 1975, **97**, 528-533.

32. R. A. Henderson and K. E. Oglieve, *J. Chem. Soc., Dalton Trans.*, 1993, 1467-1472.

33. R. A. Henderson and K. E. Oglieve, *J. Chem. Soc., Dalton Trans.*, 1993, 1473-1476.

34. R. A. Henderson and K. E. Oglieve, *J. Chem. Soc., Chem. Commun.*, 1994, 377-379.

35. R. A. Henderson and K. E. Oglieve, *J. Chem. Soc., Dalton Trans.*, 1998, 1731-1733.

36. A. J. Dunford and R. A. Henderson, *J. Coord. Chem.*, 2010, **63**, 2507-2516.

37. K. Izutsu, *Acid-Base Dissociation Constants in Dipolar Aprotic Solvents*, Blackwell Scientific, Oxford, UK, 1990.

38. R. A. Henderson and K. E. Oglieve, *J. Chem. Soc., Dalton Trans.*, 1999, 3927-3934.

39. B. Garrett and R. A. Henderson, *J. Chem. Soc., Dalton Trans.*, 2005, 2395-2402.

40. R. A. Henderson, *BioInorg. React. Mech.* , 2012, **8**, 1-27.

41. R. A. Henderson, *Coord. Chem. Rev.*, 2005, **249**, 1841-1856.

42. I. M. Kolthoff and M. K. Chantooni, *J. Chem. Eng. Data*, 1999, **44**, 124-129.

43. S. C. Davies, D. J. Evans, R. A. Henderson, D. L. Hughes and S. Longhurst, *J. Chem. Soc., Dalton Trans.*, 2001, 3470-3477.

44. R. C. Job and T. C. Bruice, *P. Natl. Acad. Sci. USA*, 1975, **72**, 2478-2482.

45. K. Bates, L. Johnson and R. A. Henderson, *Inorganic Chemistry*, 2006, **45**, 9423-9433.

46. K. Bates and R. A. Henderson, *Inorg. Chem.*, 2008, **47**, 5850-5858.

47. K. L. C. Gronberg and R. A. Henderson, *J. Chem. Soc., Dalton Trans.*, 1996, 3667-3675.

48. Y. K. Do, E. D. Simhon and R. H. Holm, *Inorg. Chem.*, 1985, **24**, 4635-4642.

49. A. J. Dunford and R. A. Henderson, *J. Chem. Soc., Chem. Commun.*, 2002, 360-361.

50. K. Bates, B. Garrett and R. A. Henderson, *Inorg. Chem.*, 2007, **46**, 11145-11155.

51. J. Bell, A. J. Dunford, E. Hollis and R. A. Henderson, *Angew. Chemie Int. Ed.*, 2003, **42**, 1149-1152.

52. S. C. Lee and R. H. Holm, *Chem. Rev.*, 2004, **104**, 1135-1157.

53. B. Garrett and R. A. Henderson, *J. Chem. Soc., Dalton Trans.*, 2010, **39**, 4586-4592.

54. A. J. Dunford and R. A. Henderson, *J. Chem. Soc., Dalton Trans.*, 2002, 2837-2842.

55. A. J. Dunford and R. A. Henderson, *J. Chem. Soc., Chem. Commun.*, 2002, 360-361.

56. R. A. Henderson and K. E. Oglieve, *J. Chem. Soc., Dalton Trans.*, 1993, 1467-1472.

57. A. Alwaaly, I. Dance and R. A. Henderson, *J. Chem. Soc., Chem. Commun.*, 2014, **50**, 4799-4802.

58. I. Dance and R. A. Henderson, *J. Chem. Soc., Dalton Trans.*, 2014, **43**, 16213-16226.

59. I. Dance, *J. Chem. Soc., Dalton Trans.*, 2015, **44**, 4707-4717.

60. R. R. Eady, *Chem. Rev.*, 1996, **96**, 3013-3030.

61. B. M. Hoffman, D. R. Dean and L. C. Seefeldt, *Account. Chem. Res.*, 2009, **42**, 609-619.

62. I. Dance, *J. Chem. Soc., Dalton Trans.*, 2008, 5977-5991.

63. I. Dance, *J. Chem. Soc., Dalton Trans.*, 2010, **39**, 2972-2983.

Chapter 2: Exploring the Acid-Catalyzed Substitution Mechanism of $[Fe_4S_4Cl_4]^{2-}$

2.1 Introduction.

In certain metalloenzymes the active sites (where substrates bind and are transformed) are Fe-S based clusters. These enzymes range from those involved in non-redox transformations (*e.g.* aconitase)[1, 2] to those involved in multi-electron, multi-proton transformations (*e.g.* nitrogenases)[3-6]. Clearly, these enzymes operate in an aqueous (protic) environment and, in some cases, employ protons as a reactant. Because of the complexity of the biological systems, it is difficult to explore the protonation chemistry of natural Fe-S-based clusters, but studies on synthetic clusters allow the factors which affect both the position and rates of proton transfer in Fe-S-based clusters to be defined. The protonation chemistry of synthetic Fe-S-based clusters has been established from studies on acid-catalyzed substitution reactions: a reaction whose mechanism has recently been scrutinised[7-9].

Kinetic studies on the substitution reactions of the terminal ligands in synthetic Fe-S-based clusters, in the presence of acid, such as $NHEt_3^+$ (pK_a = 18.4 in MeCN)[10], show that protonation of the cluster invariably accelerates the rate of substitution[11-14]. In a series of studies, the kinetics indicate an acid-catalyzed substitution mechanism involving rapid cluster protonation, followed by rate-limiting substitution. The evidence indicates that the sites of protonation are the core μ_3-S[15] and early work on $[Fe_4S_4X_4]^{2-}$ (based purely on the dependence of the rate on the concentration of nucleophile) suggested that the substitution step involves either dissociative (X = thiolate or phenolate) or associative (X = halide) pathways (***see section 1.3*** Figure 1.16). However, these acid-catalyzed reactions exhibit some unusual features, which are difficult to reconcile with a simple protonation of the cluster. The most notable issues have been discussed in detail recently but are briefly summarised here[7-9]. (i) The rates of proton transfer to Fe-S-based clusters are slower than the diffusion-controlled limit, even for thermodynamically-favourable protonation reactions. (ii) Under conditions where proton transfer is rate-limiting the reaction is not associated with a measurable kinetic isotope effect in studies with deuterated acid. (iii) Protonation of the cluster accelerates the rate of substitution, irrespective of the nature of the terminal ligand (X = thiolate, phenolate or halide) or the kinetics of the substitution step (for X = thiolate or phenolate, rate of substitution independent of the concentration of nucleophile, and for X = halide, rate exhibits a first order dependence on the concentration of nucleophile). (iv) Changes to the ligation and metal composition of cuboidal Fe-S-based cluster,

when the protonation step of a μ_3-S is coupled to cleavage of a Fe-(μ_3-SH) bond, modulate the rates of proton transfer in an unusual manner, suggestive of structural changes to the cluster being a significant barrier to protonation. (v) If the mechanism in Figure 1.16 operates, the pK_a of the cluster can be calculated from the kinetic data. Such calculations indicate that the pK_a of all Fe-S-based clusters fall in the narrow range (17.9-18.9) and the μ_2-S has same pK_a as μ_3-S, independent of overall charge, nuclearity, terminal ligands and cluster composition.

2.1.1 How the revised mechanism explains the unusual acid-catalysed reactivity of $[Fe_4S_4X_4]^{2-}$ clusters.

Most of earliest kinetic studies on synthetic Fe-S-based clusters focused on determining the rates of protonation, the pK_a values of the Fe-S-based clusters and investigation of impact of proton transfers on the rates of substitution[12-14]. However, these studies have not provided a reasonable explanation for the enigmatic acid-catalyzed reactivity of Fe-S-based clusters indicated above. Consequently, it seems that a key feature associated with the protonation chemistry of Fe-S-based clusters remains unclear.

Recent density functional theory (DFT) calculations on cubanoid $[Fe_4S_4X_4]^{2-}$ (X = thiolate, phenolate or halide)[7-9], inspired by earlier calculations on the active site of the Mo-based nitrogenase {$MoFe_7S_9C$(*R* -homocitrate)} cluster indicate that protonation of a μ_3-S is coupled to cleavage of a Fe-(μ_3-SH) bond. In addition, these DFT calculations show that $[Fe_4S_3(SH)X_4]^{-}$ (X = SPh, SEt, Cl, OMe or OPh) cluster is present in two geometrical isomers (*endo* and *exo*), which depend of the direction of the hydrogen in μ-SH either towards or away from the unique Fe atom, as shown in (Figure 2.1).

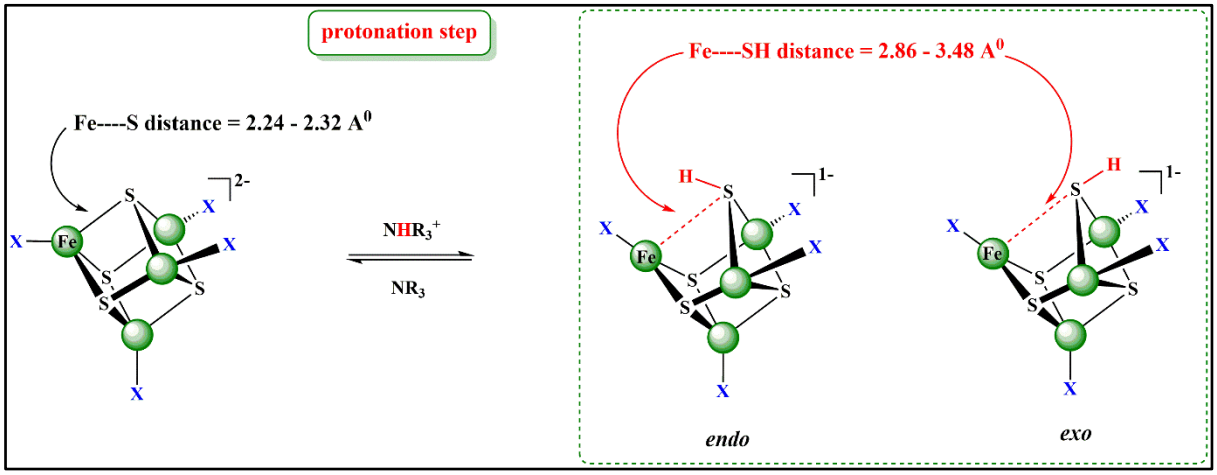

Figure 2.1. Geometrical isomers for $[Fe_4S_3(SH)X_4]^{-}$ cluster proposed by DFT calculations.

In addition, DFT calculations show that the Fe-S distance has extended from *ca.* 2.24-2.32 Å to *ca.* 2.86-3.48 Å for Fe-SH, and the SH function is trigonal pyramidal stereochemistry, see Figure (2.1). The results of these theoretical studies have provided simple explanations for the general features concerning the reactivity of the protonated $[Fe_4S_3(SH)X_4]^-$ cluster, which were described in (***section 2.1.***). DFT calculations indicate that the protonation step of $[Fe_4S_4X_4]^{2-}$ cluster is coupled to significant elongation or even cleavage of a Fe-SH bond. As a result, the estimated or measured rate constant of proton transfer from NHR_3^+ acid to $[Fe_4S_4X_4]^{2-}$ cluster does not correspond to the simple addition of a protona to a core μ_3-S of a cluster which remains structurally intact. So, it seems that the unexpectedly slow rate of proton transfer to $[Fe_4S_4X_4]^{2-}$ is a consequence of structural disruption to the cluster. Moreover, for the same reason when the bond cleavage step is energetically the most demanding process in the protonation, no isotope effect would be expected by using deuterated acid because the bond cleavage is not associated with movement of the proton. The pK_as calculated for protonation of $[Fe_4S_4X_4]^{2-}$ are not valid. A pK_a is an acid dissociation constant associated with no significant change to the conjugate base. However, for Fe-S-based clusters, protonation of the core μ_3-S of cluster is coupled to cleavage of Fe-SH bond.

Furthermore, it is clear now why transfer of proton from acid to the core μ_3-S labilises substitution of any terminal ligand of the cluster. The unique Fe site, which is under-coordinate with essentially planar three-coordination, is generated after the protonation of the cluster. It seems likely this Fe site is more susceptible than the four-coordinate Fe sites to binding of a nucleophile. Generally, both isomers (*endo* and *exo*) of $[Fe_4S_3(SH)X_4]^-$ facilitate the substitution reaction.

The key steps in the revised mechanism are as follows. Initial protonation of a μ_3-S results in concomitant Fe-(μ_3-SH) bond cleavage which generates an under-coordinated (3-coordinate) Fe. This 3-coordinate Fe is thus primed as the site of substitution by an associative mechanism. To be consistent with the experimentally observed kinetics, it is suggested that the displacement of X by PhSH (or PhS^-) occurs by two consecutive associative steps which involve initial displacement of X^- by MeCN (the solvent), followed by displacement of coordinated MeCN by PhSH. Depending on the lability of Fe–X, the rate-limiting step can be either displacement of X^- by MeCN (rate independent of concentration of nucleophile because the rate of dissociation of XH (X = SEt, SBu^t or OPh) is being slower than attack by PhSH), or displacement of coordinated MeCN by PhSH (rate exhibits first order dependence on concentration of nucleophile), as described in Chapter 1 (***section 1.3***) Figure 1.17.

Irrespective of whether the mechanism is that shown in Figure 1.16 or Figure 1.17, there are two principal steps: the protonation and the substitution steps. The intimate mechanism of each of these steps is different in the two mechanisms. In this chapter, the studies which explore both the protonation and substitution steps in the acid-catalyzed substitution reactions of $[Fe_4S_4Cl_4]^{2-}$ will be discussed and then will be distinguished between the simple and the recent revised mechanisms.

2.1.2 Kinetics of protonation of $[Fe_4S_4X_4]^{2-}$ clusters.

Several recent reviews[12-14] on the protonation of synthetic clusters have summarised our current knowledge in this research area.

Because the binding of protons to $[Fe_4S_4X_4]^{2-}$ (X = thiolate, phenolate or halide) clusters is associated with a negligible spectroscopic change, protonation of these clusters was investigated by an indirect method, by measuring the effect protonation has on the rates of substitution of the terminal ligand (X). Using the stopped-flow method depends on the observation that the rates of substitution reaction of the terminal ligands on the clusters are sensitive to whether or not proton is bound to the cluster. Briefly, the method involves studying the effect that protonation has on the rate of substitution of the terminal ligands in Fe-S-based clusters. The substitution reactions are associated with a significant spectroscopic change. Thus, by analyzing the effect acid has on the rate of substitution gives information about the spectroscopically-silent protonation. The essential feature of this approach is that the protonation is detected when it affects the lability of the terminal ligands. A limitation of the methodology used is that a variety of sites on the Fe-S-based cluster could be protonated, but the kinetic method will only "detect" the protonation which affects the lability of the terminal ligands.

In this chapter, the kinetic studies on the acid-catalyzed substitution reactions of the terminal chloro-ligands in $[Fe_4S_4Cl_4]^{2-}$ by PhS^- in the presence of the acids NHR_3^+ (R = Me, Et, Pr^n or Bu^n) will be presented. Despite these acids having very similar pK_as (17.6 – 18.4 in MeCN)[10] the reactions show a variety of different kinetics, some of which is inconsistent with a mechanism involving simple protonation of the cluster followed by substitution of a terminal ligand. The reactivity is more consistent with the recently proposed mechanism in which Fe-S bond elongation/cleavage occurs upon protonation of a μ_3-S, and indicates that both the acidity and bulk of the acid is important in the protonation step.

2.2 Experimental and Methodology.

2.2.1 General Experimental.

All experiments which include both the preparation of compounds and the kinetics studies were all done under an atmosphere of dinitrogen because all compounds are very sensitive to air.

2.2.2 Solvents.

All solvents were dried and distilled under dinitrogen immediately prior to use. Tetrahydrofuran (THF) and diethyl ether were distilled in presence of sodium wire. Acetonitrile was distilled and dried over calcium hydride, and methanol was distilled from $Mg(OMe)_2$ (generated *in situ*).

2.2.3 Proton Nuclear Magnetic Resonance Spectroscopy (^{1}H NMR Spectroscopy).

^{1}H NMR spectra were recorded on 300 MHz Brucker Avance spectrometers operating at 121.5 MHz. Samples were prepared in dry, degassed CD_3CN under an atmosphere of dinitrogen and chemical shifts are referenced relative to tetramethylsilane (TMS).

2.3 Preparation of Compounds.

The following chemicals were purchased from Sigma-Aldrich and used as received: thiophenol (PhSH), tetrabutylammonium bromide (NBu^n_4Br), benzoyl chloride (PhCOCl), trimethylammonium hydrochloride (Me_3NHCl), triethylamine (Et_3N), tetraethylammonium chloride mono hydrate ($NEt_4Cl.H_2O$) which was dried by heating under *vacuo*, tripropylamine (Pr^n_3N), tributylamine (Bu^n_3N), chlorotrimethylsilane (Me_3SiCl), sodium tetraphenylborate ($NaBPh_4$), and anhydrous iron(III) chloride ($FeCl_3$). The deuterated solvents, CD_3CN was purchased from Goss Scientific and used as received, methanol-d_1 (CH_3OD) and D_2O were purchased from Sigma-Aldrich and used as received.

2.3.1 Clusters.

2.3.1.1 Preparation of $[NBu^n_4]_2[Fe_4S_4(SPh)_4]$[16].

Sodium (1.84 g, 80 mmol), was carefully dissolved with stirring in methanol (50 ml). After the solution had been left to cool to room temperature, thiophenol (8.3 ml, 80 mmol) was added to give a clear solution. Anhydrous $FeCl_3$ (3.12 g, 20 mmol) was dissolved in methanol (20 ml) and added slowly to the thiolate solution to give a dark green mixture. After stirring for about

20 minutes, elemental sulphur (0.64 g, 20 mmol) was added. The mixture was then stirred overnight. The solution becomes a dark brown-red colour.

The mixture was filtered and a solution of $[NBu^n_4]Br$ (4.84 g, 15 mmol) in methanol (20 ml) was added (without stirring) to the filtrate. A black precipitate was immediately formed. The mixture was left for about one hour at room temperature to ensure complete precipitation. The mixture was then filtered and the black precipitate was washed with methanol, and anhydrous diethyl ether, and then dried *in vacuo*, see Equation (2.1).

The crude solid was recrystallized by dissolving in the minimum (~20 ml) of warm (~50 ^oC) MeCN then adding an excess (~80 ml) of warm (~50 ^oC) methanol. The solution was left to cool slowly to room temperature to give black needle-like crystals. (Average yield is 62%).

$$8FeCl_3 + 32NaSPh \xrightarrow{MeOH} 8Fe(SPh)_3 + 8NaSPh + 24NaCl$$

$$\downarrow 8S \quad 4[NBu_4]Br$$

$$2[NBu_4]_2[Fe_4S_4(SPh)_4] + 24\ PhSSPh + 4NaBr$$

$$\downarrow \text{Crystallized by } MeCN/Et_2O$$

$$[NBu^n_4]_2[Fe_4S_4(SPh)_4] \qquad (2.1)$$

The purity of $[NBu^n_4]_2[Fe_4S_4(SPh)_4]$ was established by comparison with the previously reported[17], as shown in (Figure 2.2), ^{1}H NMR spectrum in CD_3CN: δ 0.85 (br., 24H, *CH₃*), δ 1.32 (br., 16H, *CH₂*), δ 1.58 (br., 16H, *CH₂*), δ 3.1 (br., 16H, *CH₂*); δ 8.15 (*meta*-H), δ 5.87 (*ortho*-H), δ 5.26 (*para*-H) for terminal *SPh*$^-$.

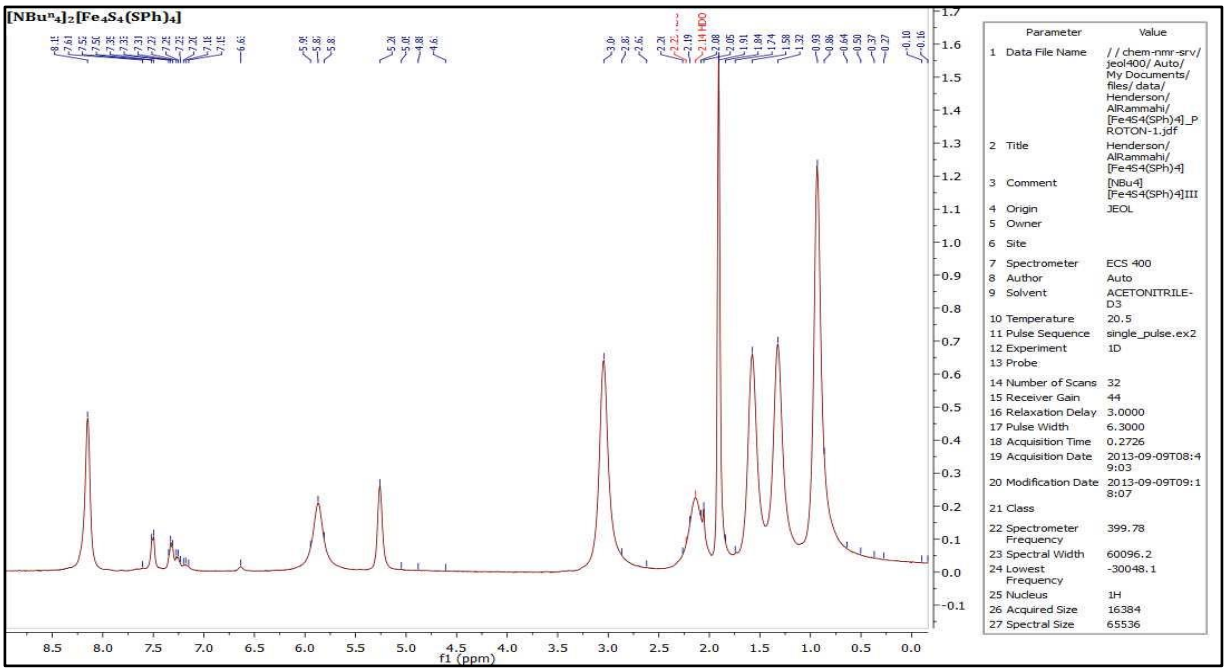

Figure 2.2. ^{1}H NMR spectrum of $[NBu^n_4]_2[Fe_4S_4(SPh)_4]$ cluster in CD_3CN.

2.3.1.2 Conversion of $[NBu^n_4]_2[Fe_4S_4(SPh)_4]$ to $[NBu^n_4]_2[Fe_4S_4Cl_4]$[18].

$[NBu^n_4]_2[Fe_4S_4(SPh)_4]$ (3.84 g, 3.0 mmol) was suspended in MeCN (25 ml). Benzoyl chloride (previously dried over anhydrous magnesium sulfate) (8.4 ml, 60 mmol) was added to the stirred slurry. Any solid gradually dissolved and the solution converted to a deep brown colour with a purple-black cast.

The mixture was stirred for about an hour and then diethyl ether (~100 ml) was added to the solution. The product separated as a dark solid. The solid was filtered and washed with anhydrous diethyl ether, then dried *in vacuo*. The crude product is dissolved in the minimum volume (~15 ml) of warm (~50 ^{o}C) MeCN, then warm (~50 ^{o}C) isopropyl alcohol was added (~50 ml) and the solution was left to cool to room temperature. The product formed as black crystals, which were filtered and washed with cold isopropyl alcohol and cold diethyl ether then dried *in vacuo*. (Average yield is 58%).

The ^{1}H NMR spectrum of the product showed in CD_3CN: δ 0.93(br., 24H, *CH_3*), δ 1.35 (br., 16H, *CH_2*), δ 1.6 (br., 16H, *CH_2*), δ 3.0 (br., 16H, *CH_2*); and all signals for terminal PhS^- at (δ 5,26-8.15) had disappeared; indicating to the substitution of PhS^- was successfully occurred by Cl^-, as shown in (Figure 2.3).

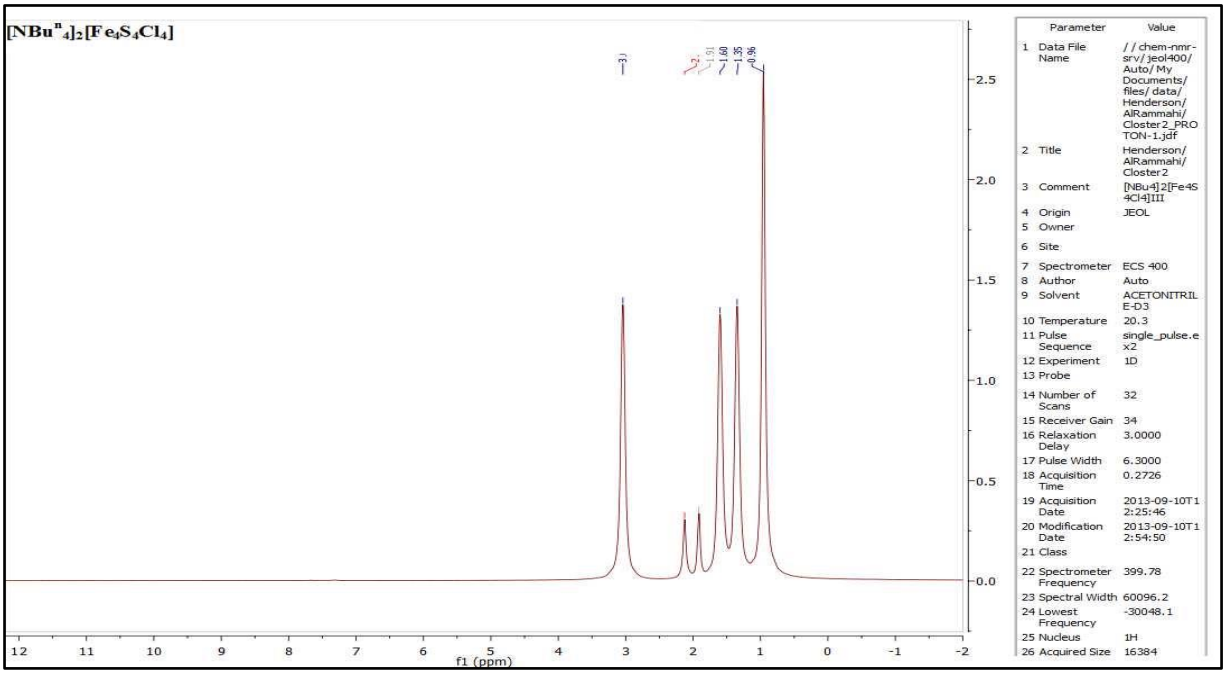

Figure 2.3. ^{1}H NMR spectrum of [NBu$^n_4$]$_2$[$Fe_4S_4Cl_4$] cluster in CD_3CN.

2.3.2 Preparation of [NEt$_4$][SPh][19].

Sodium (0.6 g, 25 mmol) was dissolved in methanol (25 ml) to form a colourless solution. After the solution had cooled at room temperature, PhSH (2.6 ml, 25 mmol) was added and the mixture was stirred for 30 minutes, and then dry [NEt_4]Cl (4.15 g, 25 mmol) was added to the mixture. The reaction was stirred for a further half an hour. A white solid precipitate (mixture of [NEt_4][SPh] and NaCl) was formed. All volatiles were removed *in vacuo*. Addition of MeCN (50 ml) dissolved the [NEt_4]SPh, and the insoluble NaCl was removed by filtration through celite. After concentrating the filtrate to ~30 ml, about 150 ml of diethyl ether was added. The solution was cooled in the freezer for several days and the white needle-like crystals were collected by filtration. The product was washed with diethyl ether then dried *in vacuo*, Equation (2.2). (Average yield is 78%).

$$PhSNa + [NEt_4]Cl \xrightarrow{MeOH} [NEt_4][PhS] + NaCl \quad (2.2)$$

^{1}H NMR spectrum of [NEt$_4$][SPh] in CD_3CN: δ 1.09 (triplet, intensity = 12, J_{HH} = 7.16 Hz, *CH$_3$*), 3.11 (quartet, intensity = 8, J_{HH} = 7.2 Hz, *CH$_2$*), δ 7.1 (*meta*-H), δ 6.69 (*ortho*-H), δ 6.56 (*para*-H) for terminal *SPh*$^-$, as shown in (Figure 2.4).

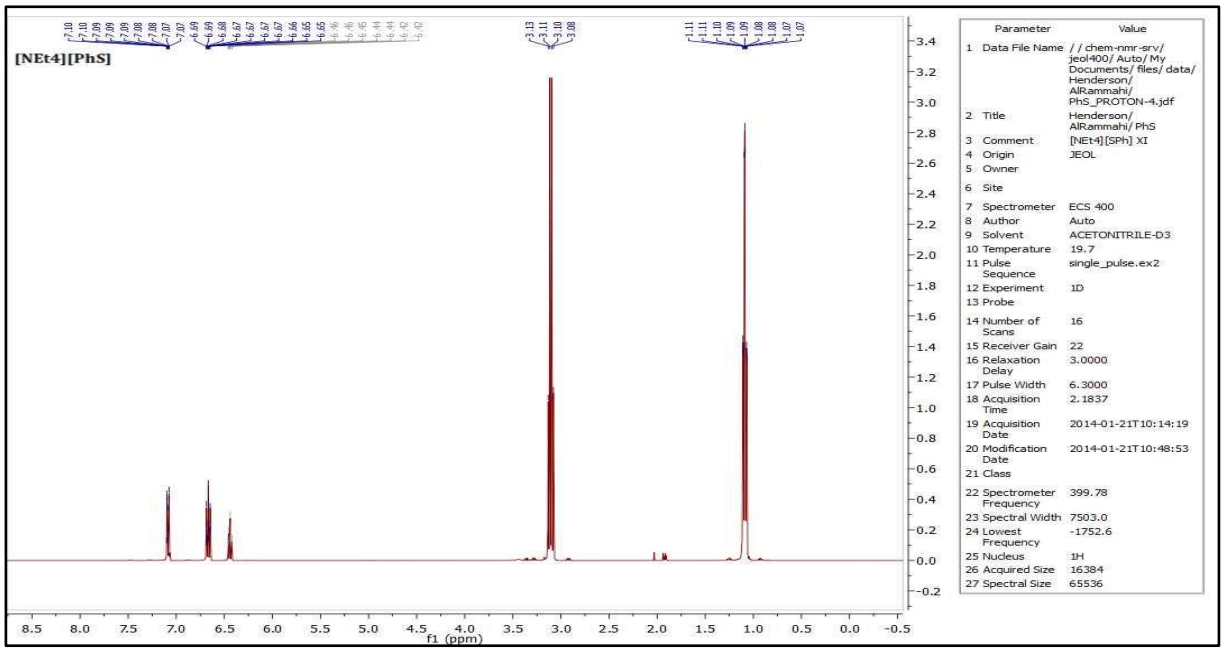

Figure 2.4. ^{1}H NMR spectrum of [NEt$_4$][SPh] in CD_3CN.

2.3.3 Acids.

2.3.3.1 Preparation of [NHMe$_3$][BPh$_4$].

The following reaction was carried out in air:

$$[NHMe_3]Cl + NaBPh_4 \xrightarrow{MeOH} [NHMe_3][BPh_4] + NaCl \quad (2.3)$$

[NHMe$_3$]Cl was dissolved in the minimum volume of methanol (~10 ml) and then filtered through celite. NaBPh$_4$ (8.55 g, 25 mmol) was also dissolved in minimum of methanol (~10 ml), and then dripped through celite into the [NHMe$_3$]Cl solution. The mixture was left to stand overnight and a white precipitate resulted. The product was collected by filtration, then was washed with a large volume of distilled water (~ 2 liters). The solid precipitate was also washed with a small volume of methanol (25 ml) and dried *in vacuo*. (Average yield is 88%)

^{1}H NMR spectrum of [NHMe$_3$][BPh$_4$] in CD_3CN: δ 2.68 (singlet, intensity = 9, *CH$_3$*), 3.27 (singlet, intensity = 1, *NH*), 6.83-7.3 (multiplet, intensity = 20, *BPh$_4$*), as shown in Figure (2.5).

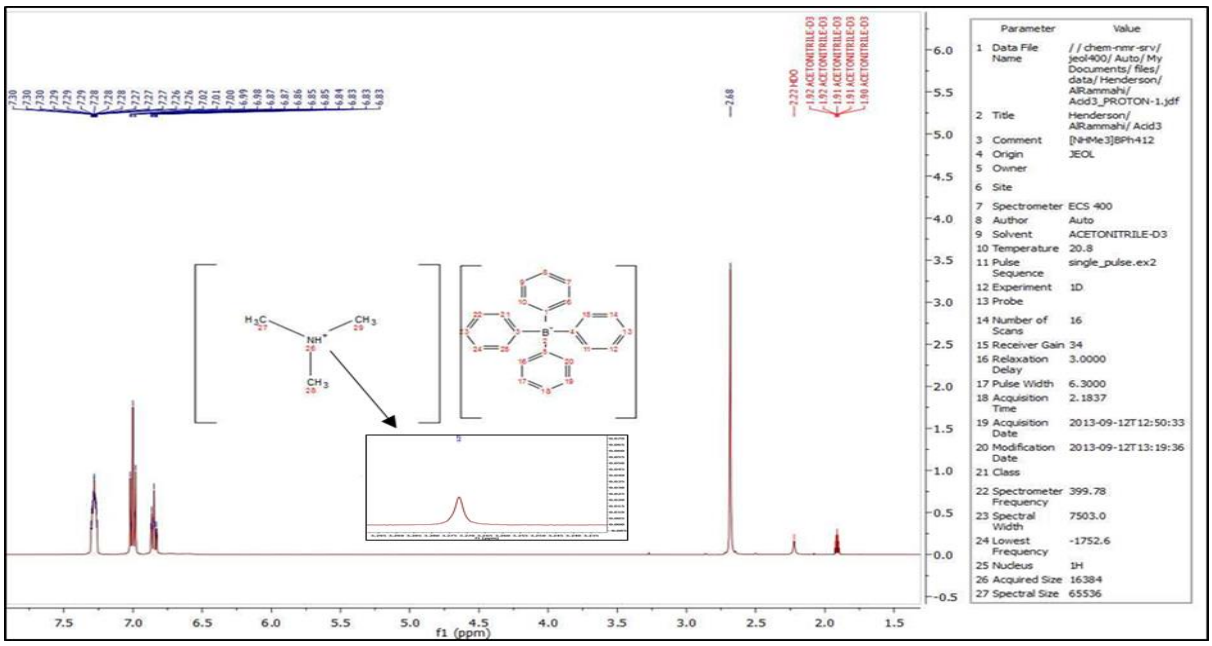

Figure 2.5. ^{1}H NMR spectrum of $[NHMe_3][BPh_4]$ in CD_3CN.

2.3.3.2 Preparation of $[NHR_3][BPh_4]$ (R = Et, Pr^n, and Bu^n.).

An analogous method to that reported for $[NHEt_3][BPh_4]$[20] , was used to prepare $[NHR_3][BPh_4]$ (R= Pr^n and Bu^n), see Equations (2.4), (2.5) and (2.6).

$$CH_3OH + (CH_3)_3SiCl \xrightarrow{THF} (CH_3)_3SiOCH_3 + HCl \quad (2.4)$$

$$NR_3 + HCl \xrightarrow{THF} [NHR_3]Cl \quad (2.5)$$

The required amount of NR_3, see Table (2.1), was added to THF (100 ml) under an atmosphere of dinitrogen. Methanol (4.05 ml, 100 mmol) was then added to the amine solution, followed, with stirring, by Me_3SiCl (12.7 ml, 100 mmol). A white precipitate is immediately formed, and the mixture was stirred for a further half an hour. The $[NHR_3]Cl$ product was filtered and washed with the minimum volume of THF, then dried *in vacuo.*

$$[NHR_3]Cl + NaBPh_4 \xrightarrow{MeOH} [NHR_3][BPh_4] + NaCl \quad (2.6)$$

The $[NHR_3]Cl$ was dissolved in the minimum of methanol (~30 ml), then filtered through celite. The required amount of $NaBPh_4$ (see table below) was dissolved in the minimum of methanol (~20 ml), and then dripped through celite into the $[NHR_3]Cl$ solution. The solution was left to stand overnight and a white solid was formed. The solid was collected by filtration, then washed

with a large volume of distilled water (~ 2 liters). The solid was finally washed with methanol (50 ml) and dried *in vacuo*. Average yields are $[NHEt_3]BPh_4$ = 90%; $[NHPr^n_3]BPh_4$ = 90% and $[NHBu^n_3]BPh_4$ = 94%.

Table 2.1. Amount of chemicals used to prepare NHR_3^+ (R= Et_3, Pr^n_3 or Bu^n_3).

Materials	**Amount of gms or mls**	**Number of mmoles**
NEt_3	13.9 ml	100
NPr^n_3	19 ml	100
NBu^n_3	23.8 ml	100
$NaBPh_4$	5.2 g	15
$[NHEt_3]Cl$	2.1 g	15
$[NHPr^n_3]Cl$	2.7 g	15
$[NHBu^n_3]Cl$	3.32 g	15

The ^1H NMR spectra of $[NHR_3][BPh_4]$ in CD_3CN are as follows:

$[NHEt_3][BPh_4]$: δ 1.24 (triplet, intensity = 9, J_{HH} = 7.3 Hz, *CH_3*), 3.13 (quartet, intensity = 6, J_{HH} = 7.3 Hz, *CH_2*), 3.3 (singlet, intensity = 1, *NH*), 6.88-7.3 (multiplet, intensity = 20, *BPh_4*), as shown in Figure (2.6).

$[NHPr^n_3][BPh_4]$: δ 0.93 (triplet, intensity = 9, J_{HH} = 7.4 Hz, *CH_3*), 1.58-1.68 (multiplet, intensity = 6, *CH_2*), 2.9-3.0 (multiplet, intensity = 6, *CH_2*), 3.28 (singlet, intensity = 1, *NH*), 6.78-7.3 (multiplet, intensity = 20, *BPh_4*), as shown in Figure (2.7).

$[NHBu^n_3][BPh4]$: δ 0.94 (triplet, intensity = 9, J_{HH} = 7.3 Hz, *CH_3*), 1.33 (hextet, intensity = 6, J_{HH} = 7.4 Hz, *CH_2*), 1.54-1.62 (multiplet, intensity = 6, *CH_2*), 2.9-3.0 (multiplet, intensity = 6, *CH_2*), 3.29 (singlet, intensity = 1, *NH*), 6.84-7.33 (multiplet, intensity = 20, *BPh_4*), as shown in Figure (2.8).

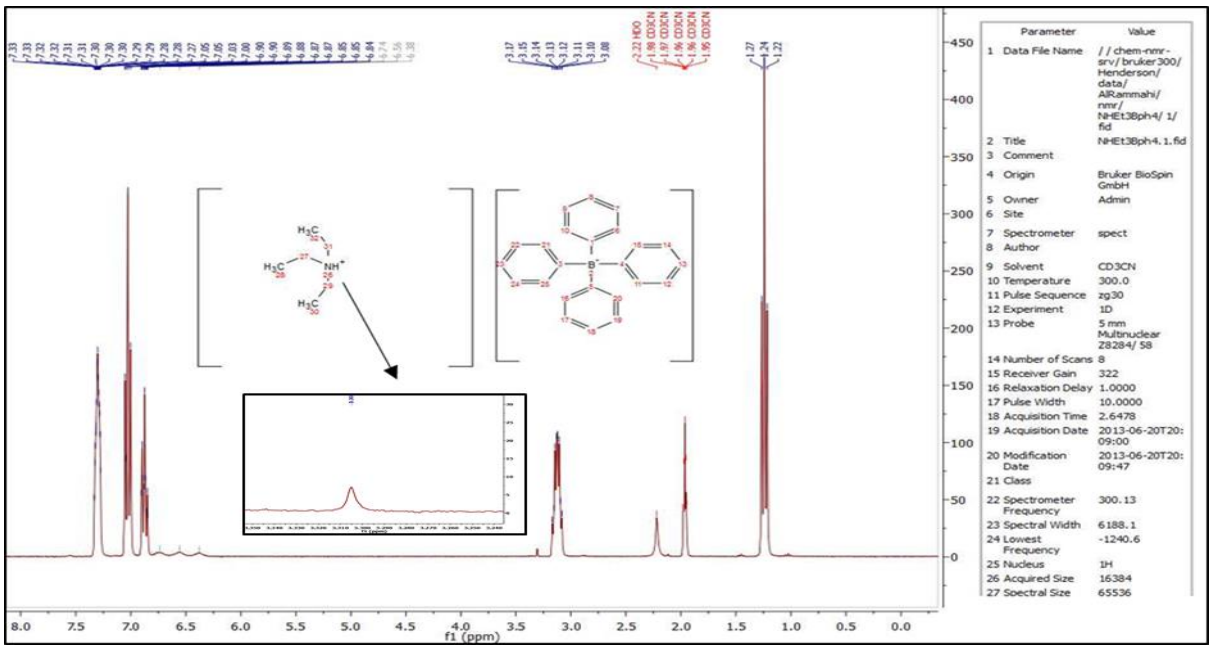

Figure 2.6.^{1}H NMR spectrum of $[NHEt_3][BPh_4]$ in CD_3CN.

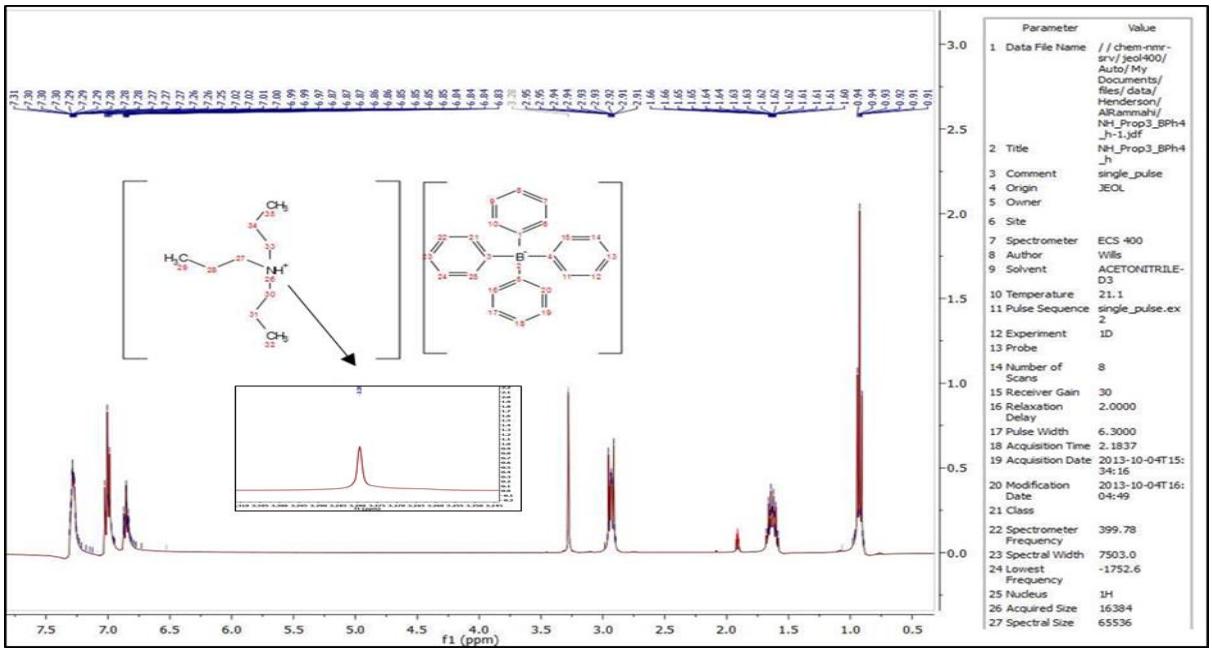

Figure 2.7.^{1}H NMR spectrum of $[NHPr^{n}_3][BPh_4]$ in CD_3CN.

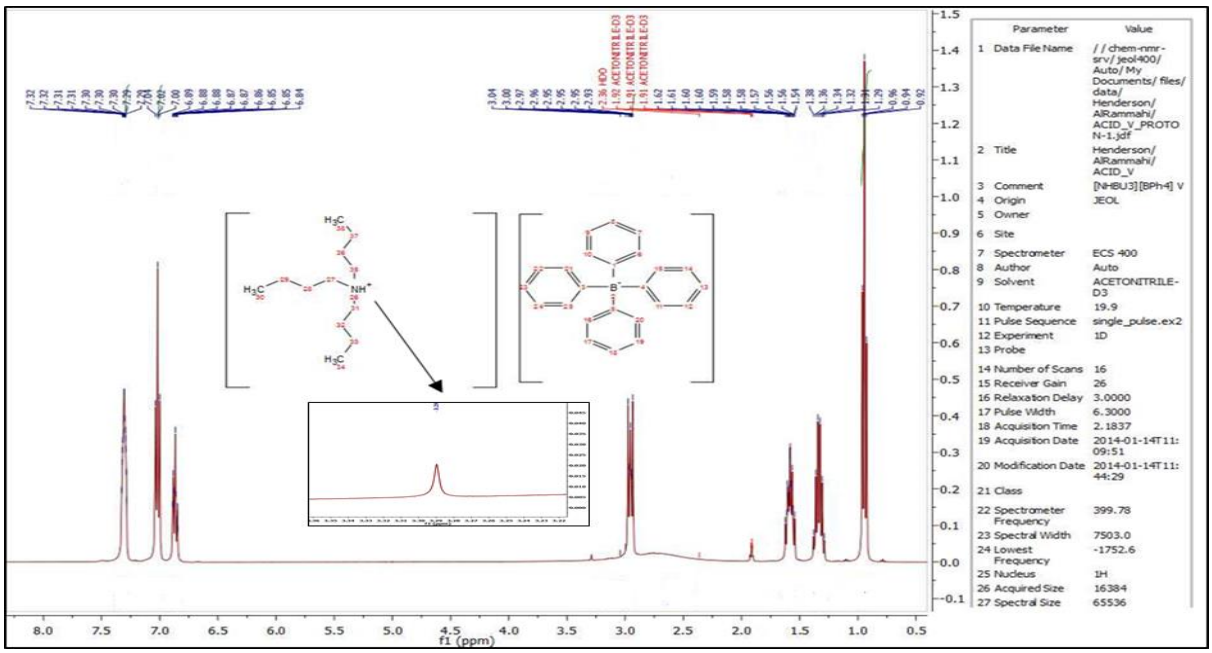

Figure 2.8. ^{1}H NMR spectrum of $[NHBu^{n}_{3}][BPh_4]$ in CD_3CN.

2.4 Kinetic Studies.

All kinetic experiments were performed using an Applied Photophysics Stopped-Flow Spectrophotometer modified to handle air-sensitive solutions connected to a RISC PC. In addition, it was connected with thermostat tank (Grant LTD 6G), which allows control of the temperature in the range (15.0 - 35.0 ±0.1 ^{o}C), and with combined re-circulating pump. The solutions of clusters and reagents (thiolate and acids) were prepared under an atmosphere of dinitrogen by using MeCN as a solvent. The stock solutions of reagents (thiolate and acid) were freshly prepared, and then the diluted concentrations were made from stock solutions, and used within an hour.

2.4.1 Stopped- Flow spectrophotometer.

Using stopped-flow spectrophotometry is important to study the substitution reactions of Fe-S-based clusters because these reactions are usually sufficiently rapid. The stopped-flow technique involves following the reaction by observing the UV/vis spectra of the reagent mixture as a function of time. Figure 2.9 shows a schematic diagram of the stopped-flow apparatus. The stopped-flow technique involves using a pneumatic ram, a small amount of reagents from syringes I and II are rapidly mixed. Usually, syringe I contains the solution of Fe-S-based cluster and syringe II consists of either a nucleophile or nucleophile/acid solution. The reagents from the syringes are driven into the observation cell and from there into the stopping syringe. Upon filling the stopping syringe, the plunger of the stopping syringe hits an

electrical contact which causes the pneumatic drive to stop and triggers the collection of the absorbance-time data of the reaction (by the computer) occurring in the observation cell at a single wavelength. On a very fast time-scale about 1 ms, the solutions in the two syringes are mixed by using the pneumatic drive. The dead- time of the apparatus is the time of mixing solutions plus the time of filling the cell and the time of stopping the solution. The end step of the dead-time includes from the time necessary for a shockwave to travel through the solution and back again. Totally the dead-time is usually around 2 ms, this is the limiting factor in monitoring reactions by stopped-flow spectrophotometry as the dead-time must be less than the half-life of reaction when we need study of the reaction accurately. After the dead-time, the data is collected for between 2 ms and 1000 s and is displayed as an absorbance-time plot on the connected PC, as shown in Figure (2.9).

An Applied Photophysics SX.18 MV stopped-flow spectrophotometer has been used for all kinetic studies. The absorbance-time curve has been fitted using the computer curve-fitting program with the option of one or two exponentials being used.

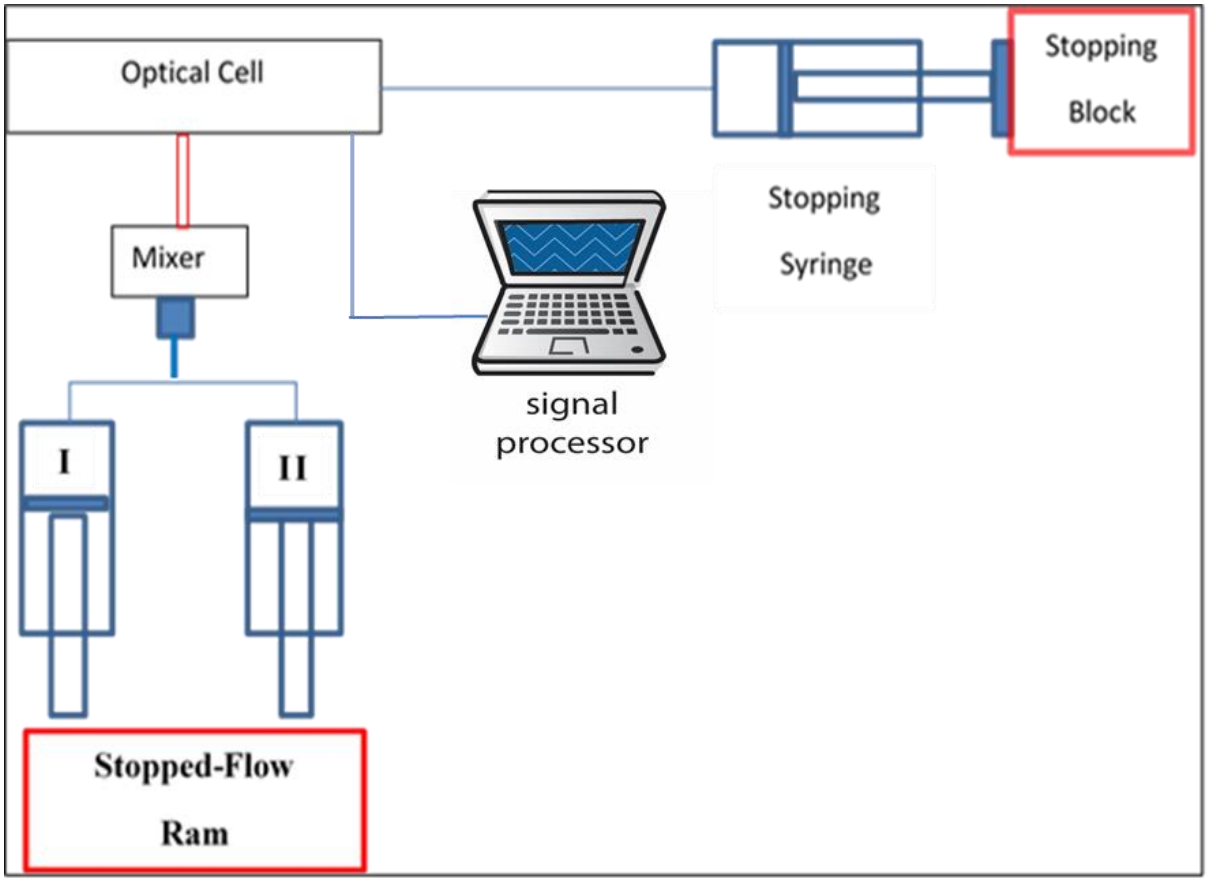

Figure 2.9. Scheme of the technique of the stopped-flow spectrophotometry.

2.5 Results and discussion.

In this presentation of the results initially we will focus on exploring the protonation step. Studies with a series of structurally similar acids, NHR_3^+ (R = Me, Et, Pr^n and Bu^n) show that the rates of the acid-catalyzed substitution reactions with PhSH do not correlate with the pK_as of the acids. This behaviour is inconsistent with the simple mechanism shown in Figure (1.16), and the results are discussed in terms of the mechanism in Figure (1.17). In the second part of the presentation, the substitution step will be considered. Studies on the temperature dependence of the rate of substitution of $[Fe_4S_3(SH)Cl_4]^-$ (rate exhibits first order dependence on concentration of PhSH) and $[Fe_4S_3(SH)(SEt)_4]^-$ (rate is independent of concentration of PhSH) yields $\Delta H^‡$ and $\Delta S^‡$ for these steps. A notable feature is that, for both clusters, the substitution step is associated with a negative $\Delta S^‡$, consistent with associative substitution mechanisms. How this observation correlates with the kinetic dependence on the concentration of nucleophile is discussed. In order to understand the analysis of the kinetics, it will first be necessary to outline how the concentrations of acid, base and nucleophile are calculated in mixtures containing NHR_3^+ and PhS^-.

2.5.1 Studying the kinetics of the acid-catalyzed substitution reactions.

To study the kinetics of the acid-catalyzed substitution reactions of Fe-S-based clusters the system shown in Figure (2.10) was developed. The details of this approach have been discussed in earlier publications[11-14]. In this system, the cluster is reacted with a mixture containing $NHEt_3^+$, PhS^- and NEt_3. All the acids employed in the studies reported herein (NHR_3^+; R = Me, Et, Pr^n or Bu^n) are sufficiently strong acids that the equilibrium between NHR_3^+ and PhS^- lies completely to the right-hand side (*vide infra*). Consequently, in the presence of an excess of acid the solution species present are NHR_3^+ (the acid), NR_3 (the base) and PhSH (the nucleophile). Furthermore, the concentrations of the various species present in solution can be calculated using the simple relationships in Equations (2.7), (2.8) and (2.9), where subscript (e) indicates the equilibrium concentration and subscript (o) indicates the concentration initially in solution.

$$[PhSH]_e = [PhS^-]_o \qquad (2.7)$$

$$[NR_3]_e = [NR_3]_o + [PhS^-]_o \qquad (2.8)$$

$$[NHR_3^+]_e = [NHR_3^+]_o - [PhS^-]_o \qquad (2.9)$$

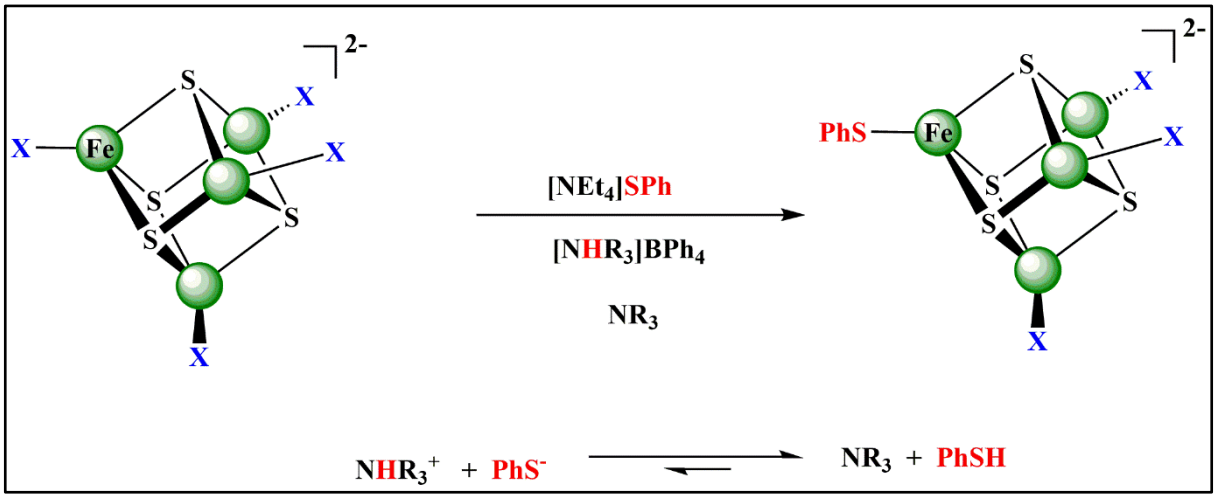

Figure 2.10. Components of the system used to study the acid-catalyzed substitution reactions of terminal ligands in $[Fe_4S_4X_4]^{2-}$ (X = thiolate, phenolate or halide), and the protolytic equilibrium which needs to be considered when calculating the nature and concentration of acid, base and nucleophile present in MeCN solution.

2.5.2 Protonation: studies with NHR_3^+ (R = Me, Et, Pr^n or Bu^n).

For the mechanism in Figure (1.16), the structural integrity of the cluster core remains intact throughout and the rate law for the reaction with $[Fe_4S_4Cl_4]^{2-}$ is that shown in Equation (2.16)[11-14]. For the mechanism in Figure (1.17), the rate law is also Equation (2.16), but in this case K_0^R corresponds to proton transfer and coupled cleavage of a Fe-S bond, and thus, the rates may not correlate with the pK_as of the acids, and could also reflect factors which affect the energetics of the Fe-S cleavage. Both the simple and revised mechanisms of acid-catalysed substitution Figure (1.16) and Figure (1.17), when (k_1^R) is the rate constant for dissociative substitution step and (k_2^R) is the rate constant for associative substitution step. Consequently, the rate law for acid-catalyzed substitution reaction for $[Fe_4S_4Cl_4]^{2-}$ with $[PhS^-]$ in presence of NHR_3^+ (R = Me, Et, Pr^n or Bu^n), can be derived as follow.

When the substitution steps (k_1^R) and (k_2^R) are rate-limiting:

$$\text{Rate} = k_1^R[Fe_4S_4Cl_4H^-]_e + k_2^R[Fe_4S_4Cl_4H^-]_e\,[PhSH] \qquad (2.10)$$

(Where the subscript (e) indicates to the concentrations formed at equilibrium)

If (k_1^R) and (k_2^R) << (k_{-1}^R)

(Where (k_{-1}^R) is rate constant for the deprotonated step for cluster)

$$K_0^R = \frac{[Fe_4S_4Cl_4H^-]_e[NR_3]}{[Fe_4S_4Cl_4^{2-}]_e[NHR_3^+]} \qquad (2.11)$$

$$[Fe_4S_4Cl_4H^-]_e = K_0^R[Fe_4S_4Cl_4^{2-}]_e[NHR_3^+]/[NR_3] \quad (2.12)$$

Substituting Equation (2.12) into Equation (2.10) leads to produce Equation (2.13):

$$\text{Rate} = K_0^R k_1^R[Fe_4S_4Cl_4^{2-}]_e[NHR_3^+]/[NR_3] + K_0^R k_2^R[Fe_4S_4Cl_4^{2-}]_e[PhSH]\,[NHR_3^+]/[NR_3] \quad (2.13)$$

Intuitively obvious that:

$$[Fe_4S_4Cl_4^{2-}]_T = [Fe_4S_4Cl_4^{2-}]_e + [Fe_4S_4Cl_4H^-]_e \quad (2.14)$$

By substituting Equation (2.12) into (2.14):

$$[Fe_4S_4Cl_4^{2-}]_T = [Fe_4S_4Cl_4^{2-}]_e\{1 + K_0^R[NHR_3^+]/[NR_3]\} \quad (2.15)$$

As a result:

$$[Fe_4S_4Cl_4^{2-}]_e = \frac{[Fe_4S_4Cl_4^{2-}]_T}{1 + K_0^R[NHR_3^+]/[NR_3]}$$

Substituting this value for $[Fe_4S_4Cl_4]_e^{2-}$ in Equation (2.13):

$$\text{Rate} = \frac{K_0^R(k_1^R + k_2^R[PhSH])[Fe_4S_4Cl_4^{2-}][NHR_3^+]/[NR_3]}{1 + K_0^R[NHR_3^+]/[NR_3]} \quad (2.16)$$

If the mechanism shown in Figure (1.16) operates, the rate observed with any acid can be calculated, provided the pK_a^{NHR} of NHR_3^+ is known[21, 22]. The value of K_0^R can be calculated as followed:

$$[Fe_4S_4Cl_4]^{2-} + NHR_3^+ \rightleftharpoons[K_0^R] [Fe_4S_4Cl_4H]^{1-} + NR_3 \quad (2.17)$$

$$K_0^R = \frac{[Fe_4S_4Cl_4H^-][NR_3]}{[Fe_4S_4Cl_4^{2-}][NHR_3^+]} \quad (2.18)$$

Equation (2.18) x $\frac{[H^+]}{[H^+]}$

$$K_0^R = \frac{[Fe_4S_4Cl_4H^-][NR_3]}{[Fe_4S_4Cl_4^{2-}][NHR_3^+]}\frac{[H^+]}{[H^+]} \quad (2.19)$$

The acid dissociation equilibrium reactions for $[Fe_4S_4Cl_4H^-]$ and NHR_3^+ are as follows.

$$[Fe_4S_4Cl_4H]^{1-} \rightleftharpoons[K_a^{cluster}] [Fe_4S_4Cl_4]^{2-} + H^+ \quad (2.20)$$

$$NHR_3^+ \rightleftharpoons[K_a^{NHR}] NR_3 + H^+ \quad (2.21)$$

$$K_a^{cluster} = \frac{[Fe_4S_4Cl_4^{2-}][H^+]}{[Fe_4S_4Cl_4H^-]} \quad (2.22)$$

$$K_a^{NHR} = \frac{[NR_3][H^+]}{[NHR_3^+]} \quad (2.23)$$

Substituting Equation (2.22) and (2.23) into (2.19) gives:

$$K_0^R = \frac{K_a^{NHR}}{K_a^{cluster}} \quad (2.24)$$

Using the relationship shown in Equation (2.24) (for $[Fe_4S_4Cl_4]^{2-}$, $pK_a^{cluster}$ = 18.8, calculated assuming the mechanism in Figure (1.16); from data where $NHEt_3^+$ is the acid)[12-14]. Furthermore, the rate constants for the substitution steps for $[Fe_4S_4Cl_4]^{2-}$ are known from earlier studies with $NHEt_3^+$, and are independent of the identity of the acid[15] (k_1^R = 2.0±0.3s^{-1} and k_2^R = 1.5±0.1 x 10^4 dm^3 mol^{-1} s^{-1}). If the rate departs from that predicted in this manner, it indicates that the mechanism is not that in Figure (1.16).

If the values of k_{obs}/[PhSH] predicted by the rate laws for associative substitution pathway shown in the Table (2.2) and the experimental values are the same then this is good evidence that the mechanism of the reaction with that acid occurs by the acid-catalysed associative substitution mechanism analogous to that shown in Figure (1.16). However, deviation from the predicted behaviour is indicative of a different mechanism operating.

Table (2.2): The theoretical rate laws for associative pathway of substitution of $[Fe_4S_4Cl_4]^{2-}$ by PhSH in the presence of various NHR_3^+

Acid	pK_a	K_0^R	k_{obs}/[PhSH]
$NHMe_3^+$	17.61	15.5	2.33 x 10^5 R/(1+15.5R)
$NHEt_3^+$	18.46	2.2	3.3 x 10^4 R/(1+2.2R)
$NHPr^n{}_3^+$	18.1	5.0	7.5 x 10^4 R/(1+5.0R)
$NHBu^n{}_3^+$	18.1	5.0	7.5 x 10^4 R/(1+5.0R)

k_2^R = 1.5±0.1 x 10^4 dm^3 mol^{-1} s^{-1}, $K_0^R = K_a^{NHR3}/K_a^{cluster}$, pK_a^{NHR3} = 17.6-18.41 in MeCN[10] and p$K_a^{cluster}$ = 18.8[12-14]. When R= $[NHR_3^+]$ / $[NR_3]$.

The kinetics of the reactions between $[Fe_4S_4Cl_4]^{2-}$ and PhS^- have been studied in MeCN and in the presence of a series of acids NHR_3^+ (R = Me, Et, Pr^n and Bu^n). These acids were chosen because they are structurally similar with little variation in their pK_as. The pK_a^{NHR} of the acids (in MeCN) are: $NHMe_3^+$ (pK_a^{NHMe} = 17.61); $NHEt_3^+$ (pK_a^{NHEt} = 18.4); $NHPr^n{}_3^+$ (pK_a^{NHPr} = 18.1); $NHBu^n{}_3^+$ (pK_a^{NHBu} = 18.1)[10].

2.5.2.1 Kinetics of Substitution of $[Fe_4S_4Cl_4]^{2-}$ in Presence NHR_3^+ (R= Et and Pr^n).

Kinetics study of the reaction of $[Fe_4S_4Cl_4]^{2-}$ with PhSH in the presence of $NHEt_3^+$ or $NHPr^n{}_3^+$ showed kinetic behaviour in good agreement with that predicted for an acid-catalysed associative substitution mechanism Table (2.2). Indeed, the kinetics of substitution reaction of PhSH to $[Fe_4S_4Cl_4]^{2-}$ in presence $NHEt_3^+$ has already been described[15]. The study with $NHPr^n{}_3^+$was performed in the following manner. Solutions of $NHPr^n{}_3^+$ (concentration = 0 to 20 mmol dm^{-3}), and $[NEt_4][SPh]$ (2.5 or 5.0 mM) were prepared in MeCN using freshly prepared stock solutions of $[NHPr_3]BPh_4$ (60 mmol dm^{-3} in 25ml) and $[NEt_4][SPh]$ (20 mmol dm^{-3} in 25ml) in MeCN . The solution of cluster (0.2 mmol dm^{-3} in 25ml MeCN) was prepared. The kinetics data for the reaction between the $[Fe_4S_4Cl_4]^{2-}$ and $[PhS^-]$ in presence $NHPr^n{}_3^+$ were collected using a stopped-flow spectrophotometer (***see section 2.4.1***), at temperature = 25 ^{0}C and wavelength = 550nm. Under all conditions, the stopped-flow absorbance-time traces were biphasic and were an excellent fit to two exponentials, indicating a first-order dependence on the concentration of the cluster.

The rate law in Equation (2.16) was originally established from kinetic studies of the reactions between $[Fe_4S_4Cl_4]^{2-}$ and PhS^- in the presence of $NHEt_3^+$. Analogous studies with $NHPr^n{}_3^+$ also

follow Equation (2.16), using the corrected value of K_0^{Pr}. The kinetic data for the reactions involving $NHPr^n{}_3^+$ are shown in Table (2.3).

Table 2.3. Stopped-Flow experimental kinetic data for the reaction of $[Fe_4S_4Cl_4]^{2-}$ (0.2 mmol dm^{-3}) with [PhSH] in presence $[NHPr^n{}_3^+]$ at λ = 550nm and T = 25 ^{0}C.

$[PhS^-]$ mmol dm^{-3}	**$[NHPr_3^+]$ mmol dm^{-3}**	**k_{obs}/s^{-1}**
2.5	0	5.21
2.5	2.5	8.76
2.5	5	11.4
2.5	10	14.5
2.5	20	15.6
5	0	9.8
5	2.5	4.5
5	5	8.4
5	10	31
5	20	36

The solid curve in Figure (2.11) is that predicted by the rate expression shown in the Table (2.2). It is clear that the experimental data points are a good fit to this curve. The comparison between the theoretical and experimental data are shown in Table (2.4).

However, the kinetics of the similar reactions with $NHMe_3^+$ and $NHBu^n{}_3^+$ show significant deviations from that predicted by Equation (2.16).

Table 2.4. Theoretical and experimental kinetics data for the substitution reaction of PhSH with $[Fe_4S_4Cl_4]^{2-}$ in the presence of $NHPr^n_3{}^+$.

R = **$[NHPr^n_3{}^+]/[NPr^n_3]$**	**Theoretical data** ***k*/[PhSH]= 7.5x10^4 R /(1+ 5.0 R)**	**Experimental data *k*/[PhSH]** **(1.25 mmol dm^{-3})**	**Experimental data** ***k*/[PhSH]** **(2.5 mmol dm^{-3})**
0	0	-	-
0.2	6500	-	-
0.4	8666.667	-	-
0.6	9750	-	-
0.8	10400	-	-
1	10833.33	9100	11000
2	11818.18	-	-
3	12187.5	12000	14000
4	12380.95	-	-
5	12500	-	-
6	12580.65	-	-
7	12638.89	12300	-
8	12682.93	-	-
9	12717.39	-	-
10	12745.1	-	-
11	12767.86	-	-

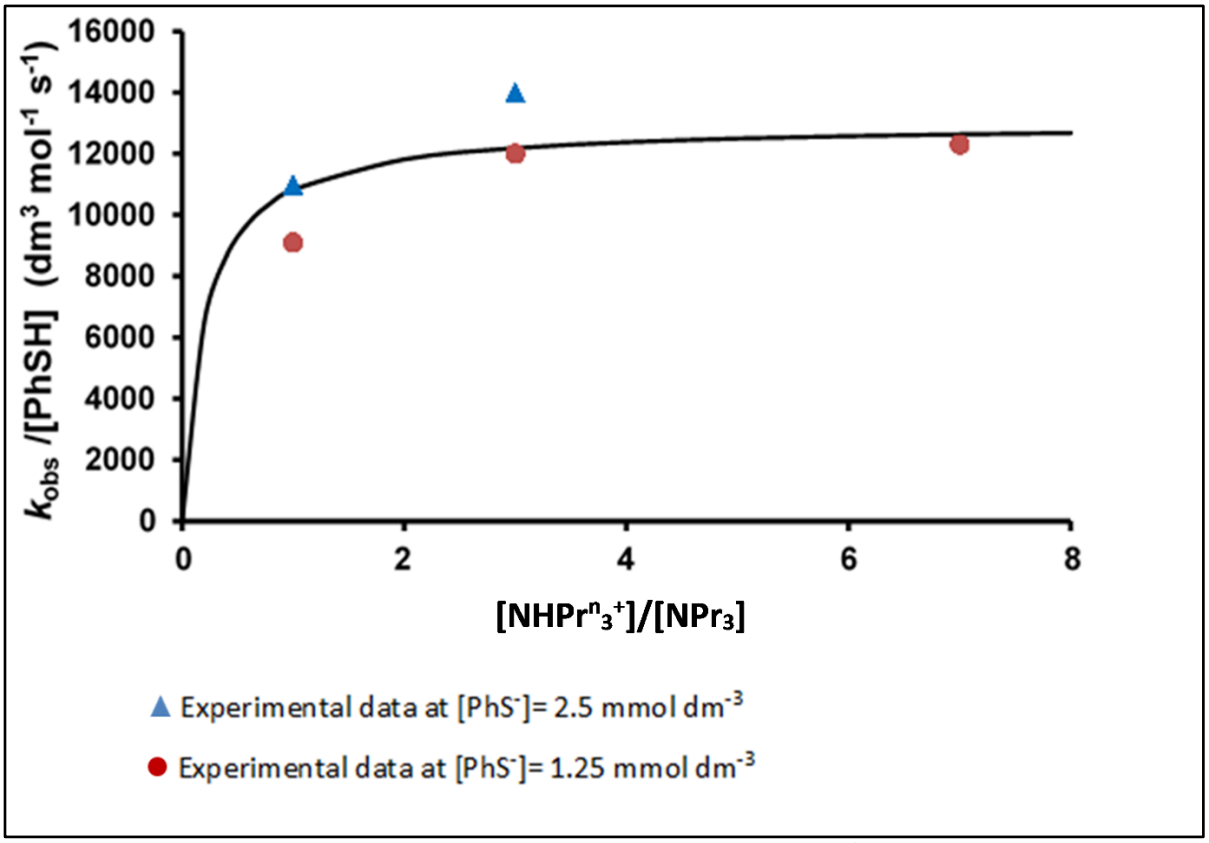

Figure 2.11. Graph of kinetics data for the substitution of $[Fe_4S_4Cl_4]^{2-}$ with PhSH in the presence of $NHPr^n{}_3^+$.

2.5.2.2 Kinetics of Substitution of $[Fe_4S_4Cl_4]^{2-}$ with PhS^- in Presence $NHBu^n{}_3^+$.

The kinetic studies on the substitution reaction of $[Fe_4S_4Cl_4]^{2-}$ with PhSH in the presence of $NHBu^n{}_3^+$ has shown that the rates of substitution are appreciably slower than predicted by rate law for the acid-catalysed substitution mechanism presented in Table (2.2). All experiments were performed under conditions where $[PhSH]_e = [NHBu^n{}_3^+]_e$. Analysis of the kinetic data indicates that the rate of substitution in the presence of $NHBu^n{}_3^+$ shows a dependence on the concentration of only $NHBu^n{}_3^+$ and is independent of the concentration of PhSH. The experimental k_{obs} data for the acid-catalyzed reaction of $[Fe_4S_4Cl_4]^{2-}$ with [PhSH] in presence $[NHBu^n{}_3^+]$ are shown in Table (2.5).

Table 2.5. Stopped-Flow experimental kinetic data for the reaction of $[Fe_4S_4Cl_4]^{2-}$ (0.2 mmol dm^{-3}) with [PhSH] in presence $[NHBu^n{}_3{}^+]$ at λ = 550nm and T = 25 ^{0}C

$[PhS^-]$ mmol dm^{-3}	**$[NHBu_3^+]$ mmol dm^{-3}**	**k_{obs}/s^{-1}**
1.25	0	2.53
1.25	2.5	0.9
1.25	5	1.9
1.25	10	2.3
1.25	20	5.3
1.25	30	9
2.5	2.5	1.48
2.5	5	2.039
2.5	10	3.3
2.5	20	5.2
5	0	7.8
5	2.5	1.4
5	5	1.9
5	10	2.2
5	20	4.8

5	30	7.3
10	0	1.5
10	2.5	2.2
10	5	3.1
10	10	3.7
10	20	5
10	30	6.2

By using the same manner described in ***section 2.5.2.***, the predicted kinetics data in Tables (2.6), (2.7), (2.8), and (2.9) show the differences between the calculated rates and experimental rates at various concentrations of PhSH. In graph shown in Figure (2.12), each colour of curve indicates the theoretical rates at different concentrations of [PhSH], orange at 5 mmol dm^{-3}, brown at 2.5 mmol dm^{-3}, green at 1.25 mmol dm^{-3}, and blue curve at 0.625 mmol dm^{-3}. Clearly, all experimental data lie below even the lowest (blue) curve.

Table 2.6. Theoretical and experimental kinetic data for the reaction of $[Fe_4S_4Cl_4]^{2-}$ with PhSH (0.625 mmol dm^{-3}) in the presence of $[NHBu^{n+}_3]$.

R= $[NHBu^n_3{}^+]/[NBu^n_3]$	**Theoretical data** ***k*= 7.5x10^4 [PhSH] R /(1+ 5.0 R)** **[PhSH] = 0.625 mmol dm^{-3}**	**Experimental data** ***k***
0.2	4.692183	-
0.5	6.70025	-
0.7	7.294902	-
1	7.8151	0.9
2	8.524274	-
3	8.790159	1.9
4	8.92942	-
5	9.015115	-
6	9.073165	-
7	9.115089	2.3
8	9.146787	-
9	9.171594	-
10	9.191536	-
11	9.207917	-
12	9.221613	-
13	9.233234	-
14	9.243218	-
15	9.251888	5.3
23	9.294341	9

Table 2.7. Theoretical and experimental kinetic data for the reaction of $[Fe_4S_4Cl_4]^{2-}$ with PhSH (1.25 mmol dm^{-3}) in the presence of $[NHBu^{n+}_3]$.

R=$[NHBu^n_3{}^+]/[NBu^n_3]$	**Theoretical data** ***k*= 7.5x10^4 [PhSH] R /(1+ 5.0 R)** **[PhSH] = 1.25 mmol dm^{-3}**	**Experimental *k***
0	0	-
0.2	9.384366	-
0.5	13.4005	-
0.7	14.5898	-
1	15.6302	2
2	17.04855	-
3	17.58032	3.3
4	17.85884	-
5	18.03023	-
6	18.14633	-
7	18.23018	-
8	18.29357	-
9	18.34319	-
10	18.38307	-
11	18.41583	5.2
12	18.44323	-
13	18.46647	-
14	18.48644	-
15	18.50378	-
23	18.58868	-

Table 2.8. Theoretical and experimental kinetic data for the reaction of $[Fe_4S_4Cl_4]^{2-}$ with PhSH (2.5 mmol dm^{-3}) in the presence of $[NHBu^{n+}_3]$.

R= $[NHBu^n_3{}^+]/[NBu^n_3]$	**Theoretical data** **k= 7.5x10^4 [PhSH] R /(1+ 5.0 R)** **[PhSH] = 2.5 mmol dm^{-3}**	**Experimental k**
0.2	18.76873	-
0.5	26.801	-
0.7	29.17961	-
1	31.2604	2.2
2	34.0971	-
3	35.16064	4.8
4	35.71768	-
5	36.06046	7.3
6	36.29266	-
7	36.46035	-
8	36.58715	-
9	36.68637	-
10	36.76614	-
11	36.83167	-
12	36.88645	-
13	36.93294	-
14	36.97287	-
15	37.00755	-
23	37.17736	-

Table 2.9. Theoretical and experimental kinetic data for the reaction of $[Fe_4S_4Cl_4]^{2-}$ with PhSH (5.0 mmol dm^{-3}) in the presence of $[NHBu^{n+}_3]$.

R= [$NHBu_3$]/[NBu_3]	**[PhSH] = Theoretical data** ***k*= 7.5 x10^4 [PhSH] R /(1+ 5.0 R)** **[PhSH] = 5.0 mmol dm^{-3}**	**Experimental *k***
0.2	37.53746	-
0.5	53.602	-
0.7	58.35922	-
1	62.5208	5
2	68.19419	6.2
3	70.32127	-
4	71.43536	-
5	72.12092	-
6	72.58532	-
7	72.92071	-
8	73.17429	-
9	73.37275	-
10	73.53229	-
11	73.66334	-
12	73.77291	-
13	73.86587	-
14	73.94574	-
15	74.0151	-
23	74.35473	-

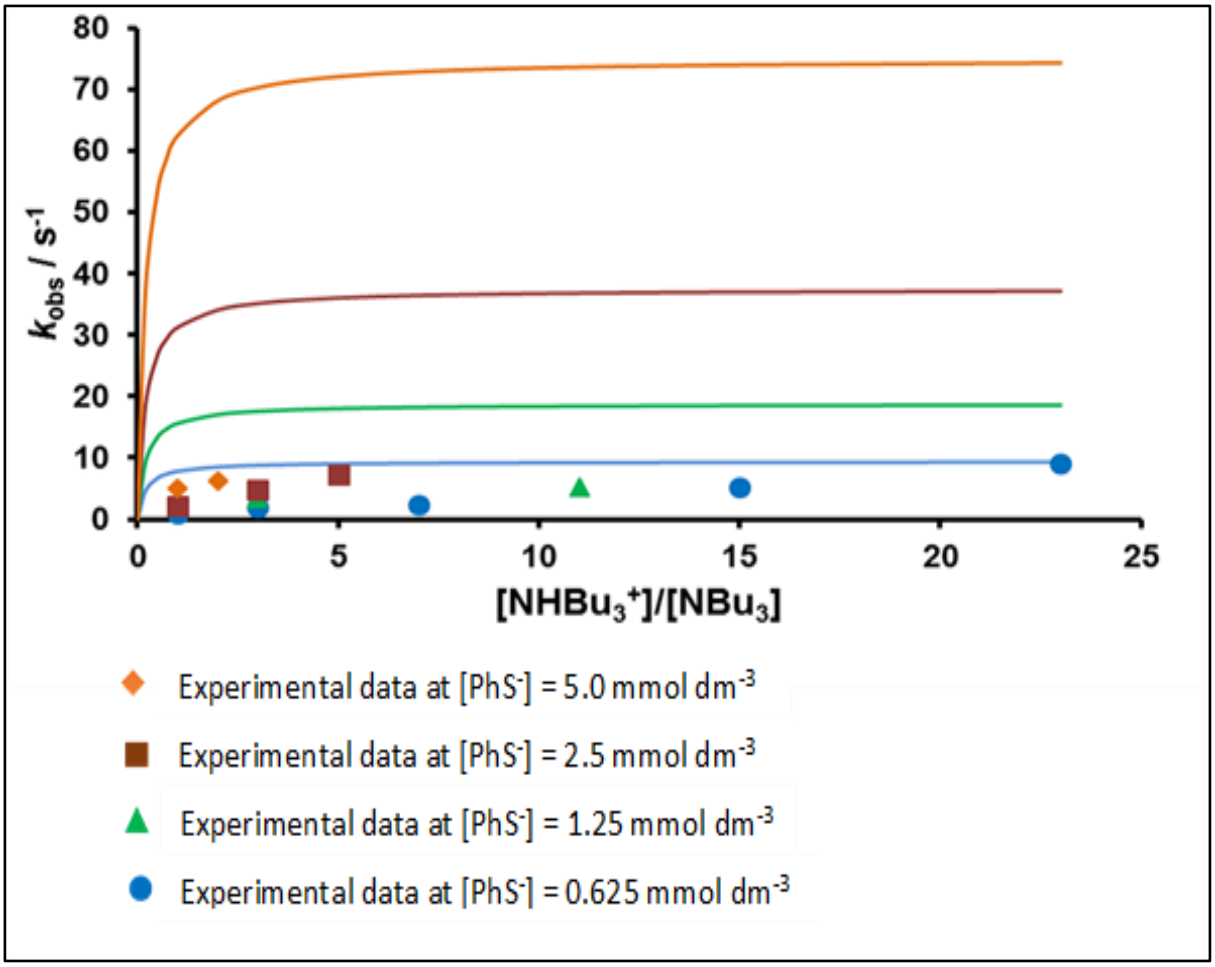

Figure 2.12. Graph shown the comparison between the predicted rates of acid-catalysed substitution reaction and the experimental rates of substitution of $[Fe_4S_4Cl_4]^{2-}$ by PhSH in the presence $[NHBu^n{}_3{}^+]$.

The kinetic data for the reaction between $[Fe_4S_4Cl_4]^{2-}$ and PhS^- in the presence of $NHBu^n{}_3{}^+$ do not fit Equation (2.16) with the calculated value of $K_0{}^{Bu} = 5.0$. This is shown in Figure (2.13) where the red dashed curve is the rate defined by Equation (2.16). Furthermore, The plot of k_{obs}/[PhSH] against $[NHBu^n{}_3]_e/[NBu^n{}_3]_e$ in Figure (2.13) shows that the rate is undergone to a first order dependence on $[NHBu^n{}_3{}^+]_e$ (indicated by the grey dotted line).

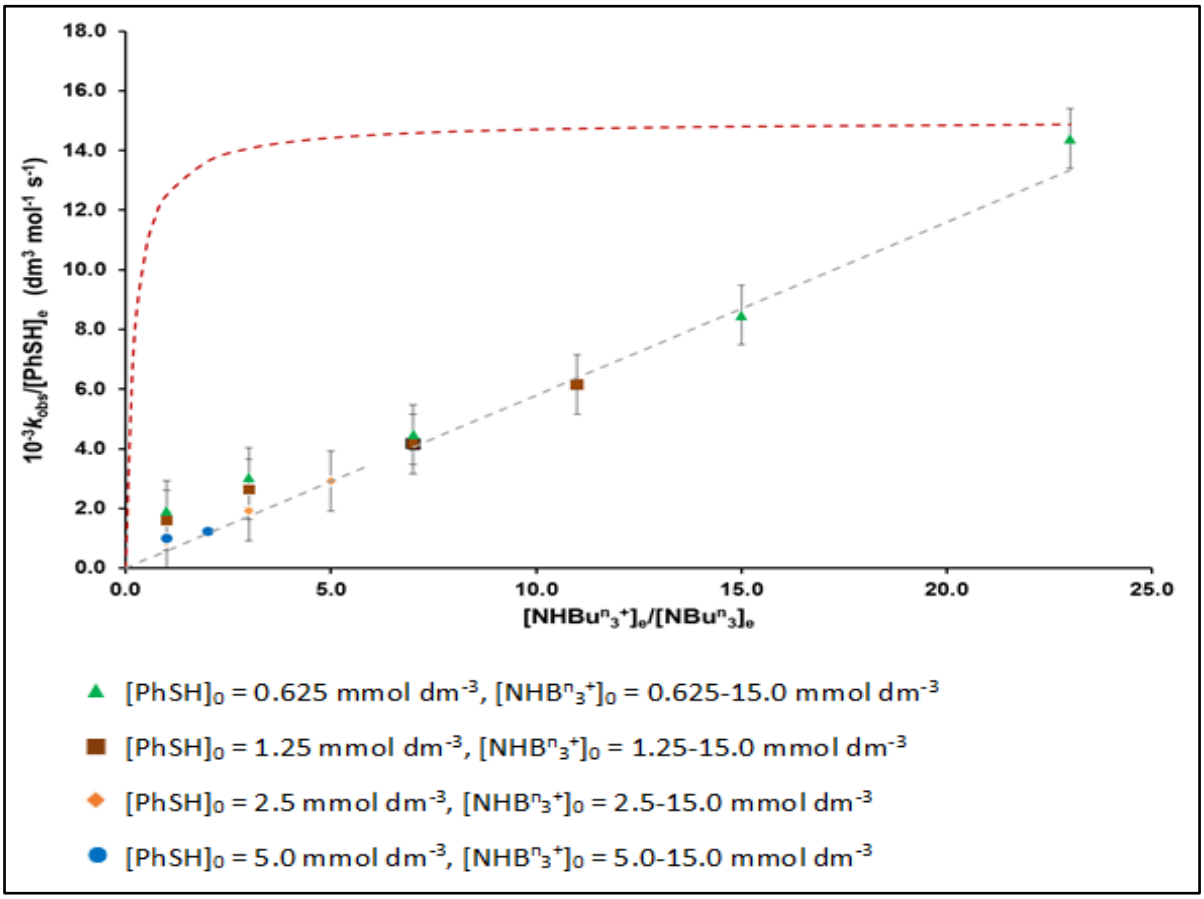

Figure 2.13. Plot of k_{obs}/[PhSH]$_e$ versus [NHBu$^n{}_3^+$]$_e$/[NBu$^n{}_3$]$_e$ for the reaction of $[Fe_4S_4Cl_4]^{2-}$ (0.2 mmol dm^{-3}) with PhS^- in the presence of NHBu$^n{}_3^+$ in MeCN at 25.0 ^oC. The red dashed curve is the rate predicted by Equation (2.16) using the pK_as of NHBu$^n{}_3^+$ (18.1) and the cluster (18.8). The grey dotted line is the experimental rate when k_{obs}/[PhSH].

The straightline fit to the data shown in Figure 2.13 yields the rate law in Equation (2.25) for the acid-catalyzed substitution reaction of $[Fe_4S_4Cl_4]^{2-}$ with PhS^- in precense NHBu$^n{}_3^+$. Since, the data in Figure 2.13 was collected under conditions where [PhSH]$_e$ = [NHBu$^n{}_3^+$]$_e$ and thus the data in Figure (2.13), the data can be re-plotted as shown in Figure (2.14).

$$\text{Rate} = \{1.4 + 490[\text{NHBu}_3^{n+}]_e\}[Fe_4S_4Cl_4]^{2-} \quad (2.25)$$

Equation (2.25) contains two terms indicating two pathways for substitution: the first term is independent of the concentration of acid and the second term exhibits a first order dependence on the concentration of acid. Both terms are independent of the concentration of nucleophile.

Table (2.10) : Kinetic data for the substitution reaction of PhSH with $[Fe_4S_4Cl_4]^{2-}$ in the presence of $[NHBu^n{}_3{}^+]$ and the straight line fit predicted by Equation (2.25).

[NHBu$_3$]	***k*$_{obs.}$ at [PhSH] = 0.625 mmol dm^{-3}**	***k*$_{obs.}$ at [PhSH] = 1.25 mmol dm^{-3}**	***k*$_{obs.}$ at[PhSH] = 2.5 mmol dm^{-3}**	***k*$_{obs.}$ at [PhSH] = 5.0 mmol dm^{-3}**	**line fit**
0	-	-	-	-	1.4
0.625	1.2	-	-	-	1.70625
1.25	-	2.0	-	-	2.0125
1.88	1.9	-	-	-	2.3212
2.5	-	-	2.2	-	2.625
3.75	-	3.3	-	-	3.2375
4.38	2.8	-	-	-	3.5462
5.0	-	-	-	5.0	3.85
7.5	-	-	4.8	-	5.075
8.75	-	5.2	-	-	5.6875
9.4	5.3	-	-	-	6.006
10.0	-	-	-	6.2	6.3
12.5	-	-	7.3	-	7.525
13.75	-	7.7	-	-	8.1375
14.38	9.0	-	-	-	8.4462
15.0	-	-	-	-	8.75

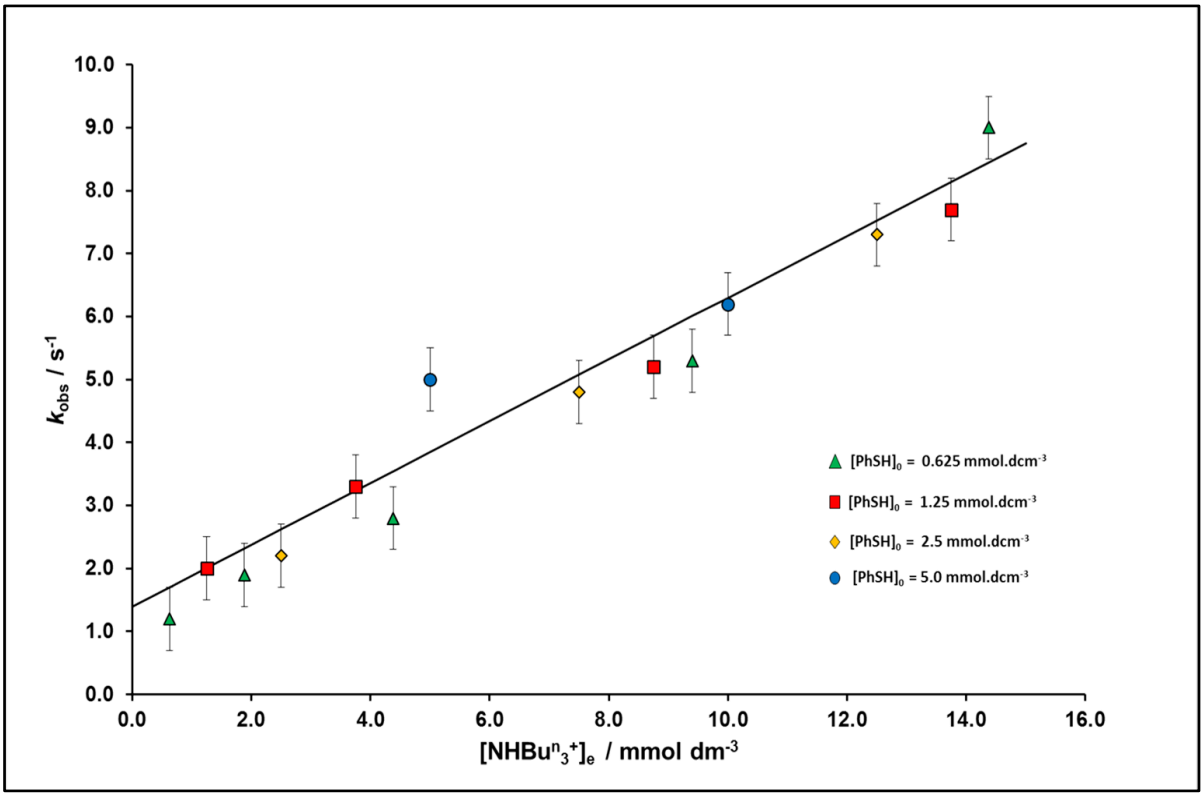

Figure 2.14. Plot of kinetics data for the reaction between $[Fe_4S_4Cl_4]^{2-}$ and $[PhS^-]$ in presence $[NHBu^n{}_3{}^+]$.

Earlier work on the kinetics of the acid-catalyzed substitution reactions of $[Fe_4S_4Cl_4]^{2-}$ with PhS^- in the presence of $NHEt_3^+$ showed that, at low concentrations of acid, the uncatalysed substitution pathway becomes evident with a rate constant (k = 2.0 ± 0.3 s^{-1})[15]. This value is in good agreement with the first term in Equation (2.25). The second term in Equation (2.25) is consistent with a mechanism for acid-catalysed substitution (either Figure 1.16 or Figure 1.17), but involving rate-limiting proton transfer. Previously, rate-limiting proton transfer of $[Fe_4S_4Cl_4]^{2-}$ has been observed in reactions involving the pyrrolidinium ion ($pyrrH^+$, pK_a = 21.5)[10] as acid, because proton transfer is thermodynamically unfavourable[23, 24]. However, the pK_a of $NHBu^n{}_3{}^+$ is essentially the same as the other acids used in the studies reported herein and hence proton transfer cannot have become slow with $NHBu^n{}_3{}^+$ because there has been a change in the thermodynamic driving force of the reaction. It seems likely that proton transfer to $[Fe_4S_4Cl_4]^{2-}$ is slow with $NHBu^n{}_3{}^+$ because of steric factors; the long Bu^n chains are sufficiently bulky to make it difficult for this acid to get close to the cluster for optimal proton transfer (*i.e.* the acidic NH group in $NHBu^n{}_3{}^+$ is buried by the Bu^n groups), as shown in Figure (2.15). Finally, it should be noted that proton transfer to $[Fe_4S_4Cl_4]^{2-}$ from $pyrrH^+$ is significantly faster (k_o^{pyr} = 2.1 ±0.2 x 10^3 dm^3 mol^{-1} s^{-1})[24-28] than from $NHBu^n{}_3{}^+$ (k_o^{NHBu} = 490 ±20 dm^3 mol^{-1} s^{-1}). However, it is difficult to interpret this difference in rates because (as

outlined above) the reasons $pyrrH^+$ and $NHBu^n{}_3{}^+$ transfer protons slowly to the cluster are different.

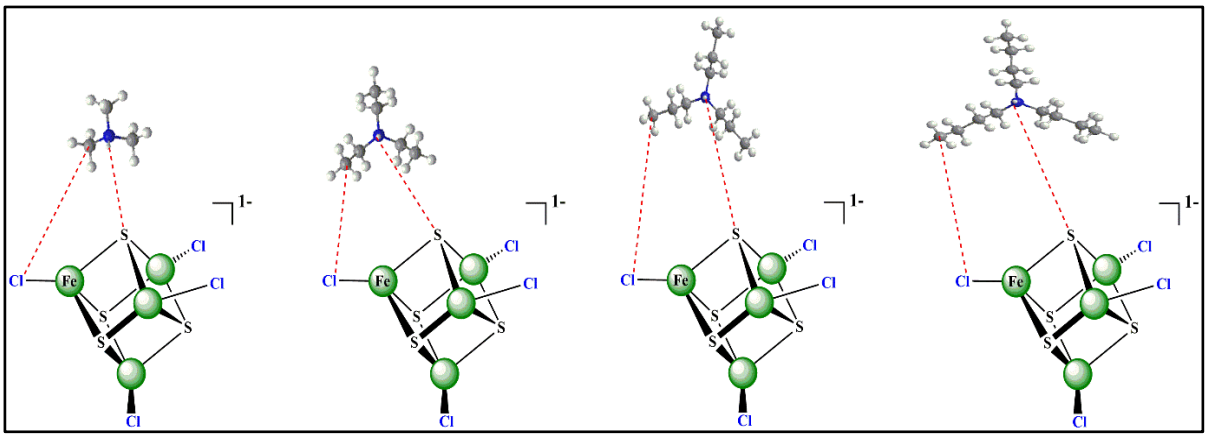

Figure 2.15. Structures of various $NHR_3{}^+$ (R = Me, Et, $Pr^n{}_3{}^+$ and $Bu^n{}_3{}^+$) and how Bu group buries the acidic NH group by steric factor for $NHBu^n{}_3{}^+$.

2.5.2.3 Kinetics of Substitution of $[Fe_4S_4Cl_4]^{2-}$ with PhSH in the presence of $NHMe_3{}^+$.

The kinetic studies of substitution reaction of $[Fe_4S_4Cl_4]^{2-}$ with PhSH in the presence of $NHMe_3{}^+$ are performed using a constant concentration of cluster (0.2 mmol dm^{-3}, in 25ml MeCN), different concentrations of $[NEt_4][SPh]$ for each experiment (1.25 mmol dm^{-3}, 2.5 mmol dm^{-3} and 5.0 mmol dm^{-3} in MeCN) and a range of concentrations $[NHMe_3{}^+]$ (2.5-25 mmol dm^{-3}). The kinetics data were collected using a stopped-flow spectrophotometer, as shown in ***(section 2.4.1***), at temperature = 25 °C and wavelength = 550 nm. The experimental kinetics data are presented in Table (2.11).

Table (2.11) Stopped-Flow experimental kinetics data for the reaction of $[Fe_4S_4Cl_4]^{2-}$ (0.2 mmol dm^{-3}) with [PhSH] in presence $[NHMe_3^+]$ at λ = 550nm and T = 25 °C

$[PhS^-]$ mmol dm^{-3}	**$[NHMe_3^+]$ mmol dm^{-3}**	**k_{obs}/s^{-1}**
1.25	2.5	2.2
1.25	5.0	3.4
1.25	10	6.1
1.25	15	8.9
1.25	20	10.5
1.25	25	12.25
2.5	2.5	6.2
2.5	5.0	6.96
2.5	10	12.3
2.5	15	14.3
2.5	20	17.5
2.5	25	17.9
5.0	10	13.2
5.0	15	14.9
5.0	20	15.6
5.0	25	20

The pK_a^{NHMe3} is calculated as follow:

First, consider the concentrations of species formed at equilibrium in the presence of an excess of $NHMe_3^+$.

	$NHMe_3^+$	+	PhS^-	⇌	NMe_3	+	PhSh	(2.26)
In initially	a		b		0		0	
If $[NHMe_3^+] > [PhS^-]$								
At equilibrium	a-b		0		b		b	

Now consider the change in concentrations caused by the homoconjugation equilibrium.

$$NHMe_3^+ + NMe_3 \underset{}{\overset{K_H^{10} = 6\ mmol^{-1}\ dm^3}{\rightleftharpoons}} NHMe_3^+.NMe_3 \qquad (2.27)$$

	$NHMe_3^+$	NMe_3	$NHMe_3^+.NMe_3$
Initially:	a-b	b	0
Equilibrium:	a-b-x	b-x	x

$$K_H = \frac{[NHMe_3^+.NMe_3]_e}{[NHMe_3^+]_e[NMe_3]_e} \quad (2.28)$$

$$K_H = \frac{x}{(a-b-x)(b-x)} \quad (2.29)$$

For each experiment, the value of $[NHMe_3^+]_e$ = (a-b), and $[NMe_3]_e$= (b) are readily calculated.

Using Equation (2.29), the $[Me_3NHNMe_3^+]_e$ (= x) can be calculated.

Hence: $\frac{[NHMe_3^+]}{[NMe_3]} = \frac{(a-b-x)}{(b-x)}$; and: [PhSH] = $[NMe_3]$ = (b-x)

These calculations make allowance that the homoconjugation equilibrium has on the concentrations of $[NHMe_3^+]_e$, $[NMe_3]_3$ and $[Me_3NHNMe_3^+]_e$. This correction is not needed for any of the acids which have been studied ($NHEt_3^+$, $NHPr^n{}_3^+$ or $NHBu^n{}_3^+$) because the corresponding homoconjugation constants for the other acids are much smaller and so do not affect the concentrations.

It seems likely that the substitution reaction of $[Fe_4S_4Cl_4]^{2-}$ with PhSH in the presence of $NHMe_3^+$ will occur without steric issues, see Figure (2.15), and this acid is the strongest of the acids (pK_a = 17.61) studied in this investigation so there is no thermodynamic barrier to proton transfer. The kinetic data for the reaction between $[Fe_4S_4Cl_4]^{2-}$ and PhS^-, in the presence of $NHMe_3^+$ are shown in Figure (2.16). The red dashed curve shows the dependence of k_{obs}/[PhSH] on $[NHMe_3^+]/[NMe_3]$ predicted by Equation (2.16), using K_0^{Me} = 15.9 (calculated from the pK_as

of the cluster and $NHMe_3^+$). Obviously, the experimental data does not fit the predicted rate, and the fit to the experimental data is the solid curve which is defined by Equation (2.30), as presented in Table (2.12).

$$\text{Rate} = \frac{(1.9\text{x}10^3)[Fe_4S_4Cl_4^{2-}][PhSH][NHMe_3^+]_e/[NMe_3]_e}{1 + 0.16[NHMe_3^+]_e/[NMe_3]_e} \qquad (2.30)$$

The rate law in Equation (2.30) is clearly of the same form as Equation (2.16)[11-14, 21, 22], and comparison of Equns (2.16) and (2.30) gives K_0^{Me} = 0.16 and k_2^{Me} = 1.2±0.1 x 10^4 dm^3 mol^{-1} s^{-1}. Thus, at high values of $[NHMe_3^+]/[NMe_3]$, the rate is independent of $[NHMe_3^+]/[NMe_3]$ and is identical to that observed with $NHEt_3^+$ and $NHPr^n{}_3^+$ (k_2^R = 1.2±0.1 x 10^4 dm^3 mol^{-1} s^{-1}), corresponding to substitution of the protonated cluster, $[Fe_4S_3(SH)Cl_4]^{1-}$. However, at low values of $[NHMe_3^+]/[NMe_3]$, the rate is appreciably slower than predicted by Equation (2.16). Thus, although Equation (2.30) is of the same form as Equation (2.16), it is not consistent with the mechanism in Figure (1.16) because the value of K_0^{Me} = 0.16 is significantly different to the value K_0^{Me} = 15.9 calculated from the pK_as of the cluster and $[NHMe_3^+]$. Using the values in Equation (2.30), K_0 = 0.18 and p$K_a^{cluster}$ = 18.8, we can calculate pK_a^{NHMe3} = 19.5. This value is ~2pK_a units different from the literature value (pK_a^{NHMe3} = 17.6)[10]. It appears that in the reaction with $[Fe_4S_4Cl_4]^{2-}$, $NHMe_3^+$ is behaving as though it were a much weaker (~ 100 time weaker) acid. It is unreasonable that the literature value of pK_a^{Me} is so much in error, if for no other reason than it would mean the pK_a of $NHMe_3^+$ was very different to other NHR_3^+.

Table (2.12): Kinetic data for the substitution reaction of PhSH with $[Fe_4S_4Cl_4]^{2-}$ in the presence of $[NHMe_3^+]$ and the solid curved fit predicted by Equation (2.30).

$[NHMe_3^+]/[NMe_3]$	**Theoretical $k_{obs.}$/[PhSH]**	**$k_{obs.}$/[PhSH] [PhSH] = 1.25 mmol dm^{-3}**	**$k_{obs.}$/[PhSH] [PhSH] = 2.5 mmol dm^{-3}**	**$k_{obs.}$/[PhSH] [PhSH] = 5.0 mmol dm^{-3}**
0	2	-	-	-
0.1	7845.137	-	-	-
0.2	9758.098	-	-	-
0.3	10621.47	-	-	-
0.33	10795.13	-	-	-
0.4	11113.11	-	-	-
0.5	11430.57	-	-	-
0.6	11652.49	-	-	-
0.71	11830.4	-	-	-
0.8	11942.3	-	-	-
0.85	11994.95	-	-	-
1.0	12123.21	1760	2480	2640
1.25	12271.94	-	-	-
2.0	12502	-	-	2980
2.5	12580.62	-	-	-
3.0	12633.58	2720	2784	3120
3.12	12643.82	-	-	-

3.75	12686.99	-	-	-
4.0	12700.41	-	-	4000
5.0	12740.85	-	4920	-
5.35	12751.48	-	-	-
6.0	12767.96	-	-	-
7.0	12787.39	4880	5720	-
7.5	12795.18	-	-	-
8.0	12802	-	-	-
8.75	12810.78	-	-	-
9.0	12813.39	-	-	-
10.0	12822.51	-	-	-
11.0	12829.99	7120	7000	-
12.0	12836.22	-	-	-
12.5	12838.97	-	-	-
13.75	12844.97	-	-	-
14.0	12846.04	-	-	-
15.0	12849.97	8400	-	-
19.0	12861.56	9800	-	-

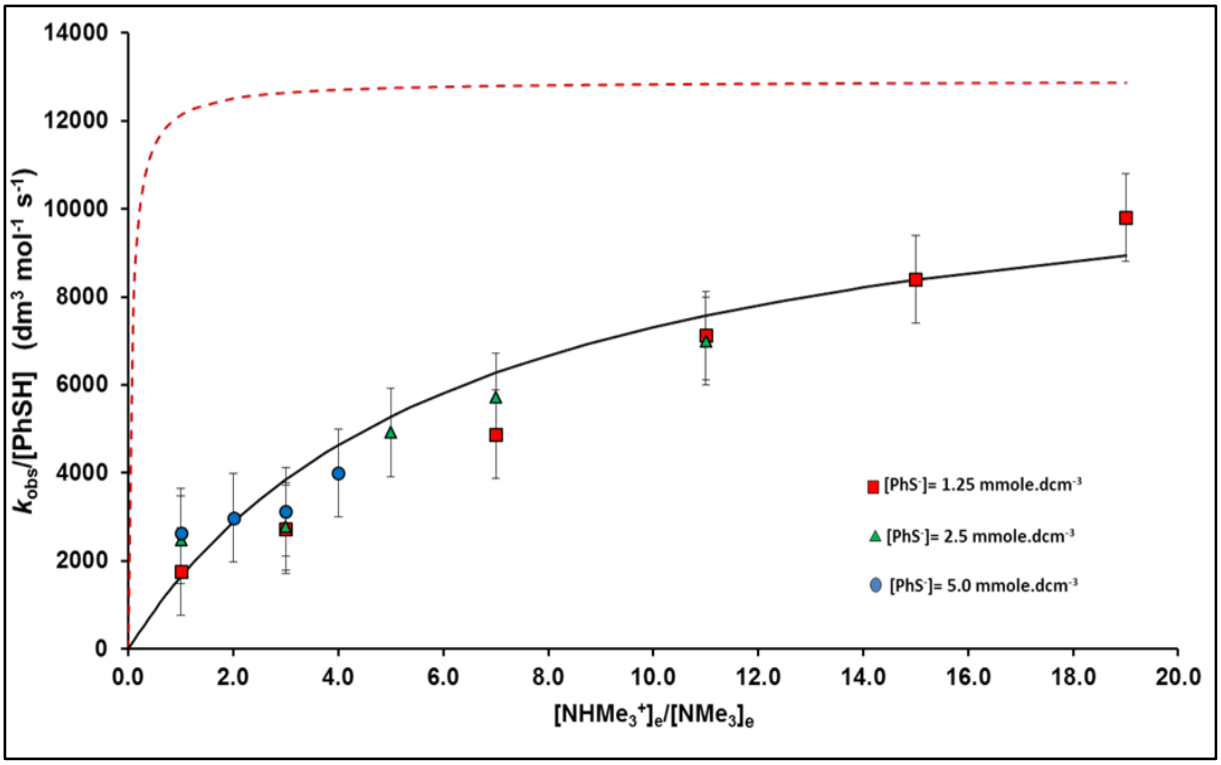

Figure 2.16. Plot of kinetics data for the acid-catalyzed substitution of $[Fe_4S_4Cl_4]^{2-}$ with PhS^- in presence of $NHMe_3^+$ acid.

The studies with $NHMe_3^+$ indicate that protonation of $[Fe_4S_4Cl_4]^{2-}$ does not involve just the simple addition of a proton to the cluster, and is inconsistent with the mechanism shown in Figure (1.16). For the mechanism in Figure (1.17), protonation of the cluster involves both proton transfer to a μ_3-S and Fe-(μ_3-SH) bond cleavage/elongation. Consequently, we need to consider how changes to NHR_3^+ affect both the proton transfer and the Fe-(μ_3-SH) bond elongation.

Of all the acids investigated in this study, it is notable that $NHMe_3^+$ is the least bulky and (slightly) the most acidic. We suggest that both the acidity and the bulk of the acid are significant in protonating the cluster. For the mechanism in Figure (1.17) it is clear that as NHR_3^+ hydrogen bonds to a μ_3-S (in preparation for proton transfer), a Fe-(μ_3-S) bond elongates in concert Figure (2.17)[7-9]. It seems likely that the incipient cluster disruption is facilitated by more bulky (longer R) groups of the acid because the longer the R groups the more they will interfere with the terminal chloro-ligand of $[Fe_4S_4Cl_4]^{2-}$ and, in order to relieve congestion, the Fe-(μ_3-SH) will elongate. This detail is shown in Figure (2.17). Thus, the transition states for proton transfer with the series of acids, NHR_3^+ (R = Me, Et, Pr^n and Bu^n) are subtly different, with the interference between the R groups and the chloro-ligands increasing as the size of R increases. With $NHBu^n{}_3^+$, the interference between the Bu^n groups and chloro-ligands is so severe that proton transfer becomes sufficiently slow that it is rate limiting.

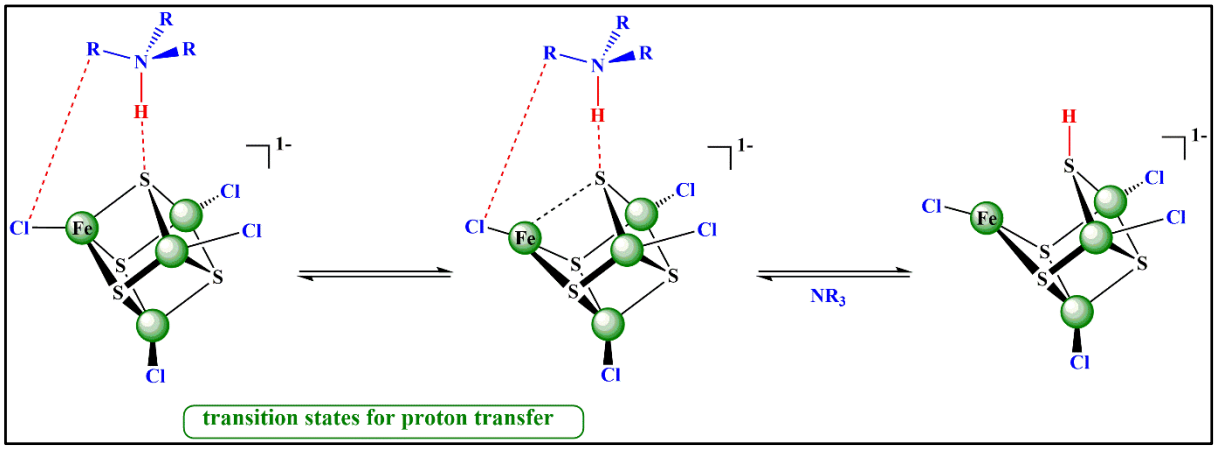

Figure 2.17. Representation of the transition state for proton transfer from NHR_3^+ to $[Fe_4S_4Cl_4]^{2-}$ indicating how interference between the terminal Cl group and the R group of the acid could facilitate Fe-(μ_3-SH) cleavage. It seems likely that the interference is most significant for the endo conformer of $\{[Fe_4S_4Cl_4]\ldots NHR_3\}^-$.

2.6 Temperature Dependence of acid-catalyzed substitution reactions of $[Fe_4S_4Cl_4]^{2-}$ with PhS^- in presence of NHR_3^+ (R= Et or Bu^n).

The rates of the acid-catalyzed substitution reactions of $[Fe_4S_4X_4]^{2-}$ are either independent of the concentration of nucleophile (X = thiolate or phenolate) or exhibit a first order dependence on the concentration of nucleophile (X = halide). The interpretation of these dependences is different for the two mechanisms shown in Figures (1.16) and (1.17). For the mechanism in Figure (1.16) it has been proposed that the different dependences on the concentration of nucleophile are due to different mechanisms of substitution (*i.e.* for X = RS or PhO, substitution occurs by a dissociative pathway but for X = halide, substitution occurs by an associative pathway)[15, 21, 22]. For the mechanism in Figure (1.17), the transient formation of a three-coordinate Fe suggests this site is primed for nucleophilic attack and that an associative mechanism will always prevail. Consequently, for this mechanism, it has been suggested that the substitution of all $[Fe_4S_3(SH)X_4]^-$ involve initial attack of MeCN (solvent), and the coordinated MeCN is subsequently displaced by PhSH[7-9]. To rationalise the observed dependencies on the concentrations of nucleophile, it has been suggested that when X = RS or PhO, displacement of coordinated X by MeCN is rate limiting. Because MeCN is the solvent its concentration will not change and hence will not be reflected in the rate law. But for the more labile $[Fe_4S_3(SH)Cl_4]^-$, the displacement of X= Cl by MeCN is rapid and the subsequent displacement of coordinated MeCN by PhSH is rate-limiting. In order to probe further the intimate mechanisms of the substitution step in the acid-catalysed substitution reactions we

have investigated the temperature dependence of the reactions to determine the extra-kinetic parameters, enthalpy of activation ($\Delta H^{\ddagger}$) and entropy of activation ($\Delta S^{\ddagger}$).

The temperature dependences of the acid-catalyzed substitution reactions of the following systems have been studied: (i) reaction of $[Fe_4S_4Cl_4]^{2-}$ with PhS^- in the presence of $NHBu_3^+$ (where proton transfer is rate-limiting); (ii) reaction of $[Fe_4S_4Cl_4]^{2-}$ with PhS^- in the presence of $NHEt_3^+$ (where substitution is rate-limiting and exhibits a first order dependence on the concentration of nucleophile) and (iii) reaction of $[Fe_4S_4(SEt)_4]^{2-}$ with PhS^- in the presence of $NHEt_3^+$ (where substitution is rate-limiting and the rate is independent of the concentration of nucleophile). In all cases, the temperature dependences of the reactions were measured over the range 15 – 35 ^oC.

The acid-catalyzed substitution reactions of $[Fe_4S_4X_4]^{2-}$ (X= Cl^- or SEt^-) with PhS^- in the presence of NHR_3^+ (R= Bu^n or Et), whose temperature dependences, are reported in this section are summarized in Table (2.13).

Table (2.13): Temperature dependent studies. Kinetics characteristic for reactions of $[Fe_4S_4X_4]^{2-}$ (X= Cl^- or SEt^-) with PhSH in the presence of acid.

Clusters	**Acid**	**Kinetics[a]**
$[Fe_4S_4Cl_4]^{2-}$	$NHBu^n{}_3^+$	$k_{obs.} = K_0^{NHBu}[NHBu^n{}_3^+]$ rate–limiting protonation
$[Fe_4S_4Cl_4]^{2-}$	$NHEt_3^+$	$k_{obs.} = K_0^{NHEt}\, k_2^{NHEt}[PhSH]A/(1+ K_0^{NHEt}\, A)$ rate-limiting substitution first order dependence on [PhSH] .
$[Fe_4S_4(SEt)_4]^{2-}$	$NHEt_3^+$	$k_{obs.} = K_0^{NHEt}\, k_1^{NHEt}A/(1+ K_0^{NHEt}\, A)$ rate-limiting substitution independent of [PhSH].

[a] $A = [NHEt_3^+]/[NEt_3]$.

For the reaction of $[Fe_4S_4Cl_4]^{2-}$ with PhS^- in the presence of $NHBu^n{}_3^+$, where proton transfer from the acid to $[Fe_4S_4Cl_4]^{2-}$ is rate-limiting, analysis for the kinetics of temperature dependence for experimental data is performed using the rate law shown in Equation (2.31), see Table (2.14).

$$k_{obs.} = k_0^{NHBu}[NHBu_3^{n+}] \qquad (2.31)$$

By using Eyring Equation (2.32), the parameters $\Delta H^{\ddagger}_{k0}$ and $\Delta S^{\ddagger}_{k0}$ can be determined:

$$\log_{10}\left(\frac{k}{\mathrm{T}}\right) = \frac{-\Delta H^{\ddagger}}{\mathrm{R}}\left(\frac{1}{\mathrm{T}}\right) + \left\{\frac{\Delta S^{\ddagger}}{\mathrm{R}} + 10.32\right\} \qquad (2.32)$$

Where k = rate constant of reaction, T = temperature in Kelvin, $\Delta H^{\ddagger}$ = enthalpy of activation, $\Delta S^{\ddagger}$ = entropy of activation, and R = gas constant which is 1.98 cal mol^{-1}. The units of $\Delta H^{\ddagger}$ and $\Delta S^{\ddagger}$ are cals.

Using Equation (2.32), a plot of $\log_{10}(k/\mathrm{T})$ versus 1/T is associated with:

$$\text{slope} = \frac{-\Delta H^{\ddagger}}{\mathrm{R}} \;;\; \text{and intercept} = \left\{\frac{\Delta S^{\ddagger}}{\mathrm{R}} + 10.32\right\}$$

For this acid-catalyzed substitution reaction, the values of thermodynamic parameters are $\Delta H^{\ddagger}$ = 0.26 ±0.1 kcal mol^{-1} and $\Delta S^{\ddagger}$= –19.1 ±0.2 cal deg^{-1} mol^{-1}. The Eyring plot for this reaction is shown in Figure (2.18) and Table (2.15). These values of $\Delta H^{\ddagger}$ and $\Delta S^{\ddagger}$ are similar to those measured earlier for the same cluster reacting with Br^{-} in the presence of $pyrrH^{+}$ ($\Delta H^{\ddagger}$ = 0.45 ±0.2 kcal mol^{-1} and $\Delta S^{\ddagger}$ = –47.0 ±5.0 cal deg^{-1} mol^{-1})[25], and are consistent with proton transfer where the transition state involves prior association (hydrogen bonding) of the acid with the cluster (*i.e.* a small $\Delta H^{\ddagger}$ and negative $\Delta S^{\ddagger}$)[29, 30]. The larger value of $\Delta H^{\ddagger}$ and more negative $\Delta S^{\ddagger}$ associated with the reactions of $pyrrH^{+}$ is presumably a consequence of the weaker acidity of this acid, resulting in a weaker (longer) hydrogen bond in the transition state. A common feature of the proton transfer reactions of synthetic Fe-S-based clusters is a small ($\Delta H^{\ddagger}$)[25, 26]. Whilst small $\Delta H^{\ddagger}$ are often associated with diffusion-controlled reactions, the rate constants for proton transfer to Fe-S-based clusters indicate that this is not the case for these reactions.

Table (2.14): The kinetics experimental data for the reaction of $[Fe_4S_4Cl_4]^{2-}$ with PhS^- in the presence of $[NHBu^n{}_3{}^+]$ at the range of temperature T = 288-308 K.

T (K)	**[PhSH]** **(mmol dm^{-3})**	**[NHBu$^n{}_3{}^+$]** **(mmol dm^{-3})**	***k*$_{obs.}$** **(s^{-1})**	***k*$_0$** **(s^{-1})**
288	5.0	7.0	7.10	4.744 x10^2
	5.0	9.0	7.50	
	5.0	13.0	8.20	
	5.0	21.0	9.55	
	5.0	29.0	10.70	
293	5.0	7.0	7.19	4.923 x10^2
	5.0	9.0	7.60	
	5.0	13.0	8.44	
	5.0	21.0	9.72	
	5.0	29.0	10.90	
298	5.0	7.0	7.22	5.105 x10^2
	5.0	9.0	7.70	
	5.0	13.0	8.49	
	5.0	21.0	9.89	
	5.0	29.0	11.02	
303	5.0	7.0	7.33	5.266 x10^2
	5.0	9.0	7.81	
	5.0	13.0	8.54	

	5.0	21.0	10.02	
	5.0	29.0	11.15	
308	5.0	7.0	7.61	5.463×10^2
	5.0	9.0	8.10	
	5.0	13.0	8.89	
	5.0	21.0	10.35	
	5.0	29.0	11.52	

Table (2.15): Thermodynamic parameters $\Delta H^{\ddagger}$ and $\Delta S^{\ddagger}$ for the reaction of $[Fe_4S_4Cl_4]^{2-}$ with PhS^- in presence of $[NHBu^n{}_3{}^+]$ at the range of temperature T = 288-308^{0}K. Using Eyring Equation.

T (K)	**1/T (K^{-1})**	**k_0 (s^{-1})**	**Log_{10} (k_0/T)**	**$\Delta H^{\ddagger}_{k0}$ (kcal mol^{-1})**	**$\Delta S^{\ddagger}_{Kk0}$ (cal mol^{-1})**
288	0.00347	4.744×10^2	0.216	0.27	-19.21
293	0.00341	4.923×10^2	0.225		
298	0.00335	5.105×10^2	0.233		
303	0.0033	5.266×10^2	0.240		
308	0.00324	5.463×10^2	0.248		

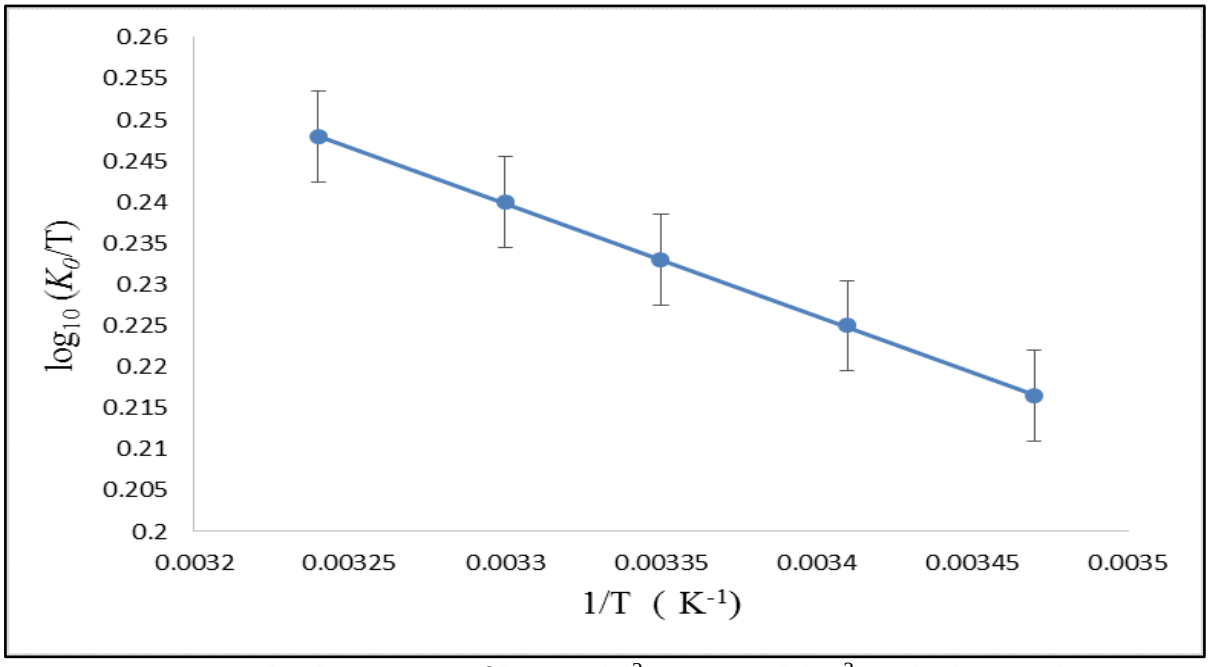

Figure 2.18. Eyring plot the reaction of $[Fe_4S_4Cl_4]^{2-}$ (0.2 mmol dm^{-3}) with PhSH in the presence of $NHBu^n{}_3^+$ in MeCN.

The reaction between $[Fe_4S_4Cl_4]^{2-}$ and PhS^- in the presence of $NHEt_3^+$ exhibits a non-linear dependence on the ratio $[NHEt_3^+]_e/[NEt_3]_e$ and a first order dependence on $[PhSH]_e$ as shown in Table (2.13)[15]. Consequently, measuring the temperature dependence over a range of $[NHEt_3^+]/[NEt_3]$ allows separate determination of the activation parameters for the protonation step (K_0^R) and the substitution step (k_2^R), see Table (2.16).

For the acid-catalyzed substitution reactions of $[Fe_4S_4Cl_4]^{2-}$ with PhS^- in the presence of $NHEt_3^+$, when ($K^R{}_0$) is equilibrium constant for the protonation pathway and (k_2^R) is rate constant for substitution reaction, the thermodynamic parameters ($\Delta H^{\ddagger}$) and ($\Delta S^{\ddagger}$) can be determined as follow:

Where ($k_{obs.}$) is the rate of overall for the acid-catalyzed substitution reactions of $[Fe_4S_4Cl_4]^{2-}$ with PhS^- in the presence of NHR_3^+.

$$k_{obs.} = \frac{K_0^R k_2^R [NHEt_3^+]/[NEt_3][PhSH]}{1 + K_0^R [NHEt_3^+]/[NEt_3]} \qquad (2.33)$$

$$\frac{k_{obs.}}{[PhSH]} = \frac{K_0^R k_2^R [NHEt_3^+]/[NEt_3]}{1 + K_0^R [NHEt_3^+]/[NEt_3]} \qquad (2.34)$$

By inverting Equation (2.34):

$$\frac{[\mathrm{PhSH}]}{k_{obs.}} = \frac{1 + K_0^{\mathrm{R}}[\mathrm{NHEt_3^+}]/[\mathrm{NEt_3}]}{K_0^{\mathrm{R}} k_2^{\mathrm{R}}[\mathrm{NHEt_3^+}]/[\mathrm{NEt_3}]} \qquad (2.35)$$

Rearrangement Equation (2.35):

$$\frac{[\mathrm{PhSH}]}{k_{obs.}} = \frac{1}{K_0^{\mathrm{R}} k_2^{\mathrm{R}}} \cdot \frac{1}{[\mathrm{NHEt_3^+}]/[\mathrm{NEt_3}]} + \frac{K_0^{\mathrm{R}}[\mathrm{NHEt_3^+}]/[\mathrm{NEt_3}]}{K_0^{\mathrm{R}} k_2^{\mathrm{R}}[\mathrm{NHEt_3^+}]/[\mathrm{NEt_3}]}$$

$$\frac{[\mathrm{PhSH}]}{\mathrm{k_{obs.}}} = \frac{1}{\mathrm{K_0^R k_2^R}} \cdot \frac{[\mathrm{NEt_3}]}{[\mathrm{NHEt_3^+}]} + \frac{1}{\mathrm{k_2^R}} \qquad (2.35)$$

From drawing of the Equation (2.35):

$$\text{slope} = \frac{1}{K_0^{\mathrm{R}} k_2^{\mathrm{R}}} \; ; \text{ and intercept} = \frac{1}{k_2^{\mathrm{R}}}$$

The parameters $\Delta H^{\ddagger}_{K0k2}$ and $\Delta H^{\ddagger}_{k2}$ can be determined using Eyring Equation (2.32):

$$\log_{10}\left(\frac{k}{\mathrm{T}}\right) = \frac{-\Delta H^{\ddagger}}{\mathrm{R}}\left(\frac{1}{\mathrm{T}}\right) + \left\{\frac{\Delta S^{\ddagger}}{\mathrm{R}} + 10.32\right\} \qquad (2.32)$$

Where k = rate constant of reaction, T = temperature in Kelvin, $\Delta H^{\ddagger}$ = Enthalpy, $\Delta S^{\ddagger}$ = Entropy, and R = gas constant which is 1.98 cal mol^{-1}.

By drawing of the Equation (2.32):

$$\text{slope} = \frac{-\Delta H^{\ddagger}}{\mathrm{R}} \; ; \text{ and intercept} = \left\{\frac{\Delta S^{\ddagger}}{\mathrm{R}} + 10.32\right\}$$

When $\Delta H^{\ddagger}_{K0k2}$ is the enthalpy of overall of the reaction and $\Delta H^{\ddagger}_{k2}$ is the enthalpy of substitution pathway, so the enthalpy of protonation pathway $\Delta H^{\ddagger}_{K0}$ can be calculated using Equation (2.36).

$$\Delta H^{\ddagger}_{K0} = \Delta H^{\ddagger}_{K0k2} - \Delta H^{\ddagger}_{k2} \qquad (2.36)$$

Also by using Equation (2.37), the entropy of protonation pathway can be found.

$$\Delta S^{\ddagger}_{K0} = \Delta S^{\ddagger}_{K0k2} - \Delta S^{\ddagger}_{k2} \qquad (2.37)$$

For the protonation of $[Fe_4S_4Cl_4]^{2-}$, ΔH^o = 0.3 ±0.05 kcal mol^{-1} and ΔS^o = –25.1 ±5 cal deg^{-1} mol^{-1}, and for the substitution step, $\Delta H^{\ddagger}$ = 0.37 ±0.1 kcal mol^{-1} and $\Delta S^{\ddagger}$ = –16.6 ±2.0 cal deg^{-1} mol^{-1}, as described in Table (2.17), Table (2.18), and Figures (2.19) and (2.20). The most notable feature is the negative $\Delta S^{\pm}$ for the substitution step, which is indicative of an associative mechanism. This conclusion correlates with the kinetics which exhibit a first order dependence on the concentration of PhSH.

Table (2.16): The kinetics experimental data for the reaction of $[Fe_4S_4Cl_4]^{2-}$ with PhS^- at different ratio $[NHEt_3^+]_e/[NEt_3]_e$ and the range of temperature T = 288-308 K .

T (K)	$[NEt_3]/[NHEt_3^+]$	10^3[PhSH] / k_{obs}	$1/k_2^R$	$1/K_0^R k_2^R$	k_2^R	$K_0^R k_2^R$
288	0.14	2.1	0.000188	0.000176	5.32 x 10^3	5.99 x 10^3
	0.20	2.34				
	0.33	2.80				
	0.66	3.20				
	1.00	3.70				
	2.00	5.00				
293	0.14	1.87	0.00018	0.00016	5.6 x 10^3	6.25 x 10^3
	0.20	2.17				
	0.33	2.33				
	0.66	2.90				
	1.00	3.40				
	2.00	4.90				
298	0.14	1.75	0.000176	0.000148	5.68 x 10^3	6.9 x 10^3
	0.20	1.93				
	0.33	2.29				
	0.66	2.96				
	1.00	3.42				
	2.00	4.50				

303	0.14 0.20 0.33 0.66 1.00 2.00	1.50 1.80 2.10 2.70 3.10 4.20	0.00017	0.000138	5.88×10^3	7.25×10^3
308	0.14 0.20 0.33 0.66 1.00 2.00	1.30 1.50 1.80 2.10 2.70 3.73	0.00016	0.000136	6.25×10^3	7.35×10^3

Table (2.17): Thermodynamic parameters $\Delta H^{\ddagger}$ and $\Delta S^{\ddagger}$ for overall reaction (K_0k_2) of $[Fe_4S_4Cl_4]^{2-}$ with PhS^- at different ratio $[NHEt_3^+]_e/[NEt_3]_e$ and the range of temperature T = 288-308 K. Using Eyring Equation.

T (K)	1/T (K^{-1})	$K_0^R k_2^R$	Log_{10} ($K_0^R k_2^R$/T)	$\Delta H^{\ddagger}_{K0k2}$ (kcal mol^{-1})	$\Delta S^{\ddagger}_{K0k2}$ (cal mol^{-1})
288	0.00347	5.99 $x10^3$	1.317	0.349	-40.12
293	0.00341	6.25 $x10^3$	1.335		
298	0.00335	6.9 $x10^3$	1.364		
303	0.0033	7.25 $x10^3$	1.378		
308	0.00324	7.35 $x10^3$	1.397		

Table (2.18): Thermodynamic parameters $\Delta H^{\ddagger}$ and $\Delta S^{\ddagger}$ for substitution pathway (k_2) of $[Fe_4S_4Cl_4]^{2-}$ with PhS^- at different ratio $[NHEt_3^+]_e/[NEt_3]_e$ and the range of temperature T = 288-308 K. Using Eyring Equation.

T (K)	1/T (K^{-1})	k_2^R	Log_{10} (k_2^R/T)	$\Delta H^{\ddagger}_{k2}$ (kcal mol^{-1})	$\Delta S^{\ddagger}_{k2}$ (cal mol^{-1})
288	0.00347	5.32 $x10^3$	1.26	0.319	-16.82
293	0.00341	5.60 $x10^3$	1.27		
298	0.00335	5.68 $x10^3$	1.28		
303	0.0033	5.88 $x10^3$	1.288		
308	0.00324	6.25 $x10^3$	1.307		

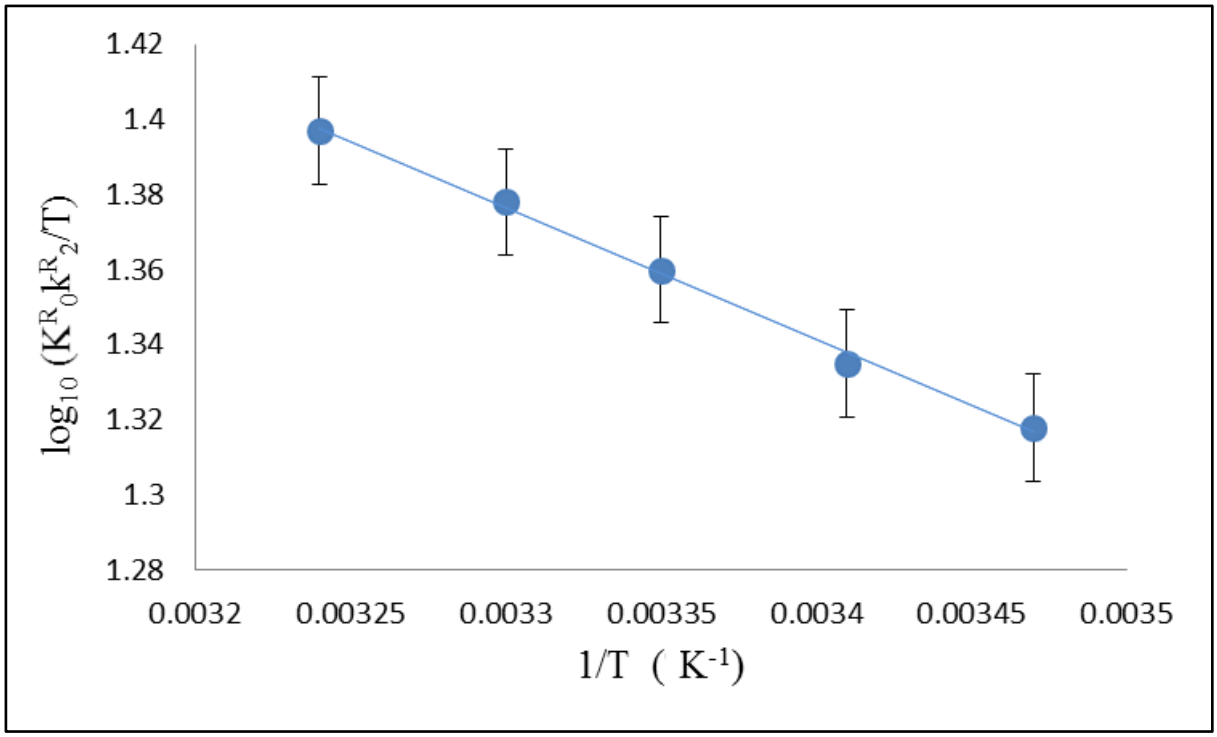

Figure 2.19. Eyring plot for overall reaction of $[Fe_4S_4Cl_4]^{2-}$ (0.2 mmol dm^{-3}) with PhSH in the presence of $NHEt_3^+$ in MeCN.

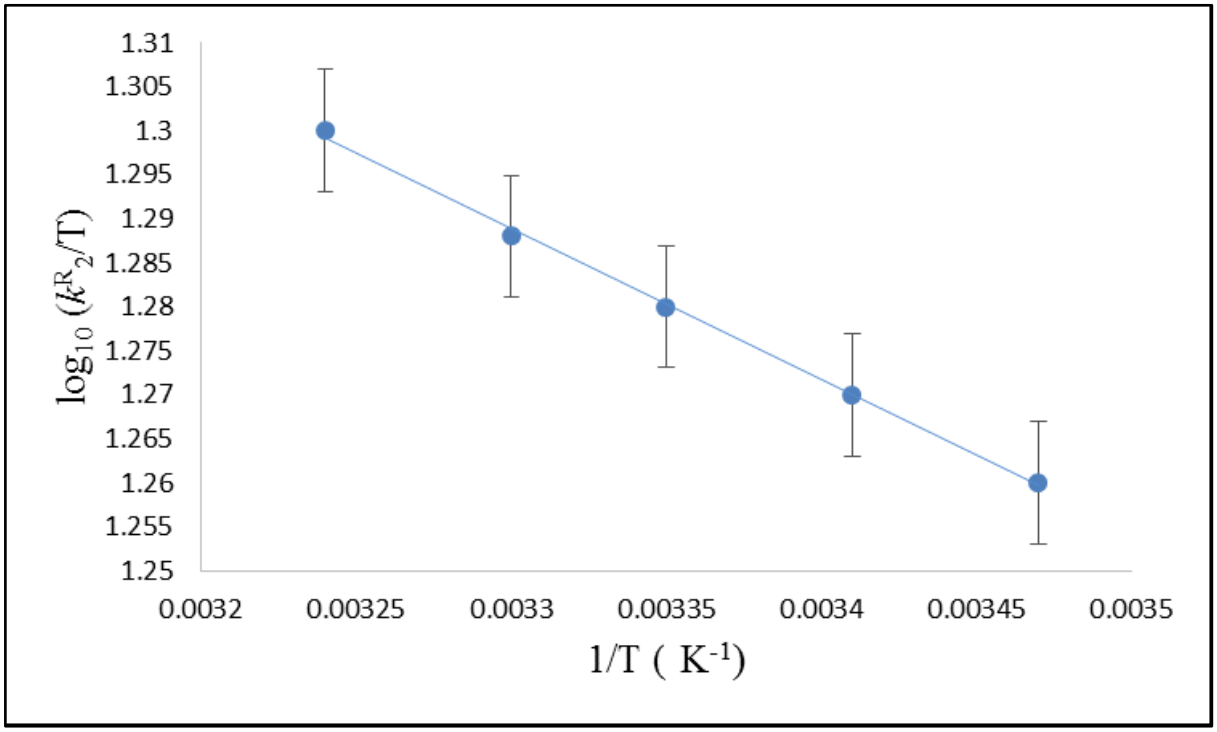

Figure 2.20. Eyring plot for substitution step for the reaction of $[Fe_4S_4Cl_4]^{2-}$ (0.2 mmol dm^{-3}) with PhSH in the presence of $NHEt_3^+$ in MeCN.

A mechanistically more revealing result comes from studies on the temperature dependence of the reaction between $[Fe_4S_4(SEt)_4]^{2-}$ and PhS^- in the presence of $NHEt_3^+$. The slowness of this reaction makes it difficult to study the temperature dependence over a wide range of $[NHEt_3^+]/[NEt_3]$. Consequently, the temperature dependence has been studied only when $[NHEt_3^+]/[NEt_3] = 9.0$. Under these conditions all of the cluster is protonated and the only solution species is $[Fe_4S_3(SH)(SEt)_4]^-$ and the calculated activation parameters ($\Delta H^{\ddagger} = 0.55 \pm 0.15$ kcal mol^{-1} and $\Delta S^{\ddagger} = -22.9 \pm 0.2$ cal deg^{-1} mol^{-1}) correspond to the substitution step. Of particular note is the negative value of $\Delta S^{\pm}$. This is inconsistent with the substitution step occurring by a dissociative mechanism, as suggested by the kinetics (*i.e.* a zero order dependence on the concentration of nucleophile, see Table (2.13))[21]. The negative $\Delta S^{\ddagger}$ is indicative of an associative mechanism. Irrespective of the mechanism (either Figure (1.16) or Figure (1.17)), the negative $\Delta S^{\ddagger}$, but zero order dependence on the concentration of nucleophile, is consistent with an associative substitution mechanism for $[Fe_4S_3(SH)(SEt)_4]^-$, involving the solvent (MeCN) as nucleophile. For either mechanism (Figure 1.16 or 1.17), this would involve displacement of a EtS ligand by MeCN, but for the mechanism in Figure (1.16) the process occurs at a tetrahedral Fe in an intact cubanoid cluster, whilst in the mechanism in Figure (1.17) the displacement occurs at a 3-coordinate Fe after protonation has disrupted the structure of the cluster. Whilst the values of $\Delta H^{\ddagger}$ and $\Delta S^{\ddagger}$ observed in this system cannot distinguish between these two possibilities, establishing that the substitution step in acid-catalyzed substitution reactions of Fe-S-based clusters occur by an associative mechanism (irrespective of whether the rate exhibits a zero order or first order dependence on the concentration of nucleophile) is consistent with the mechanism shown in Figure (1.17).

2.7 Conclusions.

Earlier studies on the mechanism of the acid-catalyzed substitution reactions of cubanoid $[Fe_4S_4X_4]^{2-}$ (X= thiolate, phenolate or halide) had identified some unusual characteristics for these reactions associated with their protonation. As pointed out recently, these characteristics are not easily explained by simple protonation of the cluster {Figure (1.16)}[7]. Recently, DFT calculations have indicated that upon protonation of a μ_3-S there is elongation/cleavage of the Fe-(μ_3-SH) bond {Figure (1.17)}, and this new mechanism rationalises all the unusual observations about protonation of Fe-S-based clusters[7-9]. In this Chapter, further studies on the acid-catalyzed substitution reactions of $[Fe_4S_4Cl_4]^{2-}$ are reported. These studies were designed to explore the two stages of the reaction: protonation of the cluster and substitution of a terminal ligand, and the aim was to distinguish between the mechanisms in Figures (1.16) and (1.17), and in particular to support or refute the recent proposal that protonation of Fe-S-based clusters leads to (transient) structural disruption of the cluster core. Although the results do not unambiguously establish that protonation disrupts the cluster core, they do identify further peculiarities in the protonation reactions of Fe-S cluster core, which are on balance, more consistent with the mechanism shown in Figure (1.17) than protonation of the cluster unaffecting the structural integrity of the cluster.

To explore the protonation step, the kinetics of the acid-catalyzed substitution reactions of $[Fe_4S_4Cl_4]^{2-}$ with PhS^- in the presence of a series of similar acids, NHR_3^+ (R = Me, Et, Pr^n or Bu^n) with very similar pK_as have been studied. The crucial result from these studies is that the rate of the reactions cannot be predicted on the basis of the acidities of these acids, but rather both the acid strength and the bulk of the R group are important in defining the rate. This observation is inconsistent with the mechanism in Figure (1.16), but is consistent with the mechanism involving cluster disruption Figure (1.17).

Further studies Table (2.13) explored the intimate mechanism of the substitution step. The activation parameters ($\Delta H^{\ddagger}$ and $\Delta S^{\ddagger}$) for the reactions of $[Fe_4S_3(SH)(SEt)_4]^-$ with PhSH (rate of reaction independent of [PhSH]) and $[Fe_4S_3(SH)Cl_4]^-$ (rate exhibits first order dependence on [PhSH]) have been measured. In both reactions, $\Delta S^{\ddagger}$ is negative which strongly indicates that the mechanism of substitution is associative. For the reaction of $[Fe_4S_3(SH)(SEt)_4]^-$, the negative $\Delta S^{\ddagger}$ but independence of the rate on the

concentration of nucleophile can be rationalised by an associative, rate-limiting displacement of thiolate by MeCN (solvent), as proposed for the revised mechanism in Figure (1.17).

2.8 References.

1. R. H. Holm, P. Kennepohl and E. I. Solomon, *Chem. Rev.*, 1996, **96**, 2239-2314.
2. H. Beinert, M. C. Kennedy and C. D. Stout, *Chem. Rev.*, 1996, **96**, 2335-2373.
3. B. K. Burgess and D. J. Lowe, *Chem. Rev.*, 1996, **96**, 2983-3011.
4. J. B. Howard and D. C. Rees, *Chem. Rev.*, 1996, **96**, 2965-2982.
5. T. Spatzal, M. Aksoyoglu, L. M. Zhang, S. L. A. Andrade, E. Schleicher, S. Weber, D. C. Rees and O. Einsle, *Science*, 2011, **334**, 940-940.
6. D. Lukoyanov, Z. Y. Yang, N. Khadka, D. R. Dean, L. C. Seefeldt and B. M. Hoffman, *J. Am. Chem. Soc.*, 2015, **137**, 3610-3615.
7. A. Alwaaly, I. Dance and R. A. Henderson, *J. Chem. Soc., Chem. Commun.*, 2014, **50**, 4799-4802.
8. I. Dance and R. A. Henderson, *J. Chem. Soc., Dalton Trans.*, 2014, **43**, 16213-16226.
9. I. Dance, *J. Chem. Soc., Dalton Trans.*, 2015, **44**, 4707-4717.
10. K. Izutsu, *Acid-Base Dissociation Constants in Dipolar Aprotic Solvents*, Blackwell Scientific, Oxford, UK, 1990.
11. G. R. Dukes and R. H. Holm, *J. Am. Chem. Soc.*, 1975, **97**, 528-533.
12. R. A. Henderson, *Chem. Rev.*, 2005, **105**, 2365-2437.
13. R. A. Henderson, *Coord. Chem. Rev.*, 2005, **249**, 1841-1856.
14. R. A. Henderson, *BioInorg. React. Mech.* , 2012, **8**, 1-37.
15. R. A. Henderson and K. E. Oglieve, *J. Chem. Soc., Chem. Commun.*, 1994, 377-379.
16. G. Christou and C. D. Garner, *J. Chem. Soc., Dalton Trans.*, 1979, 1093.
17. R. H. Holm, W. D. Phillips, B. A. Averill, J. J. Mayerle and T. Herskovi, *J. Am. Chem. Soc.*, 1974, **96**, 2109-2117.
18. G. B. Wong, M. A. Bobrik and R. H. Holm, *Inorg Chem*, 1978, **17**, 578-584.
19. R. E. Palermo, P. P. Power and a. R. H. Holm, *Inorganic Chemistry*, 1982, **21**, 173-181.
20. J. R. Dilworth and a. R. A. Henderson, *J. Chem. Soc., DaltonTrans*, 1987, 529-540.
21. R. A. Henderson and K. E. Oglieve, *J. Chem. Soc., Dalton Trans.*, 1993, 1467-1472.
22. R. A. Henderson and K. E. Oglieve, *J. Chem. Soc., Dalton Trans.*, 1993, 1473-1476.
23. R. P. Bell, *The Proton in Chemistry*, Chapman Hall, London, 2nd edn., 1973.

24. R. A. Henderson and K. E. Oglieve, *J. Chem. Soc., Dalton Trans.*, 1999, 3927-3934.

25. J. Bell, A. J. Dunford, E. Hollis and R. A. Henderson, *Angew. Chemie Int. Ed.*, 2003, **42**, 1149-1152.

26. K. Bates, B. Garrett and R. A. Henderson, *Inorg. Chem.*, 2007, **46**, 11145-11155.

27. K. Bates and R. A. Henderson, *Inorg. Chem.*, 2008, **47**, 5850-5858.

28. B. Garrett and R. A. Henderson, *J. Chem. Soc., Dalton Trans.*, 2010, **39**, 4586-4592.

29. W. J. Albery, *Annu. Rev. Phys. Chem.*, 1980, **31**, 227-263.

30. W. J. Albery, *Faraday Discuss*, 1982, **74**, 245-256.

Chapter 3: Binding Small Molecules and Ions to $[Fe_4S_4Cl_4]^{2-}$ Modulates Rate of Protonation of the Cluster

3.1 Introduction.

Small molecules and ions (*e.g.* protons, alkynes, hydrazines, CN^-, N_3^- *etc.*) can bind to the Fe-S-based clusters in certain metalloenzymes (*e.g.* nitrogenases, CODH and aconitase) and to some synthetic Fe-S-based clusters[1-15]. However, there is little experimental information about how these substrates interact with either the natural or synthetic clusters or how they modulate the clusters' reactivity[16, 17]. A major obstacle in studying substrate binding to Fe-S-based clusters is the difficulty in detecting the bound substrates using spectroscopy. There are several reasons for this, which have been discussed previously: the transient nature of the binding; the paramagnetism of the clusters (with multiple spin states) and the dominant intensity of the $\{Fe_4S_4\}$ chromophore in the UV-visible spectrum[18]. These problems are compounded in natural systems where various states of the enzyme occur during turnover. A kinetic method for detecting the binding of various small molecules and ions (henceforth called substrates = L) to synthetic Fe-S-based clusters has been developed, which avoids the problems of direct spectroscopic detection of the bound substrate. The method monitors binding of the substrate to Fe-S-based clusters indirectly: by the effect that it has on the rate of acid-catalyzed substitution of the cluster[16-19].

The kinetics of the acid-catalyzed substitution reactions of terminal ligands have been studied for a variety of Fe-S-based clusters since the 1990s[16-19]. The mechanism involves initial protonation of a μ_3-S on the cluster which labilises terminal ligands to substitution. If a substrate binds to the cluster prior to either the protonation or substitution it will modulate the rate of the acid-catalyzed substitution. Using this approach, earlier studies detected binding of substrates to $[Fe_4S_4(SEt)_4]^{2-}$, $[\{MoFe_3S_4(SEt)_3\}_2(\mu\text{-}SEt)_3]^{3-}$ and $[Fe_6S_9(SEt)_2]^{4-}$ [20]. Analysis of the kinetic data gives information about: (i) how many molecules of substrate bind to a single cluster; (ii) how tightly the substrates bind (equilibrium binding constant) and (iii) how the bound substrate modulates the rate of acid-catalyzed substitution.

Recent, DFT calculations on cubanoid $[Fe_4S_4X_4]^{2-}$ (X = thiolate, phenolate or halide) indicate that protonation of a μ_3-S is coupled to elongation/cleavage of an associated Fe-(μ_3-SH) bond Figure (3.1)[21-24]. This suggestion consolidates the proposition that protonation and substrate binding in Fe-S-based clusters are intimately coupled since the 3-coordinate Fe site, generated

upon protonation of μ_3-S, would appear to be a propitious site for the binding of a substrate. In this chapter, studies on $[Fe_4S_4Cl_4]^{2-}$ will be reported, investigating the effects that various bound substrates have on the rate of subsequent protonation of the cluster. These results, together with earlier studies, define the mutual effects that proton and substrate have on the binding of one another at an Fe-S cluster.

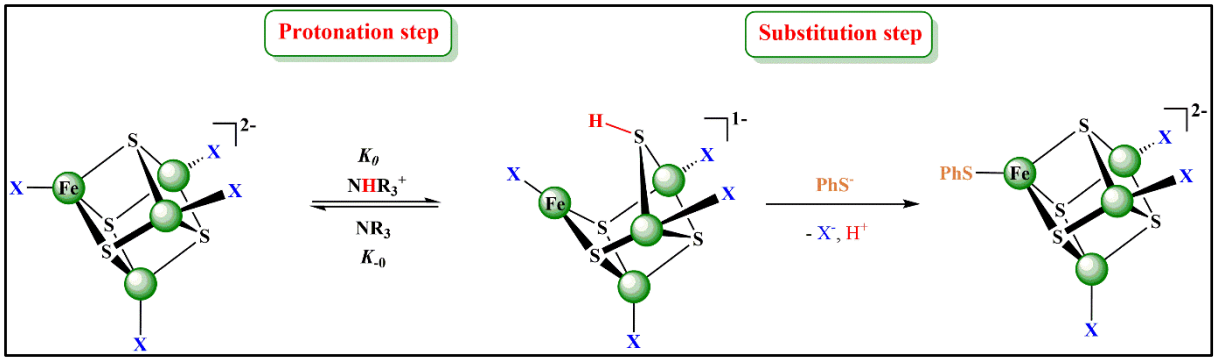

Figure 3.1. Proposed mechanism for the acid-catalyzed substitution of $[Fe_4S_4Cl_4]^{2-}$.

3.1.1 Evidence for substrate binding to synthetic clusters.

Either stoichiometrically or catalytically, the reduction of protons, acetylene, dinitrogen or hydrazine can be accomplished using various synthetic Fe-S-based clusters. Both hydrazine and dinitrogen are converted to ammonia when certain Fe-S-based clusters are electrochemically reduced in protic solvents, at a Hg electrode[25]. Hydrazine can also be reduced to ammonia in mixtures which include either the cuboidal $[Fe_4S_4(SR)_4]^{2-}$ or dicubane $[\{MoFe_3S_4(SR)_3\}_2(\mu\text{-}SPh)_3]^{3-}$ (R = Ph or CH_2CH_2OH) in water or MeOH/THF [6].

The reduction of protons to dihydrogen, or acetylene to ethylene was first performed using $[Fe_4S_4(SPh)_4]^{3-}$ [7]. Subsequently, other researchers studied the kinetics of the transformation of acetylene to ethylene and reduction of protons by $[Fe_4S_4(SPh)_4]^{3-}$ in the presence of $lutH^+$ (lut = 2,6-dimethylpyridine)[26]. This study established that before $[Fe_4S_4(SPh)_4]^{3-}$ could evolve dihydrogen or transform acetylene to ethylene, the cluster needed to be triprotonated. At high concentration of $[lutH^+]$, the cluster $[Fe_4S_2(SH)_2(SPh)_3)(SHPh)]$ was rapidly formed by binding of three protons with $[Fe_4S_4(SPh)_4]^{3-}$ and just in this protonation state the cluster will be able to transform the substrate. The kinetic studies for the reactions showed that the cluster $[Fe_4S_2(SH)_2(SPh)_3]$ was generated by subsequent dissociation of the (PhSH) from cluster $[Fe_4S_2(SH)_2(SPh)_3(SHPh)]$ and this step is essential to produce the hydrogen and ethylene molecules. This study proposed that diprotonation occurs at the cluster core and a further protonation occurs at the thiolate to form $[Fe_4S_2(SH)_2(SHPh)(SPh)_3]^+$. However, this has yet to be proven.

By useing $lutH^+$ as acid and $[Co(\eta^5\text{-}C_5H_5)_2]$ as reductant, the *in situ* reduction of $[MoFe_3S_4Cl_3(polycarboxylate)(NCMe)]^{2-}$ or $[VFe_3S_4Cl_3(dmf)_3]^{-1}$ (dmf= dimethylformamide) produces clusters capable of transforming hydrazine to ammonia or acetylene to ethylene[9, 10]. However, kinetic studies on these transformations were prevented because ammonium salts precipitated during the reaction. The authors of this study proposed that substrates preferred to bind to the heterometal (Mo or V) site but could also bind at the Fe sites. It was suggested that the transformation at the heterometal is faster than at Fe sites. Thus, the non-labile ($HBpz_3$) ligand {hydrotris(pyrazolyl)borate} occupies all potential substrate binding sites on the vanadium atom of $[VFe_3S_4Cl_3(HBpz_3)]^{2-}$ so hydrazine or acetylene is forced to bind to Fe. The transformation of acetylene or hydrazine by this cluster still occurs but is quite slow. An issue with the interpretation of the results of these experiments is that changes to the coordination sphere of one metal could affect the reactivity of all the other metals, as shown in Figure (3.2). In addition, there is the possibility that intramolecular transfer of the substrate can occur between metals. However, such intramolecular transfer of substrates between metal sites within a cluster has yet to be observed.

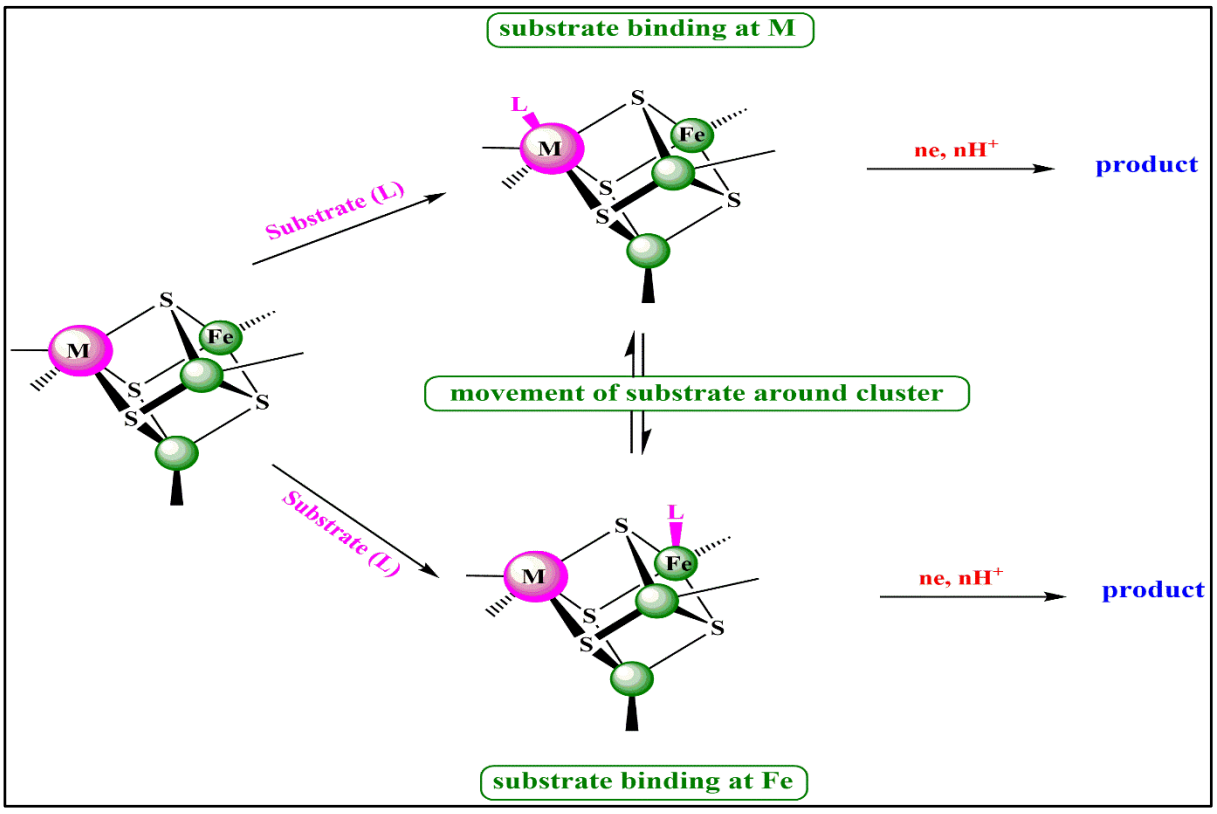

Figure 3.2. Substrate binding to different sites on $\{MFe_3S_4\}$ cluster.

There are several examples of small molecules bound to synthetic Fe-S-based clusters identified by X-ray crystallography {Figure (3.3)}. Thus, X-ray crystallography of $[VFe_3S_4Cl_3(bipy)(PhNHNH_2)]^{1-}$ (bipy = 2,2' bypyridine) has demonstrated that the hydrazine

is bound to V atom in an end-on fashion[9]. Moreover, in $[MoFe_3S_4Cl_3(tccat)(NH_2Me)]^{2-}$ the $MeNH_2$ is bound to Mo (tccat = tetrachlorocatecholate), and free $MeNH_2$ has been produced in the reaction of $[MoFe_3S_4Cl_3(tccat)(NCMe)]^{2-}$ with (*cis*-MeN=NMe)[11, 12]. Furthermore, both CN^- and N_3^- can also bind to this Mo site. In addition [13], $[NiFe_3S_4(SEt)_3(PPh_3)]^{2-}$ contains a Ni-PPh_3 bond, and other tertiary phosphines, CN^- or Bu^tNC can easily replace this PPh_3 ligand.

The four equivalent Fe sites in $[Fe_4S_4X_4]^{2-}$ clusters usually results in all sites reacting with the substrate, thus complicating any investigation of binding of substrates at this type of cluster. As a result, the $[Fe_4S_4(ArS_3)L]^{2-}$ cluster, which is shown in Figure (3.3) has been synthesised. This cluster has a specific property that three Fe sites in the cluster are bound by the tridentate thiolate ligand (ArS_3^{3-}) [14, 15]. Thus a site-differentiated cluster has been produced that allows only one Fe site to bind the substrate to form $[Fe_4S_4(ArS_3)L]^{2-}$ (L = monodentate ligand = N_3^-, CN^-, phenolate, methoxide, or thiolate and L = bidentate ligand = dithiocarbamate, acetate, benzene-1,2-dithiolates, or pyridine-2-thiolate). The substrate binding affinity of $[Fe_4S_4(ArS_3)L]^{2-}$ has been investigated by observing the substitution reactions for the single chloro-ligand of $[Fe_4S_4(ArS_3)Cl]^{2-}$ with different substrates to produce new clusters[14, 15].

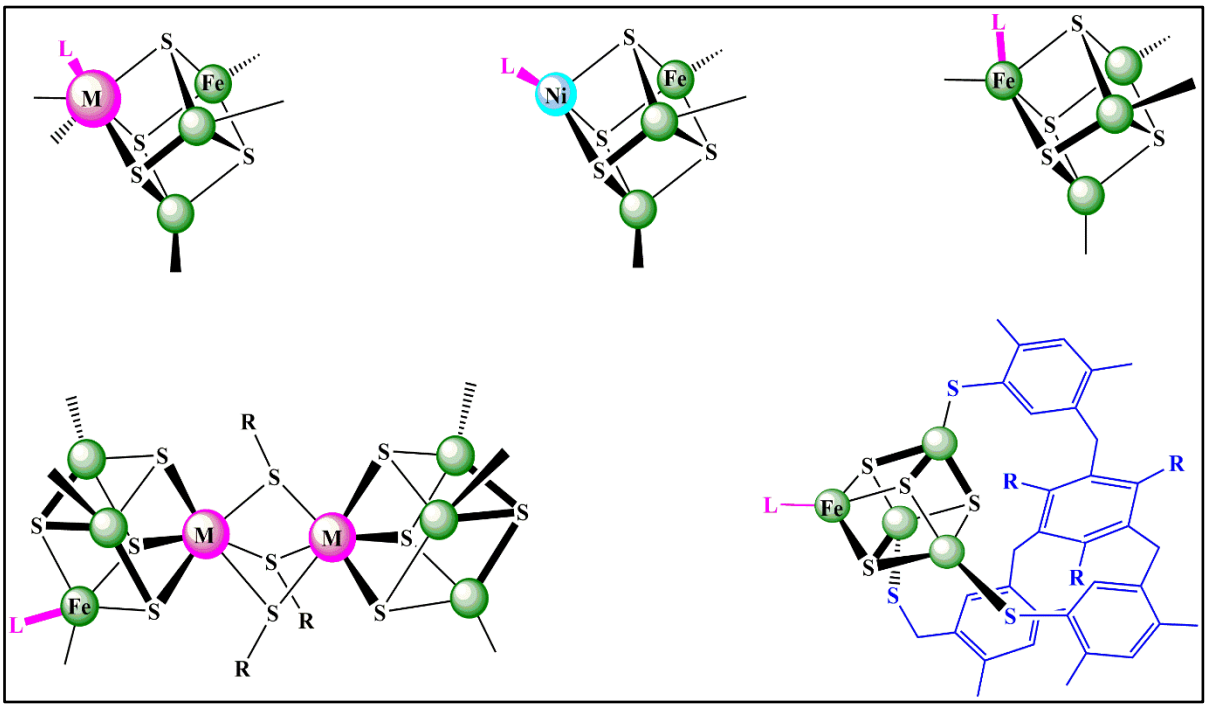

Figure 3.3. Synthetic Fe-S-based clusters which bind with substrates on different sites.

3.1.2 Transitory Binding of Substrates to Clusters.

This section will discuss reactions that involve binding of substrates to intact Fe-S-based clusters. For the substitution reaction of $[Fe_4S_4(SEt)_4]^{2-}$ with PhS^-, the addition of high

concentrations of substrate (L) to clusters produces the transient $[Fe_4S_4(SEt)_4(L)]^{2-}$ which can be detected by a kinetic method, as shown in Figure (3.4). The negligible or small change in the electronic spectrum of Fe-S-based clusters upon binding of the substrate (L) makes detecting $[Fe_4S_4(SEt)_4(L)]^{2-}$ difficult. Consequently, it is necessary to detect such species by an indirect kinetic method[27]. In general, the binding of a substrate to a cluster is monitored by measuring the change in the rate of substitution of the terminal ligand of the cluster.

In the reaction in Figure (3.4), the rate of substitution of $[Fe_4S_4(SEt)_4]^{2-}$ by PhS^- is constant provided the concentration of thiolate ligand is unchanged. However, if a substrate binds, the electron density within the cluster will be perturbed and this will change the rate of substitution. By measuring the rates of substitution of the cluster at various concentrations of the substrate the following can be determined: (i) the effect that the bound substrate has on the lability of the cluster; (ii) the number of substrate molecules which bind to the cluster, and (iii) the equilibrium constant for binding of the substrate to the cluster.

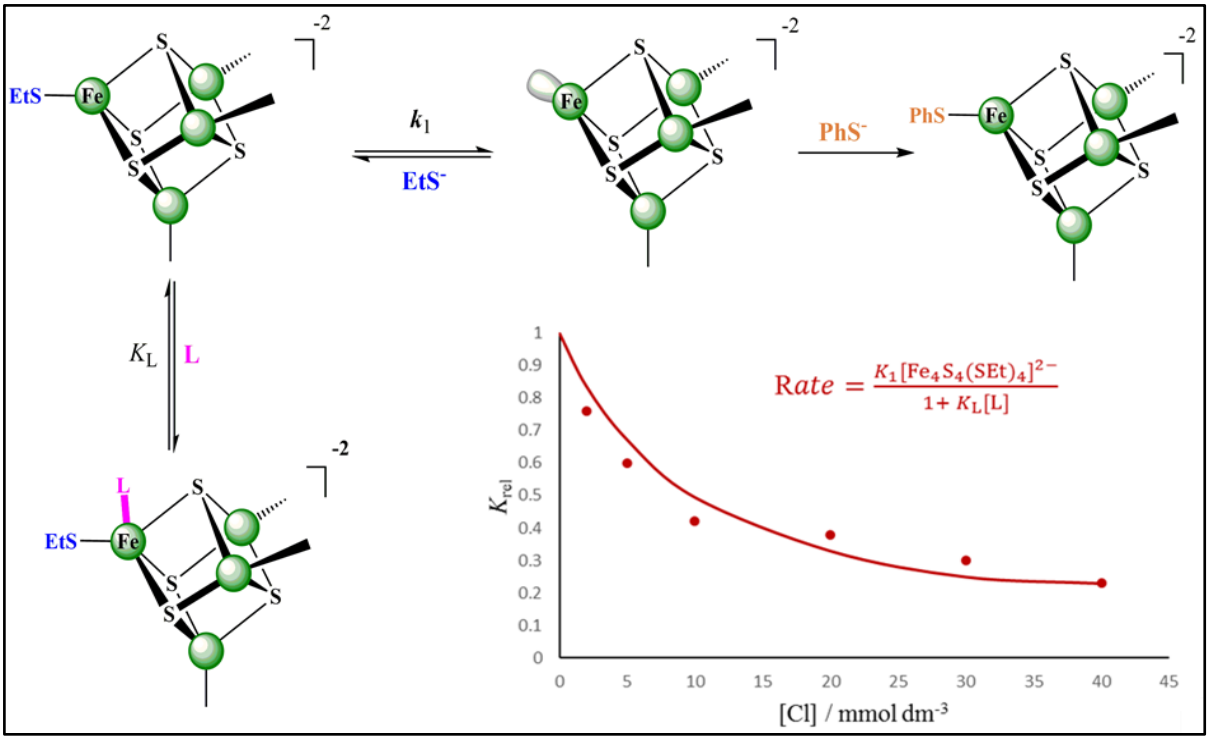

Figure 3.4. Binding of substrate L involves to substitution reaction of $[Fe_4S_4(SEt)_4]^{2-}$ by PhS^-. Graph shows the effect of binding substrate (Cl^-) on the rate of substitution of $[Fe_4S_4(SEt)_4]^{2-}$.

In $[Fe_4S_4(SEt)_4(L)]^{2-}$ a five-coordinate Fe is produced when the substrate binds. This is not unusual. There are numerous examples of Fe-S-based clusters that contain Fe sites which have a coordination number higher than four-coordinate Fe known such as $[Fe_4S_4L(CN)_4]^{3-}$, $[Fe_4S_4L_2(Bu^tNC)_6]$ (L = *p*-$MeC_6H_4O^-$ or PhS^-) and $[Fe_4S_4(CO)_{12}]$.[14, 15, 28-30].

From the kinetic data shown in Figure (3.4), two features are evident: (i) the extent of the inhibition depends on the concentration and nature of the substrate and (ii) the inhibition is particular for $[Fe_4S_4(SEt)_4]^{2-}$cluster. There is no effect on the rate of substitution of the $[Fe_4S_4(SPh)_4]^{2-}$ cluster by utilising the same range of concentration for the same substrates (substrate = L= PhS^-, Cl^-, Br^-, CO, CN^-, $N_3^-$and N_2O), indicating the substrates do not bind to $[Fe_4S_4(SPh)_4]^{2-}$ [27].

With $[Fe_4S_4(SEt)_4]^{2-}$, it can be shown that there is no effect on the rate of substitution of the terminal ligands by adding H_2, N_2, C_2H_2, C_2H_4, or PhCCH which indicates that these molecules do not bind to $[Fe_4S_4(SEt)_4]^{2-}$. However, the affinities for substrates binding will change with the redox state of the cluster. For instance, alkynes transform into alkenes in the presence of $[Fe_4S_4(SEt)_4]^{3-}$ [27], indicating that alkynes must bind to the reduced cluster but not the oxidized form.

The studies on $[Fe_4S_4(SEt)_4]^{2-}$ show that the binding of L (L = N_3^-, CN^-, Cl^-, Br^-, CO, or N_2O) to the cluster result in a decrease in the rate of substitution of the terminal ligands. Because of the limited concentration range of substrate used ([L] < 40 mmol dm^{-3}) it is difficult to establish whether substitution of the cluster is completely switched off when substrate binds, or whether $[Fe_4S_4(SEt)_4(L)]^{2-}$ still undergoes slow substitution.

A more complicated kinetic behaviour has been detected by studying binding of substrates to $[Fe_6S_9(SEt)_2]^{4-}$. These studies lead to further insight into this kind of reaction. Kinetic studies on $[Fe_6S_9(SEt)_2]^{4-}$ [31] show that the substitution and protonation characteristics of this cluster are similar to other synthetic Fe-S-based cluster. These observations show that the rate of reaction between the PhS^- and $[Fe_6S_9(SEt)_2]^{4-}$ in the presence of $NHEt_3^+$ is affected by adding L (L= CN^- , Cl^-, Bu^tNC, or imidazole). Three types of kinetic behaviour are observed upon the addition of different substrates: (i) addition of CN^- or Cl^- inhibit the substitution, (ii) addition of Bu^tCN has a slightly inhibitory effect, and (iii) the binding of imidazole causes an increase in the substitution rate. In the reactions with CN^-, Cl^- and Bu^tNC, the substitution reactions are not completely switched off. Consequently, at a high concentration of the substrate the rate of the substitution reaction is slow (not zero), showing that clusters with bound substrates still undergo substitution.

As shown in the mechanism in Figure (3.5), the coordinated EtS^- is replaced by PhS^- after protonation of cluster, but there is a competition between this substitution and the binding of L to cluster. As a result, there are two pathways for the substitution: the k_1 pathway involves the

substitution of EtS^- by PhS^- of the protonated cluster and the k_1^L pathway, where the $[Fe_6S_9(SEt)_2]^{4-}$ is both protonated and has a substrate L bound. Although the order of the binding affinities (K_L) is imidazole < Bu^tNC < Cl^- < CN^-, all the substrates have very similar binding affinities, with the strongest being only five times larger than the weakest. Thus, the binding of the various substrates has no significant discriminatory preference for $[Fe_6S_9(SEt)_2]^{4-}$.

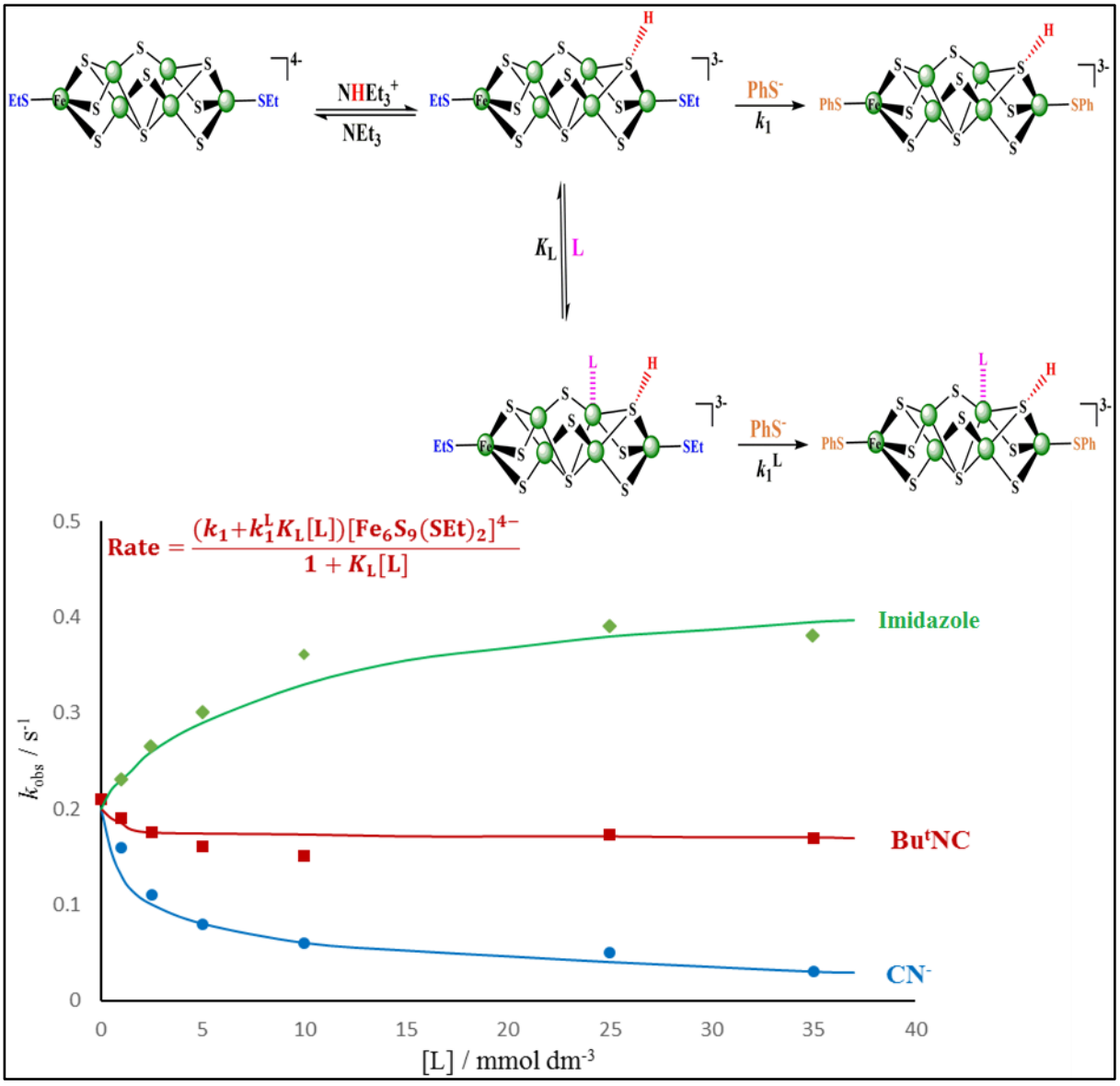

Figure 3.5. Effect of binding various substrates (CN^-, Bu^tNC and imidazole) to the $[Fe_6S_9(SEt)_2]^{4-}$ cluster on the rate of substitution.

Finally, the coordination geometries for the substrates binding to Fe-S-based clusters will be considered in this section. The normal coordination of substrates to multi-metal site containing clusters is shown by the structural characterisation of the synthetic Fe-S-based clusters which contain bound substrates. The substrates such as N_3^-, CN^-, MeCN, and Bu^tNC are coordinated to the clusters by the commom end-on mode. However, the kinetics and mechanism of the

reaction of $[Fe_4S_4(SR)_4]^{2-}$ (R= Et or Bu^t) with 4-YC_6H_4COCl (Y= H, Cl, or MeO) to produce $[Fe_4S_4Cl_4]^{2-}$ has been studied. This mechanism proposed that multiple interactions can be involved in binding of acid chloride to the cluster[32, 33], as shown in Figure (3.6).

Of particular interest is that electron-withdrawing 4-Y-substituents on the acid chloride favour binding with the cluster. It has been suggested that one Fe site of cluster binds to the acid chloride through the chloro or oxygen atom, while the sulfur of the coordinated thiolate interacts with the carbon of carbonyl group Figure (3.6). Such multi-interaction binding could be a characteristic of the binding of multifunctional substrates to Fe-S-based clusters.

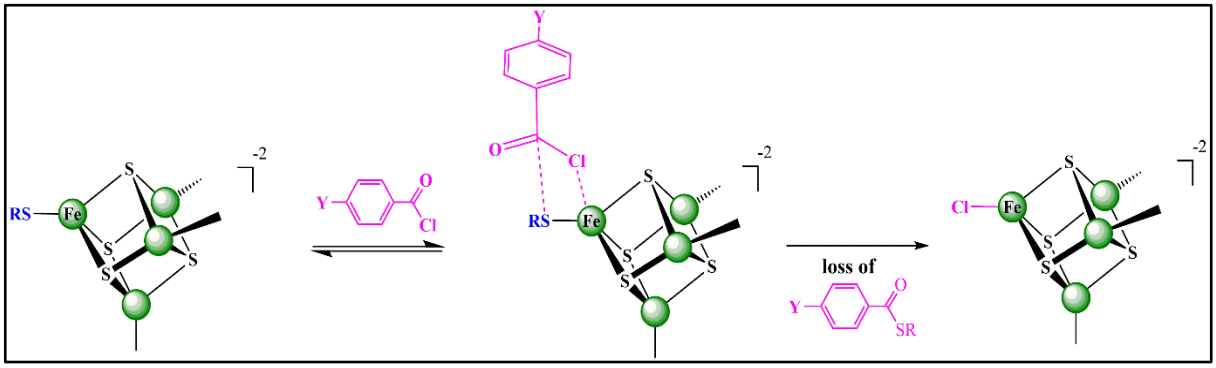

Figure 3.6. Mechanism of the reaction of $[Fe_4S_4(SR)_4]^{2-}$ with acid chlorides to produce $[Fe_4S_4Cl_4]^{2-}$, showing proposed structure of intermediate where acid chloride binds to the cluster.

3.1.3 Competition between the Binding of Protons and Substrates to Fe-S-Based Clusters.

The rates and mechanisms of proton transfer to various synthetic Fe-S-based clusters have been reviewed, and, in particular, how the proton affinities are affected by changes to the cluster. However, we need to understand how substrates bind to nitrogenases in the presence of protons. Many factors must be considered which include the following. (i) The effect that protonation has on the binding of substrates to Fe-S-based clusters. (ii) Which binds preferentially to the cluster, proton or substrate? (iii) The effect that a bound substrate has on the protonation of the cluster.

In one study, substitution in the presence of acid has been shown to occur by two pathways which differ in the order that protons and nucleophile bind to the cluster. The reaction between $[Fe_2S_2Cl_4]^{2-}$ and PhS^- has been studied[34] in the presence of $pyrrH^+$. The reaction involves both protonation and the binding of PhS^- to the cluster. The reaction can occur by two pathways. In the first pathway, PhS^-binds before protonation and in the second pathway protonation occurs before binding of PhS^-. Which pathway operates depends on the relative concentrations of thiolate and acid. Hence, when $[PhS^-] > [pyrrH^+]$, the thiolate will bind before the protonation

and this substitution step depends on concentration of [PhS^-], however, when [PhS^-] < [$pyrrH^+$], the rate of protonation is faster than the rate of substitution by PhS^- and this step depends on concentration of [$pyrrH^+$], see Figure (3.7).

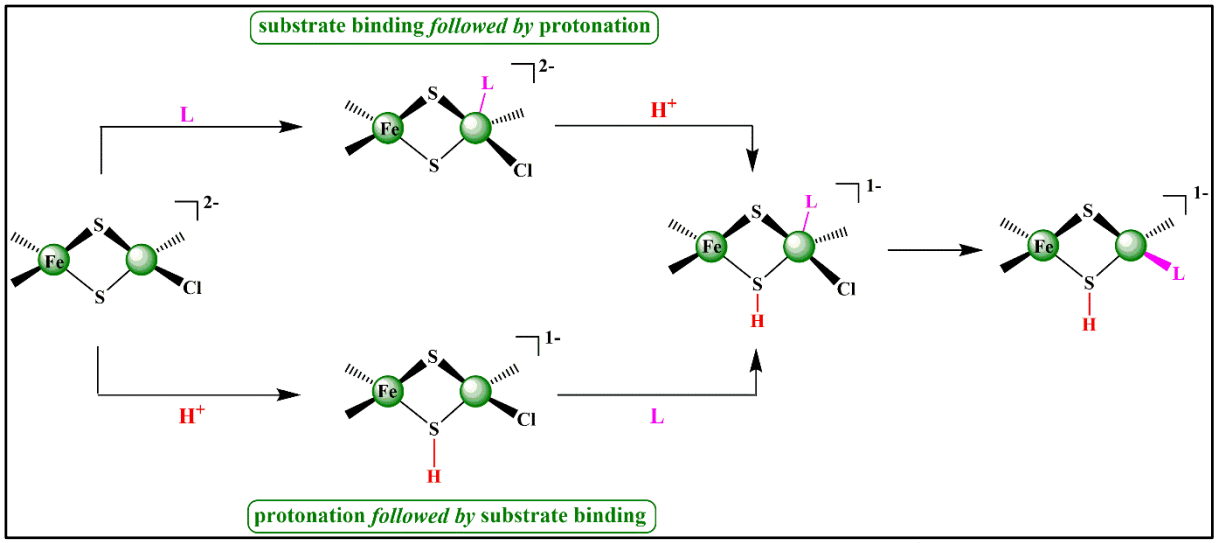

Figure 3.7. Outline of the two pathways for substitution of $[Fe_2S_2Cl_4]^{2-}$ by (L) in presence of acid showing pathways involving initial substrate (L) binding followed by protonation (top line) and initial protonation followed by substrate (L) binding (bottom line).

Studies with $[Fe_4S_4Cl_4]^{2-}$ have shown that the rate of proton transfer from $pyrrH^+$ to this cluster is affected by binding of various substrates to the cluster [35]. Binding of PhS^- or Bu^tNC results in an increase in the rate of proton transfer, whilst binding of halide or EtS^-, inhibits proton transfer to the cluster (k_4^{Br}/k_1 = 0.82, k_4^{I}/k_1 = 0.029, and k_4^{EtS}/k_1 = 0.31), see Figure (3.8). It has been suggested that the observed behaviour is a consequence of significant structural reorganisation to the cluster when being protonated.

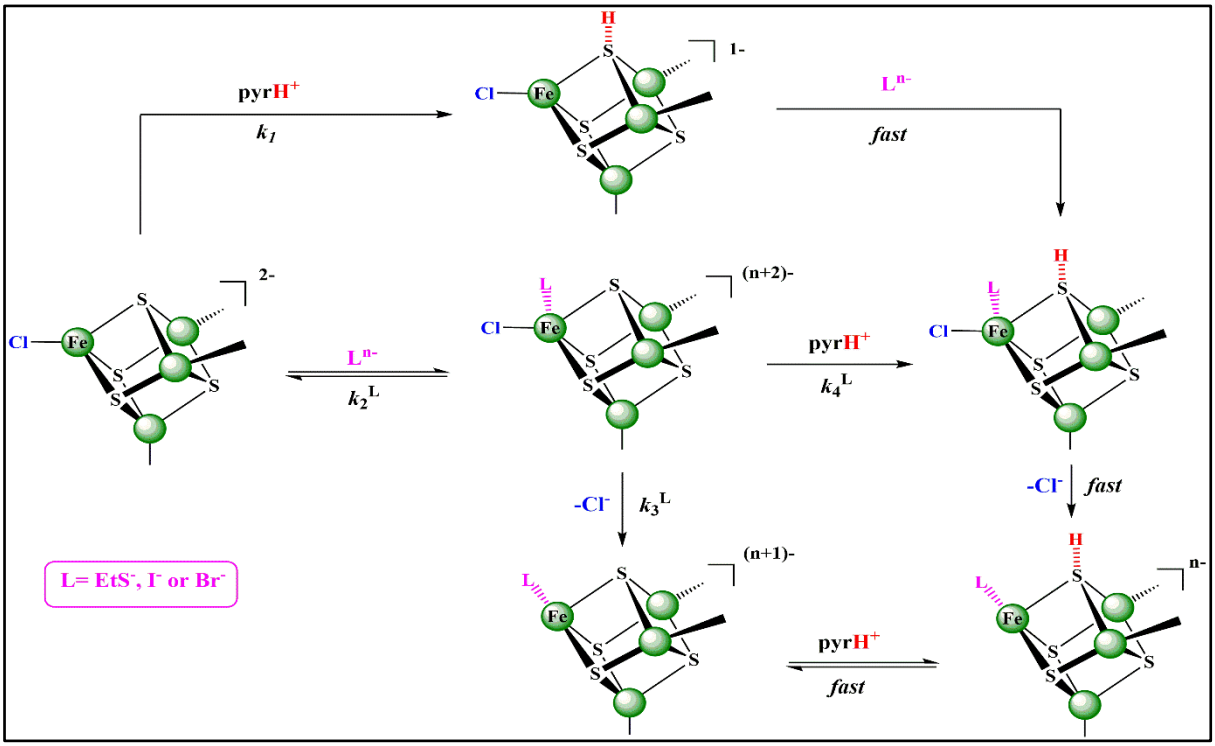

Figure 3.8. Effected of binding of various substrates (EtS^-, I^- or Br^-) on the protonation of $[Fe_4S_4Cl_4]^{2-}$ cluster in presence of $pyrrH^+$.

This Chapter will report studies on $[Fe_4S_4Cl_4]^{2-}$, investigating the effects that various bound substrates (L = substrate = Cl^-, Br^-, I^-, $RNHNH_2$(R = Me or Ph), Me_2NNH_2, HCN, NCS^-, N_3^-, Bu^tNC or pyr = pyridine) have on the rate of subsequent protonation of the cluster. These results, together with earlier studies, define the mutual effects that proton and substrate have on the binding of one another at an Fe–S cluster.

3.2 Experimental and Methodology.

3.2.1 General Experimental.

All experiments in both the synthesis of compounds and the kinetics studies were performed under an atmosphere of dinitrogen using Schlenk or syringe techniques, as appropriate because all compounds are sensitive to air. Drying of solvents and (^{1}H NMR) spectroscopy were performed as described in Experimental of Chapter 2 (***section 2.2.3***).

3.2.1.1 Fourier Transform Infrared Spectroscopy (FTIR Spectroscopy).

FTIR spectra were recorded on a Varian 800 FT-IR spectrophotometer and the results were analysed by VARIAN RESOLUTIONS Software.

3.3 Preparation of Compounds.

The following chemicals were purchased from Sigma-Aldrich and used as received: thiophenol (PhSH), tetrabutylammonium bromide (NBu^n_4Br), anhydrous iron(III) chloride ($FeCl_3$), benzoyl chloride (PhCOCl), sulfur, tetraethylammonium chloride (NEt_4Cl), tributylamine (Bu^n_3N), chlorotrimethylsilane (Me_3SiCl), sodium tetraphenylborate ($NaBPh_4$), tetraethylammonium azide $[NEt_4]N_3$, tetramethylammonium bromide (NMe_4Br), potassium thiocyanate (KCNS), phenylhydrazine ($PhNHNH_2$), methylhydrazine ($MeNHNH_2$), dimethylhydrazine (Me_2NNH_2), tetraethylammonium cyanide (NEt_4CN), tert-butyl isocyanide (Bu^tNC) and tetrabutylammonium iodide (NBu^n_4I). CD_3CN was purchased from Goss Scientific and used as received.

3.3.1 Preparation of Cluster, Acid and Thiophenolate.

All the following compounds were prepared using methods described in Chapter 2, see (***section 2.3.1*** to ***2.3.3***.) (i) cluster $[NBu^n_4]_2[Fe_4S_4Cl_4]$, (ii) acid $[NHBu^n_3][BPh_4]$ and (iii) tetraethylammonium thiophenolate $[NEt_4][SPh]$

3.3.2 Preparation of $[NMe_4][SCN]$[36].

Tetramethylammonium bromide $[NMe_4]Br$ (9.24 g, 60 mmol) was dissolved in absolute ethanol (150 ml) to form a colourless solution. Potassium thiocyanate K[SCN] (5.82 g, 60 mmol) was then added and the mixture was stirred and heated to reflux for 2 h. A white solid precipitate (KBr) was formed, which was removed by filtration from the hot solution. The volume of the solution was reduced to half *in vacuo* and left to cool to room temperature. When cool, any

further residual KBr was removed by filtration again. The solvent were removed *in vacuo* to produce a white solid precipitate of crude [NMe_4][SCN].

Addition of MeCN (10 ml) and absolute ethanol (20 ml) dissolved the crude [NMe_4][SCN]. The mixture was stirred for 30 min to ensure that the compound was completely dissolved. After concentrating the solution to ~10 ml, about 75 ml of diethyl ether was added. The solution was cooled in the freezer overnight and the white crystals were collected by filtration. The product was washed with diethyl ether then dried *in vacuo*.

$$[NMe_4]Br + KSCN \xrightarrow{EtOH} [NMe_4]SCN + KBr \qquad (3.1)$$

IR spectrum: 3025 cm^{-1} (δ C-H), 1407-1484 cm^{-1} (ν C-H) for methyl; 1067-1286 cm^{-1} (δ C-N) for amine; 2065 cm^{-1} (ν C-N) nitrile; 740 cm^{-1} (ν C-S); and 502 cm^{-1} (δ SCN), as shown in Figure (3.9).

^{1}H NMR spectrum of [NMe_4][SCN] in CD_3OD: δ 1.84 (singlet, intensity = 3, *CH_3*), as shown in Figure (3.10).

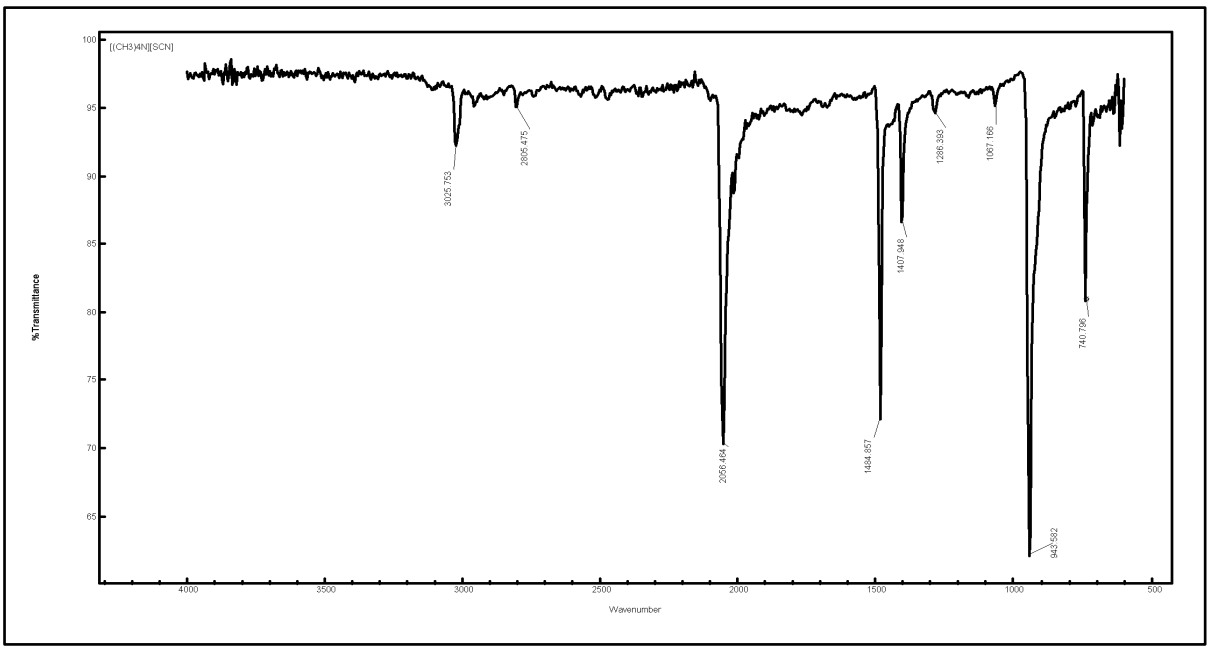

Figure 3.9. FTIR Spectrum for [NMe_4][SCN].

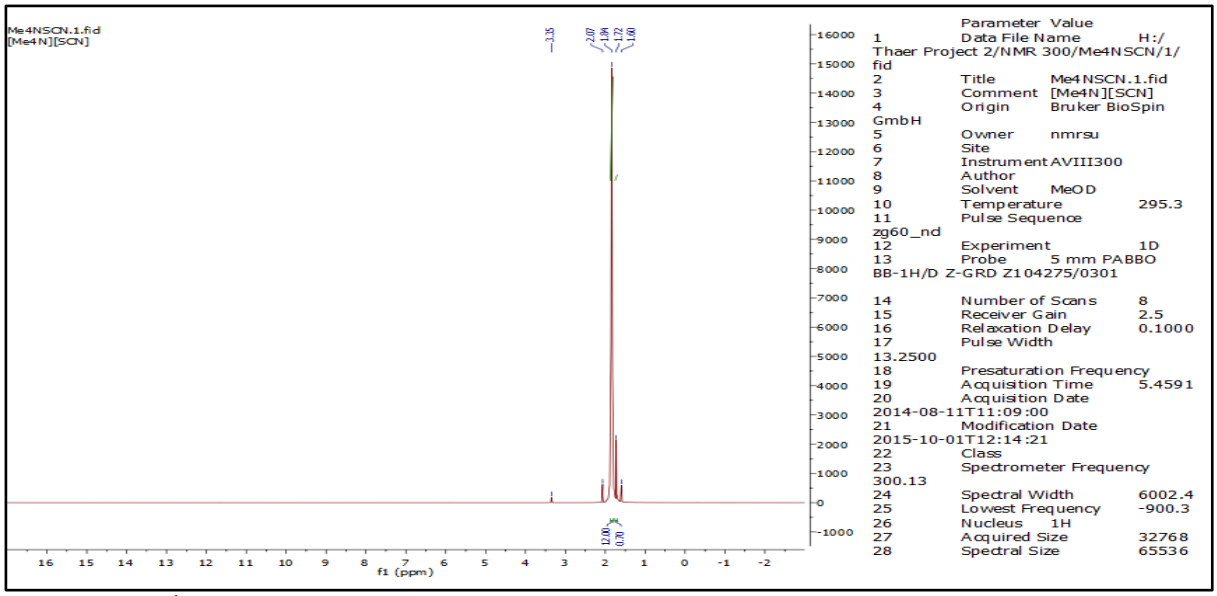

Figure 3.10. ^{1}H NMR Spectrum for $[NMe_4][SCN]$ in CD_3OD.

3.4 Kinetic studies.

All kinetic studies were performed using an Applied Photophysics SX.18 MV stopped-flow spectrophotometer, see Chapter 2 (***section 2.4.1.***), modified to handle air-sensitive solutions, connected to a RISC computer. The temperature was maintained using a Grant LTD6G thermostat tank with combined recirculating pump. The experiments were performed at 25.0 °C and the wavelength used was λ = 550 nm. All kinetics were studied in MeCN. The MeCN was dried over CaH_2 and distilled under an atmosphere of dinitrogen immediately prior to use. The solutions of $[NBu^n_4]_2[Fe_4S_4Cl_4]$ and reagents {$NHBu^n_3^+$, PhS^- and L = substrate = Cl^-, Br^-, I^-, $RNHNH_2$ (R = Me or Ph), Me_2NNH_2, HCN, NCS^-, N_3^-, Bu^tNC or pyridine} were prepared under an atmosphere of dinitrogen. The diluted solutions containing mixtures of $NHBu^n_3^+$, PhS^- and L were prepared from freshly prepared stock solutions. All solutions were used within 1 h.

Under all conditions, the stopped-flow absorbance-time traces were biphasic and were an excellent fit to two exponentials, indicating a first-order dependence on the concentration of the cluster. Similar behaviour has been observed in the substitution reactions of most $[Fe_4S_4X_4]^{2-}$ (X = thiolate or halide)[18]. The total absorbance changes observed herein, in the reactions of $[Fe_4S_4Cl_4]^{2-}$ are consistent with all four chloro-ligands being replaced by PhS^-. It has been suggested[18] that the absorbance-time curves can be fitted to two exponentials because either: (i) the first and second substitution steps are similar in rates but much slower than the rates of the third and fourth substitutions, or (ii) all four substitution steps occur at similar rates but the absorbance change for the first and second steps are appreciably larger than for the last two

steps. The dependences on the concentrations of $NHBu^n_3{}^+$, NBu^n_3 and PhSH were determined from analysis of the appropriate graphs as will be explained in the next sections.

The kinetic studies for the reactions of $[Fe_4S_4Cl_4]^{2-}$ with PhS^- in the presence of L (L = $RNHNH_2$ (R= Me or Ph), Me_2NNH_2, NCS^-, N_3^-, Bu^tNC or pyridine) and $NHBu^n_3{}^+$ are performed using the following manner: (i) determining appropriate concentration of [$NHBu^n_3{}^+$] is monitored through using constant concentration of cluster (0.2 mmol dm^{-3}), constant concentration of [PhS^-] and constant concentration of [L] with series of solutions for the different concentrations of [$NHBu^n_3{}^+$] (ii) after limitation the concentration of [$NHBu^n_3{}^+$] is kept constant for all experiments and using a constant concentration cluster (0.2 mmol dm^{-3}) and constant concentration of [PhS^-] (2.5 mmol dm^{-3}) with various concentrations of [L] to observe the impact of binding substrate (L) on the proton transfer from the acid to cluster for the substitution reaction.

Kinetic study for the reaction of $[Fe_4S_4Cl_4]^{2-}$ with PhS^- in presence of $NHBu^n_3{}^+$ and substrates (L = Cl^-, Br^- and I^-) was performed using standard solutions as follows: (i) constant concentration of cluster (0.2 mmol dm^{-3}), (ii) constant concentration of thiophenol (1.25 mmol dm^{-3}), (iii) constant concentration of acid (5.0 mmol dm^{-3}) and (iv) series of various concentrations from substrate L (1.0 - 50 mmol dm^{-3}), all solutions were prepared in MeCN. The reaction between $[Fe_4S_4Cl_4]^{2-}$ (0.2 mmol dm^{-3}) and $NHBu^n_3{}^+$ (2.5–40.0 mmol dm^{-3}) with PhS^- (1.25–5.0 mmol dm^{-3}) was monitored in the presence of various concentrations of CN^-.

3.5 Results and discussions.

In chapter two the acid-catalyzed substitution reaction of the terminal chloro-ligands in $[Fe_4S_4Cl_4]^{2-}$ by PhS^- in the presence of $NHBu^n{}_3^+$ was described and shown to involve rate-limiting proton transfer from $NHBu^n{}_3^+$ to $[Fe_4S_4Cl_4]^{2-}$ (k_0^{NHBu} = 490 ± 20 $dm^3\ mol^{-1}\ s^{-1}$)[37]. Consequently, studies on the effects that substrates have on this reaction allow evaluation of whether substrates bind to the cluster before or after protonation by this acid and, if substrate binds before protonation, to measure how the bound substrate affects the rate of protonation of the cluster. In the presentation that follows, the kinetics of the reaction between $[Fe_4S_4Cl_4]^{2-}$ and PhS^- in the presence of $NHBu^n{}_3$ and the various (L) will be presented and how all the results can be accommodated by the pathways shown in Figure (3.11). With various substrates (L = substrate = Cl^-, Br^-, I^-, $RNHNH_2$ (R = Me or Ph), Me_2NNH_2, HCN, NCS^-, N_3^-, Bu^tNC or pyridine) the different kinetics reflect the effects that (L) have on the rate of protonation of $[Fe_4S_4Cl_4]^{2-}$ by $NHBu^n{}_3^+$. This presentation will be followed by a discussion of how binding of (L) affects the rate of protonation, and how protonation affects the rate of binding of (L). Finally, the results from previous studies on substrate binding are considered in the light of the studies reported here.

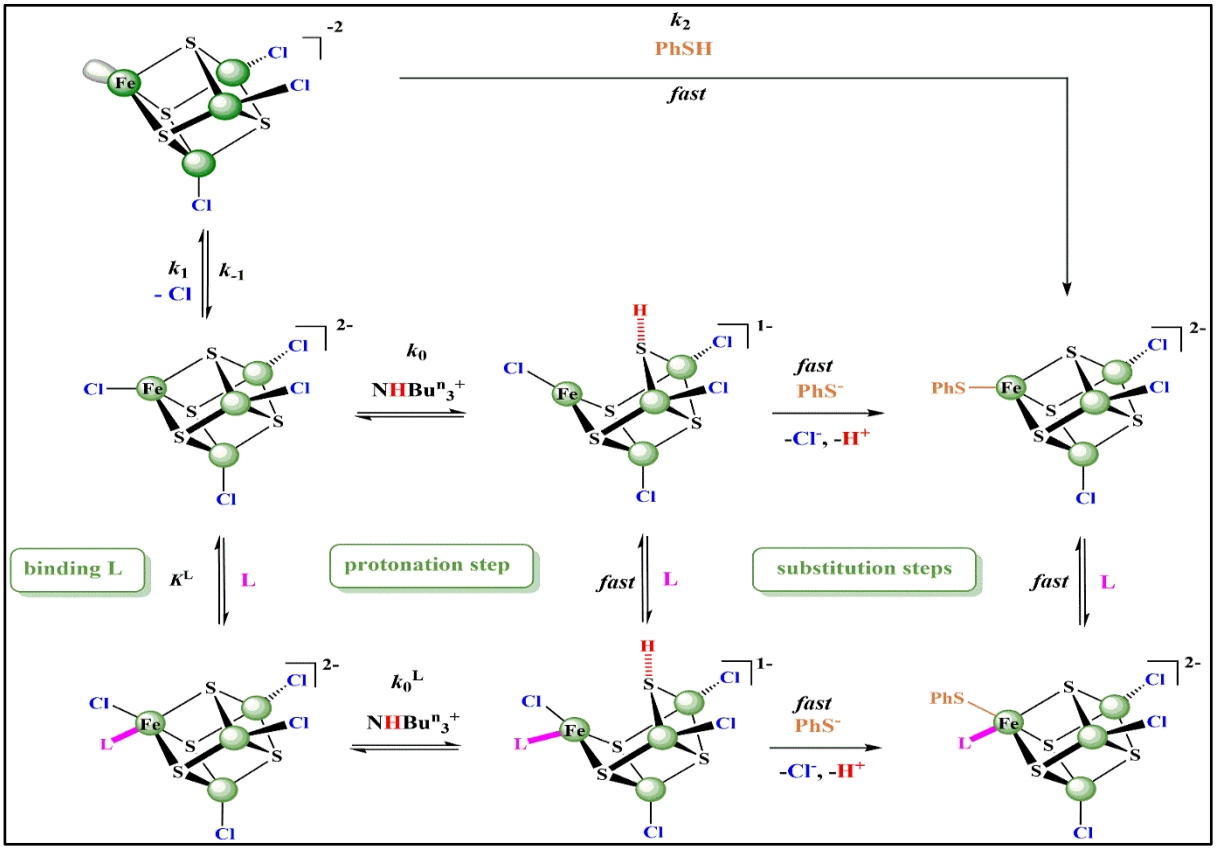

Figure 3.11. Outline of the mechanism for the reaction between $[Fe_4S_4Cl_4]^{2-}$ and PhSH in the presence of $NHBu^n{}_3^+$ and substrate (L).

In the mechanism shown in Figure (3.11), the top and middle lines show the pathways which operate when no substrate (L) is present. These pathways have been established in earlier work and are consistent with (top line) the dissociative substitution pathway for $[Fe_4S_4Cl_4]^{2-}$ involving rate-limiting dissociation of a chloro-ligand to generate a vacant site on one of the Fe sites at which PhSH can attack[38]. The middle pathway shows (in simplified form) the acid-catalyzed substitution mechanism which, when the acid is $NHBu^n_3{}^+$, is rate-limited by proton transfer from $NHBu^n_3{}^+$ to the cluster[37]. The bottom line shows the pathway in which rapid binding of (L) to the cluster forms $[Fe_4S_4Cl_4(L)]^{2-}$ which is then protonated by $NHBu^n_3{}^+$.

Using the relative rate law with each case, all kinetics data will be analyzed and the effects that a variety of substrates {L = substrate = Cl^-, Br^-, I^-, N_3^-, NCS^-, CN^-, HCN, Bu^tNC, pyr = pyridine, $RNHNH_2$ (R = Me or Ph) and Me_2NNH_2} have on the rates of protonation of the cluster by $NHBu^n_3{}^+$ will be discussed.

In order to analyze the kinetics of these reactions, it is important to consider what species are present in the solution. In solutions containing mixtures of $NHBu^n_3{}^+$ (pK_a = 18.1)[39] and PhS^- (pK_a = 20.8)[40] the protolytic equilibrium shown in Equation (3.2) is rapidly established and, in the presence of an excess of $NHBu^n_3{}^+$, the equilibrium lies to the right hand side.

$$NHBu^n_3{}^+ + PhS^- \rightleftharpoons NBu_3 + PhSH \qquad (3.2)$$

Consequently, in the presence of an excess of $NHBu^n_3{}^+$, the solution species are $NHBu^n_3{}^+$, NBu^n_3, PhSH and L. The concentrations of the species present in solution can be calculated from the simple relationships, as shown in Equations (3.3) and (3.4):

$$[NHBu^n_3{}^+]_e = [NHBu^n_3{}^+]_0 - [PhS^-]_0 \qquad (3.3)$$

$$[PhSH]_e = [NBu^n_3]_e = [PhS^-]_0 \qquad (3.4)$$

(subscript e denotes the concentration formed in the mixture and subscript 0 denotes the concentration prepared).

The pK_a of the substrate is also an important parameter in the analysis of the kinetics presented herein. The pK_as of the various protonated substrates (LH) are collected in Table (3.1)[39-42]. It is evident that the pK_a of $NHBu^n_3{}^+$ in MeCN (pK_a = 18.1)[42] is significantly larger than the pK_a of all LH except HCN. Consequently, of all the substrates studied herein, only CN^- is protonated

by $NHBu^n{}_3^+$, this leads to a more complicated analysis of the kinetics in the presence of CN^- and so the results for the kinetics in the presence of HCN/CN^- will be presented separately.

Table (3.1): The pK_a^{LH}s values for protonated substrates (LH)[39].

L	$\mathbf{pK_a^{LH}}$
Cl^-	8.9
Br^-	5.5
I^-	2.3
N_3^-	12.4
NCS^-	10.2
HCN[a]	23.4
Bu^tNC	-
pyridine	12.6
$MeNHNH_2$	15.5
Me_2NNH_2	14.9
$PhNHNH_2$	12.9

[a] With CN^- in the presence of HCN, Rate = 7.1±0.5 x $10^4[CN^-][Fe_4S_4Cl_4^{2-}]$.

3.5.1 Kinetics of reactions with L= $RNHNH_2$ (R= Me or Ph), Me_2NNH_2, NCS^-, N_3^-, Bu^tNC or pyridine.

The absorbance-time traces for the reactions of $[Fe_4S_4Cl_4]^{2-}$ with PhS^- in the presence of (L) and $NHBu^n{}_3^+$ are biphasic and can be fitted to two exponential curves, the experimental data are shown in Tables (3.2) and (3.3). This behaviour has been observed before for the substitution reactions of $[Fe_4S_4Cl_4]^{2-}$ and is a consequence of all the chloro-groups being substituted[18]. In this study, the focus is on the binding of (L) to $[Fe_4S_4Cl_4]^{2-}$ and so the following discussion relates only to the kinetics for the first (faster) phase. The kinetic data for both phases are presented in Table (3.4).

That the absorbance-time traces can be fitted to exponential curves is consistent with the reaction exhibiting a first order dependence on the concentration of cluster. The dependence on the concentration of substrate (L) was determined from plots of $k'_{obs}/[NHBu^n{}_3^+]_e$ against the concentration of L (k'_{obs} is k_{obs} corrected for the background uncatalysed substitution reaction which occurs with a rate constant of $2.5 \pm 0.5\ s^{-1}$; $k'_{obs} = k_{obs} - 2.5$)[38].

For the reactions with L = NCS^-, N_3^-, pyridine, or hydrazines, $k'_{obs}/[NHBu^n{}_3^+]_e$ increases in a non-linear fashion with the concentrations of (L), as shown in Table (3.4), Figures (3.12) and (3.13). Analysis of these data by a plot of $[NHBu^n{}_3^+]_e/k'_{obs}$ versus 1/[L] gives a straight line graph from which the experimental rate law shown in Equation (3.12), which can be derived as following:

For the mechanism shown in Figure (3.11), The pathways of substitution involving rate-limiting protonation of $[Fe_4S_4Cl_4]^{2-}$ and $[Fe_4S_4Cl_4(L)]^{2-}$ clusters by $NHBu^n{}_3^+$ (middle and bottom lines).

$$\text{Rate} = k_0[Fe_4S_4Cl_4^{2-}]_e[NHBu_3^{n+}]_e + k_0^L[Fe_4S_4(L)Cl_4^{2-}]_e[NHBu_3^{n+}]_e \quad (3.5)$$

(subscript e denotes the concentration formed at equilibrium and subscript 0 denotes the initial concentration).

The binding of L (L = NCS^-, N_3^-, pyridine, or hydrazines) is considered a rapid equilibrium prior to protonation and substitution, so when (K^L) is the equilibrium constant of the binding substrate (L) step:

$$K^L = \frac{[Fe_4S_4(L)Cl_4^{2-}]_e}{[Fe_4S_4Cl_4^{2-}]_e[L]} \quad (3.6)$$

$$[Fe_4S_4(L)Cl_4^{2-}]_e = K^L[Fe_4S_4Cl_4^{2-}]_e[L] \quad (3.7)$$

$$[Fe_4S_4Cl_4^{2-}]_0 = [Fe_4S_4Cl_4^{2-}]_e + [Fe_4S_4(L)Cl_4^{2-}]_e \quad (3.8)$$

By substituting the value of $[Fe_4S_4Cl_4(L)]_e^{2-}$ into Equation (3.8):

$$[Fe_4S_4Cl_4^{2-}]_e = \frac{[Fe_4S_4Cl_4^{2-}]_0}{1 + K^L[L]} \quad (3.9)$$

Substituting Equations (3.7) and (3.9) into Equation (3.5) leads to form the rate law for the protonation of $[Fe_4S_4Cl_4]^{2-}$ and $[Fe_4S_4Cl_4(L)]^{2-}$ clusters by $NHBu^n{}_3^+$ acid, as shown in Equation (3.10):

$$\text{Rate} = \{\frac{(k_0 + k_0^L K^L[L])}{1 + K^L[L]}[NHBu_3^{n+}]_e\}[Fe_4S_4Cl_4^{2-}] \quad (3.10)$$

By adding the background uncatalyzed substitution reaction which occurs k_1 to the rate law:

$$\text{Rate} = \{k_1 + \frac{(k_0 + k_0^L K^L[L])}{1 + K^L[L]}[NHBu_3^{n+}]_e\}[Fe_4S_4Cl_4^{2-}] \quad (3.11)$$

To simplified Equation (3.11), it will use the terms (a = k_0, b = $K^Lk_0{}^L$ and c = K^L) to obtain the Equation (3.12).

$$\text{Rate} = \{k_1 + \frac{(a + b[L])}{1 + c[L]}[NHBu_3^{n+}]_e\}[Fe_4S_4Cl_4^{2-}] \quad (3.12)$$

For the reaction with L = Bu^tNC, the plot of $k'_{obs}/[NHBu^n{}_3^+]_e$ versus $[Bu^tNC]$ is linear Figure (3.14). This behaviour is also consistent with Equation (3.12). When the binding of Bu^tNC to $[Fe_4S_4Cl_4]^{2-}$ is weak, c[L] < 1, Equation (3.12) simplifies to Equation (3.13). A limit to the value of c (c = K^{BuNC} is the equilibrium constant of the binding substrate (Bu^tNC) with the cluster) can be estimated for the binding of Bu^tNC to the cluster.

$$\text{Rate} = \{k_1 + (a + b[L])[NHBu_3^{n+}]_e\}[Fe_4S_4Cl_4^{2-}] \quad (3.13)$$

When the terms (k_1 = 2.5 ±0.5, a = $k_0{}^{BuNC}$ and b = $K^{BuNC}k_0{}^{BuNC}$).

The data for the reactions in the presence of N_3^- and NCS^- yield slightly different values of K^L and $k_0{}^L$, Table (3.3), Figures (3.12) and (3.13). However, the data for these two systems are so similar that they could both be fitted satisfactorily using K^L = 160 ± 10 $dm^3\ mol^{-1}$ and $k_0{}^L$ = 1.25 ±0.05 × 10^4 $dm^3\ mol^{-1}\ s^{-1}$.

Table (3.2): Experimental data for the reaction of $[Fe_4S_4Cl_4]^{2-}$ (0.2 mmol dm^{-3}) with PhS^- in presence of $NHBu^n{}_3{}^+$ and substrates (L = $RNHNH_2$ (R= Me or Ph), Me_2NNH_2 or NCS^-). Process to determine the appropriate concentration of $[NHBu^n{}_3{}^+]$.

Substrate **L**	**[PhS^-]** **(mmol dm^{-3})**	**[L]** **(mmol dm^{-3})**	**[$NHBu^n{}_3{}^+$]** **(mmol dm^{-3})**	k_{obs} s^{-1}
$MeNHNH_2$	5.0	3.75	7.5	40.0
	5.0	3.75	10.0	62.0
	5.0	3.75	15.0	80.0
	5.0	3.75	25.0	100.0
	5.0	3.75	30.0	120.0
	5.0	3.75	40.0	140.0
	5.0	7.5	7.5	60.7
	5.0	7.5	10.0	86.7
	5.0	7.5	15.0	127.0
	5.0	7.5	25.0	214.0
	5.0	7.5	30.0	242.0
	5.0	7.5	40.0	270
	5.0	15.0	7.5	80.64
	5.0	15.0	10.0	95.0
	5.0	15.0	15.0	129.0
	5.0	15.0	25.0	140.0
	5.0	15.0	30.0	216.0

	5.0	15.0	40.0	280.0
$PhNHNH_2$	5.0	5.0	7.5	15.3
	5.0	5.0	10.0	19.36
	5.0	5.0	15.0	23.9
	5.0	5.0	25.0	29.8
	5.0	5.0	30.0	30.21
	5.0	5.0	40.0	34.9
	5.0	25.0	7.5	13.2
	5.0	25.0	10.0	17.9
	5.0	25.0	15.0	20.12
	5.0	25.0	25.0	23.4
	5.0	25.0	30.0	27.3
	5.0	25.0	40.0	30.5
Me_2NNH_2	5.0	5.0	7.5	17.3
	5.0	5.0	10.0	18.0
	5.0	5.0	15.0	20.0
	5.0	5.0	25.0	28.6
	5.0	5.0	30.0	32.6
	5.0	5.0	40.0	37.0
	5.0	25.0	7.5	18.3
	5.0	25.0	10.0	19.5

	5.0	25.0	15.0	28.3
	5.0	25.0	25.0	32.6
	5.0	25.0	30.0	47.5
	5.0	25.0	40.0	50.0
NCS^-	1.25	5.0	2.5	11.9
	1.25	5.0	5.0	25.4
	1.25	5.0	7.5	39.8
	1.25	5.0	10.0	62.0
	1.25	5.0	15.0	99.0
	1.25	5.0	25.0	116.0
	1.25	5.0	30.0	116.0
	1.25	5.0	40.0	116.0

Table (3.3): Experimental data for the reaction of $[Fe_4S_4Cl_4]^{2-}$ (0.2 mmol dm^{-3}) with PhS^- in presence of constant concentration of $[NHBu^n{}_3{}^+]$ and variety concentrations of substrates [L]. Process to study the effect of binding substrate on proton transfer from acid to cluster.

Substrate **L**	**$[PhS^-]_e$** **(mmol dm^{-3})**	**$[NHBu^n{}_3{}^+]_e$** **(mmol dm^{-3})**	**$[L]_e$** **(mmol dm^{-3})**	***k*obs** **s^{-1}**
$MeNHNH_2$	1.25	3.75	0.0	5.12
	1.25	3.75	1.0	27.63
	1.25	3.75	2.0	35.98
	1.25	3.75	3.0	43.75
	1.25	3.75	4.0	50.13
	1.25	3.75	5.0	58.0
	1.25	3.75	7.5	72.51
$PhNHNH_2$	1.25	3.75	0.0	5.09
	1.25	3.75	1.0	6.7
	1.25	3.75	2.0	5.4
	1.25	3.75	3.0	5.98
	1.25	3.75	4.0	6.7

	1.25	3.75	5.0	8.2
	1.25	3.75	7.5	9.21
	1.25	3.75	10.0	10.5
	1.25	3.75	15.0	10.5
	1.25	3.75	25.0	10.5
Me_2NNH_2	1.25	3.75	0.0	5.0
	1.25	3.75	1.0	15.0
	1.25	3.75	2.0	17.01
	1.25	3.75	3.0	19.5
	1.25	3.75	4.0	21.0
	1.25	3.75	5.0	22.37
	1.25	3.75	7.5	24.5
	1.25	3.75	10.0	28.0
	1.25	3.75	15.0	30.0
	1.25	3.75	25.0	32.5

NCS^-	1.25	3.75	0.0	5.0
	1.25	3.75	1.0	12.4
	1.25	3.75	2.5	21.82
	1.25	3.75	5.0	27.1
	1.25	3.75	10.0	29.84
	1.25	3.75	20.0	37.79
	1.25	3.75	30.0	42.6
	1.25	3.75	40.0	44.61
	1.25	3.75	50.0	45.51
N_3^-	1.25	3.75	0.0	5.09
	1.25	3.75	1.0	16.0
	1.25	3.75	2.5	20.09
	1.25	3.75	5.0	24.9
	1.25	3.75	10.0	34.6
	1.25	3.75	20.0	39.59

	1.25	3.75	30.0	45.58
	1.25	3.75	40.0	50.01
	1.25	3.75	50.0	50.01
pyridine	1.25	3.75	0.0	5.0
	1.25	3.75	1.0	6.25
	1.25	3.75	2.5	7.49
	1.25	3.75	5.0	8.5
	1.25	3.75	10.0	9.28
	1.25	3.75	20.0	10.9
	1.25	3.75	30.0	11.39
	1.25	3.75	40.0	13.0
	1.25	3.75	50.0	13.0
Bu^tNC	1.25	3.75	0.0	4.8
	1.25	3.75	1.0	5.2
	1.25	3.75	2.5	5.61

	1.25	3.75	5.0	6.21
	1.25	3.75	10.0	7.42
	1.25	3.75	20.0	10.49
	1.25	3.75	30.0	12.9
	1.25	3.75	40.0	17.68
	1.25	3.75	50.0	19.34

Table (3.4): Analysis of kinetics data for the reaction of $[Fe_4S_4Cl_4]^{2-}$ with PhS^- in presence of $NHBu^n{}_3^+$ and substrates (L = $RNHNH_2$ (R= Me or Ph), Me_2NNH_2, NCS^-, N_3^-, Pyr. or Bu^tNC). Using Equations (3.19) and (3.20), when the term ($k'_{obs} = k_{obs} - 2.5$).

Substrate L	**$[L]_e$ (mmol dm^{-3})**	**$[NHBu^n{}_3^+]_e$ (mmol dm^{-3})**	**$10^{-3}k'_{obs}/[NHBu_3^+]_e$ (dm^3 mol^{-1} s^{-1})**
$MeNHNH_2$	0.0	3.75	0.7
	1.0	3.75	6.7
	2.0	3.75	8.93
	3.0	3.75	11.0
	4.0	3.75	12.7
	5.0	3.75	14.8
	7.5	3.75	18.67
$PhNHNH_2$	0.0	3.75	0.69

	1.0	3.75	1.12
	2.0	3.75	0.77
	3.0	3.75	0.93
	4.0	3.75	1.12
	5.0	3.75	1.52
	7.5	3.75	1.79
	10.0	3.75	2.13
	15.0	3.75	2.13
	25.0	3.75	2.13
Me_2NNH_2	0.0	3.75	0.6
	1.0	3.75	3.33
	2.0	3.75	3.87
	3.0	3.75	4.53
	4.0	3.75	4.93
	5.0	3.75	5.3
	7.5	3.75	5.86
	10.0	3.75	6.8
	15.0	3.75	7.33
	25.0	3.75	8.0
NCS^-	0.0	3.75	0.6
	1.0	3.75	2.64

	2.5	3.75	5.15
	5.0	3.75	6.56
	10.0	3.75	7.28
	20.0	3.75	9.41
	30.0	3.75	10.69
	40.0	3.75	11.23
	50.0	3.75	11.47
N_3^-	0.0	3.75	0.69
	1.0	3.75	3.6
	2.5	3.75	4.69
	5.0	3.75	5.97
	10.0	3.75	8.56
	20.0	3.75	9.89
	30.0	3.75	11.49
	40.0	3.75	12.67
	50.0	3.75	12.67
pyridine	0.0	3.75	0.6
	1.0	3.75	1.0
	2.5	3.75	1.33
	5.0	3.75	1.6
	10.0	3.75	1.81

	20.0	3.75	2.24
	30.0	3.75	2.37
	40.0	3.75	2.8
	50.0	3.75	2.8
Bu^tNC	0.0	3.75	0.58
	1.0	3.75	0.72
	2.5	3.75	0.83
	5.0	3.75	0.99
	10.0	3.75	1.31
	20.0	3.75	2.13
	30.0	3.75	2.77
	40.0	3.75	4.05
	50.0	3.75	4.49

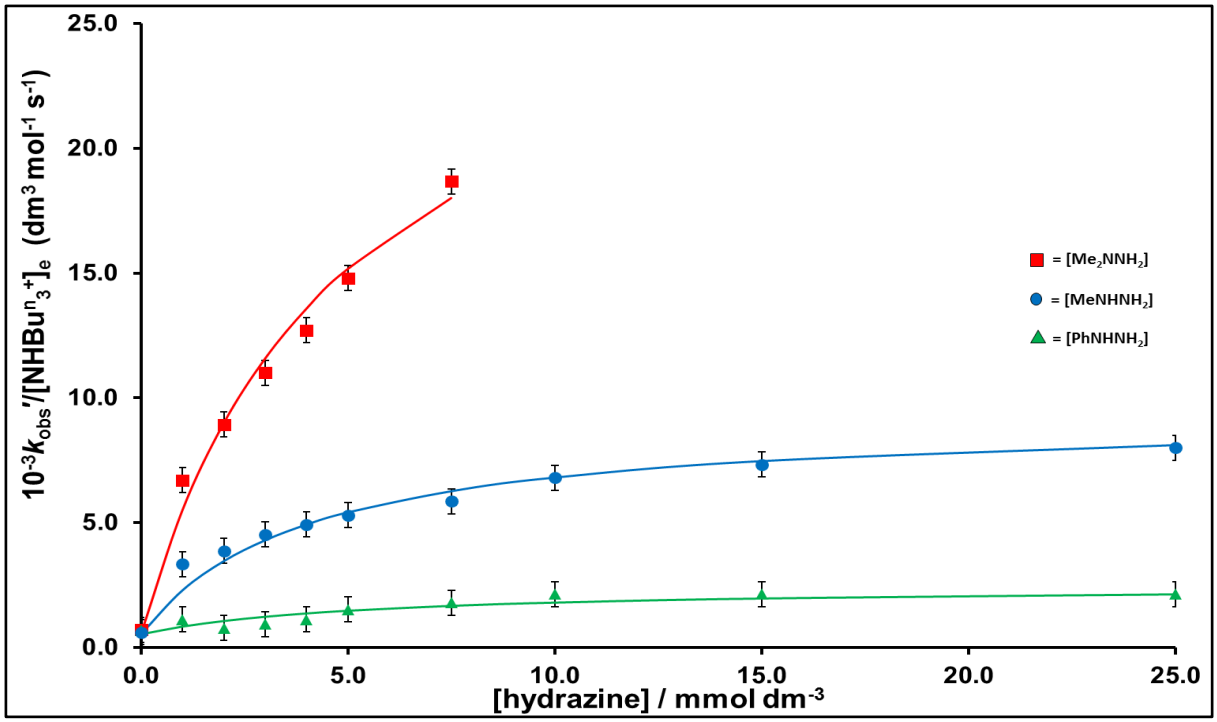

Figure 3.12. Graph for the reaction of $[Fe_4S_4Cl_4]^{2-}$ with PhS^- in presence of $NHBu^n{}_3^+$ and substrates (L = $RNHNH_2$ (R= Me or Ph) and Me_2NNH_2), using Equations (3.12).

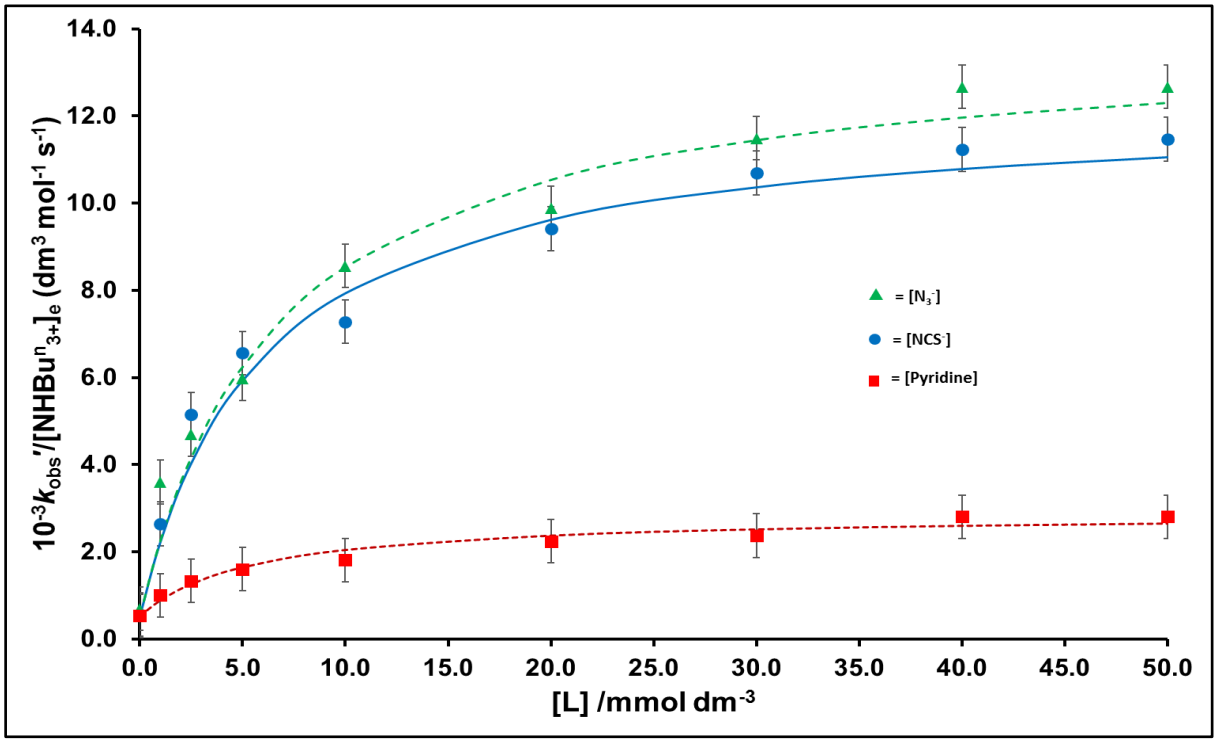

Figure 3.13. Graph for the reaction of $[Fe_4S_4Cl_4]^{2-}$ with PhS^- in presence of $NHBu^n{}_3^+$ and substrates (L = NCS^-, N_3^- and pyridine), the kinetic fitting data shown as: the green dashed curve for (N_3^-); the blue solid curve for (NCS^-) and the red dotted curve for (pyridine), using Equations (3.12).

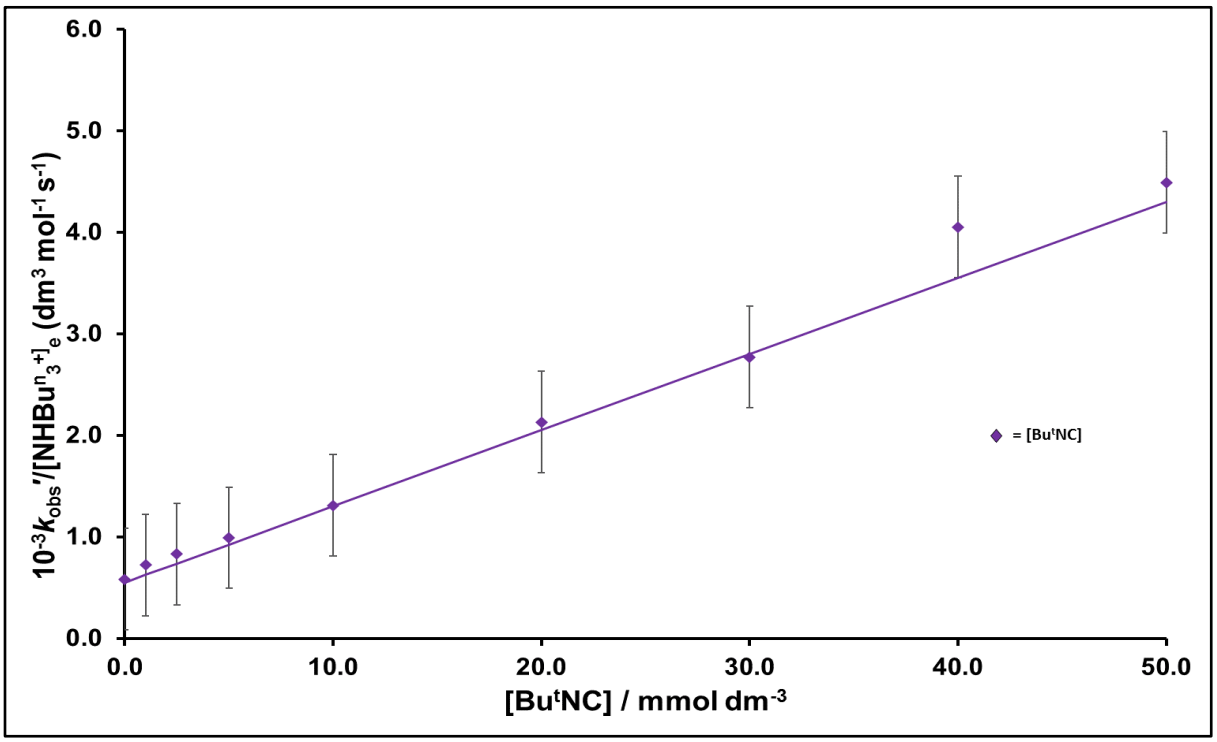

Figure 3.14. Graph for the reaction of $[Fe_4S_4Cl_4]^{2-}$ with PhS^- in presence of $NHBu^n{}_3^+$ and substrate (L = Bu^tNC), using Equations (3.13) and K^L = 160 ± 10 dm^3 mol^{-1} and $k_0{}^L$ = 1.25 ±0.05 × 10^4 dm^3 mol^{-1} s^{-1}.

Table (3.5) summarises the parameters derived from the various kinetic studies in the presence of various L. The results presented in Table (3.5) indicate that the rate of proton transfer from $NHBu^n{}_3^+$ to $[Fe_4S_4Cl_4]^{2-}$ is modulated in the presence of L = N_3^-, NCS^-, Bu^tNC, pyridine, $RNHNH_2$ (R =Me or Ph) and Me_2NNH_2, indicating that these L bind to$[Fe_4S_4Cl_4]^{2-}$. Furthermore, this observation indicates that these L bind to $[Fe_4S_4Cl_4]^{2-}$ faster than protonation of this cluster by $NHBu^n{}_3^+$ (when $[NHBu^n{}_3^+]_e$ = 3.75 mmol dm^{-3}). Since the lowest concentration of L used was 1.0 mmol dm^{-3}, it can be calculated that the rate of L binding is greater than *ca* 2 × 10^3 dm^3 mol^{-1} s^{-1} by using Equation (3.12).

Table (3.5): The values of kinetic parameters are presented in Equations (3.19) and (3.20) for the reaction of $[Fe_4S_4Cl_4]^{2-}$ with PhS^- in presence of $NHBu^n{}_3^+$ and substrates (L = $RNHNH_2$ (R= Me or Ph), Me_2NNH_2, NCS^-, N_3^-, Pyr. or Bu^tNC), in MeCN at 25.0 ºC.

Substrate **L**	**a = k_0** **($dm^3\ mol^{-1}\ s^{-1}$)**	**b = $K^L k_0^L$** **($dm^6\ mol^{-2}\ s^{-1}$)**	**c = K^L** **($dm^3\ mol^{-1}$)**	**k_0^L** **($dm^3\ mol^{-1}\ s^{-1}$)**	**k_0^L / k_0**
$MeNHNH_2$	530 ±20	6.0 ±0.5 x 10^6	210 ±10	2.9 ±0.3 x 10^4	53.9
$PhNHNH_2$	530 ±20	3.7 ±0.4 x 10^5	190 ±10	2.0 ±0.3 x 10^3	3.7
Me_2NNH_2	530 ±20	2.2 ±0.2 x 10^6	250 ±10	8.8 ±0.5 x 10^3	16.6
NCS^-	530 ±20	2.0 ±0.4 x 10^6	170 ±10	1.2 ±0.2 x 10^4	22.1
N_3^-	530 ±20	2.0 ±0.4 x 10^6	150 ±10	1.3 ±0.2 x 10^4	24.5
Pyr.	530 ±20	4.3 ±0.4 x 10^5	180 ±10	2.4 ±0.3 x 10^3	4.5
Bu^tNC	550 ±20	7.5 ±0.5 x 10^4	≤ 2	≥ 3.8 x 10^4	≥ 72

3.5.1.1 Kinetics of reactions with L = Cl^-, Br^- or I^-.

The experimental data for the reaction of $[Fe_4S_4Cl_4]^{2-}$ with PhS^- in the presence L = Cl^- and $NHBu^n{}_3^+$ are presented in Table (3.6). Analysis of kinetics data for the reaction with PhS^- in the presence of $NHBu^n{}_3^+$ and Cl^- is shown in Figure (3.15). This study shows that at low concentrations of Cl^- the rate decreases but at higher concentrations of Cl^- the rate increases in a linear fashion. The rate law can be derived as following:

For the mechanism shown in Figure (3.11), the overall pathways of the reaction are:

$$\text{Rate} = k_1[Fe_4S_4Cl_4^{2-}]_0 - k_{-1}[Fe_4S_4Cl_3^{2-}]_e[Cl^-] + k_0[Fe_4S_4Cl_4^{2-}]_e[NHBu_3^{n+}]_e + k_0^L[Fe_4S_4(L)Cl_4^{2-}]_e[NHBu_3^{n+}]_e \qquad (3.14)$$

(subscript e denotes the concentration formed at equilibrium and subscript 0 denotes the initial concentration).

To simplify the derivation of the rate law, so it can be divided the reaction into two main pathways:

(i) The dissociative substitution pathway for $[Fe_4S_4Cl_4]^{2-}$ involving rate-limiting dissociation of a chloro-ligand to generate a vacant site on one of the Fe sites at which PhSH can attack (top line).

The rate law is:

$$\text{Rate} = k_1[Fe_4S_4Cl_4^{2-}]_0 - k_{-1}[Fe_4S_4Cl_3^{2-}]_e[Cl^-] \quad (3.15)$$

To find the value of $[Fe_4S_4Cl_3]_e^{2-}$, it should be monitored the change of $[Fe_4S_4Cl_3]_e^{2-}$ during the reaction, as following:

$$\frac{-\partial[Fe_4S_4Cl_3^{2-}]_e}{\partial t} = -k_2[Fe_4S_4Cl_3^{2-}]_e[PhSH] + k_1[Fe_4S_4Cl_4^{2-}]_0 - k_{-1}[Fe_4S_4Cl_3^{2-}]_e[Cl^-] \quad (3.16)$$

At equilibrium $\{\frac{-d[Fe_4S_4Cl_3^{2-}]_e}{dt} = 0\}$ as a result:

$$k_2[Fe_4S_4Cl_3^{2-}]_e[PhSH] + k_{-1}[Fe_4S_4Cl_3^{2-}]_e[Cl^-] = k_1[Fe_4S_4Cl_4^{2-}]_0 \quad (3.16)$$

$$[Fe_4S_4Cl_3^{2-}]_e = \frac{k_1[Fe_4S_4Cl_4^{2-}]_0}{k_2[PhSH] + k_{-1}[Cl^-]} \quad (3.17)$$

Substituting Equation (3.17) into (3.15):

$$\text{Rate} = k_1[Fe_4S_4Cl_4^{2-}]_0 - \frac{k_{-1}k_1\,[Fe_4S_4Cl_4^{2-}]_0[Cl^-]}{k_2[PhSH] + k_{-1}[Cl^-]} \quad (3.18)$$

Rearrangement of Equation (3.18) leads to produce the rate law involving rate-limiting dissociation of a chloro-ligand, as shown in Equation (3.19):

$$\text{Rate} = \frac{k_1[Fe_4S_4Cl_4^{2-}]_0}{1 + k_{-1}[Cl^-]/k_2[PhSH]} \quad (3.19)$$

(ii) For the pathways of substitution involving rate-limiting protonation of $[Fe_4S_4Cl_4]^{2-}$ and $[Fe_4S_4Cl_4(L)]^{2-}$ clusters by $NHBu^n{}_3^+$ (middle and bottom lines), the derivation of rate law has been described in (***section 3.4.1.1***).

The general rate law for the reaction Equation (3.20) is formed by accumulating Equations (3.10) and (3.19):

$$\text{Rate} = \left\{\frac{k_1}{1 + k_{-1}[Cl^-]/k_2'} + \frac{(k_0 + k_0^L K^L[L])[NHBu_3^{n+}]_e}{1 + K^L[L]}\right\}[Fe_4S_4Cl_4^{2-}]_0 \quad (3.20)$$

Where: $(k_2' = k_2[PhSH])$ and (L = Cl^-)

Using an iterative method, the kinetic data was fitted to Equation (3.21).

$$\text{Rate} = \{\frac{2.5}{1 + 6000[Cl^-]} + (500 + 1.6 \times 10^4[Cl^-])[NHBu_3^{n+}]_e\} \times [Fe_4S_4Cl_4^{2-}] \quad (3.21)$$

The rate law for the reaction in the presence of Cl^-, as shown in Equation (3.21), is the only case where both terms shown in Equation (3.20) are observed. Comparison of Equations (3.21) and (3.20) gives $k_1^{Cl} = 2.5 \pm 0.3\ s^{-1}$, $k_{-1}^{Cl}/k'^{Cl}_2 = 6 \pm 1 \times 10^3$, $k_0^{Cl} = 500 \pm 20\ dm^3\ mol^{-1}\ s^{-1}$ and $k_0^{Cl}K^{Cl} = 1.6 \pm 0.4 \times 10^4\ dm^6\ mol^{-2}\ s^{-1}$. The dependence on the concentration of Cl^- is linear even at the highest concentration of Cl^- ($[Cl^-]_{max} = 20$ mmol dm^{-3}), and hence we can calculate $K^{Cl} \leq 50\ dm^3\ mol^{-1}$. It is worth noting that the values of k_1 and k_0 are in good agreement with those determined in earlier work ($k_1 = 2.0 \pm 0.3\ s^{-1}$ and $k_0 = 530 \pm 20\ dm^3\ mol^{-1}\ s^{-1}$)[37, 38].

Table (3.6): Experimental data for the reaction of $[Fe_4S_4Cl_4]^{2-}$ (0.2 mmol dm^{-3}) with PhS^- in presence of constant concentration of $[NHBu^n_3{}^+]$ and variety concentrations of substrates (L = Cl^-, Br^- and I^-). Process to study the effect of binding substrate on proton transfer from acid to cluster.

Substrate **L**	**[PhS$^-$]** **(mmol dm^{-3})**	**[NHBu$^n_3{}^+$]** **(mmol dm^{-3})**	**[L]** **(mmol dm^{-3})**	**k_{obs}** **s^{-1}**
Cl^-	1.25	5.0	0.0	4.7
	1.25	5.0	1.0	3.4
	1.25	5.0	2.5	2.0
	1.25	5.0	5.0	2.0
	1.25	5.0	10.0	2.2
	1.25	5.0	20.0	2.9
	1.25	5.0	30.0	3.7
	1.25	5.0	40.0	4.4
	1.25	5.0	50.0	5.6
Br^-	1.25	5.0	0.0	4.8
	1.25	5.0	1.0	4.9
	1.25	5.0	2.5	4.6

	1.25	5.0	5.0	4.6
	1.25	5.0	10.0	4.4
	1.25	5.0	20.0	4.4
	1.25	5.0	30.0	4.4
	1.25	5.0	40.0	4.4
	1.25	5.0	50.0	4.4
I^-	1.25	5.0	0.0	4.8
	1.25	5.0	1.0	4.8
	1.25	5.0	2.5	4.8
	1.25	5.0	5.0	4.7
	1.25	5.0	10.0	4.6
	1.25	5.0	20.0	4.5
	1.25	5.0	30.0	4.5
	1.25	5.0	40.0	4.5
	1.25	5.0	50.0	4.6

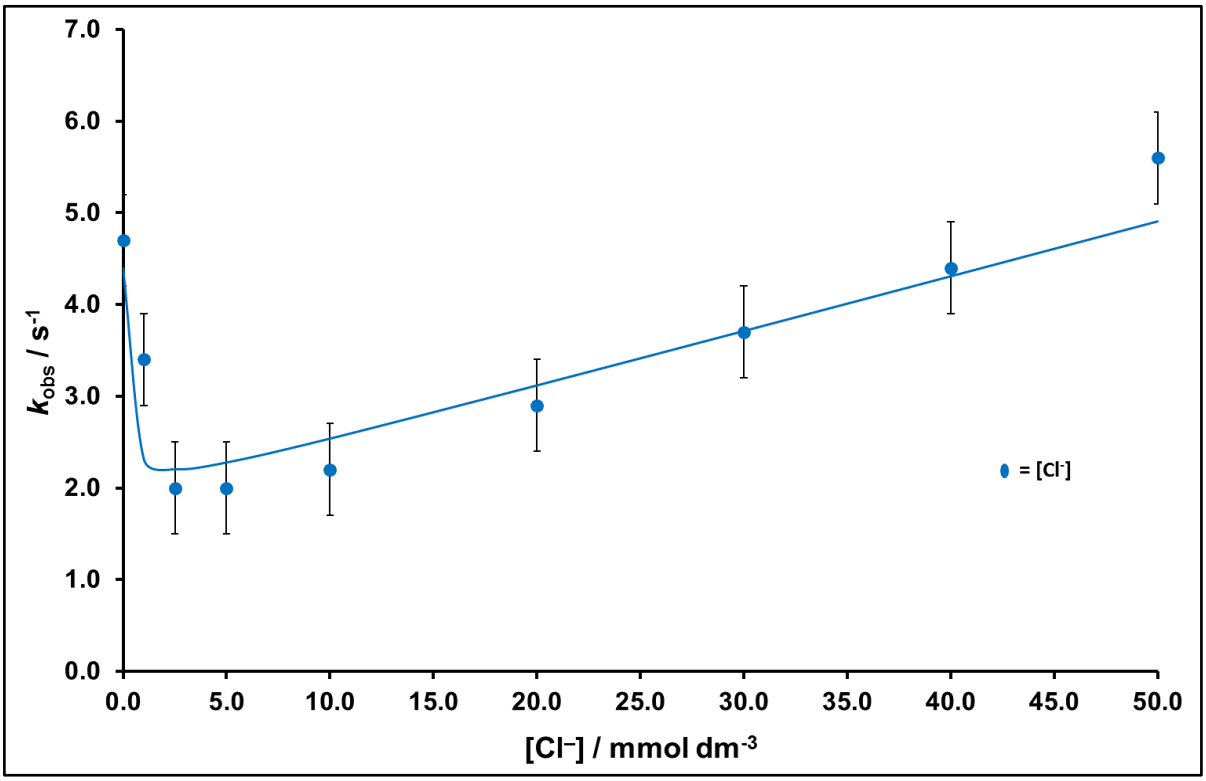

Figure 3.15. Graph for the reaction of $[Fe_4S_4Cl_4]^{2-}$ with PhS^- in presence of $NHBu^n{}_3^+$ and substrate ($L = Cl^-$), using Equation (3.21).

In contrast, kinetic studies for the same reaction in the presence of $L = Br^-$ or I^- show that neither Br^- nor I^- has a detectable effect on the rate of reaction between $[Fe_4S_4Cl_4]^{2-}$ and PhS^- in presence of $NHBu^n{}_3^+$, see Table (3.6). This behaviour could be because: (i) Br^- and I^- do not bind to $[Fe_4S_4Cl_4]^{2-}$ or (ii) they bind more slowly than proton transfer from $NHBu^n{}_3^+$. Earlier studies showed that Br^- and I^- affect the rate of protonation of $[Fe_4S_4Cl_4]^{2-}$ by $pyrrH^+$ (pyrr = pyrrolidine)[38], indicating that Br^- and I^- do bind to $[Fe_4S_4Cl_4]^{2-}$. Furthermore, the rate of protonation of $[Fe_4S_4Cl_4]^{2-}$ by $pyrrH^+$ ($k = 2.1 \pm 0.5 \times 10^4$ dm^3 mol^{-1} s^{-1})[43, 44] is significantly faster than that with $NHBu^n{}_3^+$, demonstrating that binding of Br^- and I^- to the cluster must be faster than protonation by $NHBu^n{}_3^+$. Consequently, it appears that although Br^- or I^- do bind to $[Fe_4S_4Cl_4]^{2-}$, their binding does not affect the rate of proton transfer from $NHBu^n{}_3^+$ appreciably.

3.5.1.2 Kinetics of Reactions with L = CN^-.

The kinetic of reactions between $[Fe_4S_4Cl_4]^{2-}$ and $NHBu^n{}_3^+$ with PhS^- have been investigated in presence of various concentrations of $L = CN^-$. All experimental data are presented in Table (3.7).

Table (3.7): Experimental data for the reaction of $[Fe_4S_4Cl_4]^{2-}$ (0.2 mmol dm^{-3}) with PhS^- in presence of $NHBu^n{}_3^+$ as acid and CN^- as substrate.

$[PhS^-]$ (mmol dm^{-3})	**$[NHBu^n{}_3^+]$ (mmol dm^{-3})**	**$[CN^-]$ (mmol dm^{-3})**	**k_{obs} s^{-1}**
1.25	5.0	1.0	4.0
1.25	10.0	1.0	6.0
1.25	15.0	1.0	8.5
1.25	25.0	1.0	11.5
1.25	30.0	1.0	13.5
1.25	40.0	1.0	18.7
1.25	10.0	3.0	5.5
1.25	15.0	3.0	9.4
1.25	25.0	3.0	13.2
1.25	30.0	3.0	15.1
1.25	40.0	3.0	18.0
1.25	2.5	1.75	34.4
1.25	2.5	2.0	47.3
1.25	2.5	2.25	61.7
2.5	5.0	3.0	43.0
2.5	5.0	3.5	61.0
2.5	5.0	3.75	93.7
2.5	5.0	4.0	97.5

2.5	5.0	4.25	128.5
2.5	5.0	4.5	159.8
5.0	10.0	5.5	35.0
5.0	10.0	5.75	50.1
5.0	10.0	6.0	70.4
5.0	10.0	6.25	83.3
5.0	10.0	6.5	118.2
5.0	10.0	6.75	138.4
5.0	10.0	7.0	145.0

The added complication in the studies with CN^- is that $NHBu^n{}_3^+$ (pK_a = 18.1 in MeCN)[42] is sufficiently strong to protonate CN^- (pK_a^{HCN} = 23.4)[42]. Consequently, it is necessary to analyse the kinetic data under two different conditions.

(i) **$[NHBu^n{}_3^+]_e \geq [CN^-]$**

Under these conditions all CN^- is converted into HCN and, thus, the species present in solution are $NHBu^n{}_3^+$, PhSH and HCN. In order to calculate the concentrations of all solution species, the equilibrium reactions shown in both Equations (3.16) and (3.22) need to be considered.

$$NHBu^n{}_3^+ + CN^- \rightleftharpoons NBu^n{}_3 + HCN \qquad (3.22)$$

When:

$$[NHBu_3^{n+}]_0 \geq ([PhS^-]_0 + [CN^-]_0) \qquad (3.23)$$

$$[NHBu_3^{n+}]_e = [NHBu_3^{n+}]_0 - [PhS^-]_0 - [CN^-]_0 \qquad (3.24)$$

$$[PhSH]_e = [PhS^-]_0 \qquad (3.25)$$

$$[HCN]_e = [CN^-]_0 \qquad (3.26)$$

Analysis of the kinetic data shows that the rate of reaction is independent of the concentration of HCN, as shown in Table (3.8) and Figure (3.16), and the rate law derived from this graph Equation (3.27) is an excellent agreement with that observed earlier for the reaction of $[Fe_4S_4Cl_4]^{2-}$ with PhS^- in the presence of $NHBu^n{}_3^+$, but no added substrate[37].

$$\text{Rate} = \{2.0 + 500[\text{NHBu}_3^{n+}]_e\}[\text{Fe}_4\text{S}_4\text{Cl}_4^{2-}] \qquad (3.27)$$

Where k_1^{CN} = 2.0 s^{-1} is the rate constant for uncatalysed substitution reaction and (k_0^{CN} + $K^{CN}k_0^{CN}$ = 500) at 1.0 mmol dm^{-3} of $[CN^-]$.

Table (3.8): Analysis of kinetics data for the reaction of $[Fe_4S_4Cl_4]^{2-}$ with PhS^- in presence of $NHBu^n{}_3^+$ and CN^-, when $[NHBu^n{}_3^+]_e \geq [CN^-]$.

$[CN^-]_0$ (mmol dm^{-3})	**$[NHBu^n{}_3^+]_e$ (mmol dm^{-3})**	**k_{obs} s^{-1}**
1.0	2.75	4.0
1.0	7.75	6.0
1.0	12.75	8.5
1.0	22.75	11.5
1.0	27.75	13.5
1.0	37.75	18.7
3.0	5.75	5.5
3.0	10.75	9.4
3.0	20.75	13.2
3.0	25.75	15.1
3.0	35.75	18.0

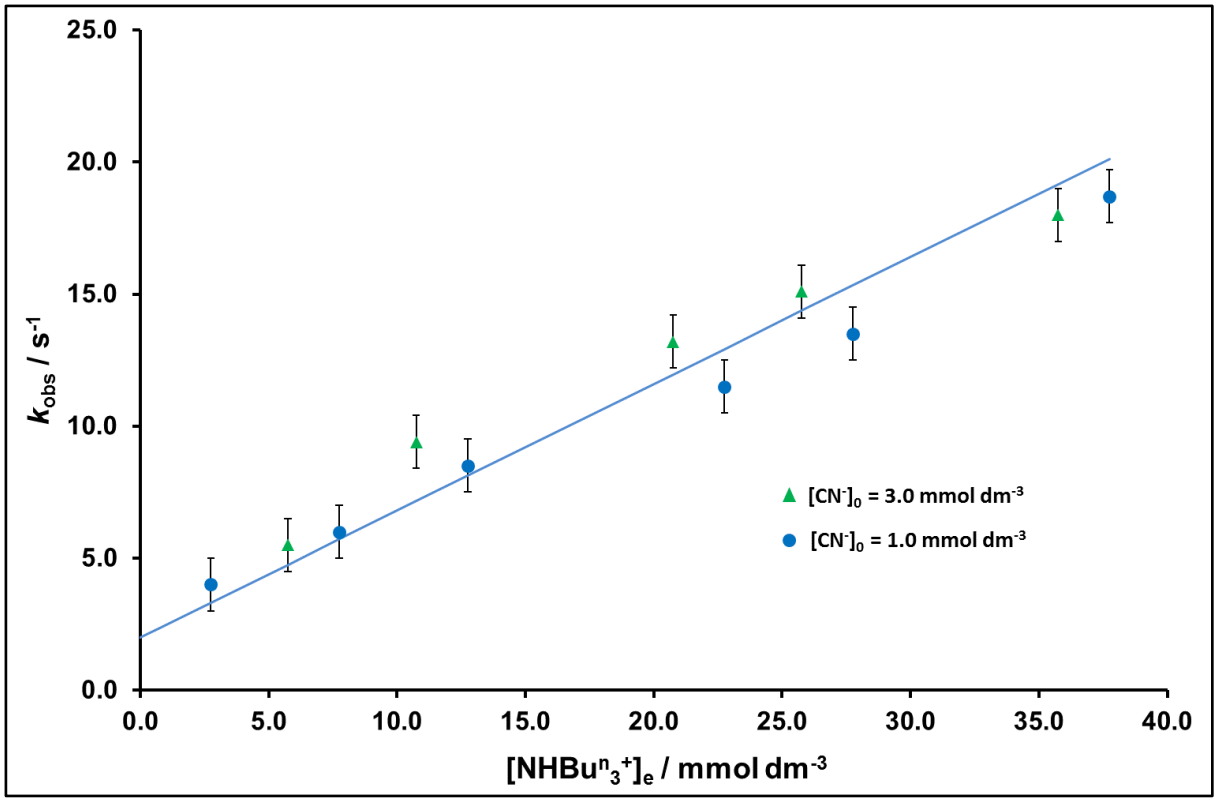

Figure (3.16): Graph for the reaction of $[Fe_4S_4Cl_4]^{2-}$ with PhS^- in presence of $NHBu^n{}_3^+$ and CN^-, consistent with Equation (3.27).

(ii) **$[NHBu^n{}_3^+]_e < [CN^-]$**

When $[NHBu^n{}_3^+]_0 > [PhS^-]_0$, but $([NHBu^n{}_3^+]_0 - [PhS^-]_0) < [CN^-]_0$, the reaction solutions will contain PhSH and mixtures of HCN and CN^-, but no $NHBu^n{}_3^+$. The concentrations of the various species present in solution were calculated using the following relationships:

$$[PhSH]_e = [PhS^-]_0 \qquad (3.25)$$

$$[HCN]_e = [CN^-]_0 - ([NHBu^{n+}_3]_0 - [PhS^-]_0) \qquad (3.28)$$

$$[CN^-]_e = [CN^-]_0 - [HCN]_e \qquad (3.29)$$

Under these conditions the analysis of kinetics data is presented in Table (3.9) and is shown in Figure (3.17). The rate law is that shown in Equation (3.30).

$$\text{Rate} = 7.1 \times 10^4 [CN^-]_e [Fe_4S_4Cl_4^{2-}] \qquad (3.30)$$

And the kinetic parameters are: (k_0^{HCN} = 500 ± 20 dm^3 mol^{-1} s^{-1} and $K^{HCN} \leq 33$ dm^3 mol^{-1}).

Table (3.9): Analysis of kinetics data for the reaction of $[Fe_4S_4Cl_4]^{2-}$ with PhS^- in presence of $NHBu^n{}_3^+$ and CN^-, when $[NHBu^n{}_3^+]_e < [CN^-]$.

$[HCN]_e$ (mmol dm^{-3})	**$[CN^-]_e$ (mmol dm^{-3})**	**k_{obs} s^{-1}**
1.25	0.5	34.4
1.25	0.75	47.3
1.25	1.0	61.7
2.5	0.5	43.0
2.5	1.0	61.0
2.5	1.25	93.7
2.5	1.5	97.5
2.5	1.75	128.5
2.5	2.0	159.8
5.0	0.5	35.0
5.0	0.75	50.1
5.0	1.0	70.4
5.0	1.25	83.3
5.0	1.5	118.4
5.0	1.75	138.4
5.0	2.0	145.0

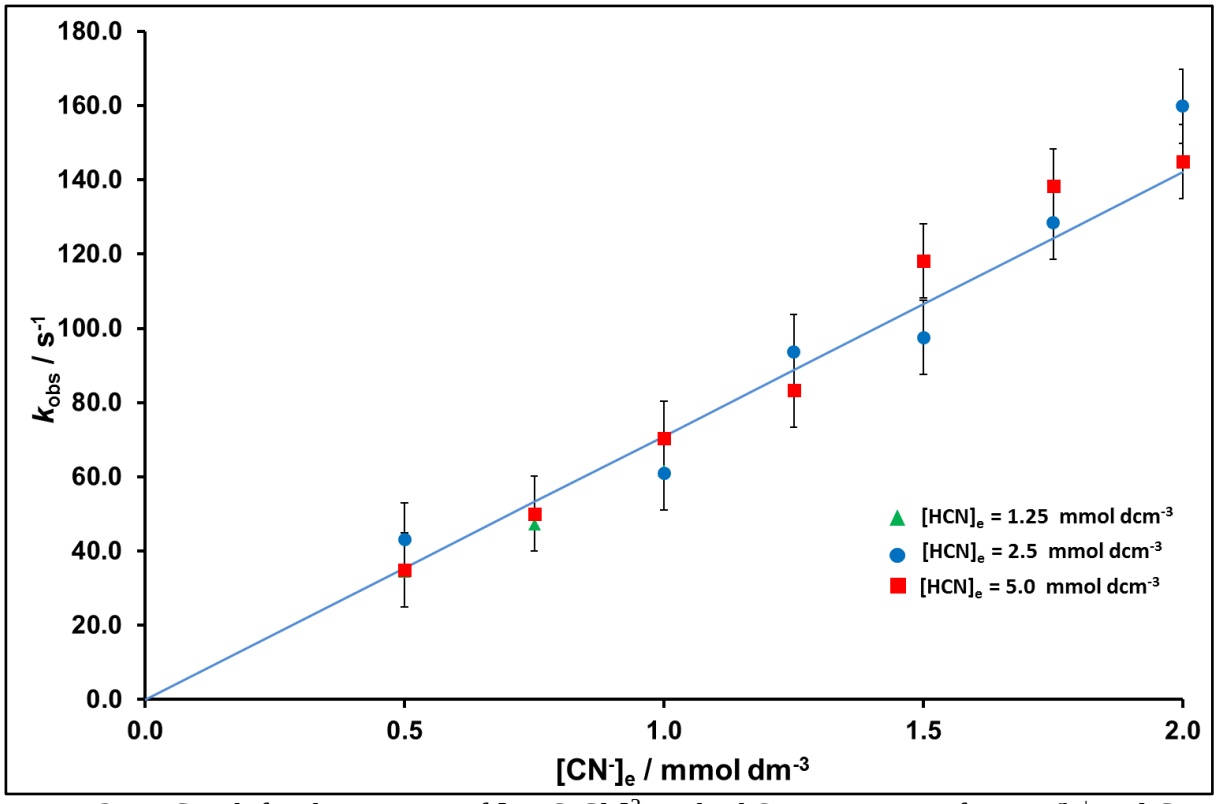

Figure 3.17. Graph for the reaction of $[Fe_4S_4Cl_4]^{2-}$ with PhS^- in presence of $NHBu^n{}_3^+$ and CN^-, line drawn is that defined by Equation (3.30).

Analysis of the kinetics of the reaction between $NHBu^n{}_3^+$ and $[Fe_4S_4Cl_4]^{2-}$ in the presence of CN^- is complicated because $NHBu^n{}_3^+$ protonates this substrate. Consequently, it is only possible to study the reactions in solutions containing mixtures of $NHBu^n{}_3^+$ and HCN or mixtures of HCN and CN^-. The kinetics for the reaction of $[Fe_4S_4Cl_4]^{2-}$ with HCN in the presence of $NHBu^n{}_3^+$, Equation (3.27), are identical to those observed for the reaction of $[Fe_4S_4Cl_4]^{2-}$ with only PhS^- in the presence of $NHBu^n{}_3^+$, indicating that HCN neither protonates nor binds to the cluster. A limit for the value of $K^{HCN} \leq 33$ dm^3 mol^{-1} can be estimated, since there is no evidence that the rate is perturbed by HCN even at the highest concentration of HCN employed ($[HCN]_{max} = 3$ mmol dm^{-3}). However, our studies cannot rule out the possibility that HCN binds slowly and hence binds to $[Fe_4S_3(SH)Cl_4]^-$ (*i.e.* after protonation of the cluster)

The kinetics for the reaction of $[Fe_4S_4Cl_4]^{2-}$ with CN^- in the presence of HCN, Equation (3.30), show that the reaction is independent of the concentration of HCN, consistent with the earlier conclusion[27] that HCN is neither an acid nor a substrate for $[Fe_4S_4Cl_4]^{2-}$. The simplicity of Equation (3.30) makes unambiguous interpretation difficult, but it might suggest that this rate law corresponds to an associative substitution mechanism, in which CN^- displaces the chloro-ligand in $[Fe_4S_4Cl_4]^{2-}$ as shown in Figure (3.18), with $K^{CN}k = 7.1 \pm 0.5 \times 10^4$ dm^3 mol^{-}1 s^{-1}. A

similar associative substitution mechanism has been proposed for the reaction of PhS^- with $[Fe_4S_4Cl_4]^{2-}$ [38].

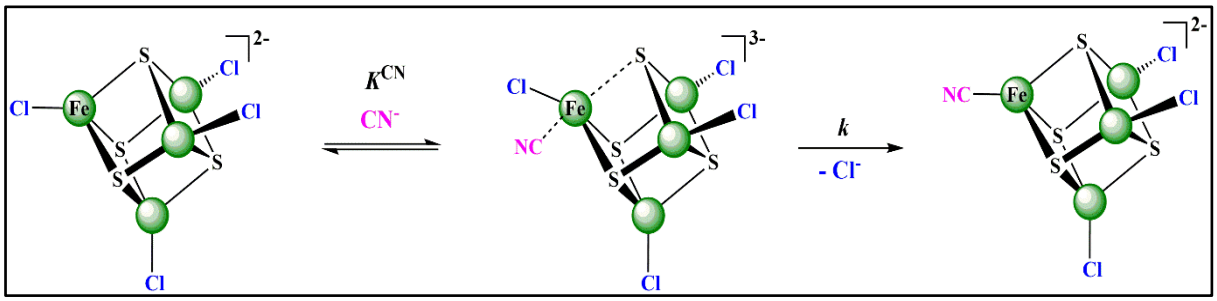

Figure 3.18. Proposed mechanism for the substitution reaction of the chloro-ligands in $[Fe_4S_4Cl_4]^{2-}$ by CN^-.

3.5.2 Protonation of $[Fe_4S_4Cl_4(L)]^{n-}$.

The most notable feature of the data presented in Table (3.5) is that, in all cases, $[Fe_4S_4Cl_4(L)]^{n-}$ protonates faster than $[Fe_4S_4Cl_4]^{2-}$. Thus, the increase in the rate of proton transfer does not depend on the overall charge of $[Fe_4S_4Cl_4(L)]^{n-}$; for n = 2 (binding neutral L), it can see a range for k_0^L/k_0 (i.e. L =$PhNHNH_2$, $k_0^{PhNHNH2}/k_0$ = 1.9; L = $MeNHNH_2$, $k_0^{MeNHNH2}/k_0$ = 53.9), and for n =3 (binding anionic L) k_0^L/k_0 is essentially constant, k_0^L/k_0 =22.1–24.5. Interestingly, for all substrates which are N-donor ligands {$RNHNH_2$ (R = Me or Ph), Me_2NNH_2, NCS^-, N_3^- and pyridine} the values of K^L and k_0^L vary only slightly (K^L = 150–250 $dm^3\ mol^{-1}$ and k_0^L = 0.2 × 10^4 –2.9 × 10^4 $dm^3\ mol^{-1}\ s^{-1}$). This observation suggests that: (i) the binding affinity of L and the modulation of k_0^L is principally defined by the donor atom and (ii) that NCS^-, coordinates using the N atom.

In the light of the recently proposed mechanism for acid-catalyzed substitution of cubanoid Fe–S-based clusters, Figures (3.1) and (3.11), it might have been anticipated that binding L to $[Fe_4S_4Cl_4]^{2-}$ would facilitate subsequent proton transfer because the intermediate containing a 3-coordinate Fe site would be replaced by an intermediate containing a (presumably more stable) 4-coordinate Fe. The data in Table (3.5) certainly shows that the rate of proton transfer to $[Fe_4S_4Cl_4(L)]^{n-}$ is faster than to $[Fe_4S_4Cl_4]^{2-}$ but the increase in rate (k_0^L/k_0) is rather modest, suggesting that (in the absence of L) either formation of the 3-coordinate Fe site is not energetically very demanding or that a 'naked' 3-coordinate Fe site is never formed because the Fe–(μ_3-SH) bond only elongates but never breaks, or the incipient 3-coordinate Fe site binds a solvent MeCN molecule prior to or during protonation, as shown in Figure (3.19). In the latter

case, k_0^L/k_0 represents the difference in stabilities of the transition states for protonation in which the unique 'dissociated' Fe is 4-coordinate, bound to either a substrate or a MeCN.

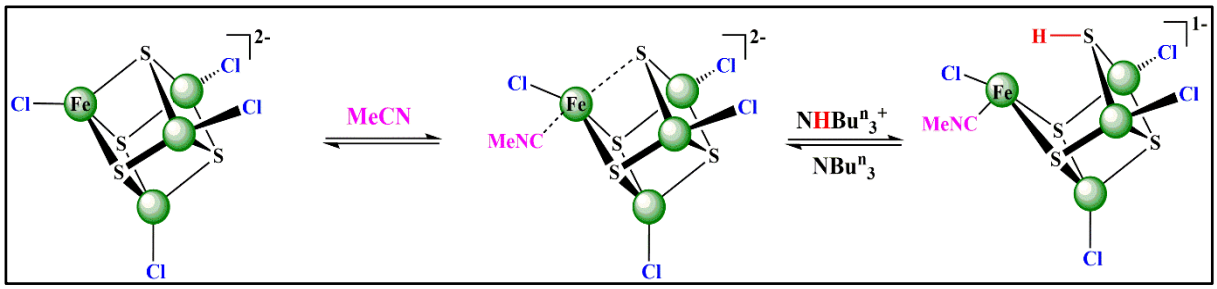

Figure 3.19. Possible involvement of solvent (MeCN) binding to $[Fe_4S_4Cl_4]^{2-}$ prior to protonation.

The data in Table (3.5) indicate that k_0^L/k_0 varies with the bonding characteristics of L. The ligand electrochemical (E_L) parameters (shown in Table (3.10) for selected substrates) is a quantitative measure of whether a ligand is a σ-donor/π-donor (negative E_L) or a σ-donor/π-acceptor (positive E_L)[45]. E_L parameter plays a significant role to predict the metal complexes' redox potentials, which are fundamentally dependent upon where redox process occurs (either on metal centre or on the ligand). Pickett and Pletcher introduced E_L for the general complexes type $[M(CO)_{6-n}L_n]^{y+}$ as shown in Equation (3.31)[46, 47]:

$$E(\text{ox}) = A + \text{n}[\partial E^{\circ}/\partial \text{n}]_L + Cy \qquad (3.31)$$

Where E(ox) is the metal oxidation potential, $\partial E^{\circ}/\partial$n is the change in potential upon replacement of *n*-CO by *n*-ligands, and *A* and *C* are constants.

Inspection of Table (3.10) shows that as the substrate becomes a stronger σ-donor/π-acceptor, the values of k_0^L/k_0 increase. A similar trend is evident when comparing the effect of the hydrazines. Although the E_L values for the hydrazines are not known, it is to be noted that as the pK_a of the hydrazine (see Table 3.1) increases so does the corresponding values of k_0^L/k_0 and this ratio will rise by increasing of the rate of protonation for $[Fe_4S_4Cl_4(L)]^{n-}$ by $NHBu^n{}_3^+$, see Table (3.5).

Table (3.10): The relationship between the values of k_0^L/k_0 and the ligand electrochemical (E_L) parameters for selected substrates.

Substrate = L	E_L	k_0^L/k_0
Cl^-	-0.24	≥ 1.6
N_3^-	-0.30	24.5
NCS^-	-0.06	22.1
Bu^tNC	+0.45	≥ 72
pyridine	+0.25	4.5

Interestingly, it is evident that binding good σ-donor/π-acceptors (Bu^tNC) also results in a large k_0^{BuNC}/k_0. This behaviour is not consistent with k_0^{BuNC}/k_0 reflecting the electron-donating capability of the bound Bu^tNC. It is difficult to explain why a good π-acceptor ligand (like Bu^tNC) would facilitate the rate of proton transfer to the cluster if protonation just involves simple addition of a proton to a μ_3-S with the cluster maintaining its structural integrity. However, this observation is consistent with the proposal that protonation of a μ_3-S is coupled to Fe–(μ_3-SH) bond elongation/cleavage. Binding Bu^tNC to a Fe site pulls π-electron density from the Fe, presumably affecting the Fe–S bond strength and hence the activation energy for proton transfer. Previous work has also shown that other electron-withdrawing ligands facilitate the rate of proton transfer to $[Fe_4S_4Cl_4]^{2-}$ [48]. In the reactions of $[Fe_4S_4Cl_4]^{2-}$ with $4\text{-}RC_6H_4S^-$ (R = CF_3, Cl, H, Me or MeO) in the presence of $pyrrH^+$, the thiolate binds to the cluster prior to protonation by $pyrrH^+$. Binding R = CF_3 results in faster protonation (k^{CF3} = 26.4 × 10^6 dm^3 mol^{-1} s^{-1}) than binding R = MeO (k^{MeO} = 0.47 × 10^6 dm^3 mol^{-1} s^{-1}).

3.5.3 Binding L to $[Fe_4S_3(SH)Cl_4]^-$.

Measuring the effect that protonation has on the rates of subsequent binding of L to $[Fe_4S_4Cl_4]^{2-}$ complements the studies presented herein (on the effect that bound substrates have on the rates of protonation). Earlier studies showed that protonation of $[Fe_4S_4Cl_4]^{2-}$ increases the rate of binding of Bu^{t}NC, but the effect is small (k_H^{BuNC}/k^{BuNC} = 3.8); for binding of Bu^{t}NC to $[Fe_4S_4Cl_4]^{2-}$ k^{BuNC} = 2.1 × 10^3 dm^3 mol^{-1} s^{-1} and binding to $[Fe_4S_3(SH)Cl_4]^{1-}$, k_H^{BuNC} = 8.0 × 10^3 dm^3 mol^{-1} s^{-1} [49, 50]. If protonation of a μ_3-S is coupled to Fe–(μ_3-SH) bond cleavage then it might be assumed that initial protonation of a μ_3-S would facilitate the binding of L because the 3-coordinate Fe site is primed to bind a substrate {Figure (3.1)}. The small effect that protonation has on the rate of binding of Bu^{t}NC does not support this suggestion. However, the small effect observed may be because (as discussed above), in a coordinating solvent such as MeCN, a solvent molecule can bind to the incipient 3-coordinate Fe site prior to protonation Figure (3.19). Consequently, the effect measured in these experiments may not be comparing formation of a 3-coordinate and 4-coordinate Fe site. It is worth emphasising that whilst our studies show that protonation of the cluster has only a minor effect on the rate of substrate binding, our experiments do not address whether or not protonation increases the binding affinity of the substrate.

3.5.4 Earlier studies on substrate binding.

Finally, in this chapter, the results from some earlier studies on binding substrates to $[Fe_4S_4Cl_4]^{2-}$ will be considered and compared with those presented in this chapter. Previous studies have investigated binding L = I$^-$, Br$^-$, PhS$^-$, EtS$^-$ or Bu^{t}NC to $[Fe_4S_4Cl_4]^{2-}$ and the effects this has on the rates of protonation by pyrrH$^+$ [44]. It was observed that some substrates increase the rates of proton transfer (L = PhS$^-$ or Bu^{t}NC), whilst others inhibit the rate of proton transfer (L = I$^-$, Br$^-$ or EtS$^-$). This is different to the behaviour reported in this chapter for the reactions with NHBu$^n{}_3^+$, see Figures (3.14) and (3.15). PyrrH$^+$ is a weaker acid (pK_a = 21.5 in MeCN)[40] than NHBu$^n{}_3^+$ (pK_a = 18.1 in MeCN)[42], and so proton transfer from pyrrH$^+$ to $[Fe_4S_4Cl_4]^{2-}$ is thermodynamically less favourable than the transfer from NHBu$^n{}_3^+$. Consequently, the effects that bound L has on the rates of subsequent proton transfer by pyrrH$^+$ may be due (at least in part) to the bound L modulating the pK_a of the cluster. For the thermodynamically-unfavourable proton transfer reactions with pyrrH$^+$, modulating the pK_a of the cluster would affect the rate because of the ΔpK_a value (p$K_a^{cluster}$ - pK_a^{pyrrH} = -2.8).

In general, the relationship between the rate constant of protonation (k_0) and equilibrium constant (K_0) for the reaction shown in Equation (3.32) is introduced by the Brönsted Equation[51], as shown in Equation (3.33).

$$[Fe_4S_4Cl_4]^{2-} + pyrrH^+ \underset{}{\overset{K_0}{\rightleftharpoons}} [Fe_4S_3(SH)Cl_4]^- + pyrr \quad (3.32)$$

$$k_0 = G_A K_0^{\alpha} \quad (3.33)$$

Where G_A and α are Brönsted constant for the series of similar acids, with $\alpha \geq 1$.

In studies with the stronger acid, $NHBu^n{}_3^+$, where proton transfer must be thermodynamically more favourable, modulating the pK_a of the cluster by binding L is not reflected in the rate of the subsequent proton transfer. Rather, sterics may be a more important factor in reactions with $NHBu^n{}_3^+$.

Earlier studies showed that the rate of acid-catalyzed substitution of the terminal EtS ligands in $[Fe_6S_9(SEt)_2]^{4-}$ was inhibited when L = Cl^-, CN^-, N_3^- or Bu^tNC bind to the cluster. These studies were performed with $[NHEt_3^+]/[NEt_3] = 7.0$ [31]. Under these conditions all the cluster in solution is protonated and the rate law for acid-catalyzed substitution is that shown in Equation (3.31) (k = rate constant for dissociation of EtS^- from $[Fe_6S_8(SH)(SEt)_2]^{3-}$ and k^L = rate constant for dissociation of EtS^- from $[Fe_6S_8(SH)(SEt)_2(L)]^{n-}$). In all cases, binding L to $[Fe_6S_8(SH)(SEt)_2]^{3-}$ (K^L) inhibits the rate of substitution of the protonated cluster (k^L).

$$\text{Rate} = \frac{(k + k^L K^L[L])[Fe_6S_8(SH)(SEt)_2^{3-}]}{1 + K^L[L]} \quad (3.31)$$

The binding of L = Cl^-, Br^-, CO or N_2O to $[Fe_4S_4(SEt)_4]^{2-}$ has also been detected by the effect that it has on the rate of acid-catalyzed substitution of the terminal EtS^- ligands[19]. These experiments were performed using $[NHEt_3^+]_e/[NEt_3]_e$ = 2.0 and, under these conditions, a mixture of $[Fe_4S_4(SEt)_4]^{2-}$ and $[Fe_4S_3(SH)(SEt)_4]^{1-}$ are present in solution. The rate law for the reaction under these conditions is that shown in Equation (3.32). The binding of L to $[Fe_4S_4(SEt)_4]^{2-}$ results in a decrease in the rate of the acid-catalyzed substitution.

$$\text{Rate} = \frac{(kK_0 + k^L K_0^L K_L[L])[Fe_4S_4(SEt)_4^{2-}]\,[NHEt_3^+]_e/[NEt_3]_e}{1 + K^L[L]} \quad (3.32)$$

This decrease in rate indicates that $[Fe_4S_4(SEt)_4(L)]^{n-}$ undergoes acid-catalyzed substitution reactions slower than $[Fe_4S_4(SEt)_4]^{2-}$, either because the rate of substitution (k^L) and/ or the protonation constant (K_0^L) is smaller. However, because of the simplicity of the kinetics, it is not possible to establish which elementary step is affected.

The results presented in this chapter on the reactions of $[Fe_4S_4Cl_4]^{2-}$ with $NHBu^n_3^+$ in the presence of L, together with the results from the studies with $[Fe_6S_8(SH)(SEt)_2]^{3-}$ suggest that, in general, binding L increases the rate of protonation but inhibits the rate of substitution. Thus, it can be concluded, that in studies with $[Fe_4S_4(SEt)_4]^{2-}$, the observed inhibition is because the rate of protonation is increased but the rate of substitution is inhibited, and the effect on the substitution step dominates.

3.6 Conclusions.

In the acid-catalyzed substitution reactions of $[Fe_4S_4Cl_4]^{2-}$ by PhS^- in the presence of $NHBu^n_3{}^+$ the proton transfer from $NHBu^n_3{}^+$ to the cluster is rate-limiting. In addition, Dance's calculations[24] indicate that protonation of a Mo-(μ_3-S)-Fe results in Fe-(μ_3-SH) bond cleavage, analogous to the synthetic clusters. It has been suggested that the under-coordinated Fe is the N_2 binding site. However, studies on $[Fe_4S_4Cl_4]^{2-}$ indicate that protonation is not particularly advantageous for substrate binding. In this Chapter, we have presented the effect that protonation has on rate of substrate binding and effect substrate binding has on rate of protonation. By studying the kinetics of this reaction in the presence of various substrates {L = Cl^-, N_3^-, NCS^-, CN^-, HCN, Bu^tNC, pyridine, $RNHNH_2$ (R = Me or Ph) and Me_2NNH_2} it has shown that binding L to the cluster increases the rate of protonation of the cluster. That both σ-donor/π-donor and σ-donor/π-acceptor ligands facilitate proton transfer is difficult to explain using a mechanism involving just simple proton transfer to the cluster which remains structurally intact. Rather, the observation seems more consistent with the recent proposal that protonation of a μ_3-S site is coupled to Fe–(μ_3-SH) bond elongation/cleavage, Figure (3.1), where both protonation and Fe–S bond weakening are important[21-24].

It is surprising that the increase in the rate of proton transfer when L binds is rather small, Table (3.5). This observation, perhaps, suggests that in the absence of L, a solvent molecule binds to the incipient 3-coordinate Fe site prior to or during the protonation step, Figure (3.19).

All the kinetic data (and in particular the dependence on the concentration of $NHBu^n_3{}^+$) can be accommodated entirely by the pathways shown in Figure (3.11). Consequently, there is no evidence for protonation of L when bound to the cluster from these kinetic studies. If protonation of the bound L in $[Fe_4S_4Cl_4(L)]^{n-}$ does occur it must be slower than the rate-limiting steps associated with the pathways in Figure (3.11).

Finally, the studies reported in this chapter show that initial binding of L to $[Fe_4S_4Cl_4]^{2-}$ only increases the rate of subsequent proton transfer by a modest amount, and earlier studies showed that initial protonation of $[Fe_4S_4Cl_4]^{2-}$ only slightly increases the rate of subsequent L binding. However, we have no information about the effect that protonation has on the binding affinity of L. Future studies should explore if protonation of the cluster (either before or after L binding) affects the substrates' binding affinities.

3.7 References.

1. R. H. Holm, P. Kennepohl and E. I. Solomon, *Chem. Rev.*, 1996, **96**, 2239-2314.

2. H. Matsubara and K. Saeki, *Adv. Inorg. Chem.*, 1992, **38**, 223-280.

3. R. Cammack, *Adv. Inorg. Chem.*, 1992, **38**, 281-322.

4. B. K. Burgess and D. J. Lowe, *Chem. Rev.*, 1996, **96**, 2983-3011.

5. T. Spatzal, M. Aksoyoglu, L. M. Zhang, S. L. A. Andrade, E. Schleicher, S. Weber, D. C. Rees and O. Einsle, *Science*, 2011, **334**, 940-940.

6. Y. Hozumi, Y. Imasaka, K. Tanaka and T. Tanaka, *Chem. Lett.* , 1983, 897-900.

7. R. S. McMiUan, J. Renaud, J. G. Reynolds and and R. H. HoIm, *J. Inorg. Biochem.*, 1979, **11**, 213-227.

8. K. L. C. Gronberg, R. A. Henderson and K. E. Oglieve, *J. Chem. Soc., Dalton Trans.*, 1998, 3093-3104.

9. S. M. Malinak, K. D. Demadis and D. Coucouvanis, *J. Am. Chem. Soc.*, 1995, **117**, 3126-3133.

10. K. D. Demadis, S. M. Malinak and and D. Coucouvanis, *Inorg. Chem.*, 1996, **35**, 4038-4046.

11. S. M. Malinak, A. M. Simeonov, P. E. Mosier, C. E. McKenna and D. Coucouvanis, *J. Am. Chem. Soc.*, 1997, **119**, 1662-1667.

12. R. E. Palermo, R. Singh, J. K. Bashkin and R. H. Holm, *J. Am. Chem. Soc.*, 1984, **106**, 2600-2612.

13. S. Ciurli, P. K. Ross, M. J. Scott, Shi-Bao Yu and R. H. Holm, *J. Am. Chem. Soc.* , 1992, **114**, 5415-5423.

14. T. A. Scott and and H. C. Zhou, *Angew Chem. Int. Ed. Engl.*, 2004, **43**, 5628-5631.

15. J. A. Weigel and R. H. Holm, *J. Am. Chem. Soc.* , 1991, **113**, 4184-4191.

16. R. A. Henderson, *BioInorg. React. Mech.* , 2012, **8**, 1-37.

17. R. A. Henderson, in *Bioinspired Catalysis*, eds. Wolfgang Weigand and Philippe Schollhammer, Wiley-VCH, Weinheim, Germany, 2015, ch. 11, pp. 289-321.

18. R. A. Henderson, *Chem. Rev.*, 2005, **105**, 2365-2437.

19. R. A. Henderson and K. E. Oglieve, *J. Chem. Soc., Dalton Trans.*, 1993, 1473-1476.

20. A. J. Dunford and R. A. Henderson, *J. Coord. Chem.*, 2010, **63**, 2507-2516.

21. I. Dance, *Inorg. Chem.*, 2013, **52**, 13068-13077.

22. A. Alwaaly, I. Dance and R. A. Henderson, *J. Chem. Soc., Chem. Commun.*, 2014, **50**, 4799-4802.

23. I. Dance and R. A. Henderson, *J. Chem. Soc., Dalton Trans.*, 2014, **43**, 16213-16226.

24. I. Dance, *J. Chem. Soc., Dalton Trans.*, 2015, **44**, 4707-4717.

25. K. Tanaka, Y. Hozumi and and T. Tanaka, *Chem. Lett.*,, 1982, 1203-1206.

26. K. L. C. Grönberg, R. A. Henderson and and K. E. Oglieve, *J. Chem. Soc., Dalton Trans.*, 1998, 3093-3104.

27. R. A. Henderson and K. E. Oglieve, *J. Chem. Soc., Dalton Trans.*, 1993, 1467-1472.

28. C. Goh, J. A. Weigel and R. H. Holm, *Inorg. Chem.*, 1994, **33**, 4861-4868.

29. E. L. Bominaar, S. A. Borshch and J. J. Girerd, *J. Am. Chem. Soc.*, 1994, **116**, 5362-5372.

30. Q. T. Liu, L. G. Huang, H. Q. Liu, X. J. Lei, D. X. Wu, B. S. Kang and and J. X. Lu, *Inorg. Chem.*,, 1990, **29**, 4131-4137.

31. A. J. Dunford and R. A. Henderson, *J. Coord. Chem.*, 2010, **63**, 2507-2516.

32. K. Bates, L. Johnson and and R. A. Henderson, *Inorg. Chem.*,, 2006, **45**, 9423-9433.

33. K. Bates, M. Wouldhave and R. A. Henderson, *J. Chem. Soc., Dalton Trans.*, 2008, 6527-6529.

34. K. Bates, B. Garrett and R. A. Henderson, *Inorganic Chemistry*, 2007, **46**, 11145-11155.

35. K. Bates and R. A. Henderson, *Inorg. Chem.*, 2008, **47**, 5850-5858.

36. Peter D. Ford, Leslie F. Larkworthy, David C. Povey and Andrew J. Roberts, *Polyhedron*, 1983, **2**, 1317-1322.

37. T. M. M. Al-Rammahi and R. A. Henderson, *J. Chem. Soc., Dalton Trans.*, 2016, **45**, 307-314.

38. R. A. Henderson and K. E. Oglieve, *J. Chem. Soc., Chem. Commun.*, 1994, 377-379.

39. B. G. Cox, *Acids and Bases Solvent Effects on Acid-Base Strength*, Oxford University Press, UK, 2013.

40. R. A. Henderson and K. E. Oglieve, *J. Chem. Soc., Dalton Trans.*, 1999, 3927-3934.

41. J. F. Coetzee, in *Progress in Physical Organic Chemistry*, eds. J. Andrew Streitwieser and W. T. Robert, John Wiley and Sons, Inc., USA, 1976, vol. 4, pp. 45-92.

42. K. Izutsu, *Acid-Base Dissociation Constants in Dipolar Aprotic Solvents*, Blackwell Scientific, Oxford, UK, 1990.

43. R. A. Henderson and K. E. Oglieve, *J. Chem. Soc., Dalton Trans.*, 1999, 3927-3934.

44. K. Bates and R. A. Henderson, *Inorg. Chem.*, 2008, **47**, 5850-5858.

45. A. B. P. Lever, *Inorg. Chem.*, 1990, **29**, 1271-1285.

46. C. J. Pickett and D. J. Pletcher, *Organomet. Chem.*, 1975, **102**, 327-333.

47. J. Chatt, C. T. Kan, G. J. Leigh, C. J. Pickett and D. R. Stanley, *J. Chem. Soc., Dalton Trans.*, 1980, 2032-2038.

48. A. J. Dunford and R. A. Henderson, *J. Chem. Soc., Chem. Commun.*, 2002, 360-361.

49. A. J. Dunford and R. A. Henderson, *Inorg. Chem.*, 2002, **41**, 5487-5494.

50. A. J. Dunford and R. A. Henderson, *J. Chem. Soc., Dalton Trans.*, 2002, 2837-2842.

51. R. P. Bell, in *The Proton in Chemistry*, Chapman Hall, London, 2nd edn., 1973, p. 195.

Chapter 4: X-Ray Crystal Structures of $[NHR_3]_2[Fe_4S_4X_4]$ (X = PhS, R = Et or Bu^n; X = Cl, R = Bu^n): Implications for Sites of Protonation in Fe–S Clusters

4.1 Introduction.

The protonation chemistry of Fe–S-based clusters is crucial in understanding the action of metalloenzymes which involve Fe–S-based clusters as (part) of the active site (*e.g.* nitrogenases, hydrogenases, CODH and certain hydrolases typified by aconitase), because they operate in a protic medium and, in some cases, use protons as a substrate[1-7]. Because of the complexity of the biological systems, studies on synthetic clusters play a crucial role in defining the protonation chemistry of Fe–S-based clusters.

The protonation of Fe–S-based clusters was first implicated in the earliest study on the substitution of the terminal ligands in the cubanoid $[Fe_4S_4(SR)_4]^{2-}$ (R = Et or Bu^t) by ArSH (Ar = *p*-$C_6H_4NH_2$, *p*-tolyl, *o*-$C_6H_4NO_2$ or *p*-$C_6H_4NO_2$), Equation (4.1). Kinetic studies indicated that the acid strength of the arylthiol affected the rate of the reaction, suggesting that protonation of the cluster occurred during the substitution process and the reaction rates were second order, first-order dependence on both concentrations of cluster and thiol where *k* is the rate constant of protonation step (*k* = *p*-$C_6H_4NH_2$ = 2.1 ±0.2; *p*-tolyl = 4.5 ±0.6; *o*-$C_6H_4NO_2$ = 110 ±8.0 and *p*-$C_6H_4NO_2$ = 3600 ±200 $dm^3\ mol^{-1}\ s^{-1}$)[8]. In a series of further kinetic studies (using a slightly different system, Figure 4.1), protonation has been shown to be a pervasive reaction of synthetic Fe–S-based clusters[9-11]. In the reactions of (for example) $[Fe_4S_4X_4]^{2-}$ (X = halide, thiolate or phenolate), it has been shown that the mechanism of substitution of the terminal ligands (X) by PhS^-, in the presence of acid, involves initial protonation of the cluster followed by substitution of the protonated cluster. In principle, there are three sites which can be protonated: the terminal ligands, the Fe or the cluster core μ_3–S. The kinetic studies indicate that the protonation which is labilising occurs at a μ_3–S[12].

$$[Fe_4S_4(SR)_4]^{2-} + 4ArSH \longrightarrow [Fe_4S_4(SAr)_4]^{2-} + 4RSH \qquad (4.1)$$

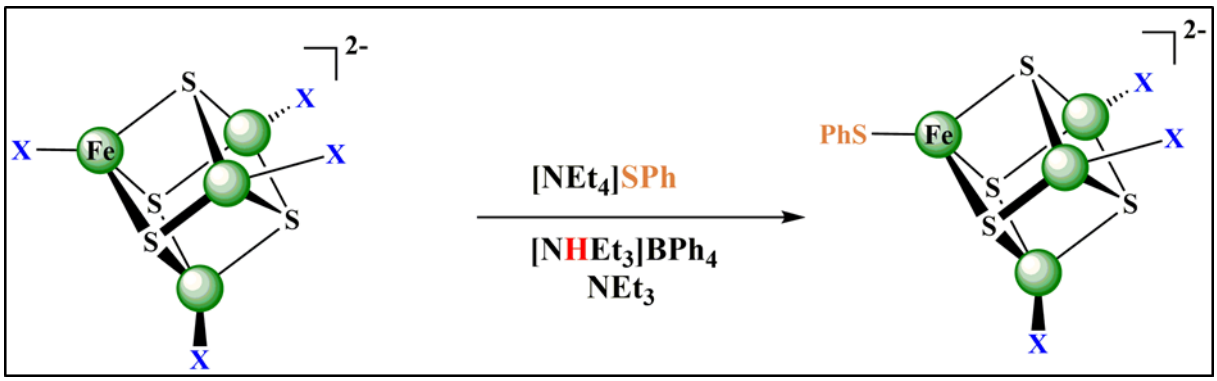

Figure 4.1. Components of the system used to study the kinetics of the acid-catalyzed substitution reactions of Fe–S-based cluster.

The kinetic studies for the substitution reactions of $[Fe_4S_4(SEt)_4]^{2-}$ with PhS^- in presence of $NHEt_3^+$ showed that the reactions are likely undergone to the mechanism shown in Figure (4.2)[13]. In this mechanism, the initial protonation occurs at the thiolate sulfur of terminal ligand, which is more basic than μ_3-S, and it seems that the protonation at this site has no detectable effect on the rate of substitution reaction of cluster. In spite of that protonation of the coordinated terminal thiolate is not labilising the cluster, it is followed by further protonation of the μ_3-S of the cluster core. After that the terminal EtSH dissociates to produce a vacant site and then the nucleophile PhSH attacks on this vacant site to form the substituted cluster.

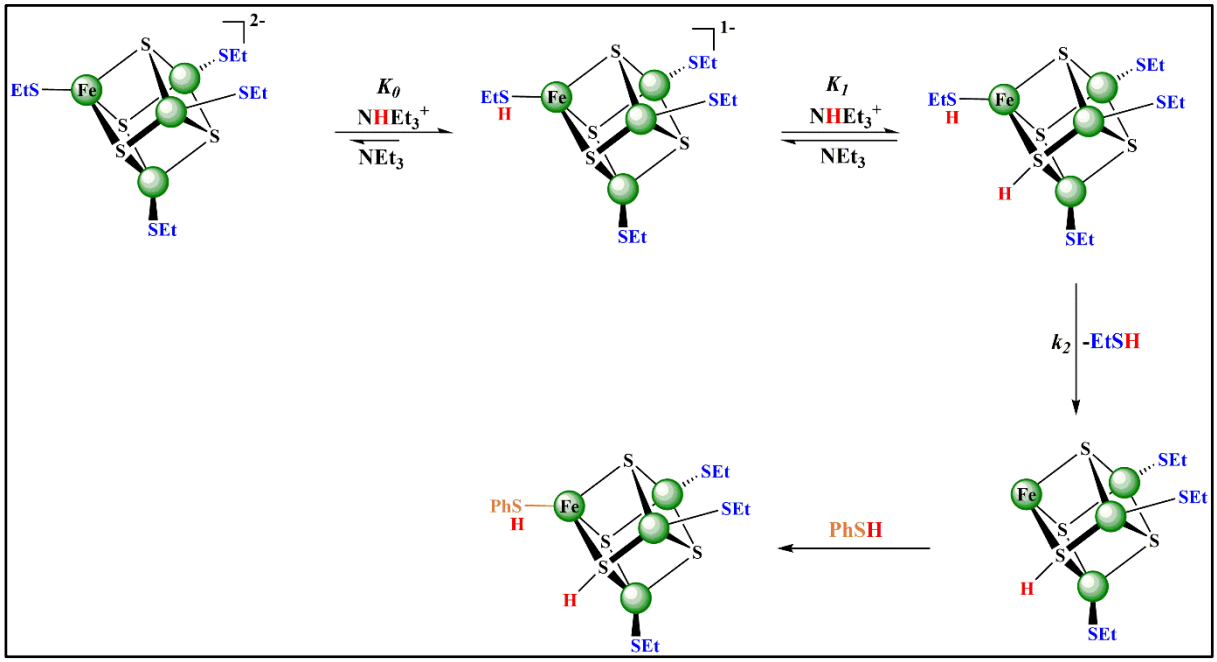

Figure 4.2. Mechanism for the reaction of $[Fe_4S_4(SEt)_4]^{2-}$ with PhSH in the presence of $NHEt_3^+$ and Et_3 in MeCN, showing protonation of the μ-S_3 (detected in the kinetics) and protonation of the thiol (undetected but presumed).

It can be noted that the binding of proton to the coordinated thiolate leads to produce the corresponding thiol in which the S-to-Fe σ-bond is weakened while the Fe-to-S π-backbonding

is increased, as shown in Figure (4.3). The overall impact is that the bond strength of Fe-thiolate is similar to Fe-thiol and thus there is a slight change in lability. Further study showed the same sort of effect reflected in the bond lengths of mononuclear Fe-thioether and Fe-thiolate complexes[14]. Protonation of a bridging sulfur site competes for the π-backbonding to the thiol and hence labilising the thiol to dissociate.

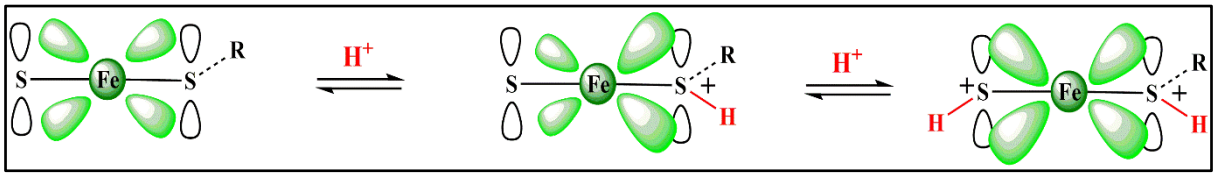

Figure 4.3. Representation of the bonding between Fe, thiolate and bridging sulfur in Fe–S-based clusters, and the effect of protonation at thiolate and then bridging sulfur.

As described in Chapter 2 (***section 2.1.1.***), the extensive kinetic studies indicate that the protonation of Fe–S-based clusters is not simple and is associated with a variety of unusual features including slow proton transfer; absence of isotope effect with deuterated acids; and protonation of the cluster accelerating the rate of substitution, irrespective of the nature of the terminal ligand. It has been suggested that these observations indicate protonation is associated with significant structural changes to the cluster[15-17].

Recent DFT calculations indicate that these structural changes are localised within the cluster to a significant elongation/cleavage of the Fe–(μ_3–SH) bond, Figure (4.4). This cluster disruption produces a 3-coordinate Fe site which appears to be primed for nucleophilic attack in the substitution stage of the reaction[15-17].

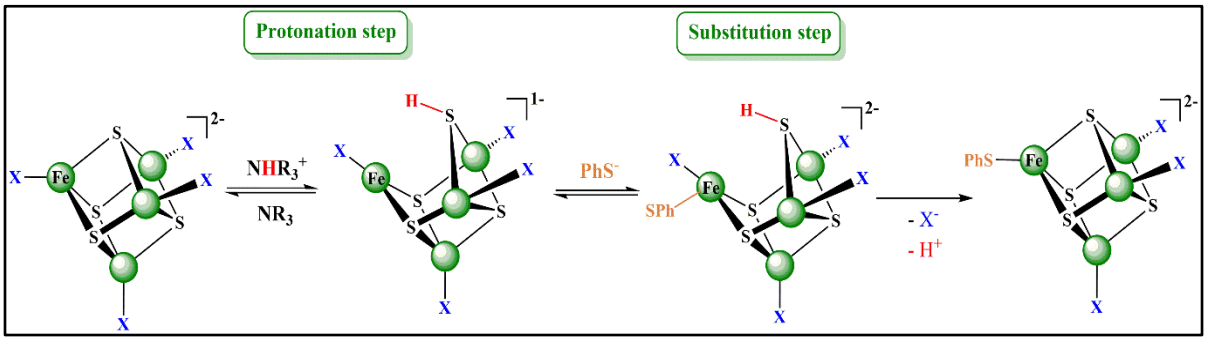

Figure 4.4. Acid-catalyzed substitution mechanism for the reaction of $[Fe_4S_4X_4]^{2-}$ with PhS^- in presence of NHR_3^+.

4.1.1 Limitations of controlling the protonation sites on either the terminal-ligand or the core of Fe-S-based clusters.

The first kinetic study on the reactions of synthetic Fe–S-based was reported more than 40 years ago[8]. In this study, the kinetics of the substitution reactions of the terminal alkyl thiolate in

$[Fe_4S_4(SR)_4]^{2-}$ (R = Et or Bu^t) with various of 4-R′C_6H_4SH (R′= CH_3, NH_2 or NO_2) showed that the substitution reaction of terminal RS^- ligand obeys simple overall second order rate law: first-order dependence on the concentration of $[Fe_4S_4(SR)_4]^{2-}$ cluster and a first-order dependence on the concentration of [4-R′C_6H_4SH] thiol. Moreover, the rate of the reaction was faster with the more electron-withdrawing 4-R′-aryl substituents, which are more acidic thiols. Consequently, it was suggested: (i) that proton transfer from 4-R′C_6H_4SH to the $[Fe_4S_4(SR)_4]^{2-}$ was involved in the substitution reaction, and it seemed reasonable to propose that protonation likely occurred to the coordinated RS^-, as shown in Figure (4.5) and (ii) that the proton-transfer step was the rate-limiting step of the reaction.

However, the major disadvantage of this study is that the 4-R′C_6H_4SH is playing several roles in this reaction: it is the nucleophile, the acid and it becomes the conjugate base after deprotonation. It is important to distinguish these three roles and also be able to independently control the concentrations of the nucleophile, acid and base in the mixture.

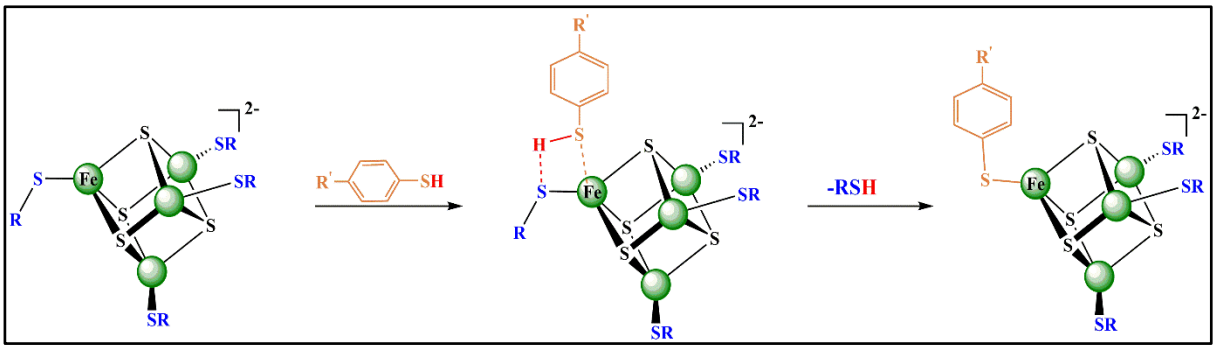

Figure 4.5. Proposed mechanism for the reaction between $[Fe_4S_4(SR)_4]^{2-}$ and 4-R′C_6H_4SH.

An alternative system for studying the substitution reactions of Fe–S-based clusters in presence of acid was developed as shown in Figure (4.1). Using this system, the reaction of any synthetic Fe–S cluster can be studied under comparable conditions. Indeed, it is the comparison of various clusters that allows the general reactivity patterns for the whole family of Fe–S-based clusters to be established[13, 18, 19]. In the system shown in Figure 4.1, the nucleophile is provided as the thiolate salt $[NEt_4][RS]$ (R= alkyl or phenyl) . The acid is provided as $[BPh_4]^-$ salt since this anion will not be involved in reaction which would complicate the kinetic analysis. The kinetic studies showed that the ammonium cations $[NHR_3]^+$ are good acids to catalyse the substitution reactions of synthetic Fe–S-based clusters because they are sufficiently strong acids to be able to protonate the cluster while they are not so strong acids to decompose the cluster. In mixture containing RS^- and NHR_3^+, the equilibrium is rapidly established, and the concentrations of solutions at equilibrium state can be defined as discussed earlier Chapter 2 (***section 2.5.1.***).

Consequently, the concentrations of reagents can be controlled independently and the true kinetic dependence on each determined. Furthermore, it is notable that the RSH is also an acid, but it is a significantly weaker acid (*i.e.* pK_a> 19.3, for PhSH in MeCN)[20] than NHR_3^+, and so $[NHR_3]^+$ always wins out as the acid.

In general, observing the reaction of any cluster with just an acid would be the simplest and most direct method to look at the protonation of cluster. However, the addition of a proton to Fe–S-based clusters is usually associated with negligible spectroscopic changes[11]. Consequently, the kinetic studies to detect the protonation of the clusters were performed by monitoring the effect that proton transfer has on the rate of the substitution reaction of cluster[21]. The substitution reactions of terminal ligands of $[Fe_4S_4X_4]^{2-}$ (X= thiol or chloride) by RS^- (R= alkyl or phenyl) are associated with significant changes in the UV-vis absorption spectrum. Hence, the protonation of Fe-S-based clusters can be detected by the way it affects the lability of the cluster.

For the clusters containing terminal chloro-ligands, the bridging sulfur atoms (μ_3-S) are the most basic sites (p$K_a^{cluster}$ = 18.8)[9-11], so the proton will bind to the core μ_3-S of cluster in the protonation step. However, in the clusters containing terminal thiolate ligands, the thiolate sulfur is more basic (pK_a^{PhS} = 20.8)[20] than any μ_3-S of cluster core. In this situation, the proton will bind to the terminal ligand (and this seems likely) and that will not affect the rate of substitution. It is only upon protonation of the μ_3-S cluster core that the lability of the cluster is significantly affected. This discussion highlights a limitation to the method, which has been used to study the protonation reactions: the kinetic method only effectively detects protonations which affect the lability of the cluster.

Despite the extensive evidence from kinetic studies that synthetic Fe–S-based clusters can be protonated; the isolation and structural characterisation of protonated clusters have been elusive. In part, the problem is a consequence of the observation that reactions with (particularly strong) acids can lead to the decomposition of the clusters. This Chapter will describe the X-ray crystal structures of $[NHR_3]_2[Fe_4S_4X_4]$ (X = PhS, R = Et or Bu^n; X = Cl, R = Bu^n), in which NH…X interactions are evident. The relevance of these structures to understanding the protonation chemistry of Fe–S-based clusters is discussed.

4.2 Experimental and Methodology.

4.2.1 General Experimental.

All manipulations in this work were performed under an atmosphere of dinitrogen using Schlenk or syringe techniques, as appropriate. Solvents were freshly distilled from the appropriate drying agent immediately prior to use: acetonitrile (CaH_2); diethyl ether (Na); and methanol (Mg). The following chemicals were purchased from Sigma-Aldrich and used as received without any further purifications: anhydrous $FeCl_3$, thiophenol, sulfur and NBu^n_3 and $NaBPh_4$. CD_3CN was purchased from Goss Scientific and used as received.

^1H NMR spectroscopy for all synthesised clusters were performed as described in Experimental of Chapter 2 (***section 2.2.3***).

4.2.2 Preparation of Compounds.

4.2.2.1 Preparation of [NHR$_3$]Cl (R= Et and Bu^n).

Both $[NHEt_3]Cl$ and $[NHBu^n_3]Cl$ were prepared using analogous manner which was described in Chapter 2 (***see section 2.3.3.2***.).

4.2.2.2 Preparation of clusters.

The clusters $[NHEt_3]_2[Fe_4S_4(SPh)_4]$, $[NHBu^n_3]_2[Fe_4S_4(SPh)_4]$ and $[NHBu^n_3]_2[Fe_4S_4Cl_4]$ were prepared by methods analogous to those reported in the literature for $[NR'_4]_2[Fe_4S_4X_4]$, but using $[NHR_3]Cl$ (R= Et or Bu^n) rather than $[NR'_4]Cl$ (R′= Me, Et or Bu^n)[22].

(i) Preparation of [NHR$_3$]$_2$[Fe$_4$S$_4$(SPh)$_4$] (R= Et and Bu^n).

Sodium (1.84 g, 80 mmol) was carefully dissolved with stirring in methanol (50 ml). After the solution had been left to cool to room temperature, thiophenol (8.3 ml, 80 mmol) was added to give a clear solution. Anhydrous $FeCl_3$ (3.12 g, 20 mmol) was dissolved in methanol (20 ml) and added slowly to the thiolate solution to give a dark green mixture. After stirring for about 20 min, elemental sulfur (0.64 g, 20 mmol) was added. The mixture was then stirred overnight and became a dark brown–red colour. The mixture was filtered and a solution of $[NHR_3]Cl$ (Et = 2.06 g, Bu^n = 3.32 g, 15 mmol) in methanol (20 ml) was added (without stirring) to the filtrate. The mixture was left for 1 h and then concentrated in *vacuo* to (*ca* 25 ml). A grey precipitate was formed (mixture of cluster and NaCl). The mixture was then filtered and the grey precipitate was dissolved in acetonitrile (80 ml) with stirring. After 1 h, a white precipitate

(NaCl) formed and was removed by filtration through Celite. The black filtrate was reduced to (*ca* 20 ml), and then, diethyl ether (200 ml) was added and the mixture was left in the refrigerator overnight, during which time a black precipitate formed. The black precipitate was removed by filtration, washed with methanol and anhydrous diethyl ether and then dried *in vacuo*. (Average yields for $[NHEt_3]_2[Fe_4S_4(SPh)_4]$ = 65% and for $[NHBu^n_3]_2[Fe_4S_4(SPh)_4]$ = 68%).

The solid was recrystallised by dissolving the crude material in the minimum of warm (50 ºC) MeCN (*ca* 20 ml) and then adding an excess of diethyl ether (*ca* 150 ml). The solution was left to cool slowly at 3 °C and stand *ca* 1 week to give black needle-like crystals.

^{1}H NMR for $[NHEt_3]_2[Fe_4S_4(SPh)_4]$ in CD_3CN: δ 0.99 (triplet, 18H, J_{HH} = 7.24 Hz, *CH*$_3$), δ 3.1 (quartet, 12H, *CH*$_2$), δ 7.3 & 7.5 (singlet, 2H, *NH*), δ 8.23 (*meta*-H), δ 5.94 (*ortho*-H), δ 5.33 (*para*-H) and a weak signal about δ 7.4 for free thiophenol, as shown in Figure (4.6).

^{1}H NMR for $[NHBu^n_3]_2[Fe_4S_4(SPh)_4]$ in CD_3CN: δ 0.91 (triplet, 18H, J_{HH} = 6.9 Hz, *CH*$_3$), δ 1.09-1.12 (multiplet, 12H, *CH*$_2$), δ 1.32-1.34 (multiplet, 12H, *CH*$_2$), δ 1.62-1.91 (multiplet, 12H, *CH*$_2$), δ 7.33 & 7.5 (singlet, 2H, *NH*), δ 8.17 (*meta*-H), δ 5.89 (*ortho*-H) and δ 5.30 (*para*-H), as shown in Figure (4.7).

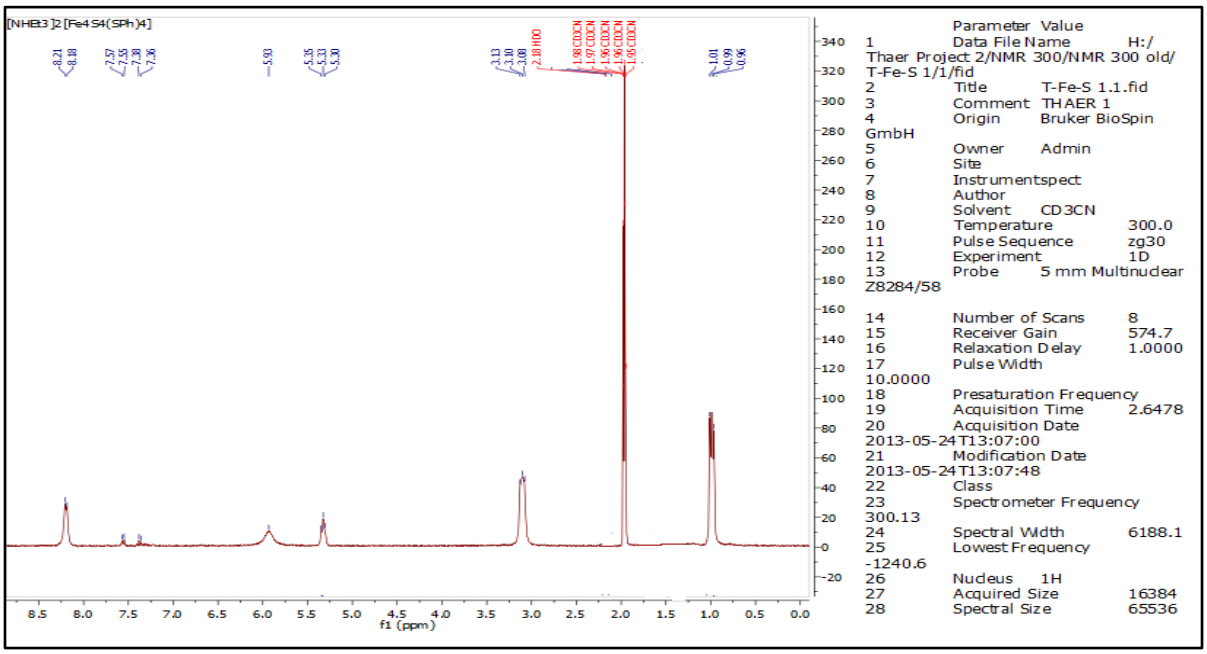

Figure 4.6. ^{1}H NMR spectrum for $[NHEt_3]_2[Fe_4S_4(SPh)_4]$ in CD_3CN.

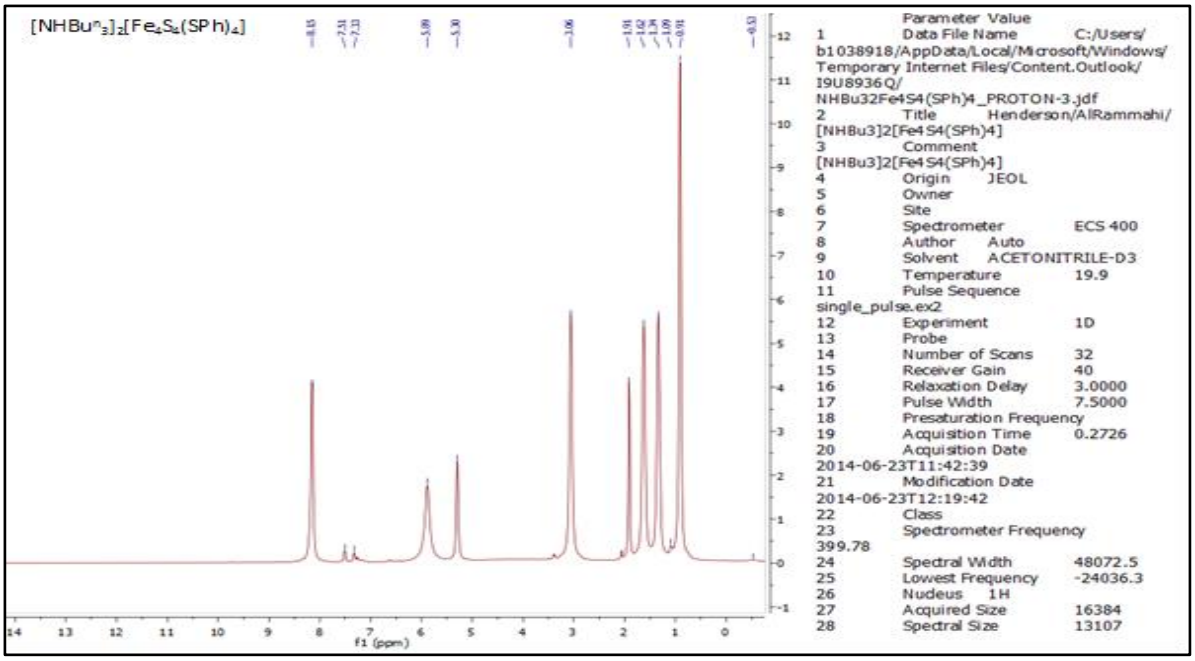

Figure 4.7. ^{1}H NMR spectrum for [NHBu$^n_3$]$_2$[Fe$_4$S$_4$(SPh)$_4$] in CD$_3$CN.

(ii) Preparation of [NHBu$^n_3$]$_2$[Fe$_4$S$_4$Cl$_4$].

Benzoyl chloride (8.4 ml, 60 mmol) was added to a stirred slurry of [NHBu$^n_3$]$_2$[Fe$_4$S$_4$(SPh)$_4$] (3.48 g, 3.0 mmol) in MeCN (25 ml). Any solid gradually dissolved and the solution turned purple-black. The solution was stirred for 1 h, and then, diethyl ether (*ca* 100 ml) was added. The product separated as a dark solid. The solid was removed by filtration, washed with diethyl ether and then dried in *vacuo.*

The crude product was dissolved in the minimum volume of warm (50 ºC) MeCN (15 ml), and then, diethyl ether (*ca* 200 ml) was added. The solution was left to cool at *ca* 3°C temperature and formed black crystals after *ca* 1 week, which were removed by filtration, washed with diethyl ether and then dried *in vacuo*. (Average yield = 59%).

^{1}H NMR for [NHBu$^n_3$]$_2$[Fe$_4$S$_4$Cl$_4$] in CD$_3$CN: δ 0.91 (triplet, 18H, J_{HH} = 7.8 Hz, *CH$_3$*), δ 1.31-1.34 (multiplet, 12H, *CH$_2$*), δ 1.59-1.61 (multiplet, 12H, *CH$_2$*), δ 1.97-2.1 (multiplet, 12H, *CH$_2$*), δ 6.69 (singlet, 2H, *NH*), as shown in Figure (4.8). This spectrum of the product showed that there were no signals associated with the thiolate ligands of [NHBu$^n_3$]$_2$[Fe$_4$S$_4$(SPh)$_4$] indicating complete substitution of thiolate for chloride in the cluster.

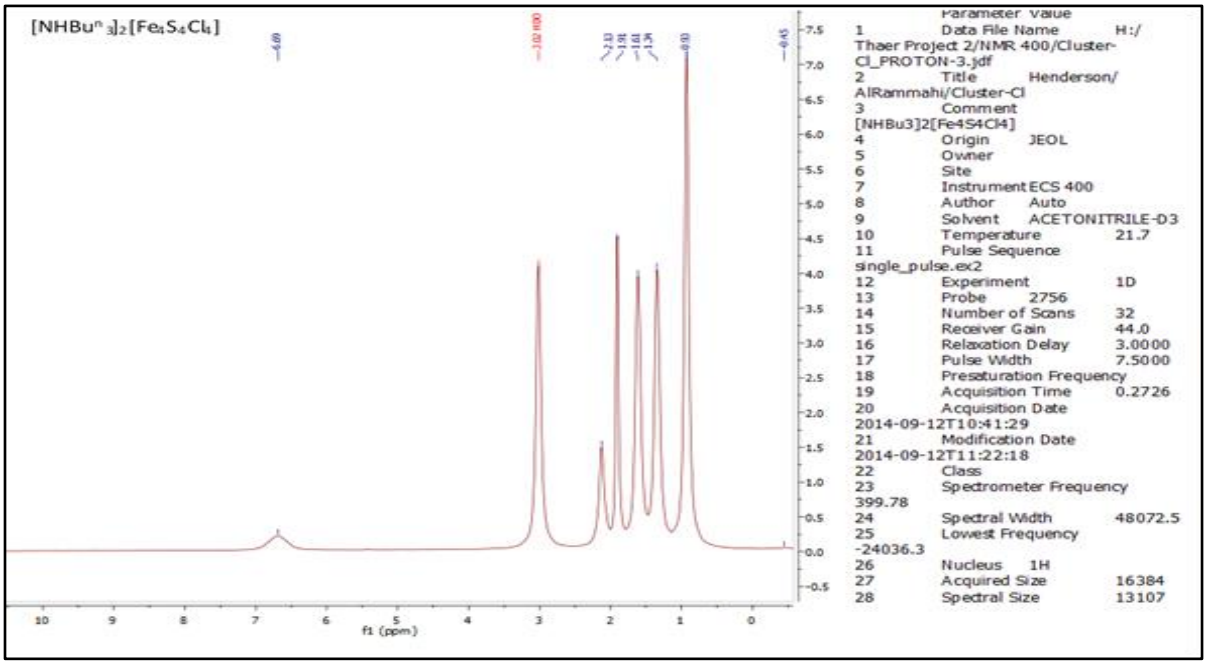

Figure 4.8. ^{1}H NMR spectrum for [NHBu$^n_3$]$_2$[Fe$_4$S$_4$Cl$_4$] in CD$_3$CN, showing disappearance for the signals associated with the PhS$^-$ ligands.

(iii) Preparation of [NHBu$_3^n$][Fe$_4$(SH)S$_3$Cl$_4$(Bu^{t}NC)].

[Bu^{t}NC] (3.0 g, 36.08 mmol) was added to a stirred slurry of [NHBu$^n_3$]$_2$[Fe$_4$S$_4$Cl$_4$] (2.6 g, 3.0 mmol) in MeCN (30 ml). Any solid gradually dissolved and the solution turned purple-black. The solution was stirred for *ca* 2 h, and then, the solvent was reduced to (*ca* 10 ml) followed by adding diethyl ether (*ca* 100 ml). The solution was left overnight to cool at *ca* 3°C temperature and formed dark purple precipitate. The solid was isolated by filtration, washed with diethyl ether and then dried in *vacuo*.

The product was dissolved in the minimum volume of warm (50 ºC) MeCN (15 ml), and then, diethyl ether (*ca* 200 ml) was added. The solution was left to cool at *ca* 3 °C for 2 weeks to produce the crystals, but this effort to get the good crystals had failed. The microcrystals were separated by filtration, washed with diethyl ether and then dried *in vacuo*. (Average yield = 54%).

^{1}H NMR for [NHBu$^n_3$][Fe$_4$(SH)S$_3$Cl$_4$(Bu^{t}NC)] in CD$_3$CN: δ 0.84 (singlet, 9H, *CH$_3$*); δ 0.97 (triplet, 9H, J_{HH} = 7.4 Hz, *CH$_3$*), δ 1.23 (multiplet, 6H, *CH$_2$*), δ 1.38 (multiplet, 6H, *CH$_2$*), δ 2.2 (multiplet, 6H, *CH$_2$*); δ 10.4 (singlet, 2H, *NH*), as shown in Figure (4.9).

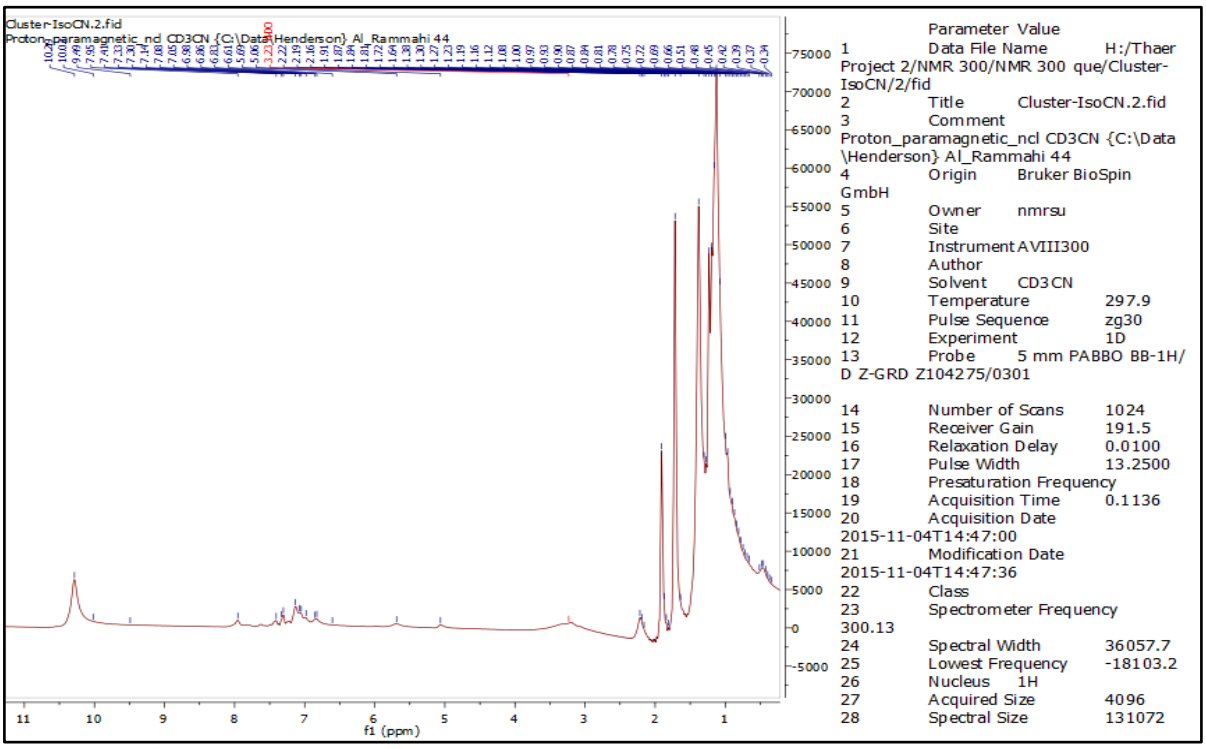

Figure 4.9. ^{1}H NMR spectrum for [NHBu$^n_3$][Fe$_4$(SH)S$_3$Cl$_4$(Bu^{t}NC)], showing disappearance for the signals associated with the PhS$^-$ ligands.

4.3 X-ray crystallography.

Crystal structure data for [NHEt$_3$]$_2$[Fe$_4$S$_4$(SPh)$_4$], [NHBu$^n_3$]$_2$[Fe$_4$S$_4$(SPh)$_4$] and [NHBu$^n_3$]$_2$[Fe$_4$S$_4$Cl$_4$] were collected at 150K on an Xcalibur, Atlas, Gemini ultra-diffractometer equipped with an Oxford Cyrostream Plus open-flow N_2 cooling device using Cu ($\lambda_{CuK\alpha}$ = 1.54184 Å) radiation, except for where X = SPh and R = Bu^n in which case, Mo ($\lambda_{MoK\alpha}$ = 0.71073 Å). Cell refinement, data collection and data reduction were undertaken using CrysAlisPro[23]. Data were corrected for absorption empirically, using spherical harmonics except for where X = Cl and R = Bu^n in which case an analytical absorption correction method was applied using a multifaceted crystal model[24].

Using Olex2[25], all structures were solved by direct methods using XT[26] and refined on F^2 values for all unique data using XL[27]. All non-hydrogen atoms were refined anisotropically. The positions of hydrogen atoms attached to fully occupied heteroatoms were picked from peaks in the Fourier difference map. All other hydrogen atoms were positioned with idealised geometry using the riding model with U_{iso}(H) set at 1.2 times U_{eq} for the parent atom.

Figures (4.9), (4.10) and (4.11) show the X-ray structure for $[NHEt_3]_2[Fe_4S_4(SPh)_4]$, $[NHBu^n_3]_2[Fe_4S_4(SPh)_4]$ and $[NHBu^n_3]_2[Fe_4S_4Cl_4]$ respectively.

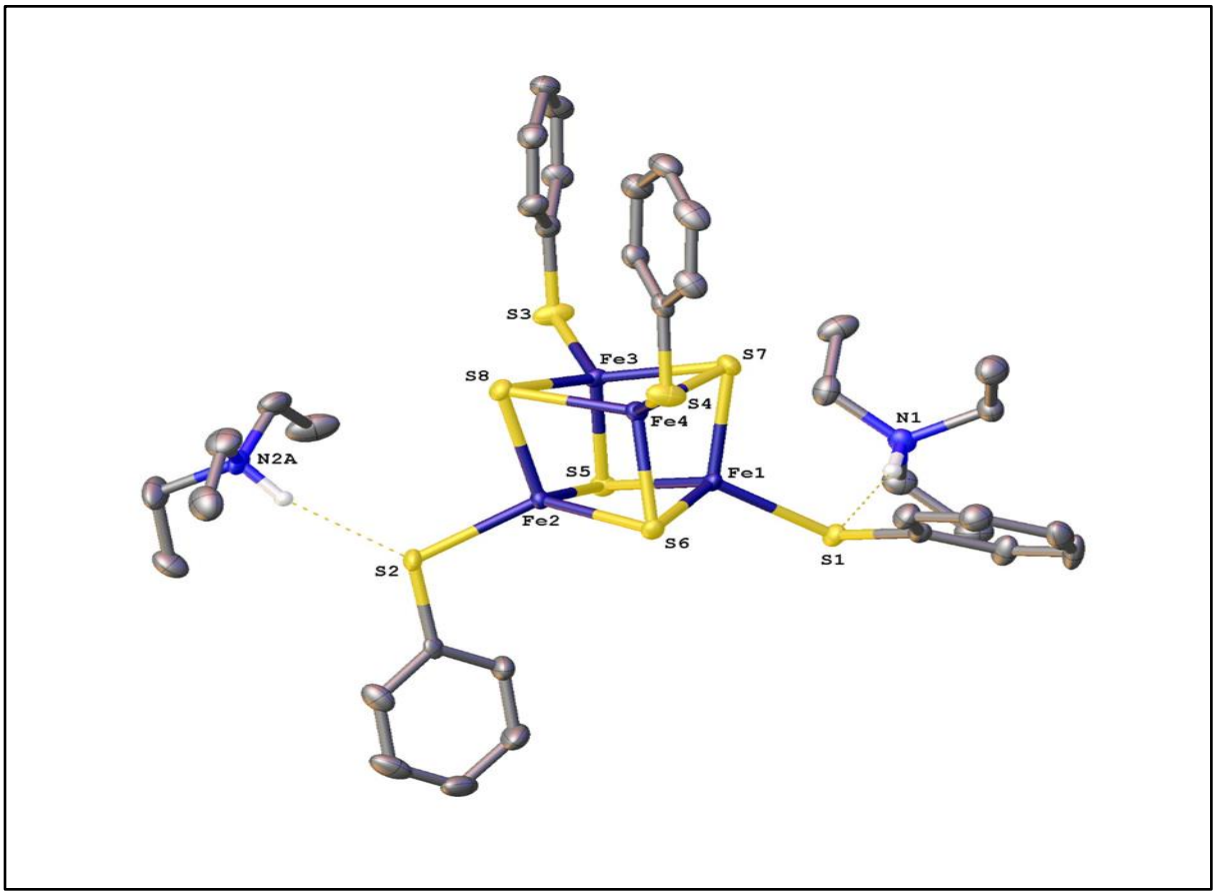

Figure 4.9. X-ray structure for $[NHEt_3]_2[Fe_4S_4(SPh)_4]$, showing the interactions of the $NHEt_3^+$ cations with terminal PhS^- ligands.

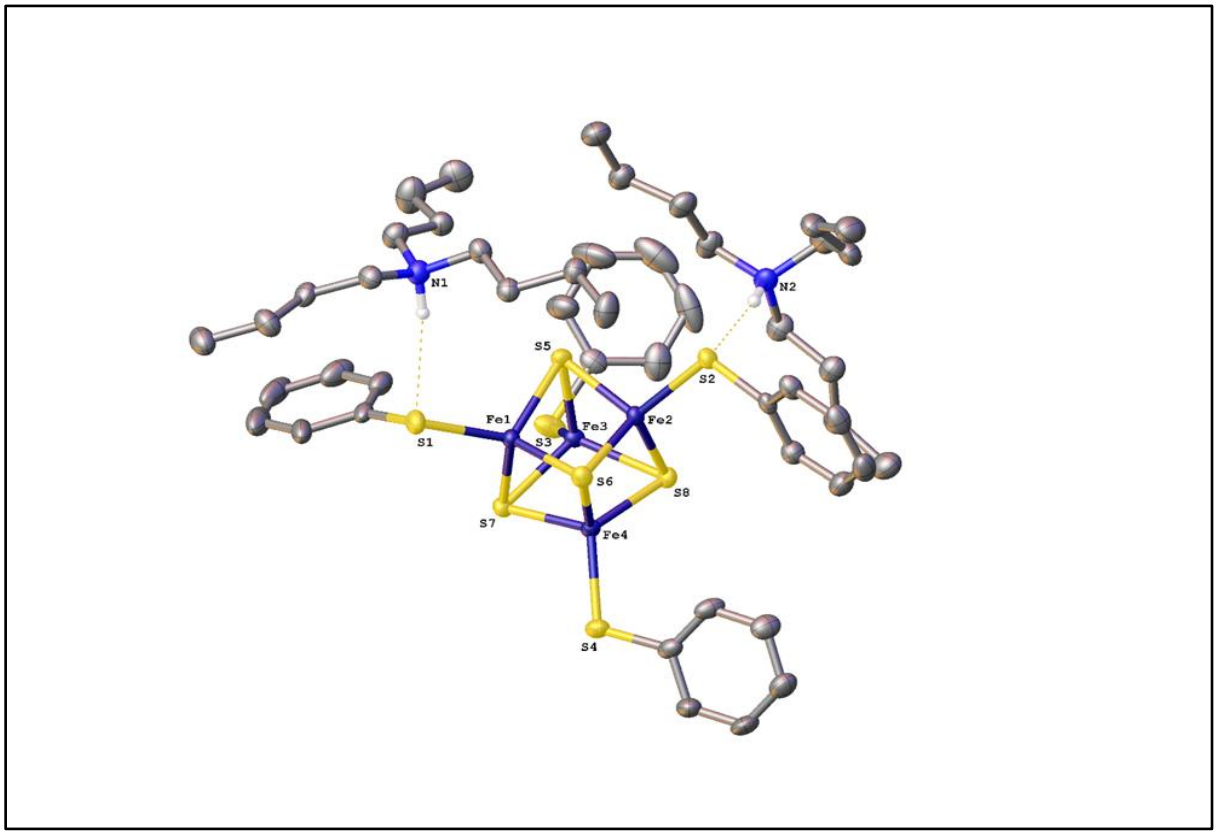

Figure 4.10. X-ray structure for $[NHBu^{n}_{3}]_2[Fe_4S_4(SPh)_4]$ showing the interactions of the $NHBu^{n}_{3}{}^{+}$ cations with terminal PhS^{-} ligands.

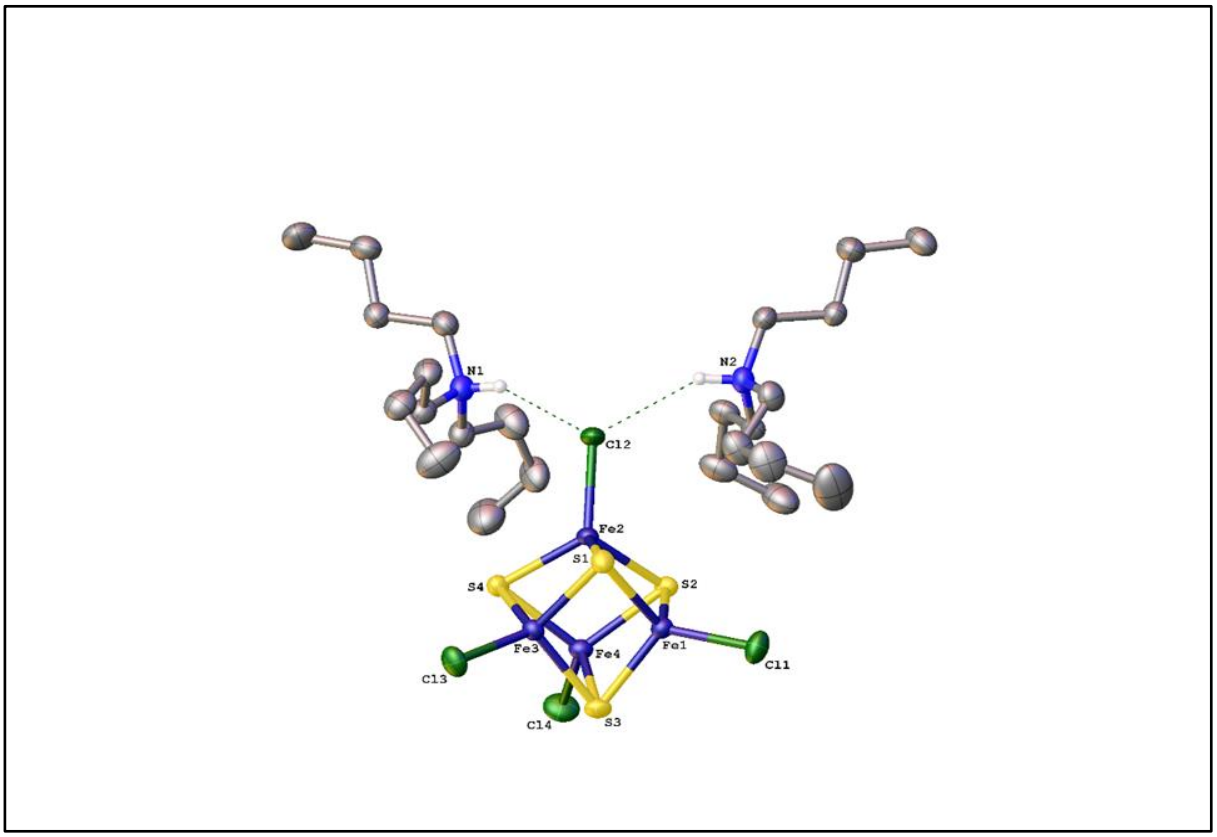

Figure 4.11. X-ray structure for $[NHBu^{n}_{3}]_2[Fe_4S_4Cl_4]$, showing the interactions of the $NHBu^{n}_{3}{}^{+}$ cations with terminal Cl^{-} ligand.

4.4 Results and Discussion.

Recent kinetic studies on the reaction between $[Fe_4S_4Cl_4]^{2-}$ and PhS^- in the presence of $NHBu^n{}_3^+$ are consistent with the mechanism shown in Figure (4.2), but, in this case, the initial protonation of the cluster is slow and rate limiting (k = 500 dm^3 mol^{-1} s^{-1})[28, 29]. Although rate-limiting proton transfer to $[Fe_4S_4Cl_4]^{2-}$ has been observed with other acids[30-34], the rate constant for proton transfer from $NHBu^n{}_3^+$ to $[Fe_4S_4Cl_4]^{2-}$ is the slowest measured so far. This observation prompted us to prepare $[NHBu^n{}_3]_2[Fe_4S_4X_4]$ (X = SPh or Cl). Determining the X-ray crystal structures of these compounds reveals the interactions between the N–H group of the cation (acid) and the various components of the cluster (*i.e.* Fe, μ_3–S and X).

The crystallographic data for all structures are presented in Table (4.1). All structures contain discrete cations and anions, and the structures of the cluster anions are essentially identical to those reported in the literature for these clusters in other salts[35, 36]. Selected bond lengths and angles associated with the clusters are shown in Table (4.2).

For $[NMe_4]_2[Fe_4S_4(SPh)_4]$, the bond angles fall in the ranges, S_c–Fe–S_c = 103.77(2)º–104.57(2)º, Fe–S_c–Fe = 72.204(18)º–74.063(19)º, S_c-Fe–SPh = 102.49(2)°–120.48(3)°, and the bond lengths Fe–S_c = 2.2190(6)–2.3080(6) Å and Fe–SPh = 2.2486(7)–2.2637(6) Å. All dimensions are in good agreement with the those for $[NHR_3]_2[Fe_4S_4(SPh)_4]$ (R= Et or Bu^n) presented in Table (4.2)[35]. Similarly, for $[NEt_4]_2[Fe_4S_4Cl_4]$, the bond angles, S_c–Fe–S_c = 102.69(3)º–119.01(3)º, Fe–S_c–Fe = 72.94(2)º–74.90(2)º, S_c–Fe–Cl = 109.58(3)–120.21(3), and the bond lengths, Fe–S_c = 2.2425(7)–2.3125(7) Å and Fe–Cl = 2.2057(7)–2.2388(7) Å , are in good agreement with the dimensions for $[NHBu^n{}_3]_2[Fe_4S_4Cl_4]$ presented in Table (4.2)[36].

The N–H···S interactions between the cations and the clusters are of particular interest in understanding the protonation chemistry of Fe–S-based clusters. In the crystal structure of $[NHBu^n{}_3]_2[Fe_4S_4(SPh)_4]$, the N–H groups in both cations point towards the sulfurs of two different thiophenolate ligands. The principal (shortest) interaction of the two $NHBu^n{}_3^+$ is to sulfur in coordinated thiophenolates {N–H(2)···S(2)Ph = 2.35(3) Å and N–H(1)···S(1)Ph = 2.46(2) Å}. The distance between either cation to any core sulfur is significantly longer {N–H···S_c distances = 3.59(3) Å and 4.64(2) Å}. A similar picture is evident for $[NHEt_3]_2[Fe_4S_4(SPh)_4]$ with the principal interaction of the two $NHEt_3^+$ being to sulfur in two different coordinated thiophenolates {N–H···SPh distances = 2.31(2) Å and 2.40(2) Å}, whilst the N–H···S_c distance to any core sulfur is significantly longer {4.49(2) Å and 4.00(2) Å}.

Table (4.1): X-ray crystallographic data for $[NHR_3]_2[Fe_4S_4X_4]$.

Cluster	R = Et, X = SPh	R = Bu^n, X = SPh	R = Bu^n, X = Cl
Formula	$C_{36}H_{52}N_2S_8Fe_4$	$C_{48}H_{76}N_2S_8Fe_4$	$C_{24}H_{56}N_2S_4Cl_4Fe_4$
M_r / g mol^{-1}	992.67	1160.98	866.14
Crystal system	Monoclinic	Triclinic	Monoclinic
a / Å	11.20053(5)	10.7503(5)	13.5238(3)
b / Å	21.11811(11)	11.0619(5)	18.6392(3)
c / Å	18.18147(9)	23.9485(9)	16.0547(3)
α / °	90	99.840(4)	90
β / °	91.9933(4)	90.614(3)	107.453(2)
γ / °	90	91.215(4)	90
V / Å^3	4297.93(4)	2805.1(2)	3860.67(13)
T/K	150(2)	150(2)	150(2)
Space group	$P2_1/n$	$P\bar{1}$	$P2_1/n$
Z	4	2	4
Reflections measured	57,256	45,493	28,011
Independent reflections	7672	12,877	6824
Refined parameters	484	571	357
R_{int}	0.0534	0.0402	0.0387
R_I ($I > 2\sigma$)	0.0241	0.0347	0.0300
$wR(F^2)$ ($I > 2\sigma$)	0.0560	0.0607	0.0733
R_I (all data)	0.0279	0.0549	0.0357
$wR(F^2)$ (all data)	0.0578	0.0692	0.0733
GoF on F^2	1.019	1.042	1.033
Max., min. e density/e Å^{-3}	0.41 -0.35	0.51 -0.42	1.01 -0.40
CCDC reference [a]	1.472,850	1.472,848	1.472,849

[a] CCDC 1472850, CCDC 1472848 and CCDC 1472849 contain the supplementary crystallography data for this chapter.

Table (4.2): Selected bond length and angle ranges for $[NHR_3]_2[Fe_4S_4X_4]$.

Cluster [a]	R = Et, X =SPh	R = Bu^n, X = SPh	R = Bu^n, X = Cl
bond angle ranges / ^{o}			
S_c-Fe-S_c	103.68(2) - 105.84(2)	103.77(2) - 105.54(2)	102.69(3) - 105.42(3)
Fe-S_c-Fe	72.109(17) - 73.723(17)	72.204(18) - 74.063(19)	72.94(2) - 74.90(2)
S_c-Fe-SPh	100.08(2) - 122.42(2)	102.49(2) - 120.48(3)	
S_c-Fe-Cl			109.58(3) - 120.21(3)
bond length ranges /Å			
Fe-S_c	2.2411(5) - 2.3218(6)	2.2190(6) - 2.3192(6)	2.2425(7) - 2.3125(7)
Fe-SPh	2.2580(6) - 2.2746(5)	2.2486(7) - 2.2637(6)	
Fe-Cl			2.2057(7) - 2.2388(7)

[a] $S_c = \mu_3$-S

Theoretical studies have indicated that the optimal N–H···S distance for hydrogen bonding is *ca* 2.50 Å[37] (assuming N–H = 0.97 Å). From the X-ray crystal structures of $[NHR_3]_2[Fe_4S_4(SPh)_4]$, the N–H···SPh distances are consistent with a hydrogen bond interaction, whilst the N–H···S_c distances are too long for any significant interaction. It is also worth noting that in $[NHR_3]_2[Fe_4S_4(SPh)_4]$ (R = Bu^n or Et), the N–H···SPh distances are slightly shorter for the $NHEt_3^+$ salt. For $NHEt_3^+$ and $NHBu^n{}_3^+$, the pK_as of the acids in MeCN are similar ($NHEt_3^+$, pK_a = 18.4; $NHBu^n{}_3^+$, pK_a = 18.1)[38]. It is reasonable that the strength of the hydrogen bonding (and hence the N–H···SPh distance) between NHR_3^+ and the cluster will depend on the difference in the pK_as of NHR_3^+ and $[Fe_4S_4(SPh)_3(SHPh)]^{-1}$, and if this were the only factor, it would be anticipated that the N–H···S distance would be shorter with $NHBu^n{}_3^+$. That the shorter N–H···S distance is observed with $NHEt_3^+$ is consistent with the steric bulk of the acid being a contributing factor, as described in the work reported earlier in Chapter 2 (***section 2.5.2.2***) and (***section 2.5.2.3***).

In the crystal structure of $[NHBu^n{}_3]_2[Fe_4S_4Cl_4]$, the N–H groups of both cations point towards a single chloro-group, as shown in Figure (4.11) {distances: N–H(1)···Cl(2) = 2.34(7) and N–H(2)···Cl(2) = 2.55(4) Å} . The distance to any core sulfur atoms is significantly longer {*e.g.* N–H(2)···S_c(1) = 5.18(3) Å and N–H(2)···S_c(2) = 4.74(3) Å}. Furthermore, the N–H groups do not point towards any core sulfur.

4.5 Conclusions.

The X-ray crystal structures of $[NHR_3]_2[Fe_4S_4X_4]$ show that, in the solid state, the acid NHR_3^+ associates with the anionic cluster, but the interactions are restricted to the terminal PhS or Cl ligands and there is no interaction with the core μ_3–S. Earlier structural studies on natural cubanoid $\{Fe_4S_4\}^{2+}$ clusters have shown that amide NH groups from the surrounding polypeptide hydrogen bonds to both cluster terminal cysteinate ligands and μ_3–S[39]. However, in the synthetic cluster, $[NEt_4]_2[Fe_4S_4(S\text{-}2\text{-}Bu^tCONHC_6H_4)_4]$, intramolecular amide NH hydrogen bonding is exclusively to the thiolate S[40]. It is pertinent to note that other electrophiles (notably Na^+) can interact with μ–S sites in some clusters[41-44].

How the structures of $[NHR_3]_2[Fe_4S_4X_4]$ relate to the earlier proposal (based on the kinetics and DFT calculations) that protonation of the cluster is associated with major structural changes[9-11, 15-17, 28, 29] will now be considered. It is difficult to study the protonation of Fe–S-based clusters directly because of the poor spectroscopic changes associated with this process. Our approach has been to study protonation of Fe–S-based clusters by monitoring the effects that acids have on the rate of substitution of the terminal ligands. As discussed in Section 4.1, this kinetic approach has one severe limitation: it only monitors the protonation which affects the substitution lability of the cluster[9-11]. In solution, it is possible that NHR_3^+ can protonate (or even just hydrogen bond to) either the terminal ligands or μ_3–S, Figure (4.12).

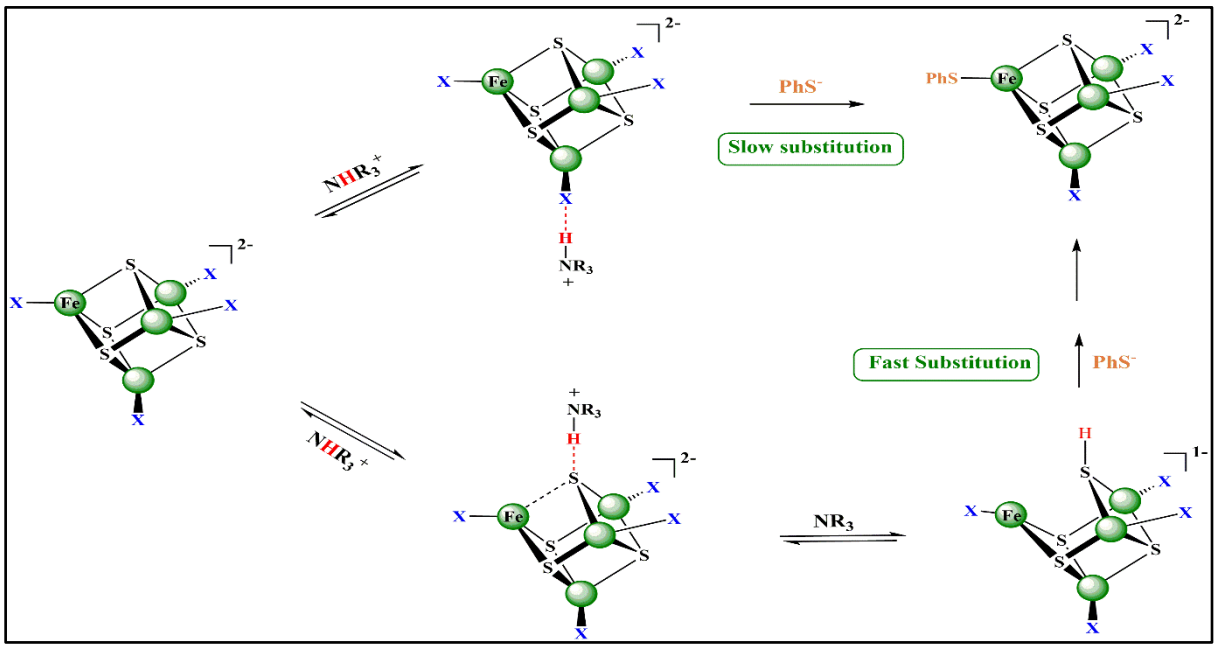

Figure 4.12. Competitive dynamic hydrogen bonding to μ_3-S and terminal X groups in $[Fe_4S_4X_4]^{2-}$ and the consequent reactivities of protonated clusters.

In the structures reported herein, hydrogen bonding of NHR_3^+ is restricted to the terminal ligands of the clusters and causes no appreciable changes to the structure of the cluster core, Table (4.2). This hydrogen bonding suggests potential sites of protonation. The kinetic studies suggest that the 'labilising' protonation (which facilitates substitution of terminal ligands) causes significant structural changes to the cluster, and DFT calculations[15-17] indicate this is a Fe–(μ_3–SH) bond elongation or cleavage, see Figures (4.4) and (4.12). The structures of $[NHR_3]_2[Fe_4S_4X_4]$ suggest that interaction of the acid with terminal ligands occurs but does not cause any structural change to the cluster and so is not particularly labilising. The work reported in this chapter allows a more complete description of the solution protonation chemistry (and its effect on substitution lability) to be presented, Figure (4.12). In this fuller description, protonation can occur at the terminal ligand, but does not appreciably affect the structure of the cluster core and consequently is not labilising. In addition, protonation can occur at a μ_3–S with concomitant Fe–(μ_3–SH) bond cleavage, but protonation at this site is labilising.

Furthermore, we attempted to isolate the crystals of $[NHBu^n_3][Fe_4(SH)S_3Cl_4(Bu^tNC)]$ to see how the protonated cluster containing the bound Bu^tNC may affect the structure of the cluster. However, our attempts failed to achieve appropriate crystals for analysis by X-ray crystallography.

4.6 References.

1. R. H. Holm, P. Kennepohl and E. I. Solomon, *Chem. Rev.*, 1996, **96**, 2239-2314.
2. H. Beinert, M. C. Kennedy and C. D. Stout, *Chem. Rev.*, 1996, **96**, 2335-2373.
3. B. K. Burgess and D. J. Lowe, *Chem. Rev.*, 1996, **96**, 2983-3011.
4. S. C. Lee and R. H. Holm, *Chem. Rev.*, 2004, **104**, 1135-1157.
5. B. M. Hoffman, D. R. Dean and L. C. Seefeldt, *Acc. Chem. Res.*, 2009, **42**, 609-619.
6. T. Spatzal, M. Aksoyoglu, L. M. Zhang, S. L. A. Andrade, E. Schleicher, S. Weber, D. C. Rees and O. Einsle, *Science*, 2011, **334**, 940-940.
7. D. Lukoyanov, Z. Y. Yang, N. Khadka, D. R. Dean, L. C. Seefeldt and B. M. Hoffman, *J. Am. Chem. Soc.*, 2015, **137**, 3610-3615.
8. G. R. Dukes and R. H. Holm, *J. Am. Chem. Soc.*, 1975, **97**, 528-533.
9. R. A. Henderson, *Chem. Rev.*, 2005, **105**, 2365-2437.
10. R. A. Henderson, *Coord. Chem. Rev.*, 2005, **249**, 1841-1856.
11. R. A. Henderson, *BioInorg. React. Mech.* , 2012, **8**, 1-37.
12. A. J. Dunford and R. A. Henderson, *J. Coord. Chem.*, 2010, **63**, 2507-2516.
13. R. A. Henderson and K. E. Oglieve, *J. Chem. Soc., Dalton Trans.*, 1993, 1467-1472.
14. D. Sellmann and J. Sutter, *Acc. Chem. Res.*, 1997, **30**, 460-469.
15. A. Alwaaly, I. Dance and R. A. Henderson, *J. Chem. Soc., Chem. Commun.*, 2014, **50**, 4799-4802.
16. I. Dance and R. A. Henderson, *J. Chem. Soc., Dalton Trans.*, 2014, **43**, 16213-16226.
17. I. Dance, *J. Chem. Soc., Dalton Trans.*, 2015, **44**, 4707-4717.
18. R. A. Henderson and K. E. Oglieve, *J. Chem. Soc., Dalton Trans.*, 1993, 1473-1476.
19. R. A. Henderson and K. E. Oglieve, *J. Chem. Soc., Chem. Commun.*, 1994, 1961-1962.
20. R. A. Henderson and K. E. Oglieve, *J. Chem. Soc., Dalton Trans.*, 1999, 3927-3934.
21. V. R. Almeida, C. A. Gormal, K. L. C. Gronberg, R. A. Henderson, K. E. Oglieve and B. E. Smith, *Inorgan. Chim. Acta*, 1999, **291**, 212-225.
22. K. S. Hagen, J. G. Reynolds and R. H. Holm, *J. Am. Chem. Soc.*, 1981, **103**, 4054-4063.
23. CrysAlisPro, *Virsion 1.171.35*, Oxford diffraction, 2010.

24. R. C. Clark and J. S. Reid, *Acta Cryst.*, 1995, **A51**, 887-897.

25. O. V. Dolomanov, L. J. Bourhis, R. J. Gildea, J. A. K. Howard and H. Puschmann, *J. Appl. Cryst.*, 2009, **42**, 339-341.

26. G. M. Sheldrick, *Acta Cryst.*, 2015, **71**, 3-8.

27. G. M. Sheldrick, *Acta Cryst.*, 2008, **64**, 112-122.

28. T. M. M. Al-Rammahi and R. A. Henderson, *J. Chem. Soc., Dalton Trans.*, 2016, **45**, 307-314.

29. T. M. M. Al-Rammahi and R. A. Henderson, *Dalton Trans*, 2016, **45**, 1373-1381.

30. R. A. Henderson and K. E. Oglieve, *J. Chem. Soc., Dalton Trans.*, 1999, 3927-3934.

31. A. J. Dunford and R. A. Henderson, *J. Chem. Soc., Dalton Trans.*, 2002, 2837-2842.

32. J. Bell, A. J. Dunford, E. Hollis and R. A. Henderson, *Angew. Chemie Int. Ed.*, 2003, **42**, 1149-1152.

33. K. Bates and R. A. Henderson, *Inorg. Chem.*, 2008, **47**, 5850-5858.

34. B. Garrett and R. A. Henderson, *J. Chem. Soc., Dalton Trans.*, 2010, **39**, 4586-4592.

35. L. Que, Jr., M. A. Bobrik, J. A. Ibers and R. H. Holm, *J. Am. Chem. Soc.*, 1974, **96**, 4168-4178.

36. M. A. Bobrik, K. O. Hodgson and R. H. Holm, *Inorg. Chem.*, 1977, **16**, 1851-1858.

37. S. Scheiner, *Acc. Chem. Res.*, 1985, **18**, 174-180.

38. K. Izutsu, *Acid-Base Dissociation Constants in Dipolar Aprotic Solvents*, Blackwell Scientific, Oxford, UK, 1990.

39. P. J. Stephens, D. R. Jollie and A. Warshel, *Chem. Rev.*, 1996, **96**, 2491-2513.

40. N. Ueyama, Y. Yamada, T. Okamura Ta, S. Kimura and A. Nakamura, *Inorg. Chem.*, 1996, **35**, 6473-6484.

41. H. Strasdeit, B. Krebs and G. Henkel, *Inorg. Chem.*, 1984, **23**, 1815-1825.

42. J-F You, B. S. Snyder, G. C. Papaefthymiou and R. H. Holm, *J. Am. Chem. Soc.*, 1990, **112**, 1067-1076.

43. J-F You, G. C. Papaefthymiou and R. H. Holm, *J. Am. Chem. Soc.*, 1992, **114**, 2697-2710.

44. R. A. Henderson, *J. Chem. Soc., Dalton Trans.*, 1999, 119-125.

PART II

PROTONATION OF $[Ni(THIOLATE)\{PhP(CH_2CH_2PPh_2)_2\}]^+$ COMPLEXES

Chapter 5: The Coordination Chemistry of Nickel-Thiolate Complexes and Their Protonation Reactions

5.1 Introduction.

In different metalloenzymes, in the nickel-containing proteins and enzymes (*e.g.* hydrogenase, CO-dehydrogenase (CODH), urease, methyl coenzyme M reductase (MCR), Ni-superoxide dismutase, and glyoxalase I) where the structure is known the ligation of the nickel site involves oxygen-, nitrogen- or sulfur-based donor atoms. In this part of the thesis, the involvement of sulfur-based ligands in protonation reactions will be discussed. Studies on the factors which affect the rates of proton transfer to sulfur sites are fundamental to understanding how certain enzymes operate. Over the last few years, only a few studies on the protonation of nickel complexes have been reported[1-10]. This chapter will present the significant role for the nickel complexes in biological systems. In addition, it will discuss the factors that affect the rates of proton transfer to sulfur site in mononuclear nickel-thiolate complexes.

5.2 Thiolate ligand in biology.

In biology, most metal ions bind to donor ligands involving oxygen-, nitrogen- or sulfur-based atoms. The sulfur ligands include both sulfides (found in Fe–S-based clusters), which were discussed in more details in the first part of the thesis (Chapter 1 to Chapter 4), and thiolates (cysteinate amino acid residues) which is the predominant ligand. Cysteinate can bind to either one or two metal ions, and is, for example, found as a ligand to copper in Copper Blue proteins, to iron in Fe-S clusters and other metalloproteins which are Cytochromes, Figure (5.1). In all cases, upon coordination of cysteine deprotonation will occur. Similarly, few thiol complexes have been isolated in simple transition metal complexes. The study on the reactions of thiols with metal complexes, which have a low coordination number, results in complexes with thiolate and hydrido ligands or thiolate complexes and release of proton[11].

In 1998, Allan et al. reported[1] the synthesis and characterization of a protonated binuclear complex $[Ni_2\{(SCH_2CH_2)_2NMe\}_2]$. This study indicated that the protonation will occure on sulfur site $[Ni_2\{(HSCH_2CH_2)(SCH_2CH_2)NMe\}_2]^+$. Other study on $[Fe(SPh)(CO)_2\{P(OPh)_3\}_2]^-$ complex showed[12] that the initial protonation occurs at the Fe atom to form the hydrido species $[FeH(SPh)(CO)_2\{P(OPh)_3\}_2]$. In contrast, a further protonation is observed. It seems unlikely that this protonation also occurs at the iron, since this would form a Fe^{IV} complex. Furthermore,

the features of infrared spectroscopy are not consistent with a dihydrogen complex. Hence it has been suggested that the hydrido thiol complex $[FeH(HSAr)(CO)_2\{P(OPh)_3\}_2]^+$ is formed[12].

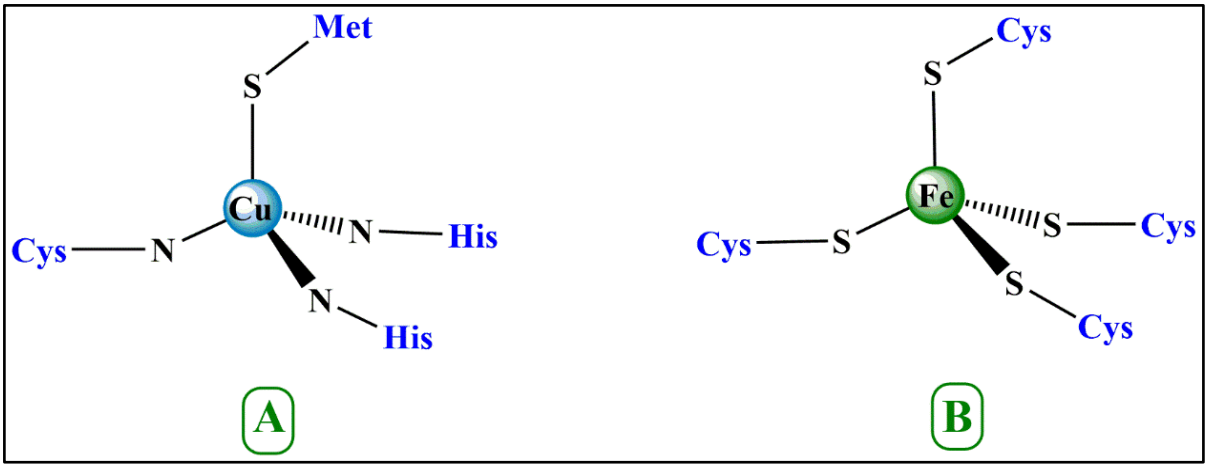

Figure 5.1. The structure of the active site in the (A) Copper Blue protein; (B) protein Rubredoxin.

5.3 Role of Nickel Enzymes in biology.

Nickel enzymes have a significant function in catalysing the biological reactions and they are particularly important in the metabolism of chemicals particularly abundant in the preoxygen evolutionary era (*e.g.* hydrogen, methane and carbon monoxide). Nickel enzymes are found in nature in a number of anaerobic bacteria and in mammals. Moreover, nickel proteins are virtually unknown in higher eukaryotes with the exception of the plant enzyme urease[13-15].

There are six known nickel enzymes (urease, hydrogenase, CO-dehydrogenase (CODH) and Acetyl-CoA-synthase, methyl coenzyme M reductase, Ni-superoxide dismutase, and glyoxalase I)[16], and this section will present the reactions and the active sites of these six nickel-dependent metalloenzymes.

5.3.1 Urease.

Urease (urea amidohydrolase) was the first enzyme ever crystallised in 1926, and 50 years later it was shown to contain nickel[17]. Urease is a metalloenzyme that catalyzes the hydrolysis of urea to ammonia and carbon dioxide, as shown in Equation (5.1).

$$(NH_2)_2CO + H_2O \longrightarrow 2NH_3 + CO_2 \qquad (5.1)$$

More specifically, in presence of metalloenzyme, the catalysis of this hydrolysis occurs by two steps: first, ammonia and carbamate are produced by hydrolysis of urea, as shown in Equation

(5.2), and then another ammonia and carbonic acid are produced by spontaneous hydrolysis of carbamate, as shown in Equation (5.3)

$$(NH_2)_2CO + H_2O \longrightarrow H_2NCO_2^- + NH_4^+ \qquad (5.2)$$

$$H_2NCO_2^- + H_2O \longrightarrow HCO_3^- + NH_3 \qquad (5.3)$$

However, the uncatalyzed aqueous degradation of urea, proceeds via an elimination reaction to produce ammonia and cyanic acid, Equation (5.4). Studies have shown that the catalytic reaction is *ca* 10^{14} times faster than the spontaneous degradation[16].

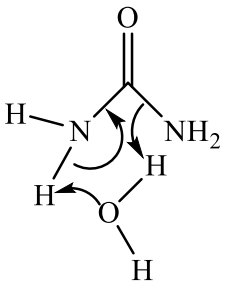

$$\longrightarrow HN{=}C{=}O + NH_3 \qquad (5.4)$$

Urea is found in plants, bacteria, fungi and soil. Urea is a source of nitrogen through metabolism by plants and bacteria. This metabolism reaction is a source of concern for agriculture (increase of urease activity leads to the efficiency of nitrogen fertilisers being severely decreased) and for medicine (bacterial ureases are significant virulence factors implicated in the formation of infection-induced urinary stones, pyelonephritis, catheter encrustation and hepatic encephalopathy)[18].

The bacterial urease is structurally characterised using protein purified from *Klebsiella aerogenes*[19] and *Bacillus pasteurii*[20]. X-ray crystallography revealed a general feature consisting of a carbamylated lysine residue as a bridging ligand to the two nickel atoms. Figure (5.2) shows the active site of *Bacillus pasteurii*.

The main features for the structure of active site of urease are as follows. (i) The two nickel atoms are bridged by the carboxylate group of the carbamylated lysine (ii) $Ni_{(1)}$ is further coordinated by $His_{(249)}$ and $His_{(275)}$, while $Ni_{(2)}$ binds to $Asp_{(363)}$, $His_{(137)}$ and $His_{(139)}$. (iii) One of the water molecules, $W_{(B)}$, symmetrically bridges the two nickel atoms, whereas the other two water molecules, $W_{(1)}$ and $W_{(2)}$, complete the coordination polyhedron around the nickel atoms. The geometry of the two Ni sites are distorted square pyramidal for $Ni_{(1)}$ and distorted octahedral for $Ni_{(2)}$.

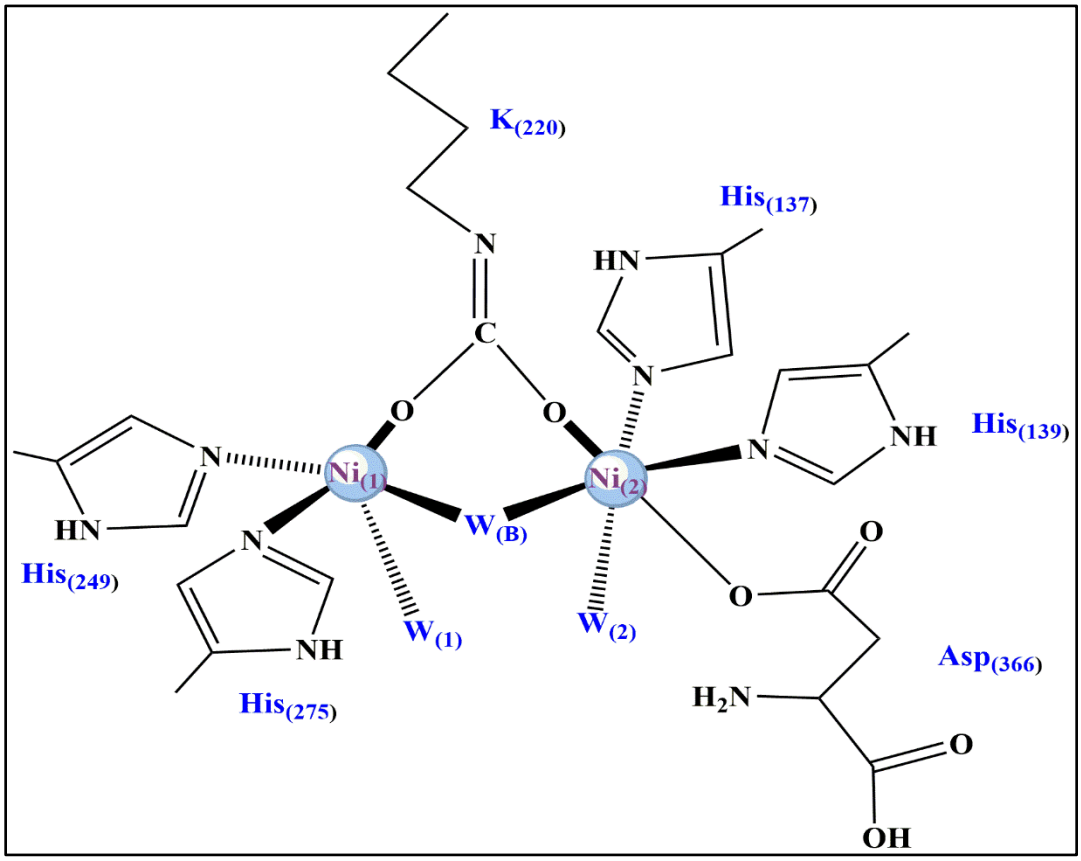

Figure 5.2. Active site of urease in *Bacillus pasteurii* (BPU) structure.

5.3.2 Hydrogenase.

Hydrogenases are metalloenzymes which interconvert dihydrogen and protons for many micro-organisms such as acetogenic bacteria, methanogenic bacteria, sulfate-reducing bacteria, nitrogen fixation and photosynthesis. Hydrogenases catalyze the two electrons interconversion of dihydrogen and protons[16], Equation (5.5).

$$H_2 \rightleftharpoons 2H^+ + 2e^- \qquad (5.5)$$

Hydrogenase have two different roles either generate hydrogen as sinks of excess electrons or oxidise H_2 to provide the organism with a source of strong reductants. According to their metal constitution, four different types of hydrogenase have been identified: [FeFe]-hydrogenase; [NiFe]-hydrogenase, [NiFeSe]-hydrogenase and only-Fe-hydrogenase. X-ray protein crystallography has shown that the active site of two hydrogenases contain iron or nickel and iron (namely [Fe] and [NiFe]), in a sulfur-rich coordination environment.

From several sources particularly *Desulfovibrio gigas*[21] and *Desulfovibrio vulgaris*[22], the structure of active site of the [NiFe] hydrogenase is shown in Figure (5.3). This site consists of

a heterobimetallic dimer. The sulfur atoms of two cysteine amino acids bridge the Ni and Fe atoms. A further two cysteines are terminally bound to the nickel atom. Three non-protein diatomic molecules ligate the iron atom. These are found to be one carbon monoxide (CO) and two cyanides (CN^-) in the case of enzymes from *Desulfovibrio gigas* and *Desulfovibrio vulgaris*. The X bridging ligand is either an oxygen or a sulfur species in the oxidised state of the enzyme from *Desulfovibrio gigas* and *Desulfovibrio vulgaris* respectively.

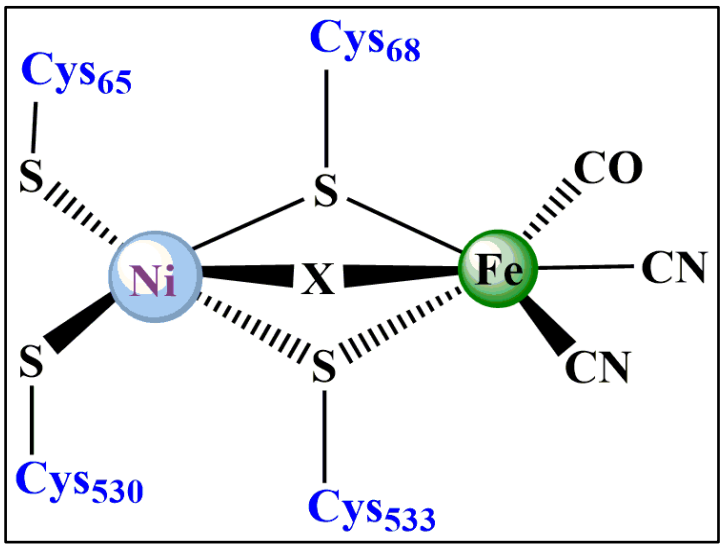

Figure 5.3. Active site of [NiFe] hydrogenase from *Desulfovibrio gigas.*

5.3.3 Carbon Monoxide Dehydrogenase and Acetyl-CoA-Synthase.

Carbon monoxide dehydrogenases (CODHs) are nickel metalloenzymes, which are found in the respiratory system of acetogenic, methanogenic and photosynthetic bacteria. Although CODHs are phylogenetically related, they vary in terms of their catalytic activity, subunit composition and metabolic role[16].

CODHs are monofunctional enzymes which catalyze the reversible oxidation of carbon monoxide (CO) to carbon dioxide (CO_2), Equation (5.6).

$$CO + H_2O \rightleftharpoons CO_2 + 2H^+ + 2e^- \qquad (5.6)$$

Moreover, carbon monoxide dehydrogenase/Acetyl-CoA synthase (CODH/ACS) are bifunctional enzymes which catalyze the synthesis of acetyl coenzyme A from a methyl group (donated from a coronoid iron/sulfur protein), coenzyme A and carbon monoxide, as shown in Equation (5.7).

$$CH_3\text{-CFeSP} + CoA^- + CO \rightleftharpoons \text{Acetyl-CoA} + \text{CFeSP} \quad (5.7)$$

Organisms housing these CODH enzymes play critical roles in the degradation of environmental pollutants[23] and the global carbon cycle[24]. The presence of carbon monoxide is hazardous to most life forms, and the bacteria annually remove about *ca* $1x10^8$ tons of (CO) from the earth and the lower atmosphere. In some bacteria, the CODH/ACS enzymes carry out the conversion of carbon monoxide to, ultimately, cellular carbon.

By purification of the protein from anaerobic CO-utilising bacteria such as *Rhodospirillum rubrum*[24] and *Carboxydothermus hydrogenoformans*[25], the structure of the monofunctional CODH has been characterised by X-ray crystallography. There are three different clusters called the B-, C- and D-cluster in the active site of the metalloenzymes.

The current hypothesis is that the oxidation of carbon monoxide to carbon dioxide occurs within the β-subunits containing the B- and C-cluster. It has been proposed {from Extended X-ray Absorption Fine Structure (EXAFS) carried out at the Nickel K-edge and Mössbauer results} that the B-cluster is an unexceptional $[Fe_4S_4]^{1+/2+}$ cluster which transfers electrons between the other clusters[26]. Studies on the X-ray structures from *Rhodospirillum rubrum*[24] (resolution 2.8 Å) and *Carboxydothermus hydrogenoformans*[25] have shown only small differences in the structure of their C-clusters. The Drennan's isolated C-cluster (from *Rhodospirillum rubrum*) is quite similar to the Dobbek's isolated C-cluster (from *Carboxydothermus hydrogenoformans*). The only notable difference is a bond between nickel and sulfur completing the $[Fe_3S_4Ni]$ cluster, and an extra unidentified ligand to the Ni (X likely CO), as shown in Figure (5.4).

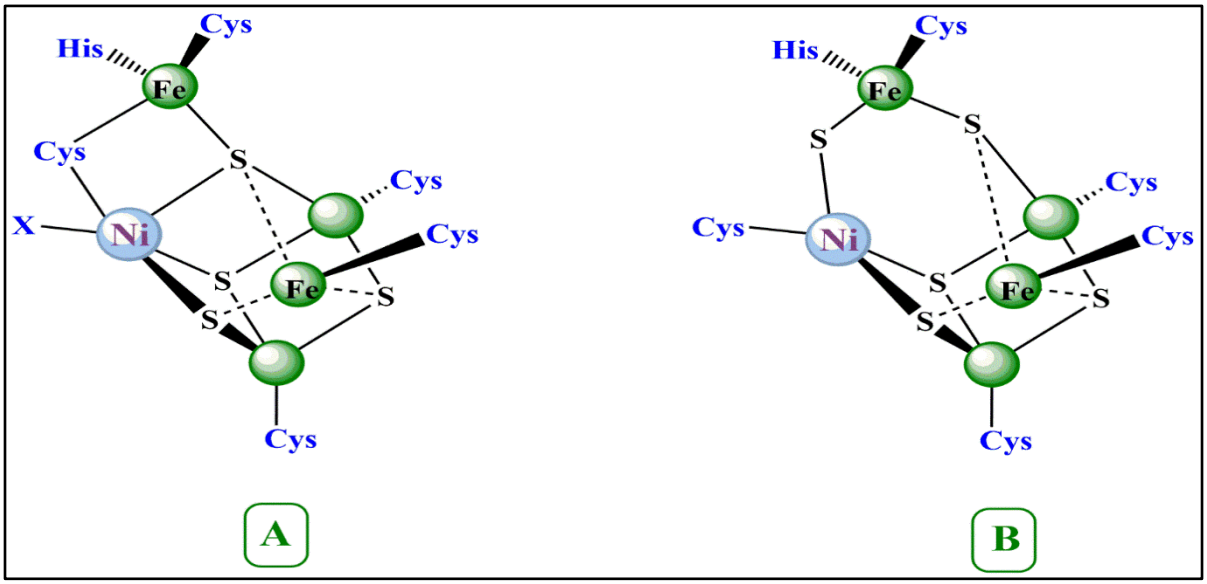

Figure 5.4. C-cluster active site; A: Drennan C-cluster from *Rhodospirillum rubrum* and B: Dobbeck C-cluster from *Carboxydothermus hydrogenoformans*.

Acetyl-CoA synthase activity of the CODH/ACS complex, catalyzing the synthesis of Acetyl-CoA, has been located on the α-subunits containing the A-cluster. As for the C-cluster, spectroscopy studies have shown that the A-cluster consists of a [4Fe-4S] cubane covalently linked to a mononuclear Ni centre *via* an unknown ligand (X = C or S)[26], Figure (5.5). An essential difference between A-cluster and C-cluster is the coordination environment of the Ni ion. The A-cluster exhibits spectroscopic features that implicate a distorted square planar coordination for Ni bound to two sulfur and two nitrogen or oxygen ligands, Figure (5.5). However, Ni in the C-cluster is located within a distorted cubane, where Ni binds with four S, three Fe atoms and an additional sulfide ligand bridging the Ni and unique Fe[24].

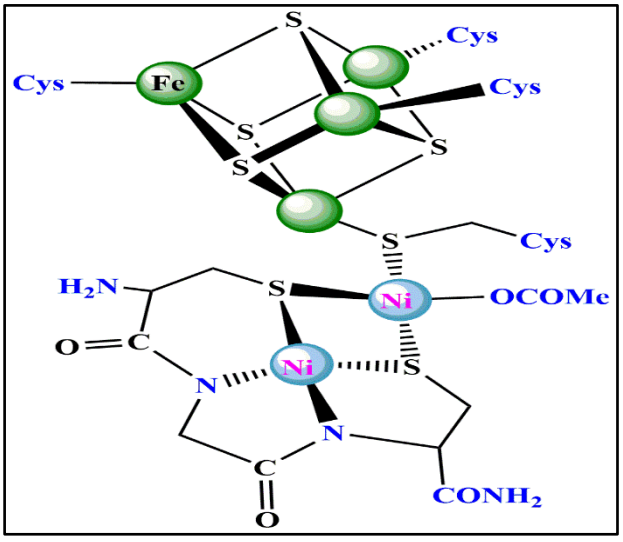

Figure 5.5. The structure of A-cluster active site.

5.3.4 Methyl Coenzyme M Reductase.

Methyl coenzyme M reductase (MCR) is a large, complex enzyme which catalyses the reaction of methane formation in the oxidative part of the methanogenic *archaea* energy metabolism[27], Equation (5.8).

$$CO_2 + 4H_2 \longrightarrow CH_4 + 2H_2O \qquad (5.8)$$

This reaction involves the overall eight electrons reduction of carbon dioxide *via* four $2e^-$ steps, and then this reduced carbon fragment being bound to series of coenzymes. In the final step of this reaction, Equation (5.9), there are two coenzymes involved: (i) coenzyme M carries the methyl group that comes from CO_2 reduction; and (ii) coenzyme B is an aliphatic thiol, as shown in Figure (5.6). The MCR contains two molecules of a nickel porphyrinoid cofactor, donated Fe_{430} along with two molecules each of coenzymes M and B[28, 29].

$$CoB\text{-}S\text{-}H + CH_3\text{-}S\text{-}CoM \longrightarrow CoB\text{-}S\text{-}S\text{-}CoM + CH_4 \qquad (5.9)$$

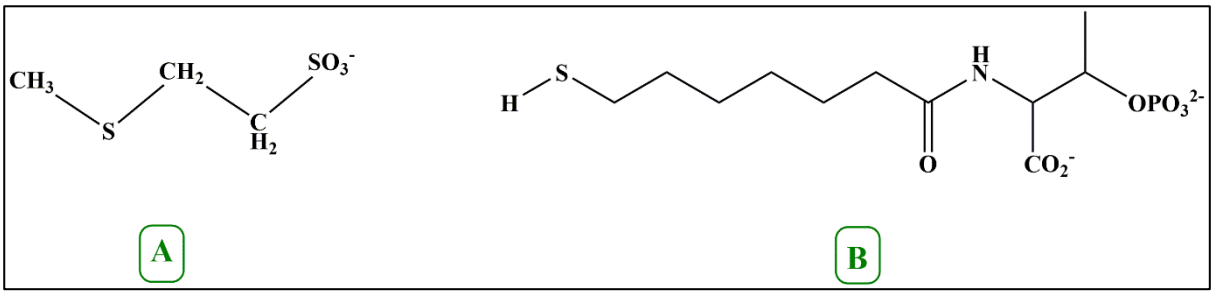

Figure 5.6. Structures of A: Methyl coenzyme M, CH_3-S-CoM and B: Coenzyme B, CoB-S-H.

Using a variety of spectroscopic techniques, the structure of native Fe_{430} was determined and this structure shows a significant non-planar geometry. Figure (5.7) shows that Fe_{430} contains a Ni(II), which can be four- or six-coordinate. The studies suggested that a Ni(II) site needs to be reduced to Ni(I) because the enzyme is only active when the resting Ni(II) state is reduced[30].

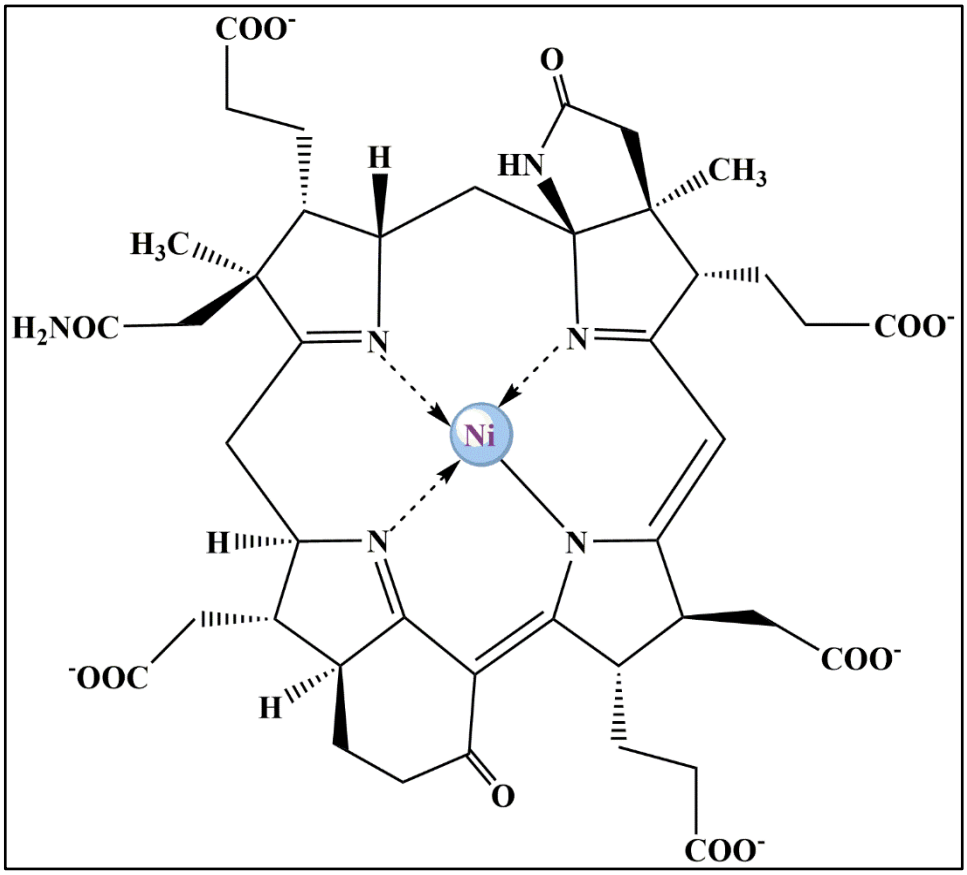

Figure 5.7. Structure of the active site Fe_{430} cofactor.

5.3.5 Superoxide Dismutase.

Superoxide dismutase (SOD) is a metalloenzyme that catalyzes the disproportionation of the superoxide radical anion (O_2^-) to molecular oxygen (O_2) and peroxide (O_2^{2-})[16]. This process occurs *via* two steps wherein the metal is first reduced and then oxidised by superoxide, as shown in Equations (5.9) and (5.10). Equation (5.11) is the overall reaction[31-34].

$$M^{(n+1)} + O_2^{\cdot -} \longrightarrow M^{(n+)} + O_2 \qquad (5.9)$$

$$M^{(n+)} + O_2^{\cdot -} + 2H^+ \longrightarrow M^{(n+1)} + H_2O_2 \qquad (5.10)$$

$$2O_2^{\cdot -} + 2H^+ \longrightarrow O_2 + H_2O_2 \qquad (5.11)$$

According to the metal species, the SODs are generally classified into five types: copper- and zinc-containing SOD, iron- and zinc-containing SOD, iron-containing SOD, manganese-containing SOD and nickel-containing SOD.

Nickel-containing SOD (NiSOD) has been isolated and structurally characterized from various *Streptomyces* species[32-37]. Studies indicated that the metalloenzyme contains Ni(III) and suggested that a nitrogen (presumably histidine), is an axial ligand to Ni(III). Furthermore, a thiolate ligand was implicated. The possible structures of the NiSODs active sites are shown in Figure (5.8). These structures for NiSOD are consistent with X-ray absorption (XAS) investigations of the enzyme from *Streptomyces seoulensis*. These investigations showed that the structures of NiSOD are characterised as two forms the mononuclear and binuclear. The mononuclear structure involves three S-donor amino acids (one methionine and two cysteines) ligating the Ni. It was inferred from the hyperfine structure observed in the EPR spectrum that an axial N-donor is present in the oxidised enzyme. By the addition of a N- and O-donor ligand, the five- coordinate site for oxidised enzyme is completed. Upon reduction, one of the N- or O-donor ligand is lost. The absence of the apical N-donor is consistent with the planar geometry determined for the reduced form and with Ni(III)/Ni(II) chemistry. The alternative binuclear structure involves only the cysteine residues in the protein. The Extended X-ray Analysis Fine Structure Spectroscopy (EXAFS) indicated that the thiolate ligands bind to the Ni as both terminal and bridging ligands, as shown in Figure (5.8).

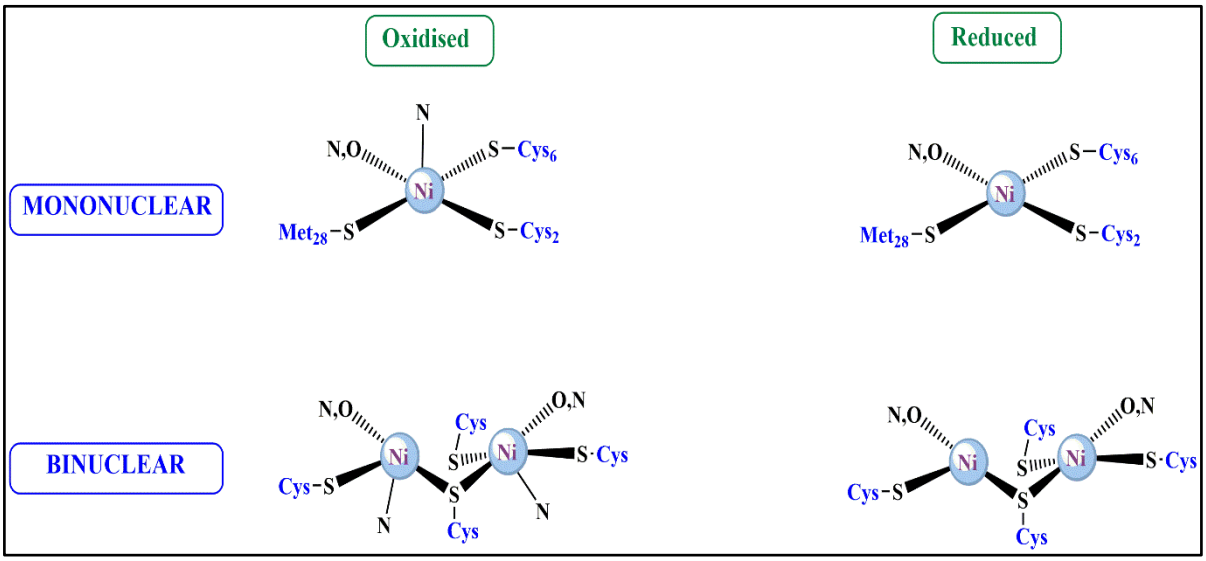

Figure 5.8. Possible structures for the NiSODs active sites.

5.3.6 Glyoxalase I.

As a normal part of metabolism, the glyoxalase system functions by converting the hemimercaptal formed from the nonenzymatic reaction of methylglyoxal and glutathione (GSH) into D-lactate[16]. As shown in Equations (5.12) and (5.13), Glyoxalase I catalyzes the first step in the process of the conversion of the hemimercaptal into the thioester of D-lactate[38]. Physiologically, this reaction is relevant in the detoxification of methylglyoxal continuously

formed as a side product of glycolysis. In addition, methylglyoxal likely has toxic effects by reacting with RNA, DNA or proteins[39].

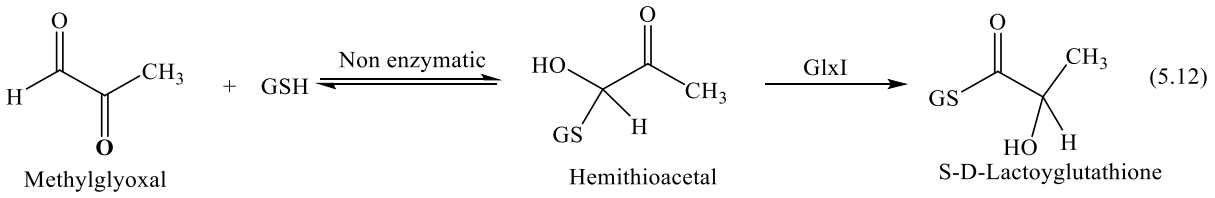

(5.12)

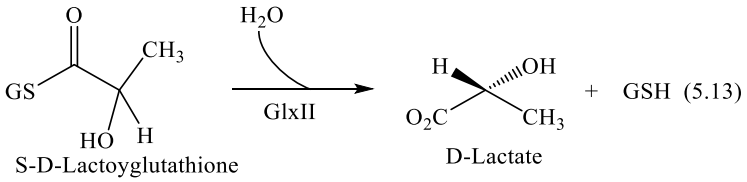

(5.13)

All studies of the glyoxalase I have shown that it requires a metal in order to be active. The study on the enzyme from *Escherichia coli* exhibited the first example of a nickel-bound isomerase (Ni-Glx I)[40].

This (Ni-Glx I) is different to other enzymes (yeast and human Glx I) which are Zn dependent[41]. In a number of pathogenic bacteria, sequence homology between *Eusherichia coli* enzyme and putative (Glx I) genes suggests that (Glx I) may be a new target for the development of antimicrobial agents[42]. X-ray crystallography studies[43-46] of the enzyme from *Escherichia coli* (Glx I) reveals an octahedral Ni site coordinated with residues of His_5, His_{74}, Glu_{56}, Glu_{122} and two (H_2O) molecules located at 2.1 and 2.2 Å, as shown in Figure (5.9). In contrast, the X-ray crystal structure of human (Glx I) reveals an octahedral Zn site coordinated with residues of His_{126}, Gln_{33}, Glu_{99}, Glu_{172} and two (H_2O) molecules located at 2.1 and 2.8 Å. Although *Escherichia coli* (Glx I) has only 36% sequence identity with *Homo sapiens* (Glx I), three of the four ligands (one histidine and two glutamine) are conserved[40]. The fourth ligand in *Escherichia coli* (Ni-Glx I) was assigned to His_5, replacing Gln_{33} in *Homo sapiens* based on sequence homology.

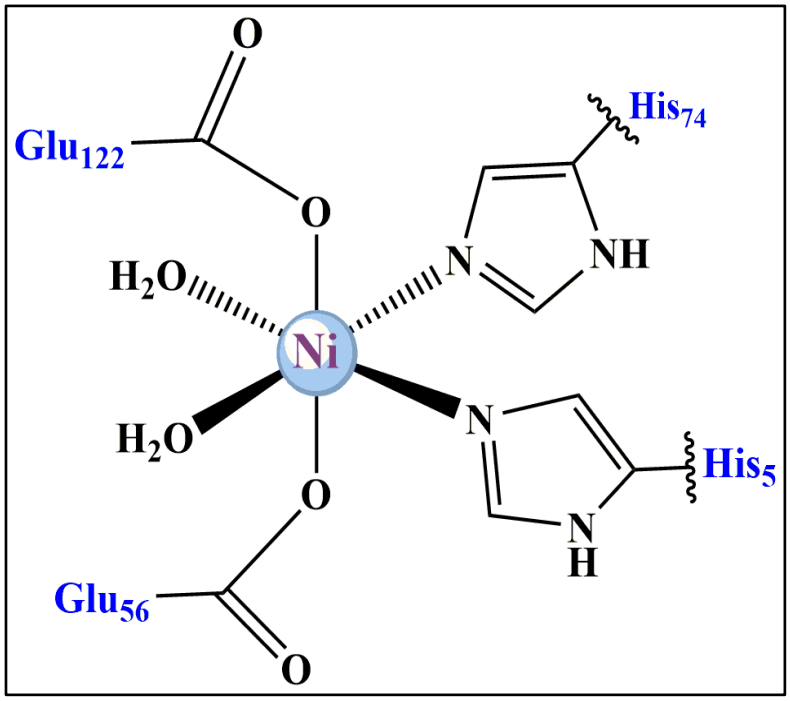

Figure 5.9. The structure of active site of Ni-Glx I.

5.4 Protonation of thiolate ligands in mononuclear complexes.

Although there are only few kinetics studies on the protonation of coordinated thiolate, a kinetically and mechanistically rich chemistry has been revealed by these few studies[6]. The studies on the reactions of the distorted square-planar complexes [Ni(SC_6H_4R-4)$_2$(dppe)] (R= H, Me, MeO or Cl; and dppe= $Ph_2PCH_2CH_2PPh_2$) with mixtures of $lutH^+$ and lut (lut= 2,6-dimethylpyridine) showed that these are equilibrium reactions involving a single protonation of complex[4], Figure (5.10).

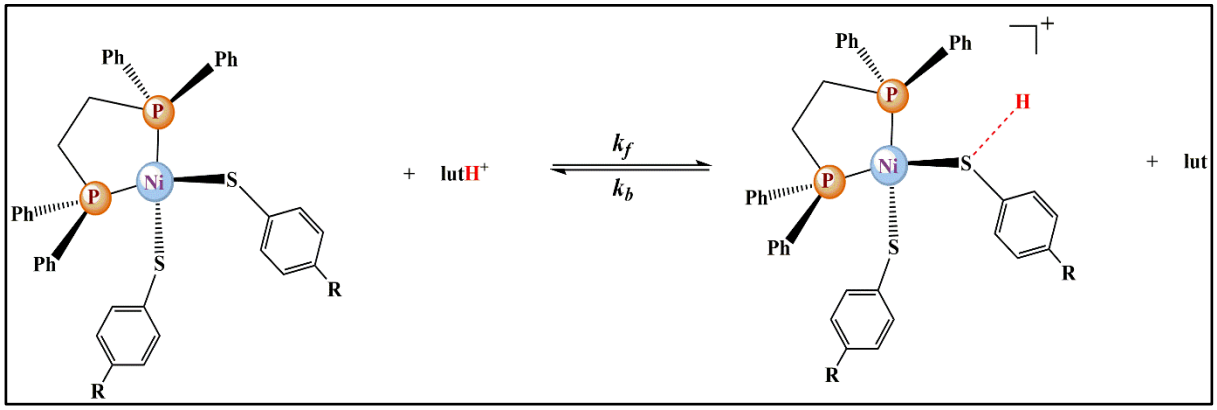

Figure 5.10. The equilibrium reaction between [Ni(SC_6H_4R-4)$_2$(dppe)] complex and $lutH^+$ acid.

Using stopped-flow spectrophotometry, the reactions are monitored at a single wavelength and the absorbance changes are typical of equilibrium reactions. Hence, at constant concentrations of [complex] and [lut], the absorbance change increases with increasing the concentration of

acid [lutH$^+$]. Similarly, at constant concentration of [complex] and [lutH$^+$], the absorbance change decreases with increasing the concentration of base [lut]. In the simplest cases, the rate law shown in Equation (5.14) is observed and is consistent with an equilibrium reaction involving a single proton transfer. A graph of k_{obs}/[lut] against [lutH$^+$]/[lut] is linear

$$k_{obs} = k_f[\text{lutH}^+] + k_b[\text{lut}] \qquad (5.14)$$

Where k_f is the rate constant for protonation of thiolate and k_b is the rate constant for deprotonation of thiol.

The pK_a of lutH$^+$ in MeCN is known (15.4), so the pK_a of the coordinated thiols can be calculated for all different (SC_6H_4R-4) derivatives. These studies show that the pK_as are remarkably insensitive to the nature of 4-R-substituent: the pK_a values cover the narrow range 15.1 (R= NO_2) to 15.8 (R= MeO) in MeCN in comparison with the two units' difference in the aqueous pK_as of the corresponding free thiols {4.68 (R= NO_2); and 6.76 (R= MeO)}. Similar effects were observed in other systems, when the "Electronic Buffer" effect on the molybdenum-sulfur interactions in molybdoenzyme model complexes were investigated by using the gas-phase photoelectron spectroscopy (PES)[47].

The study of the temperature dependence for the reactions of the complexes [Ni(SC_6H_4R-4)$_2$(dppe)] with mixtures of lutH$^+$ and lut revealed the following features. (i) The value of $\Delta G^{\ddagger}_{298}$= 13.6 ±0.3 kcal mol^{-1} for all derivatives. (ii) The $\Delta H^{\ddagger}$ and $\Delta S^{\ddagger}$ values are dependent on the nature of the 4-R substituents: $\Delta H^{\ddagger}$ becomes larger and $\Delta S^{\ddagger}$ becomes more positive; as R becomes more electron-withdrawing. (iii) No detectable kinetic isotope effect was observed when the complexes [Ni(SC_6H_4R-4)$_2$(dppe)] reacted with lutD$^+$.

A more complicated kinetic behaviour is observed for the reaction of [Ni($SC_6H_4NO_2$-4)$_2$(dppe)] with mixtures of lutH$^+$ and lut. In addition, only at a constant concentration of acid [lutH$^+$], is the plot of k_{obs}/[lut] against [lutH$^+$]/[lut] linear with a positive intercept. The slope of the line decreases as the concentration of acid increases. The intercept of each line is the same.

Further studies[3] on the reaction of square-planar complexes [Ni(SC_6H_4R-4)(triphos)]$^+$ (R= H, Me, MeO, Cl or NO_2; and triphos = $PhP(CH_2CH_2PPh_2)_2$) with mixtures of lutH$^+$ and lut revealed an analogous behaviour to that of [Ni($SC_6H_4NO_2$-4)$_2$(dppe)]. Figure (5.11) shows the mechanism associated with this reaction.

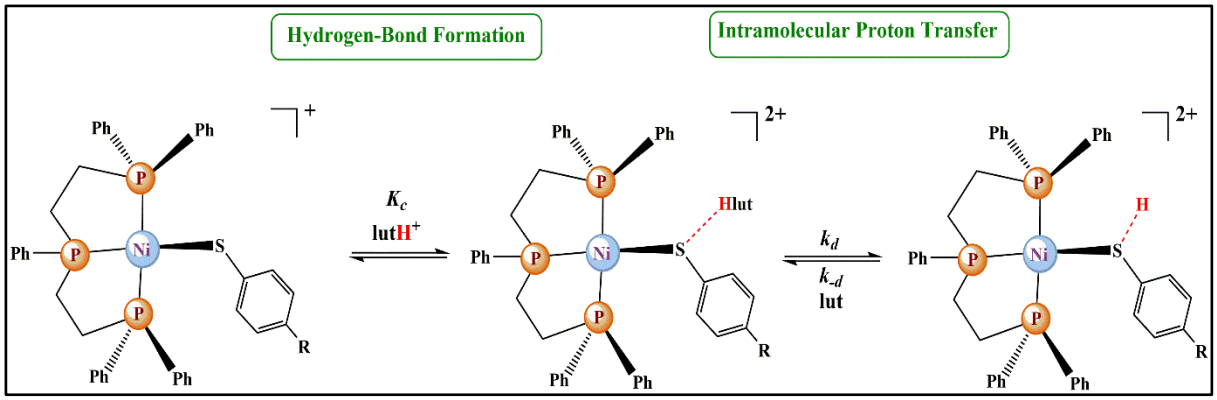

Figure 5.11. Mechanism for the reaction between $[Ni(4\text{-}RC_6H_4S)(triphos)]^+$ complex and ($lutH^+$) acid involving initial hydrogen-bonding of the acid to coordinated thiolate followed by intramolecular proton transfer step.

This mechanism involves two coupled equilibria. The first step is the formation of a species in which the $lutH^+$ hydrogen-bonds to the sulfur of the thiolate, and is followed by the second step which is an intramolecular transfer of the proton to the sulfur. In reality, this mechanism operates for all thiolate complexes described above, but it is only with $[Ni(SC_6H_4NO_2\text{-}4)_2(dppe)]$ and $[Ni(SC_6H_4R\text{-}4)(triphos)]^+$ complexes that the hydrogen-bonded precursor is detectable by the kinetics. The rate law in Equation (5.15) is that for the mechanism shown in Figure (5.11), the derivation of this rate law is presented in Appendix A (***section A.2***). This rate law can be simplified when $K_c[lutH^+] < 1$, as shown in Equation (5.16), which is identical in form to the rate law observed for the reactions of $[Ni((SC_6H_4R\text{-}4)_2(dppe)]$ (R= H, Me, MeO or Cl).

$$k_{obs} = \frac{K_c k_d [lutH^+]}{1 + K_c [lutH^+]} + k_{-d}[lut] \qquad (5.15)$$

$$k_{obs} = K_c k_d [lutH^+] + k_{-d}[lut] \qquad (5.16)$$

In these systems, the proton transfer from acid to sulfur is slow for different reasons, the first reason is likely the effect of the 4-R-substituent on the basicity of the sulfur (weak basicity) and other reason is probably the steric effect around the sulfur by the phenyl groups, which are attached to the phosphorus donors in triphos, resulting in the lone pairs of electrons on the sulfur 'buried' in the surrounding phenyl groups[7-10], this behaviour will be discussed in more details in the next Chapter.

For all $[Ni(SC_6H_4R\text{-}4)(triphos)]^+$, the complicated rate law is observed, so it is possible to investigate how various factors can affect the rate of intramolecular proton transfer. The measurement of activation parameters for the intramolecular proton transfer reveals that as the

4-R-substituent becomes more electron-donating, $\Delta H^{\pm}$ becomes smaller and $\Delta S^{\pm}$ becomes less positive. The same trends are observed for the overall reactions for [Ni(SC_6H_4R-4)$_2$(dppe)] complexes.

Studies on the isotope effect for the reaction of [Ni(SC_6H_4R-4)(triphos)]$^+$ with lutD$^+$ showed that the nature of the 4-R-substituent affects the isotope effect . When the 4-R-substituent is electron-donating, a normal isotope effect is observed (R= Me, k^H/k^D= 1.3; R= MeO, k^H/k^D= 1.2). However, with more electron-withdrawing substituent an inverse isotope effect is observed (R= NO_2, k^H/k^D= 0.39; R= Cl, k^H/k^D= 0.88). It appears that a normal isotope effect is observed when the base is strong (electron-donating R-substituent) and the transition state is product-like, whilst an inverse isotope effect is observed when the base is weaker (electron-withdrawing R-substituent) and the transition state is reactant-like.

Protonation of coordinated pyridinethiolates has been explored using a combination of kinetic studies, Amsterdam Density Functional (ADF) calculations and Modified Structural Intermediate Neglect of Differential Overlap (MSINDO) calculations. All these various methods help to understand the protonation chemistry of this type of ligand[5]. The complexes [Ni(2-Spy)(triphos)]$^+$ and [Ni(4-Spy)(triphos)]$^+$ (Spy = pyridinethiolate) have been synthesised and structurally characterised using both spectroscopicy and X-ray crystallography. For the [Ni(4-Spy)(triphos)]$^+$ complex, the 4-pyridinethiolate coordinates to Ni through the sulfur to form a distorted square-planar of the complex, whereas the 2-pyridinethiolate in the [Ni(2-Spy)(triphos)]$^+$ coordinates to Ni through both the sulfur and nitrogen (as a bidentate ligand) to produce a five coordinate with nickel.

The kinetic studies of the reaction between [Ni(4-Spy)(triphos)]$^+$ and mixtures of lutH$^+$ and lut in MeCN show that the protonation reaction is very fast (complete within 2 ms), and it is associated with a slight spectroscopic change in the UV-visible spectrum. This behaviour is consistent with rapid protonation of the uncoordinated nitrogen atom.

However, the reaction of [Ni(2-Spy)(triphos)]$^+$ with lutH$^+$ and lut in MeCN (under identical conditions) results in a much slower reaction. Furthermore, the kinetics of reactions are quite distinct and unusual from those observed in the similar equilibrium reactions of [Ni(SC_6H_4R-4)$_2$(dppe)] and [Ni(SC_6H_4R-4)(triphos)]$^+$.

The kinetics of the reaction of $[Ni(2\text{-}Spy)(triphos)]^+$ with $lutH^+$ and lut in MeCN are consistent with the rate law in Equation (5.17) and with the suggested mechanism in Figure (5.12). The mechanism of protonation of $[Ni(2\text{-}Spy)(triphos)]^+$ involves protonation at the sulfur site because the lone pair of electrons on nitrogen binds to the nickel, so protonation cannot occur at the nitrogen site. It is suggested that protonation of the sulfur site labilises the Ni-N bond, resulting in dissociation of the nitrogen, and after that the proton will transfer from sulfur to nitrogen site because the free nitrogen becomes more basic than coordinated sulfur. This proposal is consistent with the theoretical calculations which predict that the most thermodynamically favourable form of the 2-Spy ligand is that in which the nitrogen is not coordinated.

$$k_{obs} = \frac{k_e[\text{lutH}^+] + \left(\frac{k_{-e}k_{-g}}{k_g}\right)[\text{lut}]}{1 + \left(\frac{k_{-e}}{k_g}\right)[\text{lutH}^+]} \qquad (5.17)$$

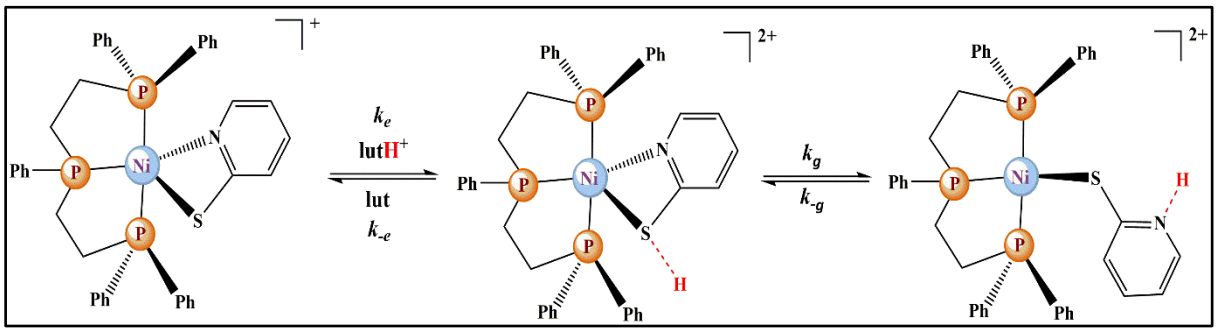

Figure 5.12. Suggested mechanism for the equilibrium reaction of $[Ni(2\text{-}Spy)(triphos)]^+$ with mixtures of $lutH^+$ and lut involving chelate ring opening of the 2-pyridinethiolate ligand and the prototropic shift from sulfur to nitrogen.

Further studies on the protonation of other bidentate pyridinethiolate ligands have been performed[48]. Both $[IrH(2\text{-}Spy)(CO)(PPh_3)_2]^+$ and $[OsH(2\text{-}Spy)(CO)(PPh_3)_2]$ complexes have been synthesised and structurally characterised by X-ray crystallography and shown that the 2-pyridinethiolate ligand is also a bidentate (as observed in $[Ni(2\text{-}Spy)(triphos)]^+$). However, the reaction for either $[IrH(2\text{-}Spy)(CO)(PPh_3)_2]^+$ or $[OsH(2\text{-}Spy)(CO)(PPh_3)_2]$ with HBF_4 did not result in protonation of the 2-pyridinethiolate ligand. Only in the case of the Os complex was the product identified as $[Os(\eta^2\text{-}H_2)(2\text{-}Spy)(CO)(PPh_3)_2]$ (*i.e.* protonation at the hydride ligand).

In the first part of the thesis, we have presented the studies on biologically relevant synthetic Fe-S-based clusters involving protonation of sulfide sites. In this part, we will focus on proton

transfer to sterically demanding thiolate ligands as models for the reactions of coordinated cysteinate which is a common ligand in metalloenzymes.

5.5 References.

1. C. B. Allan, G. Davidson, S. B. Choudhury, Z. Gu, K. Bose, R. O. Day and M. J. Maroney, *Inorg. Chem.*, 1998, **37**, 4166-4167.

2. W. Clegg and R. A. Henderson, *Inorg. Chem.*, 2002, **41**, 1128-1135.

3. V. Autissier, P. M. Zarza, A. Petrou, R. A. Henderson, R. W. Harrington and W. C. Clegg, *Inorg. Chem.*, 2004, **43**, 3106-3115.

4. V. Autissier, W. Clegg, R. W. Harrington and R. A. Henderson, *Inorg. Chem.*, 2004, **43**, 3098-3105.

5. A. L. Petrou, A. D. Koutselos, H. S. Wahab, W. Clegg, R. W. Harrington and R. A. Henderson, *Inorg. Chem.*, 2011, **50**, 847-857.

6. R. A. Henderson, *BioInorg. React. Mech.* , 2012, **8**, 1-37.

7. A. Alwaaly and R. A. Henderson, *J. Chem. Soc.,Chem. Commun.*, 2014, **50**, 9669-9671.

8. A. Alwaaly and R. A. Henderson, *J. Coord.Chem.*, 2015, **68**, 3069-3078.

9. A. Alwaaly, W. Clegg, R. A. Henderson, M. R. Probert and P. G. Waddell, *J. Chem. Soc., Dalton Trans.*, 2015, **44**, 3307-3317.

10. A. Alwaaly, W. Clegg, R. W. Harrington, A. L. Petrou and R. A. Henderson, *J. Chem. Soc., Dalton Trans.*, 2015, **44**, 11977-11983.

11. R. A. Henderson, D. L. Hughes, R. L. Richards and C. Shortman, *J. Chem. Soc., Dalton Trans.*, 1987, 1115-1121.

12. S. A. Wander, J. H. Reibenspies, J. S. Kim and M. Y. Darensbourg, *Inorg. Chem.*, 1994, **33**, 1421-1426.

13. S. B. Mulrooney and R. P. Hausinger, *FEMS Microbiology Reviews*, 2003, **27**, 239-261.

14. E. L. Hegg, *Acc. Chem. Res.*, 2004, **37**, 775-783.

15. S. W. Ragsdale, *Chem. Rev.*, 2006, **106**, 2217-3337.

16. M. J. Maroney, *Curr. Opin. Chem. Biol.*, 1999, **3**, 188-199.

17. N. E. Dixon, C. Gazzola, J. J. Watters, R. L. Blakele and B. Zerner, *J. Am. Chem. Soc.*, 1975, **97**, 4130-4131.

18. H. L. T. Mobley and R. P. Hausinger, *Microbiol. Rev.*, 1989, **53**, 85-108.

19. E. Jabri, R. P. H. M. B. Carr and P. A. Karplus, *Scince*, 1995, **268**, 998-1004.

20. S. Benini, W. R. Rypniewski, K. S. Wilson, S. Miletti, S. Ciurli and S. Mangani, *Structure*, 1999, **7**, 205-216.

21. A. Volbeda, M-H Charon, C. Pina, E. C. Hatchikian, M. Frey and J. C. Fontecilla-Camps, *Nature*, 1995, **373**, 580-587.

22. Y. Higuchi, T. Yagi and N. Yasuoka, *Structure*, 1997, **5**, 1671-1680.

23. G. W. Bartholomew and M. Alexander, *App. Environ. Microbiol.*, 1979, **37**, 932-937.

24. H. Dobbek, V. Svetlitchnyi, L. Gremer, R. Huber and O. Meyer, *Scince*, 2001, **293**, 1281-1285.

25. S. Huang, P. A. Lindahl, C. Wang, G. N. Bennett, F. B. Rudolph and J. B. Hughes, *App. Environ. Microbiol.*, 2000, **66**, 1474-1478.

26. J. Xia, Z. Hu, C. V. Popescu, P. A. Lindahl and E. Münck, *J. Am. Chem. Soc.*, 1997, **119**, 8301-8312.

27. R. K. Thauer, *Microbiology*, 1998, **144**, 2377-2406.

28. U. Ermler, W. Grabarse, S. Shima, M. Goubeaud and R. K. Thauer, *Scince*, 1997, **278**, 1457-1462.

29. H. Won, K. D. Olson, D. R. Hare, R. S. Wolfe, C. Kratky and M. F. Summers, *J. Am. Chem. Soc.*, 1992, **114**, 6880-6892.

30. S. Rospert, M. Voges, A. Berkessel, S. P. J. Albracht and K. T. R, *J. Eur. Biochem.* , 1992, **210**, 101-107.

31. D. L. Sorkin and A-F Miller, *Biochemistry*, 1997, **36**, 4916-4924.

32. D. P. Barondeau, C. J. Kassmann, C. K. Bruns, J. A. Tainer and E. D. Getzoff, *Biochemistry*, 2004, **43**, 8038-8047.

33. J. Wuerges, J-W Lee, Y-I Yim, H-S Yim, S-O Kang and K. D. Carugo, *Procee. Nat. Aca. Sci.*, 2004, **101**, 8569-8574.

34. J. Shearer, K. L. Peck, J. C. Schmitt and K. P. Neupane, *J. Am. Chem. Soc.*, 2014, **136**, 16009-16022.

35. J. Chun, H-D Youn, Y-I Yim, H. Lee, M. Y. Kim, Y. C. Hah and S-O Kang, *Int. J. Syst. Bacteriol.*, 1997, **47**, 492-498.

36. H-D Youn, H. Youn, J-W Lee, Y-I Yim, J. K. Lee, Y. C. Hah and S-O Kang, *Arch. Biochem. Biophys.*, 1996, **334**, 341-348.

37. H-D Youn, E-J Kim, J-H Roe, Y. C. Hah and S-O Kang, *J. Biochem.*, 1996, **318**, 889–896.

38. S. L. Clugston, R. Yajima and J. F. Honek, *J. Biochem.*, 2004, **377**, 309–316.

39. P. J. Thornalley, *Chem. Biol. Int.*, 1998, **112**, 137-151.

40. S. L. Clugston, J. F. J. Barnard, R. Kinach, D. Miedema, R. Ruman, E. Daub and J. F. Honek, *Biochemistry*, 1998, **37**, 8754-8763.

41. E. M. Frickel, P. Jemth, M. Widersten and B. Mannervik, *J. Biol. Chem.*, 2001, **276**, 1845-1849.

42. S. L. Clugston and J. F. Honek, *J. Mol. Evol.*, 2000, **50**, 491-495.

43. A. D.Cameron, B. Olin, M. Ridderström, B. Mannervik and T. A. Jones, *J. EMBO*, 1997, **16**, 3386-3395.

44. G. Davidson, S. L. Clugston, J. F. Honek and M. J. Maroney, *Inorg. Chem.*, 2000, **39**, 2962-2963.

45. U. Suttisansanee, K. Lau, S. Lagishetty, K. N. Rao, S. Swaminathan, J. M. Sauder, S. K. Burley and J. F. Honek, *J. Biol. Chem.*, 2011, **286**, 38367-38374.

46. U. Suttisansanee, Y. Ran, K. Y. Mullings, N. Sukdeo and J. F. Honek, *Metallomics*, 2015, **7**, 605-612.

47. B. L. Westcott, N. E. Gruhn and J. H. Enemark, *J. Am. Chem. Soc.*, 1998, **120**, 3382-3386.

48. L. Dahlenburg and M. Kühnlein, *J. Eur. Inorg. Chem.*, 2000, 2117-2125.

Chapter 6: Orientation of Coordinated Thiolate Modulates Rates of Protonation of [Ni(thiolate){PhP($CH_2CH_2PPh_2$)$_2$}]$^+$

6.1 Introduction.

Proton transfer is a fundamental reaction which pervades many areas of chemistry and biology; from the action of metalloenzymes such as hydrogenases and nitrogenases to room-temperature ferroelectricity[1-4]. In general, the mechanism of proton transfer from separated acid (AH^+) to base (B) involves initial formation of a hydrogen-bonded precursor intermediate (AH^+…B) which then undergoes intramolecular proton transfer from A to B, and finally subsequent diffusion apart to produce A and BH^+, Equation (6.1). Usually, the kinetics of equilibrium proton transfer reactions are simple because the hydrogen-bonded precursor intermediate does not attain a sufficient concentration to be detected, Equation (6.2) (k_f = rate constant for protonation of B, k_b = rate constant for deprotonation of BH^+)[5].

$$AH^+ + B \underset{}{\overset{k_f}{\rightleftharpoons}} AH...B^+ \rightleftharpoons A...HB^+ \underset{k_b}{\rightleftharpoons} A + BH^+ \qquad (6.1)$$

$$\text{Rate} = \{k_f[AH^+] + k_b[A]\}[B] \qquad (6.2)$$

Because the rate-limiting step is usually the diffusion together of the acid and base (k_{diff} = 3.7 x 10^{10} dm^3 mol^{-1} s^{-1} in MeCN)[6], varying the rates of many protons transfer reactions is difficult. Usually, proton transfer reactions are not particularly sensitive to steric factors. However, an exception to this is the reactions of square-planar [Ni(thiolate)(triphos)]$^+$ (triphos = PhP($CH_2CH_2PPh_2$)$_2$) with mixtures of $lutH^+$ and lut (lut = 2,6-dimethylpyridine), Equation (6.3). Kinetic studies on these reactions have shown that proton transfer to the sulfur is slow and the kinetics are complicated. This unusual behaviour is, at least in part, because the phenyl substituents on triphos ligand hinder the accessibility of the sulfur site from the sterically-demanding $lutH^+$. The precursor hydrogen-bonded intermediate, {[Ni(thiolate)(triphos)]…Hlut}$^{2+}$, accumulates because its formation $(k_1^R)^{lut}$ is rapid but the intramolecular proton transfer step $(k_2^R)^{lut}$ is slow. The mechanism is shown in Figure (6.1)[7-12].

$$[Ni(SC_6H_4)(triphos)]^+ + lutH^+ \rightleftharpoons [Ni(SHC_6H_4)(triphos)]^{2+} + lut \qquad (6.3)$$

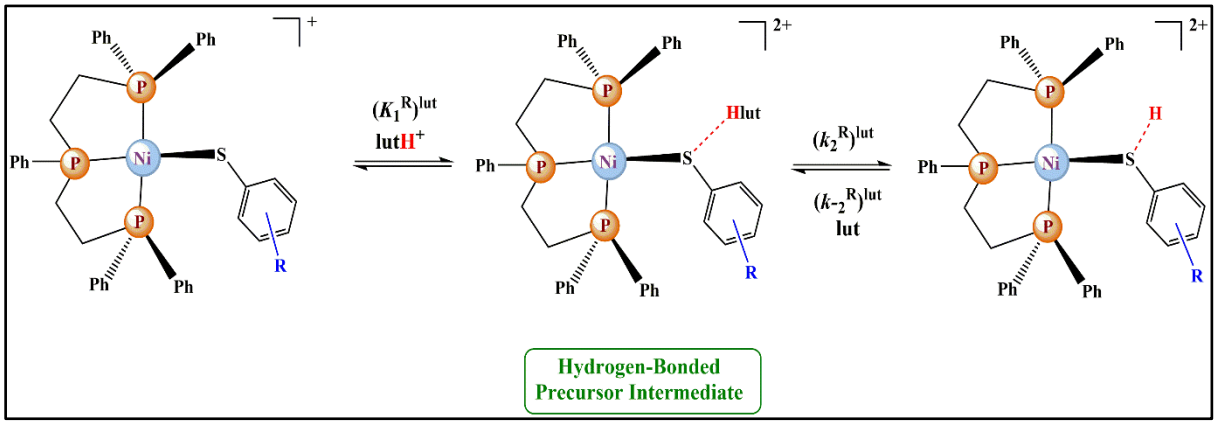

Figure 6.1. Mechanism for the reaction of [Ni(thiolate)(triphos)]$^+$ with mixtures of lutH$^+$ and lut in MeCN.

This chapter will present and compare the kinetics of the protonation reactions of [Ni(SC_6H_4R-2)(triphos)]BPh_4 (R = Me, MeO, H, Cl) and [Ni($SC_6H_3Me_2$-2,6)(triphos)]BPh_4 with lutH$^+$ or picH$^+$ (pic.= 4-methylpyridine). The studies reported herein indicate how substituents on the thiolate modulate the rates of proton transfer. The thiolate substituents themselves have only a minor direct effect on the approaching acid. The principal means by which the thiolate substituents affect the rate is by controlling the orientation of the thiolate and hence regulating from which side of the square plane the protonation occurs. However, as will be shown in this chapter, in certain circumstances, the substituents on the acids have a significant effect on the rates of the proton transfer reactions and this is because the phenyl substituents on triphos present different barriers to the approaching acid on the two sides of the square plane of [Ni(thiolate)(triphos)]$^+$.

6.2 Experimental and Methodology.

6.2.1 General Experimental.

All experiments (the preparation of compounds and the kinetics studies) were all performed under an atmosphere of dinitrogen because all compounds are sensitive to air, particularly in solution.

6.2.2 Solvents.

All solvents were dried and distilled under dinitrogen immediately prior to use. Tetrahydrofuran (THF) and diethyl ether were distilled in the presence of sodium wire. Acetonitrile was distilled and dried over calcium hydride, and methanol was distilled from $Mg(OMe)_2$ (generated *in situ*).

6.2.3 Spectroscopic Characterisation.

6.2.3.1 Proton Nuclear Magnetic Resonance Spectroscopy (^{1}HNMR Spectroscopy).

^{1}H NMR and $^{31}P\{^1H\}$ NMR spectra were recorded on a 400 MHz Jeol spectrometer. Samples were prepared in dry, degassed CD_3CN under an atmosphere of dinitrogen and chemical shifts are referenced relative to tetramethylsilane (TMS).

6.2.3.2 Fourier Transform Infrared Spectroscopy (FTIR Spectroscopy).

FTIR spectra were recorded on a Platinum-ATR (Alpha) spectrophotometer. Because all complexes are air sensitive, the measurements were performed inside the dry box (BELLE- Dry Box). The results were analysed by OPUS Software.

6.2.3.3 X-Ray Crystallography.

All the X-ray crystallographic data were collected by the X-ray service at Newcastle University (Newcastle upon Tyne). Crystal structure data for all characterised complexes were collected at 150K on an Xcalibure, Atlas, Gemini ultra differactometer equipped with an Oxford Cyrostream Plus open-flow N_2 cooling device using Mo ($\lambda_{MoK\alpha}$ = 0.71073 Å) radiation. Cell refinement, data collection and data reduction were undertaken using CrysAliPro[13].

Using Olex2[14], all structures were solved by direct methods using XT[15] and refined on F^2 values for all unique data using XL[16]. The non-hydrogen atoms were refined anisotropically. The positions of hydrogen atoms attached to fully occupied heteroatoms have been picked from

peaks in the Fourier difference map. Other hydrogen atoms have been positioned with idealised geometry using the riding model with U_{iso}(H) set at 1.2 times U_{eq} for the parent atom.

6.2.3.4 Stopped-Flow Spectroscopy.

All kinetics studies for all [Ni(thiolate)(triphos)]$^+$ complexes were performed on a stopped-flow spectrophotometer , as described in the Chapter 2 (***section 2.4.1***).

6.3 Preparation of Compounds.

The following chemicals were purchased from Sigma-Aldrich and used as received: nickel chloride hexahydrate ($NiCl_2.6H_2O$), bis(2-diphenylphosphinoethyl)phenylphosphine (triphos), thiophenol (PhSH), 2-methylthiophenol (HSC_6H_4Me-2), 2-methoxythiophenol (HSC_6H_4OMe-2), 2,6-dimethylthiophenol ($HSC_6H_3Me_2$-2,6), 2-chlorothiophenol (HSC_6H_4Cl-2), 2,6-dimethylpyridine (lut), 4-methylpyridine (pic), chlorotrimethylsilane (Me_3SiCl), sodium tetraphenylborate ($NaBPh_4$), and sodium cubes (Na). The deuterated solvent, acetonitrile (CD_3CN) was purchased from Goss Scientific and used as received.

6.3.1 Preparation of [Ni(thiolate)(triphos)]$^+$ complexes.

6.3.1.1 Preparation of [$NaSC_6H_4R$-2] (R= H, Me, MeO and Cl) and ($NaSC_6H_3Me_2$-2,6).

All sodium thiolates were prepared by mixing the corresponding thiol with an equimolar amount of sodium in diethyl ether under an atmosphere of dinitrogen. All manipulations were performed in a fume cupboard[17].

Sodium metal (0.46 g, 20 mmol) was cut into small pieces (*ca* 1.5-3.0 mm diameter), and then quickly washed in diethyl ether to remove any trace amounts of oil. These pieces of sodium were added to a Schlenk flask containing diethyl ether (25 ml) that had been degassed and was under an atmosphere of dinitrogen. The HSC_6H_4R-2 [R= H, Me, MeO and Cl] or $HSC_6H_3Me_2$-2,6 (20 mmol) was then added. At room temperature, the solution was left stirring for several days until all of the sodium had reacted. A white solid was formed which was removed by filtration, washed with diethyl ether, and then dried in *vacuo*, (average yield, 92% based on Equations (6.4) and (6.5).

$$HSC_6H_4R\text{-}2 + Na \xrightarrow{R.T} NaSC_6H_4R\text{-}2 + 1/_2H_2 \quad (6.4)$$

$$HSC_6H_3Me_2\text{-}2,6 \quad + \quad Na \xrightarrow{R.T} NaSC_6H_3Me_2\text{-}2,6 \quad + \quad 1/_2H_2 \qquad (6.5)$$

6.3.1.2 Preparation of [NiCl(triphos)]BPh₄ [18].

Bis(2-diphenylphosphinoethyl)phenylphosphine [triphos] (4 g, 7.65 mmol) was dissolved in a 50:50 mixture of toluene/methanol, and then added to a solution of $NiCl_2.6H_2O$ (1.82 g, 7.65 mmol) in methanol (*ca* 25 ml). A red solution was formed and was stirred until the solid had dissolved at room temperature (*ca* 1 hour). The solution volume was reduced to (*ca* 10 ml) in *vacuo*, then a solution containing $NaBPh_4$ (2.2 g, 6.5 mmol) in methanol (10 ml) was added dropwise to form a bright yellow solid of [NiCl(triphos)]BPh_4. The product was isolated by filtration, washed with methanol and diethyl ether, and then the solid was dried in *vacuo*, (average yield, 84%).

The solid was dissolved in THF (*ca* 15 ml) and then a large excess of MeOH (*ca* 150 ml) was added, and the solution was left for two days at room temperature. The yellow crystals were formed and isolated by filtration and dried in *vacuo*. Equations (6.6) and (6.7) describe the pathways to produce [NiCl(triphos)]BPh_4.

$$NiCl_2.6H_2O \quad + \quad PhP(CH_2CH_2PPh_2)_2 \xrightarrow{R.T} [NiCl(PhP(CH_2CH_2PPh_2)_2)]Cl \quad + 6H_2O \qquad (6.6)$$

$$[NiCl(PhP(CH_2CH_2PPh_2)_2)]Cl \quad + NaBPh_4 \xrightarrow{R.T} [NiCl(PhP(CH_2CH_2PPh_2)_2)]BPh_4 \quad + \quad NaCl \qquad (6.7)$$

The identity and purity of [NiCl(triphos)]BPh_4 was confirmed by ^1H NMR and $^{31}P\ \{^1H\}$ NMR spectroscopy and the signal values were compared with literature[18], see Figures (6.2) and (6.3).

^1H NMR: δ 8.65-6.44 (m, 45H, *Ph* groups) and 3.24-2.1 (m, 8H, CH_2).

$^{31}P\ \{^1H\}$ NMR: δ 47.48 (d, J_{pp}= 50.7 Hz) and 115.50 (t, J_{pp}= 50.7 Hz).

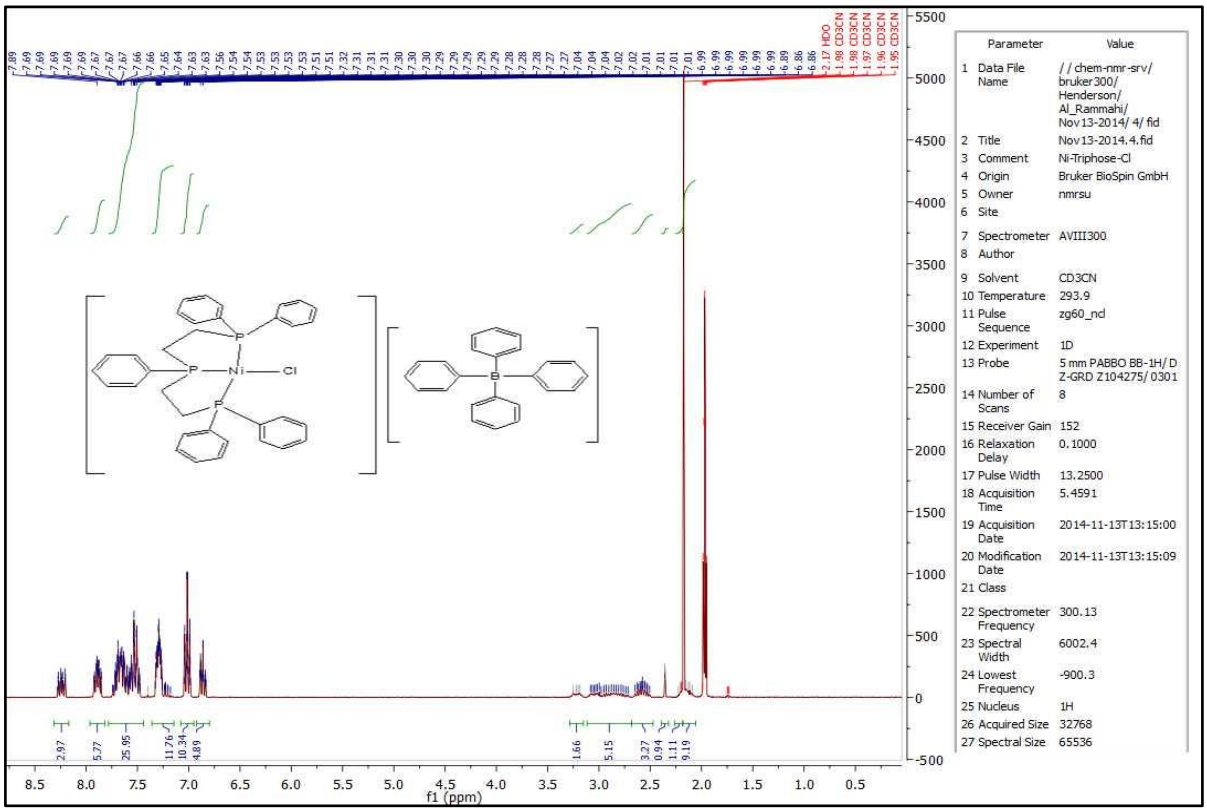

Figure 6.2. ^{1}H NMR spectrum of [NiCl(triphos)]BPh_4 in CD_3CN.

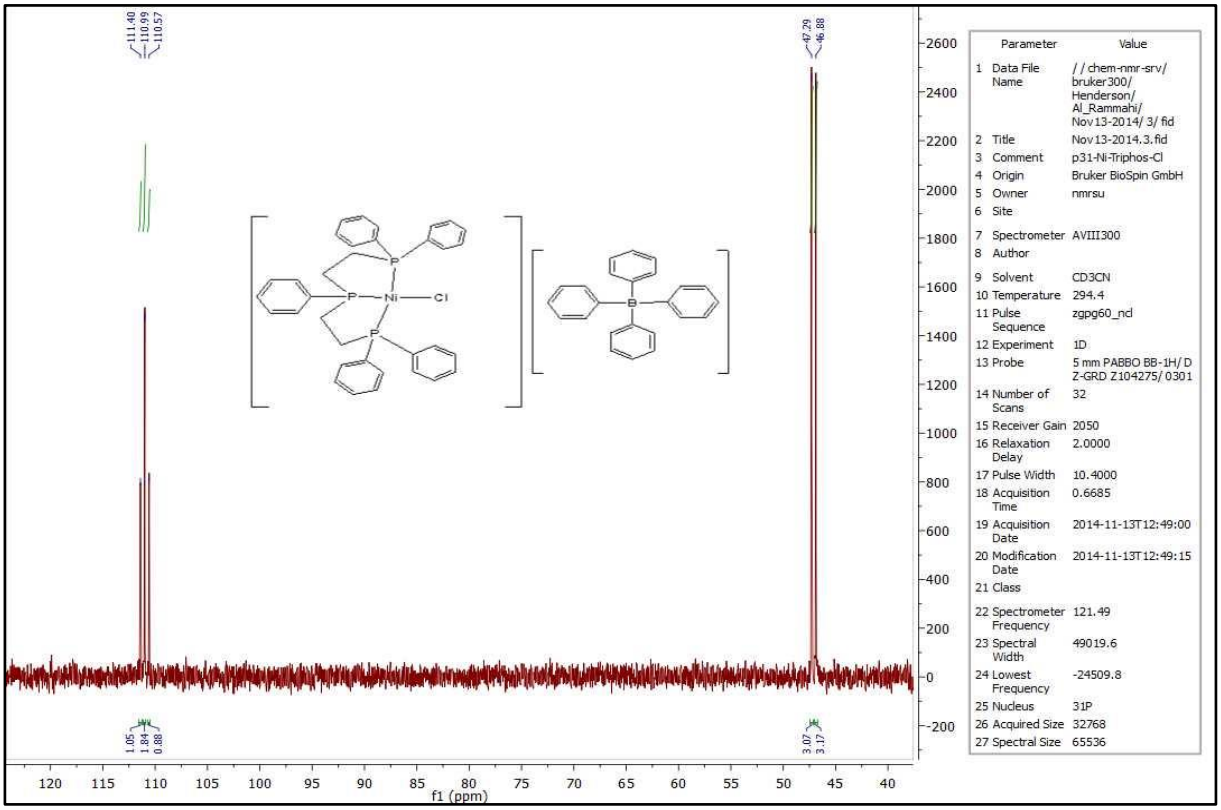

Figure 6.3. ^{31}P $\{^{1}H\}$ NMR spectrum of [NiCl(triphos)]BPh_4 in CD_3CN.

6.3.1.3 Preparation of [Ni(SC_6H_4R-2)(triphos)]BPh_4 (R= H, Me, MeO and Cl) and [Ni($SC_6H_3Me_2$-2,6)(triphos)]BPh_4 Complexes.

All complexes were prepared by an analogous route to that used to prepare [Ni(SC_6H_5)(triphos)]BPh_4, as reported by Henderson[18].

To a suspension of [NiCl(triphos)]BPh_4 (0.5g, 0.53 mmol) in dry THF (*ca* 25ml) was added a six-fold excess of solid $NaSC_6H_4$R-2 (R= H, Me, MeO and Cl) or $NaSC_6H_3Me_2$-2,6 (3.0 mmol). The yellow solution rapidly changed to red, and the mixture became homogeneous. The solution was stirred for 2 – 3 hours, and then it was filtered. The volume of the filtrate was reduced to half in *vacuo*. An excess of methanol was then added to produce a microcrystalline solid.

The solid was recrystallized by dissolving in the minimum of MeCN (*ca* 20ml), then adding a large excess of diethyl ether (*ca* 5-6 times volume of MeCN). Leaving the solution undisturbed at 3 ºC for 3-5 days produced crystals which were removed by filtration, then dried in *vacuo*. Table (6.1) describes the properties of crystals for [Ni(SC_6H_4R-2)(triphos)]BPh_4 (R= H, Me, MeO and Cl) and [Ni($SC_6H_3Me_2$-2,6)(triphos)]BPh_4 complexes.

Table (6.1): The properties of crystals and average of yield for [Ni(SC_6H_4R-2)(triphos)]BPh_4 (R= H, Me, MeO and Cl) and [Ni($SC_6H_3Me_2$-2,6)(triphos)]BPh_4 Complexes.

Complex	Crystal Form	Crystal Colour	Yield
[Ni(SC_6H_5)(triphos)]BPh_4	Needles	Red	63%
[Ni(SC_6H_4Me-2)(triphos)]BPh_4	Needles	Red	55%
[Ni(SC_6H_4OMe-2)(triphos)]BPh_4	Needles	Dark-Red	58%
[Ni($SC_6H_3Me_2$-2,6)(triphos)]BPh_4	Needles	Red-Orange	55%
[Ni(SC_6H_4Cl-2)(triphos)]BPh_4	Needles	Purple	65%

The identity and purity for all complexes were confirmed by FTIR, ^{1}H NMR, ^{31}P{^{1}H} NMR spectroscopy and X-ray crystallography. Table (6.2) shows the main ^{1}H NMR and ^{31}P{^{1}H} NMR data; and Table (6.3) shows FTIR spectroscopic data for all prepared compounds. In addition, the FTIR, ^{1}H NMR and ^{31}P{^{1}H} NMR spectra for all compounds are presented in

Appendix B. The X-ray crystallography determinations will be discussed in more details in results and discussion section.

Table (6.2): The main ^{1}H NMR spectroscopic values for[Ni(thiolate)(triphos)]BPh_4 complexes.

Complex	**^{1}H NMR**	**^{31}P{^{1}H} NMR**
[Ni(SC_6H_5)(triphos)]BPh_4	δ 8.30-6.48 (m, P*Ph* and B*Ph*, 50H),3.22-2.50 (m, CH_2, 8H)	δ 105.4 (t, J_{pp} = 41.4 Hz, P*Ph*), 52.2 (d, J_{pp} = 41.5 Hz, PPh_2)
[Ni(SC_6H_4Me-2)(triphos)]BPh_4	δ 8.22-6.45 (m, P*Ph* and B*Ph*, 49H),3.16-2.28 (m, CH_2, 8H), 1.80 (s, CH_3,3H)	δ 104.9 (t, J_{pp} = 41.0 Hz, P*Ph*), 51.7 (d, J_{pp} = 41.1 Hz, PPh_2)
[Ni(SC_6H_4OMe-2)(triphos)]BPh_4	δ 8.03-6.11 (m, P*Ph* and B*Ph*, 49H),3.38-2.21 (m, CH_2, 8H), 2.05 (s, CH_3,3H)	δ 103.9 (t, J_{pp} = 41.4 Hz, P*Ph*), 49.4 (d, J_{pp} = 41.0 Hz, PPh_2)
[Ni($SC_6H_3Me_2$-2,6)(triphos)]BPh_4	δ 8.22-6.45 (m, P*Ph* and B*Ph*, 48H),3.08-2.18 (m, CH_2, 8H), 2.05 (s, CH_3,6H)	δ 103.1 (t, J_{pp} = 42.1 Hz, P*Ph*), 50.9 (d, J_{pp} = 42.6 Hz, PPh_2)
[Ni(SC_6H_4Cl-2)(triphos)]BPh_4	δ 8.10-6.61 (m, P*Ph* and B*Ph*, 49H),4.20-2.54 (m, CH_2, 8H)	δ 105.9 (t, J_{pp} = 40.9 Hz, P*Ph*), 48.7 (d, J_{pp} = 41.1 Hz, PPh_2)

Table (6.3): The main FTIR spectroscopic values for[Ni(thiolate)(triphos)]BPh_4 complexes.

Complex	**C-H Alkyl (cm^{-1})**	**C-H Aromatic (cm^{-1})**	**C=C Aromatic (cm^{-1})**	**P-*Ph* (cm^{-1})**
[Ni(SC_6H_4Me-2)(triphos)]$^{+}$	ν 2906-3000 δ 1237-1408	ν 3036-3052 δ 702-887	1434-1579	1097
[Ni(SC_6H_4OMe-2)(triphos)]$^{+}$	ν 2963-2998 δ 1263-1470	ν 3051 δ 702-889	1407-1598	1097
[Ni($SC_6H_3Me_2$-2,6)(triphos)]$^{+}$	ν 2906-2983 δ 1408-1477	ν 3053 δ 700-890	1457-1579	1095
[Ni(SC_6H_4Cl-2)(triphos)]$^{+}$	ν 2947-3000 δ 1399	ν 3026-3047 δ 732-997	1431-1572	1093

6.3.2 Preparation of Acids.

6.3.2.1 Preparation of [lutH]BPh$_4$.

[lutH]BPh$_4$ was prepared by the method described in the literature[19], Equation (6.8).

$$[lutH]Cl + NaBPh_4 \xrightarrow{CH_3OH} [lutH]BPh_4 + NaCl \qquad (6.8)$$

Equation (6.9) shows that anhydrous HCl is produced by mixing methanol with trimethylsilylchloride, and then HCl reacts with lut to produce [lutH]Cl, Equation (6.10).

$$CH_3OH + (CH_3)_3SiCl \xrightarrow{THF} (CH_3)_3SiOCH_3 + HCl \qquad (6.9)$$

$$lut + HCl \xrightarrow{THF} [lutH]Cl \qquad (6.10)$$

Under dinitrogen atmosphere, to a stirring solution of lutidine (11.6 ml, 100 mmol) in THF (100 ml) was added MeOH (4.05 ml, 100 mmol) followed by Me$_3$SiCl (12.7 ml, 100 mmol). A white produced solid, [lutH]Cl, was stirred under dinitrogen atmosphere for another 30 min. and then filtered, washed with THF and dried in *vacuo*.

The following reaction can be performed in air. The [lutH]Cl (7.18 g, 50 mmol) was dissolved in MeOH (*ca* 20 ml) and filtered through celite. The required amount of sodium tetraphenylborate (NaBPh$_4$) (17.4 g, 50 mmol) was dissolved in MeOH (*ca* 20 ml) and dripped through celite into the solution of [lutH]Cl. The resulting mixture was left overnight to complete the formation of a white solid precipitate ([lutH]BPh$_4$ and NaCl) as shown in Equation (6.8). The next day, the white solid product was filtered, washed with a large volume of distilled water (*ca* 1L) to remove the contaminating NaCl side product. The white solid product and then washed with methanol before drying in *vacuo*, (average yield is 92%).

The identity and purity of [lutH]BPh$_4$ was confirmed by ^{1}H NMR in CD$_3$CN and the signal values were compared with literature[19]: δ 2.69 (s, 6H, *CH$_3$*), 6.84 (t, 4H, J_{HH} = 7.3 Hz, *Ph*), 7.03 (m, 8H, *Ph*), 7.30 (m, 8H, *Ph*), 7.59 (d, 2H, JHH = 7.9 Hz, *H$_3$* and *H$_5$* on lut), 8.23 (t, 1H, J_{HH} = 7.9 Hz, *H$_4$* on lut), see Figure (6.4).

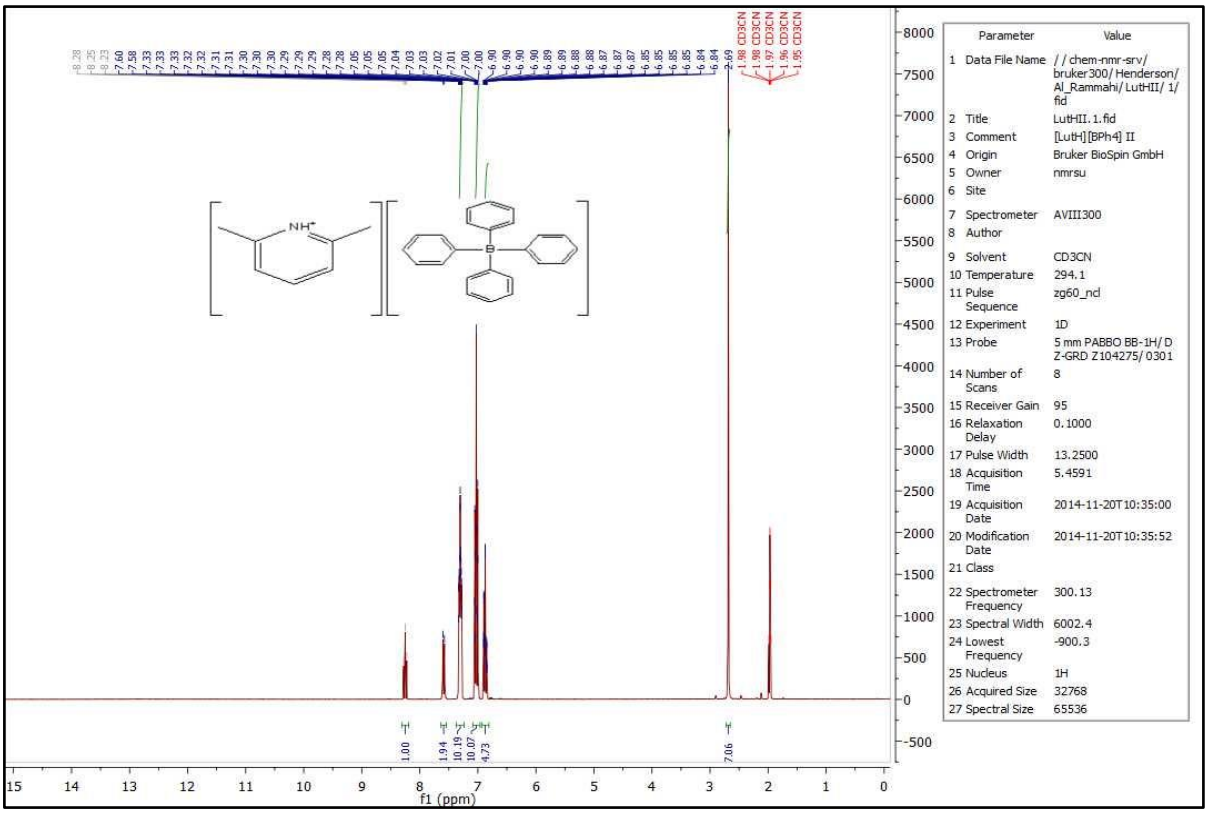

Figure 6.4. ^{1}H NMR spectrum of [lutH]BPh_4 in CD_3CN at 25 °C.

6.3.2.2 Preparation of [picH]BPh_4.

By using a similar manner described in *section (6.3.2.1)*, [picH]BPh_4 was prepared as shown in Equations (6.11), (6.12) and (6.13).

$$CH_3OH + (CH_3)_3SiCl \xrightarrow{THF} (CH_3)_3SiOCH_3 + HCl \quad (6.11)$$

$$pic + HCl \xrightarrow{THF} [picH]Cl \quad (6.12)$$

$$[picH]Cl + NaBPh_4 \xrightarrow{CH_3OH} [picH]BPh_4 + NaCl \quad (6.13)$$

The identity and purity of [picH]BPh_4 was confirmed by ^{1}H NMR in CD_3CN: δ 2.65 (s, 3H, *CH_3*), 6.88 (t, 4H, J_{HH} = 7.3 Hz, *Ph*), 7.03 (m, 8H, *Ph*), 7.30 (m, 8H, *Ph*), 7.81 (d, 2H, J_{HH} = 7.9 Hz, *H_2* and *H_6* on pic), 8.45 (d, 2H, J_{HH} = 7.9 Hz, *H_3* and *H_5* on pic), see Figure (6.5).

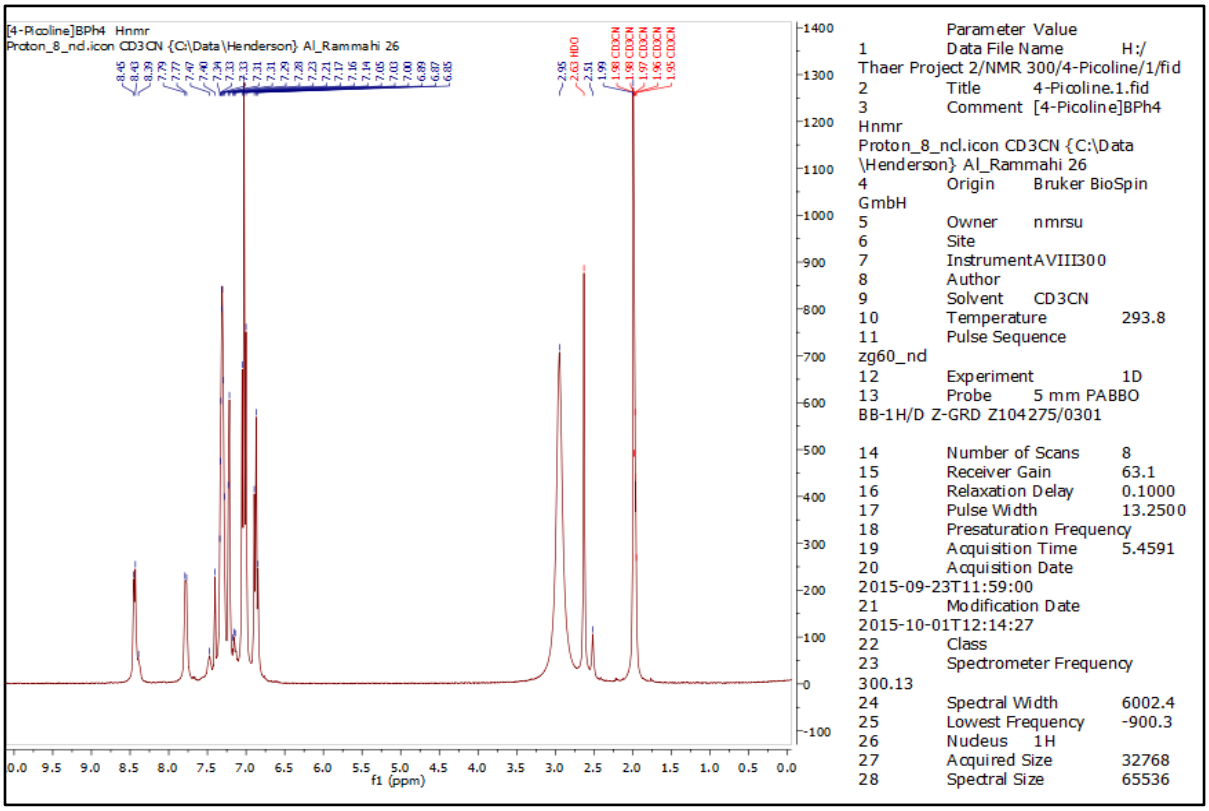

Figure 6.5. ^{1}H NMR spectrum of [picH]BPh$_4$ in CD$_3$CN at 25 °C.

6.4 Kinetic Studies.

All kinetic studies were performed using an Applied Photophysics SX.18 MV stopped-flow spectrophotometer, modified to handle air-sensitive solutions, connected to a RISC computer. The temperature was maintained using a Grant LTD 6G thermostat tank with combined recirculating pump. The experiments were normally conducted at 25.0 °C. In all kinetic studies reported in this chapter the wavelength used was λ = 350 nm. For the temperature dependence studies, the kinetics were measured in the temperature range 15 °C to 30 °C, over 5 °C intervals.

The solutions of complex and reactants were prepared under an atmosphere of dinitrogen and transferred to the stopped-flow apparatus using gas-tight, all glass syringes. The kinetics were studied in dry MeCN under pseudo first order conditions, with acid and conjugate base present in at least a 10-fold excess over the concentration of the complex. Mixtures of acid and conjugate base were prepared from stock solutions of the two reagents. All solutions were used within 1 hour of preparation.

Under all conditions, the stopped-flow absorbance-time traces were an excellent fit to a single exponential, indicating a first order dependence on the concentration of complex. The dependences on the concentrations of acid and conjugate base were determined from graphs of

k_{obs}/[base] versus [acid]/[base]. Examples of the types of plots obtained and the analysis of these plots to obtain the rate laws will be explained in the Results and Discussion section.

6.5 DFT Calculation

DFT calculations were performed using Gaussian 09 package[20], at the UB97D/ 6-311G levels of theory used to the optimization for Ni, S, P, N, C and H, with the terminal condition being a root mean square (RMS) < 1 cal mol^{-1}. For [Ni(SC_6H_4R-2)(triphos)]BPh_4 (R= Me, MeO and Cl) and [Ni($SC_6H_3Me_2$-2,6)(triphos)]BPh_4, the geometry optimization was achieved before and after protonation by $[lutH]^+$.

The computational studies were performed in the following manner. (i) The structure image used for the complex was obtained from X-ray crystallography. (ii) All angles for the structure were locked, leaving only the (Ni-S-C) angle free to allow the rotation of the R-group (R = C_6H_5, C_6H_4Me-2, C_6H_4OMe-2 or $C_6H_3Me_2$-2,6). (iii) Monitor the changes in energy during Ni-S rotation (360° in 10^o intervals) using the low theoretical levels UB97D/6-21*G. (iv) Select the structures which have the lowest energy (most stable) and the highest energy to do optimise the structure (OPT) at the higher level UB97D/ 6-311G; the difference between the two obtained energies represents the barrier to rotation about the Ni–S bond. (v) Repeat the optimisation calculations for the structure of the complex after the $lutH^+$ has bound to find the more stable status for the protonation. (vi) Finally, the frequency optimisation calculation was performed (FOPT) for the complex to measure the energies of the steric barriers caused by phenyl group of triphos.

6.6 Results and Discussion.

6.6.1 X-Ray Structures of [Ni(thiolate)(triphos)]$^+$.

The structures of [Ni(SC_6H_4R-2)(triphos)]BPh_4 (R = MeO, Me or Cl) and [Ni($SC_6H_3Me_2$-2,6)(triphos)]BPh4 have been determined by X-ray crystallography Table (6.4). For [Ni(SC_6H_4OMe-2)(triphos)]$^+$, [Ni(SC_6H_4Me-2)(triphos)]$^+$ and [Ni($SC_6H_3Me_2$-2,6)(triphos)]$^+$ the geometry at Ni is square planar, see Figures (6.6), (6.7) and (6.8). Selected bond lengths and angles are presented in Table (6.9). Orientation consequence of Xtal packing. In [Ni(SC_6H_4OMe-2)(triphos)]$^+$, the MeO group sits on the same side of the square plane as the phenyl group of the central phosphorus (hereafter called the 'open face', *vide infra*). However, for [Ni(SC_6H_4Me-2)(triphos)]$^+$ the crystal structure contains two cations: in one the C_6H_4Me group sits on the same side of the square plane as the phenyl group on P_2 (*i.e.* the open face), and in the other it sits on the opposite side of the square plane (*i.e.* in the closed face). For [Ni($SC_6H_3Me_2$-2,6)(triphos)]$^+$, the aryl group is orientated so that one Me group sits in each face Figure (6.4). These structures indicate that the R-substituents on the coordinated thiolate can occupy either the open or closed face. The bond lengths and angles for [Ni(SC_6H_4R-2)(triphos)]BPh_4 (R = MeO, Me or Cl) and [Ni($SC_6H_3Me_2$-2,6)(triphos)]BPh_4 are all in good agreement with those observed in previously reported analogous [Ni(thiolate)(triphos)]$^+$ [7-12, 18].

In [Ni(SC_6H_4Cl-2)(triphos)]$^+$ the Ni is 5-coordinate with the three phosphorus atoms of triphos, the sulfur and the 2-chloro-substituent bound to Ni, Figure (6.5). In 5-coordinate complexes, the angular structural parameter, $\tau = (\beta - \alpha)/60$ (where α = smaller of basal angle and β = larger of basal angle) has been used to distinguish between trigonal bipyramidal and square-based pyramidal structures[21]. For a perfect square-based pyramid, $\tau = 0$ and for a perfect trigonal bipyramid $\tau = 1.0$. For [Ni(SC_6H_4Cl-2)(triphos)]$^+$, $\beta = P_2NiS_1 = 174.6^o$ and $\alpha = P_1NiP_3 = 154.6^o$, and hence, $\tau = 0.33$, indicating that the structure of the cation is best described as a distorted square-based pyramid with the chloro-group occupying the apical position. The chloro-group is bound to Ni on the same side of the square plane as the phenyl group on P_2 (i.e. the open face). Selected bond lengths and angles for [Ni(SC_6H_4Cl-2)(triphos)]$^+$ are presented in Table (6.5). It is worth noting that the Ni-Cl bond length is 2.5580(5) Å. This value is significantly larger than the sum of the atomic radii (2.35 Å) and longer than the Ni-Cl bond length in [NiCl(triphos)]$^+$ {2.1671(18) Å},[22] indicating that the Ni-Cl bond in [Ni(SC_6H_4Cl-2)(triphos)]$^+$ is weak.

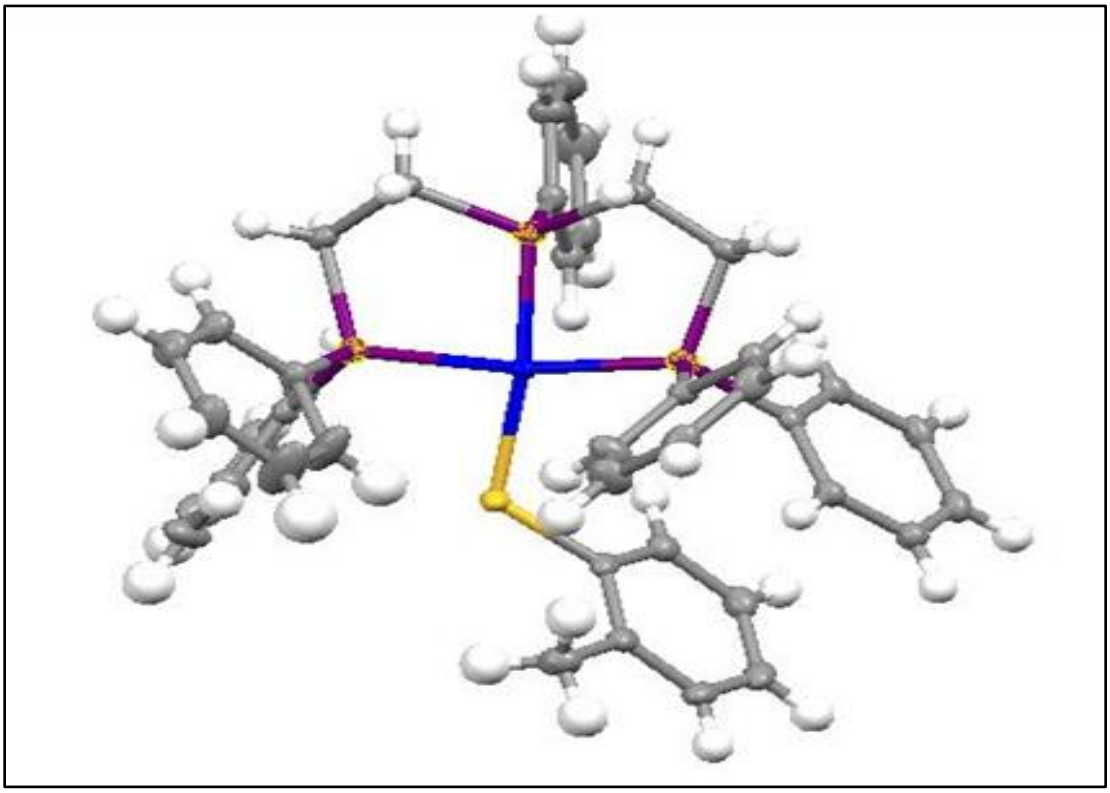

Figure 6.6. X-ray structure for $[Ni(SC_6H_4Me\text{-}2)(triphos)]^+$, where (blue = nickel, purple = phosphorus, yellow = sulfur, grey = carbon and white = hydrogen).

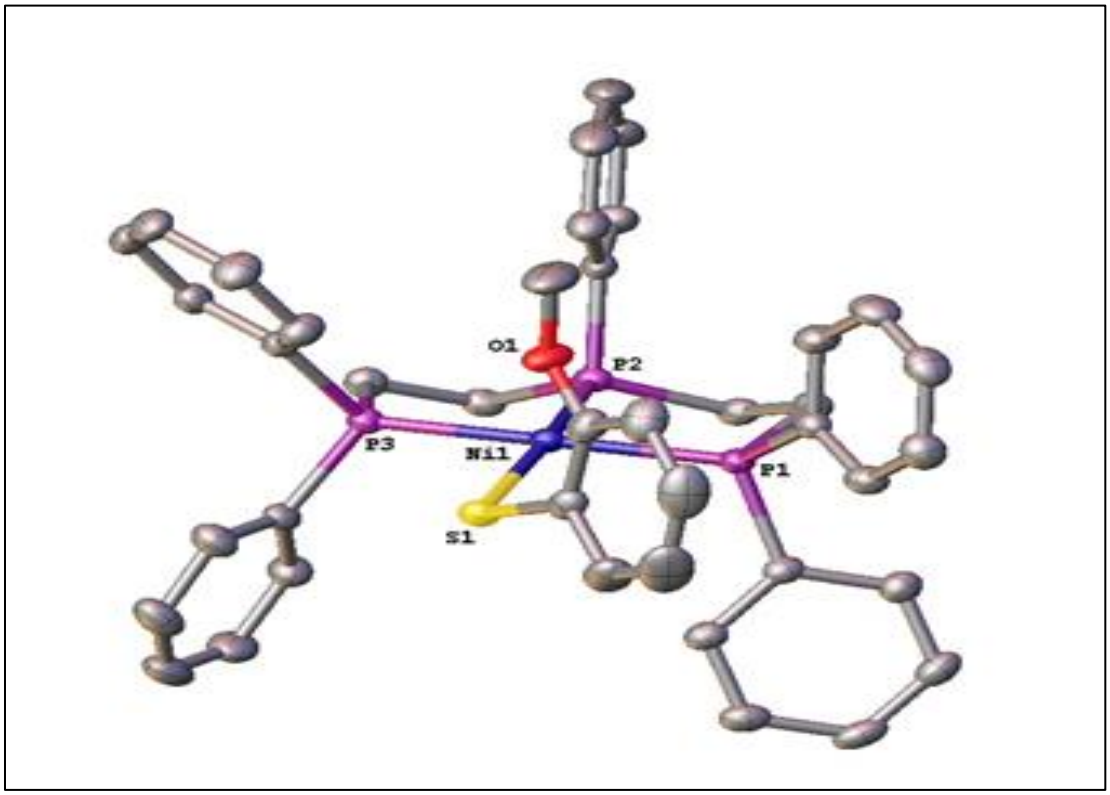

Figure 6.7. X-ray structure for $[Ni(SC_6H_4OMe\text{-}2)(triphos)]^+$, where (blue = nickel, purple = phosphorus, yellow = sulfur, red = oxygen and grey = carbon).

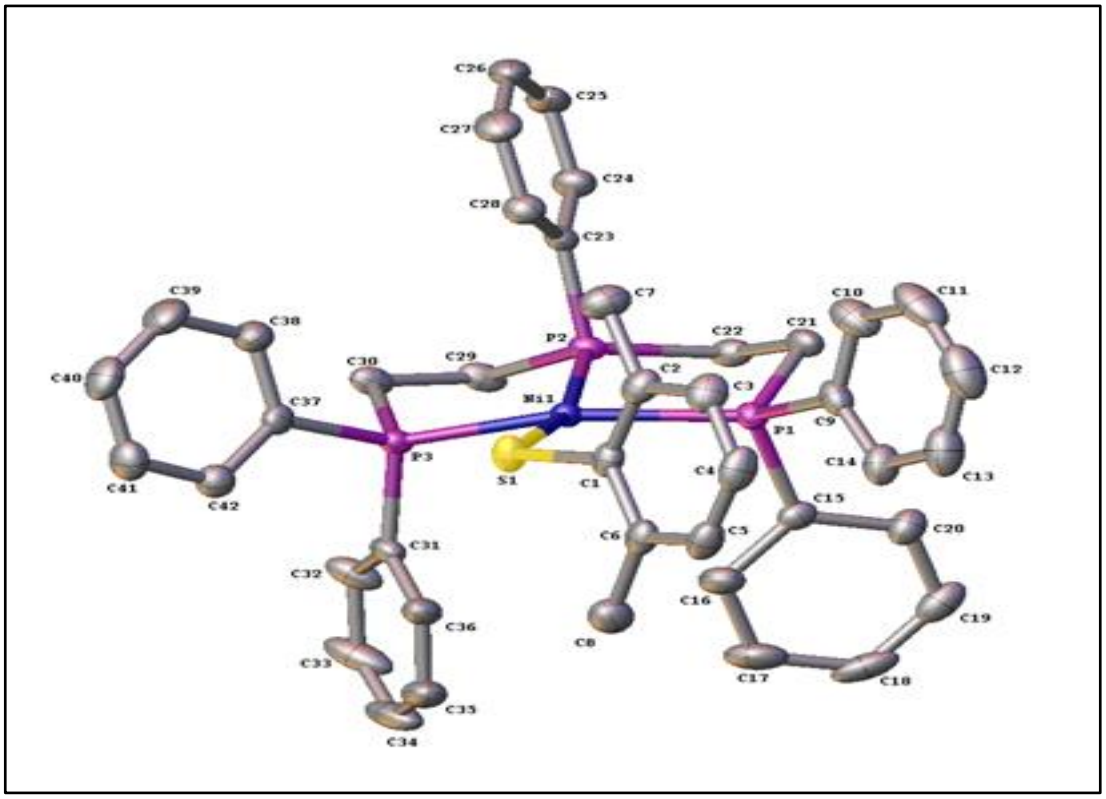

Figure 6.8. X-ray structure for [Ni($SC_6H_3Me_2$-2,6)(triphos)]$^+$, where (blue = nickel, purple = phosphorus, yellow = sulfur and grey = carbon).

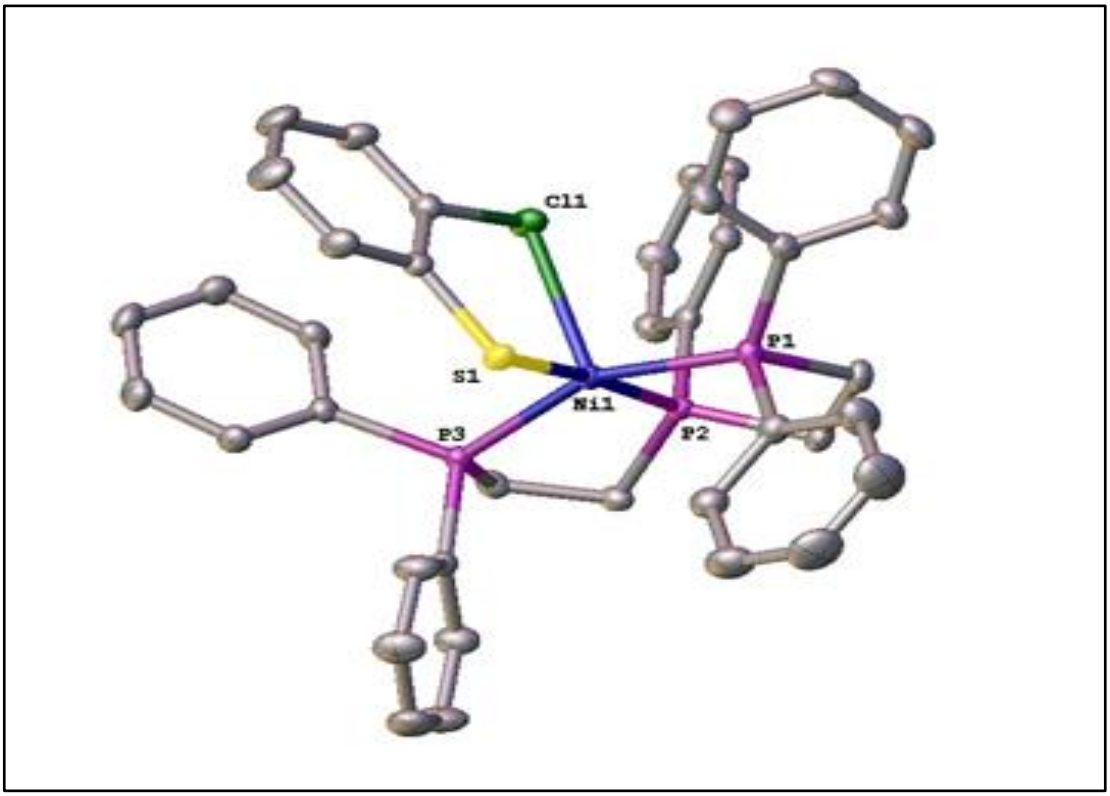

Figure 6.9. X-ray structure for [Ni(SC_6H_4Cl-2)(triphos)]$^+$, where (blue = nickel, purple = phosphorus, yellow = sulfur, green = chlorine and grey = carbon).

Table (6.4): Crystal data and refinement for [Ni(thiolate)(triphos)]BPh_4 (thiolate = SC_6H_4R-2, R = MeO, Me or Cl; $SC_6H_3Me_2$-2,6)

Thiolate	SC_6H_4OMe-2[a]	SC_6H_4Me-2	$SC_6H_3Me_2$-2,6	SC_6H_4Cl-2
Chemical formula	$C_{45}H_{50}NiOP_3S^+ .C_{24}H_{20}B^-$	$C_{41}H_{40}NiP_3S^+ .C_{24}H_{20}B^-$	$C_{42}H_{42}NiP_3S^+ .C_{24}H_{20}B^-$	$C_{40}H_{37}ClNiP_3S^+ .C_{24}H_{20}B^-$
Formula mass	1125.7	1035.6	1090.7	1056.0
Crystal system	Monoclinic	Triclinic	Triclinic	Triclinic
a/Å	15.70217(13)	14.6103(17)	11.33401(18)	13.7965(4)
b/Å	18.81495(13)	19.467(2)	15.2823(3)	14.0861(3)
c/Å	19.93006(16)	21.020(3)	18.3764(3)	14.1116(4)
α/°	90	114.1136(12)	95.1950(15)	80.814(2)
β/°	93.9118(8)	99.7781(13)	104.7717(14)	74.992(3)
γ/°	90	94.2645(13)	111.4221(16)	77.963(2)
V/Å^3	5874.33(8)	5308.4(11)	2804.86(9)	2574.40(13)
T/K	150(1)	100(2)	150(2)	150(2)
Space group	$P2_1/c$	$P\bar{1}$	$P\bar{1}$	$P\bar{1}$
Z	4	4	2	2
Reflections measured	91460	53577	89775	51619
Independent reflections	12965	24416	12655	11276
Refined parameters	697	1346	679	640
R_{int}	0.0445	0.0271	0.0480	0.0453
R_1 ($I > 2\sigma$)	0.0369	0.0359	0.0349	0.0347
$wR(F^2)$ ($I > 2\sigma$)	0.0833	0.0833	0.0758	0.0727
R_1 (all data)	0.0513	0.0535	0.0477	0.0477
$wR(F^2)$ (all data)	0.0898	0.0901	0.0813	0.0779
GoF on F^2	1.037	1.030	1.044	1.028
Max, min diff el dens/eÅ^{-1}	0.41, -0.41	0.72, −0.52	0.47, −0.30	0.37, -0.30

footnote: [a] crystallizes as thf (C_4H_{10}) solvate

Table (6.5): Selected bond lengths (Å) and angles (°) for [Ni(thiolate)(triphos)]BPh_4 (thiolate = SC_6H_4R-2, R = MeO, Me or Cl; $SC_6H_3Me_2$-2,6)

Thiolate	SC_6H_4OMe-2	SC_6H_4Me-2	$SC_6H_3Me_2$-2,6	SC_6H_4Cl-2
Bond lengths				
Ni-S	2.1913(5)	2.1689(5)	2.1736(5)	2.2457(5)
Ni-P_1	2.2213(5)	2.2013(6)	2.2076(5)	2.2129(5)
Ni-P_2	2.1441(5)	2.1360(5)	2.1425(5)	2.1515(5)
Ni-P_3	2.2138(5)	2.1948(6)	2.2127(5)	2.2078(5)
Ni-Cl				2.5580(5)
Bond angles				
Ni-S-C_{ipso}	111.90(6)	118.24(6)	119.07(6)	105.95(6)
P_1-Ni-S	100.050(18)	106.38(2)	107.029(18)	92.254(19)
P_2-Ni-S	170.59(2)	163.41(2)	163.07(19)	174.594(19)
P_3-Ni-S	88.609(18)	87.574(19)	88.187(17)	92.538(19)
P_1-Ni-P_2	86.260(19)	84.809(19)	84.53(18)	86.860(19)
P_1-Ni-P_3	169.253(19)	158.22(2)	157.20(18)	154.58(2)
P_2-Ni-P_3	84.401(18)	85.480(19)	84.875(17)	86.037(19)
Cl-Ni-S				85.532(17)
Cl-Ni-P_1				101.750(18)
Cl-Ni-P_2				99.870(18)
Cl-Ni-P_3				103.502(18)

6.6.2 Kinetics studies of protonation reactions of [Ni(SC$_6$H$_4$R-2)(triphos)]BPh$_4$ (R= Me, MeO or Cl) and [Ni(SC$_6$H$_3$Me$_2$-2,6)(triphos)]BPh$_4$ Complexes.

6.6.2.1 Products of protonation reactions of [Ni(SC$_6$H$_4$R-2)(triphos)]BPh$_4$ (R= Me, MeO or Cl) and [Ni(SC$_6$H$_3$Me$_2$-2,6)(triphos)]BPh$_4$ complexes in presence of lutH$^+$ and picH$^+$.

The kinetics of the reactions of [Ni(SC$_6$H$_4$R-2)(triphos)]BPh$_4$ (R = MeO, Me or Cl) and [Ni(SC$_6$H$_3$Me$_2$-2,6)(triphos)]BPh$_4$ with both lutH$^+$ and picH$^+$ have been investigated in MeCN. Whilst both acids are based on pyridine and have similar pK_as (pK_a^{pic} = 14.5, pK_a^{lut} = 14.1 in MeCN)[23, 24] their steric bulk is significantly different. In line with earlier studies on analogous complexes, which presented that the protonation of [Ni(SEt)(triphos)]$^+$ involves information of [Ni(HSEt)(triphos)]$^{+2}$ complex,[7-12] the reactions of mixtures of lutH$^+$ and lut with [Ni(SC$_6$H$_4$R-2)(triphos)]$^+$ or [Ni(SC$_6$H$_3$Me$_2$-2,6)(triphos)]$^+$, correspond to the simple addition of a single proton to the complex as shown in Equation (6.3).

The reactions with lutH$^+$ are characterised by small changes in the visible absorption spectrum (for all complexes: $\Delta A \sim 0.004 - 0.034$ at $\lambda = 350$ nm) and negiligible changes in the $^{31}P\{^1H\}$ NMR spectra[7-12]. In contrast, the analogous reactions with mixtures of picH$^+$ and pic show significantly larger changes in the visible absorption spectrum (about 10 times larger for all complexes: $\Delta A \sim 0.11 - 0.36$ at $\lambda = 350$ nm), Figure (6.10).

In addition, the protonation reactions of the [Ni(SC$_6$H$_4$R-2)(triphos)]BPh$_4$ (R = MeO, Me or Cl) and [Ni(SC$_6$H$_3$Me$_2$-2,6)(triphos)]BPh$_4$ with picH$^+$ associate with changing in the colour of complex solution from red-orange to yellow. These observations suggest, that in the presence of the less sterically-demanding picH$^+$, both protonation and substitution occurs, Equation (6.14). Despite being unable to isolate the [Ni(pic)(triphos)]$^+$, we have characterized the complex in solution using ^{1}H NMR spectroscopy. Solutions containing mixtures of [Ni(SC$_6$H$_4$R-2)(triphos)]$^+$ (R = H, MeO, Me or Cl) or [Ni(SC$_6$H$_3$Me$_2$-2,6)(triphos)]$^+$ and a 20-fold excess of [picH$^+$] in CD$_3$CN exhibited appreciable changes in the $^{31}P\{^1H\}$ NMR spectra.

Thus, the $^{31}P\{^1H\}$ NMR spectra for [Ni(SC$_6$H$_4$R-2)(triphos)]$^+$ (R = Me, MeO, H or Cl) and [Ni(SC$_6$H$_3$Me$_2$-2,6)(triphos)]$^+$, have chemical shifts in the range δ 103.1 – 105.9 (triplet) and δ 48.7 – 53.4 (doublet) with J_{PP} = 40.4 – 42.1 Hz, see Table (6.2), but the spectrum of the product of the reactions with picH$^+$ is identical in all cases δ 110.9 (triplet, J_{PP} = 50.5 Hz) and δ 47.1 (doublet, J_{PP} = 49.8 Hz); as shown in Table (6.6), indicating that a common product is formed.

$$[Ni(SC_6H_4R)(triphos)]^+ + picH^+ \longrightarrow [Ni(pic)(triphos)]^+ + RC_6H_4SH \quad (6.14)$$

Where R = H, Me-2, OMe-2, Cl-2 or Me_2-2,6.

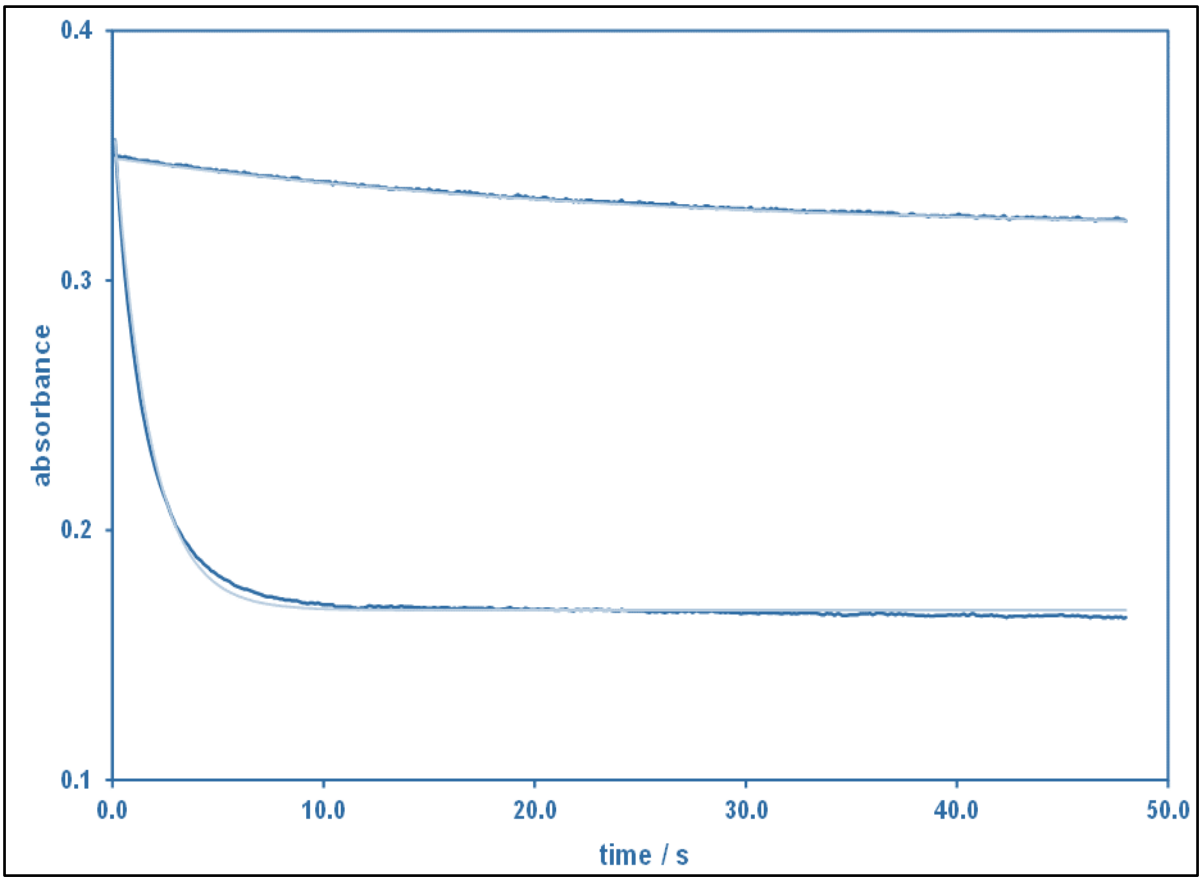

Figure 6.10. Comparison of the stopped-flow absorbance-time curves for the reactions of: (TOP) $[Ni(SC_6H_4Me\text{-}2)(triphos)]^+$ (0.25 mmol dm^{-3}) with $lutH^+$ (5.0 mmol dm^{-3}) and lut (40 mmol dm^{-3}) in MeCN at 25.0 ^oC (λ = 350nm), data is shown as dark blue curve and exponential fit is shown as light blue curve, data fitted to the equation $A_t = 0.32 + 0.029 \exp(-0.042t)$; (BOTTOM) $[Ni(SC_6H_4Me\text{-}2)(triphos)]^+$ (0.25 mmol dm^{-3}) with $picH^+$ (5.0 mmol dm^{-3}) and pic (40 mmol dm^{-3}) in MeCN at 25.0 ^oC (λ = 350nm), data is shown as dark blue curve and exponential fit is shown as light blue curve, data fitted to the equation $A_t = 0.17 + 0.20 \exp(-0.58t)$. Under all conditions, the stopped-flow absorbance-time traces were an excellent fit to a single exponential, indicating a first order dependence on the concentration of complex.

Table (6.6): $^{31}P\{^{1}H\}$ NMR spectroscopic data for the reactions of $[Ni(SC_6H_4R\text{-}2)(triphos)]^+$ (R = MeO, Me, H or Cl) or $[Ni(SC_6H_3Me_2\text{-}2,6)(triphos)]^+$ with $picH^+$ in MeCN at 25.0 °C.

	$^{31}P\{^{1}H\}$ NMR spectra / δ			
	Complex [a]		**Complex with $picH^+$ [b]**	
$[Ni(SC_6H_5)(triphos)]^+$	105.4 (t)	52.2 (d)	110.9 (t)	47.1 (d)
$[Ni(SC_6H_4Me\text{-}2)(triphos)]^+$	104.9 (t)	51.7 (d)	110.9 (t)	47.1 (d)
$[Ni(SC_6H_4OMe\text{-}2)(triphos)]^+$	103.9 (t)	49.4 (d)	110.9 (t)	47.1 (d)
$[Ni(SC_6H_4Cl\text{-}2)(triphos)]^+$	105.9 (t)	48.7 (d)	110.9 (t)	47.1 (d)
$[Ni(SC_6H_3Me_2\text{-}2,6)(triphos)]^+$	103.1 (t)	50.9 (d)	110.9 (t)	47.1 (d)

footnotes
a t = triplet, d = doublet and b $[picH^+]/[complex] = 10$.

6.6.2.2 Kinetics of protonation reactions with $lutH^+$ in the presence of lut.

The kinetics of the reactions of $[Ni(SC_6H_4R\text{-}2)(triphos)]^+$ (R = Me, MeO) or $[Ni(SC_6H_3Me_2\text{-}2,6)(triphos)]^+$ with mixtures of $lutH^+$ and lut are associated with the rate law shown in Equations (6.15) and (6.16), (where K_1^R = equilibrium constant for the protonation of complex, k_2^R = the rate constant for the protonation of complex, k_{-2}^R = the rate constant for the proton transfer from $[Ni(SHC_6H_4R\text{-}2)(triphos)]^{2+}$ to lut to form $\{[Ni(SC_6H_4R\text{-}2)(triphos)]\ldots Hlut\}^{2+}$, and R = Me or MeO) . This rate law is consistent with the mechanism shown in Figure (6.1).

$$\text{Rate} = \{\frac{(K_1^R k_2^R)^{lut}[lutH^+]}{1 + (K_1^R)^{lut}[lutH^+]} + (k_{-2}^R)^{lut}[lut]\}[Ni(SC_6H_4R-2)(triphos)^+] \qquad (6.15)$$

$$\text{Rate} = \{\frac{(K_1^{Me2} k_2^{Me2})^{lut}[lutH^+]}{1 + (K_1^{Me2})^{lut}[lutH^+]} + (k_{-2}^{Me2})^{lut}[lut]\}[Ni(SC_6H_3Me_2-2,6)(triphos)^+] \qquad (6.16)$$

The exponential absorbance-time curves are consistent with the reactions exhibiting a first order dependence on the concentration of complex. The dependence on the concentrations of $lutH^+$ and lut were determined from plots of k_{obs}/[lut] versus $[lutH^+]/[lut]$, see Tables (6.7), (6.8) and (6.9). Such plots are straight lines provided the concentration of $lutH^+$ is constant. Increasing the concentration of $lutH^+$ gives a line with the same intercept but a smaller gradient as shown in Figures (6.11), (6.12) and (6.13). All kinetic parameter values (K_1^R, k_2^R and k_{-2}^R), which are derived from comparing the experimental rate laws and Equations (6.15) and (6.16), have been presented in Table (6.11).

Table (6.7): Kinetic data for the reaction of $[Ni(SC_6H_4Me\text{-}2)(triphos)]^+$ (0.25 mmol dm^{-3}) with mixtures of $lutH^+$ and lut in MeCN at 25.0 °C. Data collected at λ = 350 nm

$[lutH^+]$ (mmol dm^{-3})	**[lut] (mmol dm^{-3})**	**$[lutH^+]$ / [lut]**	**k_{obs} (s^{-1})**	**k_{obs} / [lut] ($mmol^{-1}$ dm^3 s^{-1})**	**ΔA**	**A_f**
5	2.5	2	0.024	9.6	0.034	0.28
	5	1	0.025	4.9	0.037	0.29
	10	0.5	0.026	2.6	0.036	0.3
	20	0.25	0.028	1.4	0.032	0.3
	40	0.125	0.03	0.8	0.029	0.32
10	2.5	4	0.028	11.2	0.026	0.32
	5	2	0.03	6	0.028	0.32
	10	1	0.026	2.6	0.033	0.32
	20	0.5	0.028	1.4	0.032	0.32
	40	0.25	0.028	0.7	0.034	0.32
20	2.5	8	0.03	12	0.05	0.29
	5	4	0.033	6.6	0.057	0.28
	10	2	0.034	3.4	0.055	0.28
	20	1	0.033	1.65	0.057	0.29
	40	0.5	0.037	0.9	0.051	0.29

Table (6.8): Kinetic data for the reaction of $[Ni(SC_6H_4OMe\text{-}2)(triphos)]^+$ (0.25 mmol dm^{-3}) with mixtures of $lutH^+$ and lut in MeCN at 25.0 ºC. Data collected at λ = 350 nm.

$[lutH^+]$ (mmol dm^{-3})	**[lut] (mmol dm^{-3})**	**$[lutH^+]$ / [lut]**	**k_{obs} (s^{-1})**	**k_{obs} / [lut] ($mmol^{-1}$ dm^3 s^{-1})**	**ΔA**	**A_f**
5	2.5	2	0.048	19.2	0.008	0.27
	5	1	0.046	9.2	0.011	0.26
	10	0.5	0.04	4	0.014	0.26
	20	0.25	0.033	1.65	0.016	0.26
	40	0.125	0.032	0.8	0.02	0.26
10	2.5	4	0.055	22	0.012	0.31
	5	2	0.058	11.6	0.016	0.31
	10	1	0.051	5.1	0.018	0.31
	20	0.5	0.049	2.45	0.019	0.31
	40	0.25	0.048	1.2	0.024	0.3
20	2.5	8	0.052	20.8	0.04	0.25
	5	4	0.051	10.2	0.038	0.25
	10	2	0.05	5	0.035	0.25
	20	1	0.049	2.45	0.034	0.26
	40	0.5	0.055	1.38	0.034	0.26

Table (6.9): Kinetic data for the reaction of $[Ni(SC_6H_4Me_2\text{-}2,6)(triphos)]^+$ (0.50 mmol dm^{-3}) with mixtures of $lutH^+$ and lut in MeCN at 25.0 °C. Data collected at λ = 350 nm.

$[lutH^+]$ (mmol dm^{-3})	**[lut] (mmol dm^{-3})**	**$[lutH^+]$ / [lut]**	**k_{obs} (s^{-1})**	**k_{obs} / [lut] ($mmol^{-1}$ dm^3 s^{-1})**	**ΔA**	**A_f**
5	2.5	2	0.022	8.8	0.004	0.71
	5	1	0.022	4.4	0.005	0.71
	10	0.5	0.024	2.4	0.005	0.71
	20	0.25	0.023	1.2	0.007	0.71
	40	0.125	0.024	0.6	0.01	0.71
10	2.5	4	0.027	10.8	0.006	0.66
	5	2	0.023	4.6	0.007	0.68
	10	1	0.025	2.5	0.007	0.68
	20	0.5	0.021	1.1	0.01	0.68
	40	0.25	0.022	0.55	0.013	0.67
20	2.5	8	0.026	10.4	0.013	0.68
	5	4	0.025	5	0.014	0.69
	10	2	0.026	2.6	0.015	0.69
	20	1	0.018	0.9	0.017	0.68
	40	0.5	0.018	0.5	0.02	0.68

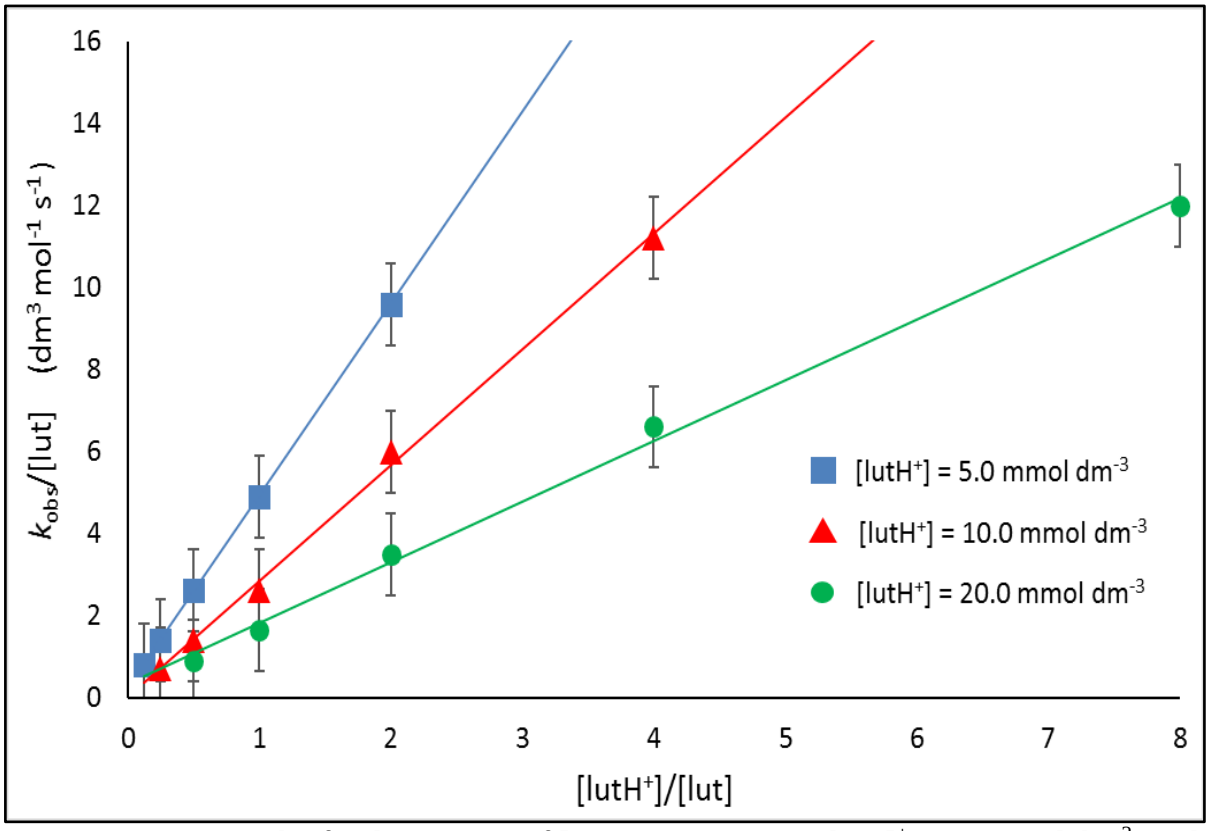

Figure 6.11. Kinetic plot for the reaction of $[Ni(SC_6H_4Me\text{-}2)(triphos)]^+$ (0.25 mmol dm^{-3}) with mixtures of lutH$^+$ and lut in MeCN at 25.0 ^{o}C. The lines are defined by Equation (6.15).

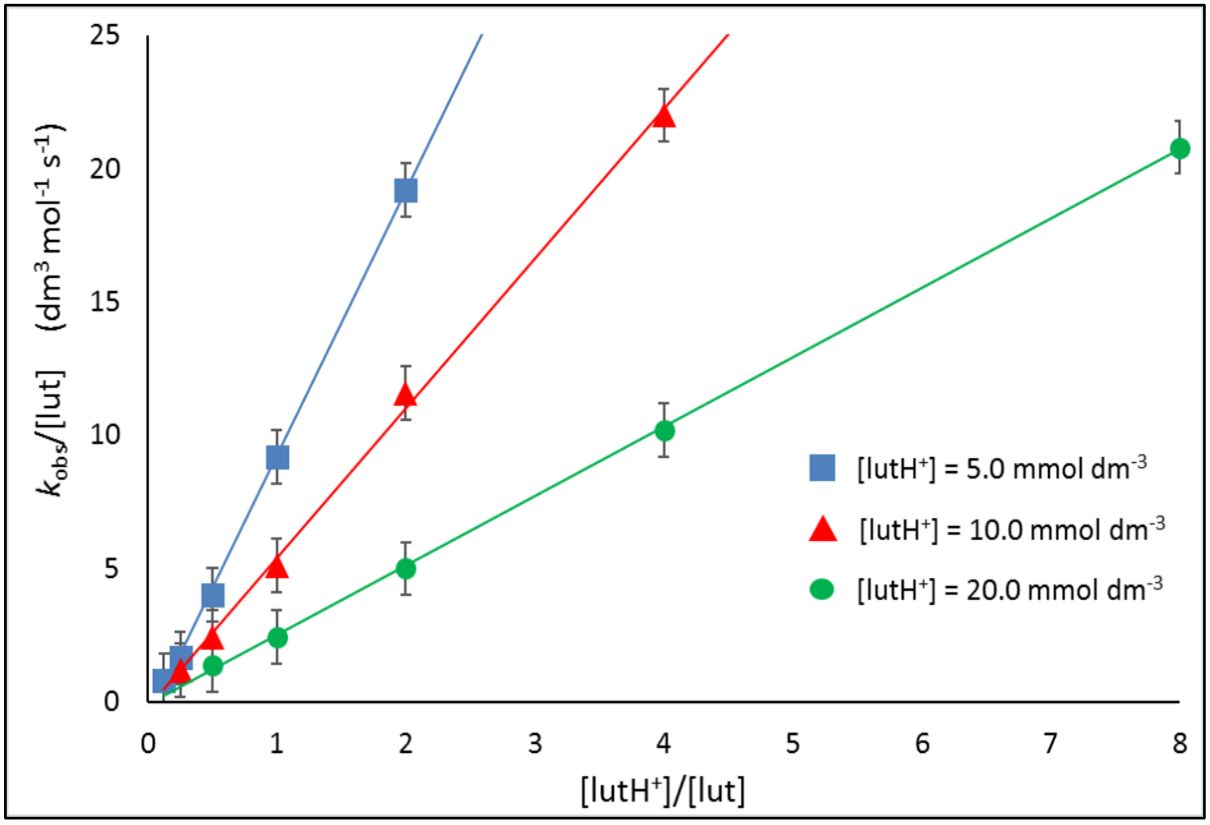

Figure 6.12. Kinetic plot for the reaction of $[Ni(SC_6H_4OMe\text{-}2)(triphos)]^+$ (0.25 mmol dm^{-3}) with mixtures of lutH$^+$ and lut in MeCN at 25.0 ^{o}C. The lines are defined by Equation (6.15).

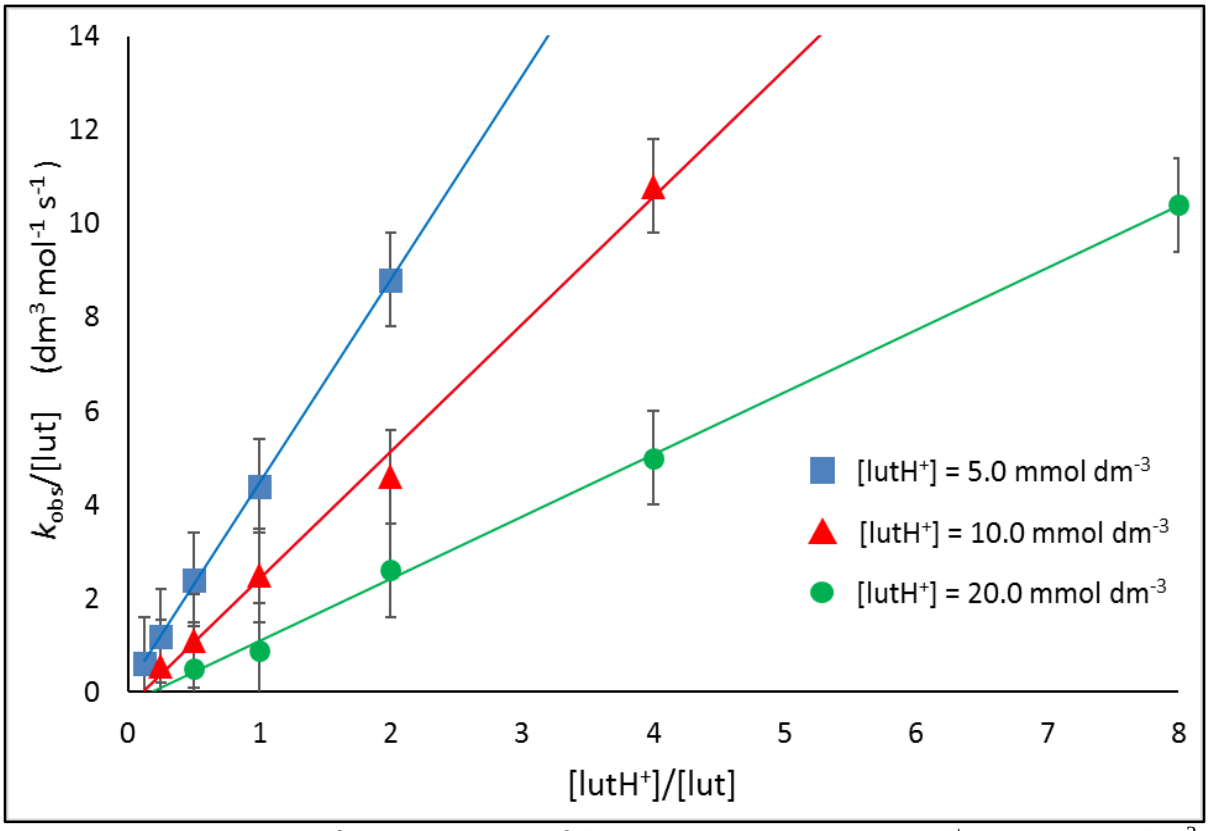

Figure 6.13. Kinetic plot for the reaction of [Ni($SC_6H_4Me_2$-2,6)(triphos)]$^+$ (0.50 mmol dm^{-3}) with mixtures of lutH$^+$ and lut in MeCN at 25.0 ^{o}C. The lines are defined by Equation (6.16).

The results for the kinetic studies of [Ni(SC_6H_4R-2)(triphos)]$^+$ (R = Me, MeO) or [Ni($SC_6H_3Me_2$-2,6)(triphos)]$^+$ with mixtures of lutH$^+$ and lut, have shown that the reactions have the same kinetics and mechanism as reported earlier for the reactions of [Ni(SC_6H_4R-4)(triphos)]$^+$ (R = H, Cl, NO_2, Me or MeO) with with mixtures of lutH$^+$ and lut[7-9].

However, the kinetics of the reaction of [Ni(SC_6H_4Cl-2)(triphos)]$^+$ with mixtures of lutH$^+$ and lut exhibits different behaviour. In the reaction of [Ni(SC_6H_4Cl-2)(triphos)]$^+$, the plot of k_{obs}/[lut] versus [lutH$^+$]/[lut] for all data defines a single straight line, from which the rate law shown in Equation (6.17) is derived, with $(K_1^{Cl}k_2^{Cl})^{lut}$ = 5.0 dm^3 mol^{-1} s^{-1} and $(k_{-2}^{Cl})^{lut}$ = 0.2 dm^3 mol^{-1} s^{-1}, see Table (6.10) and Figure (6.14).

$$\text{Rate} = \{(K_1^{Cl}k_2^{Cl})^{lut}[\text{lutH}^+] + (k_{-2}^{Cl})^{lut}[\text{lut}]\}[\text{Ni}(SC_6H_4\text{Cl}-2)(\text{triphos})^+] \qquad (6.17)$$

Equation (6.17) is consistent with the mechanism in Figure (6.1) and the rate law of Equation (6.15). When K_1^R[lutH$^+$] is small (*i.e.* $K_1^R[\text{lutH}^+]_{max} < 0.1$), Equation (6.15) simplifies to Equation (6.17).

Table (6.10): Kinetic data for the reaction of $[Ni(SC_6H_4Cl\text{-}2)(triphos)]^+$ (0.50 mmol dm^{-3}) with mixtures of $lutH^+$ and lut in MeCN at 25.0 °C. Data collected at λ = 350 nm

$[lutH^+]$ (mmol dm^{-3})	**[lut] (mmol dm^{-3})**	**$[lutH^+]$ / [lut]**	**k_{obs} (s^{-1})**	**k_{obs} / [lut] ($mmol^{-1}$ dm^3 s^{-1})**	**ΔA**	**A_f**
5	2.5	2	0.03	12	0.004	0.52
	5	1	0.035	7	0.004	0.52
	10	0.5	0.032	3.2	0.004	0.52
	20	0.25	0.036	1.8	0.005	0.52
	40	0.125	0.041	1.03	0.008	0.52
10	2.5	4	0.054	21.6	0.004	0.51
	5	2	0.049	9.8	0.004	0.51
	10	1	0.047	4.7	0.004	0.51
	20	0.5	0.038	1.9	0.005	0.52
	40	0.25	0.04	1	0.008	0.51
20	2.5	8	0.1	40	0.007	0.51
	5	4	0.11	22	0.007	0.52
	10	2	0.11	11	0.006	0.52
	20	1	0.09	4.5	0.007	0.52
	40	0.5	0.09	2.3	0.008	0.52

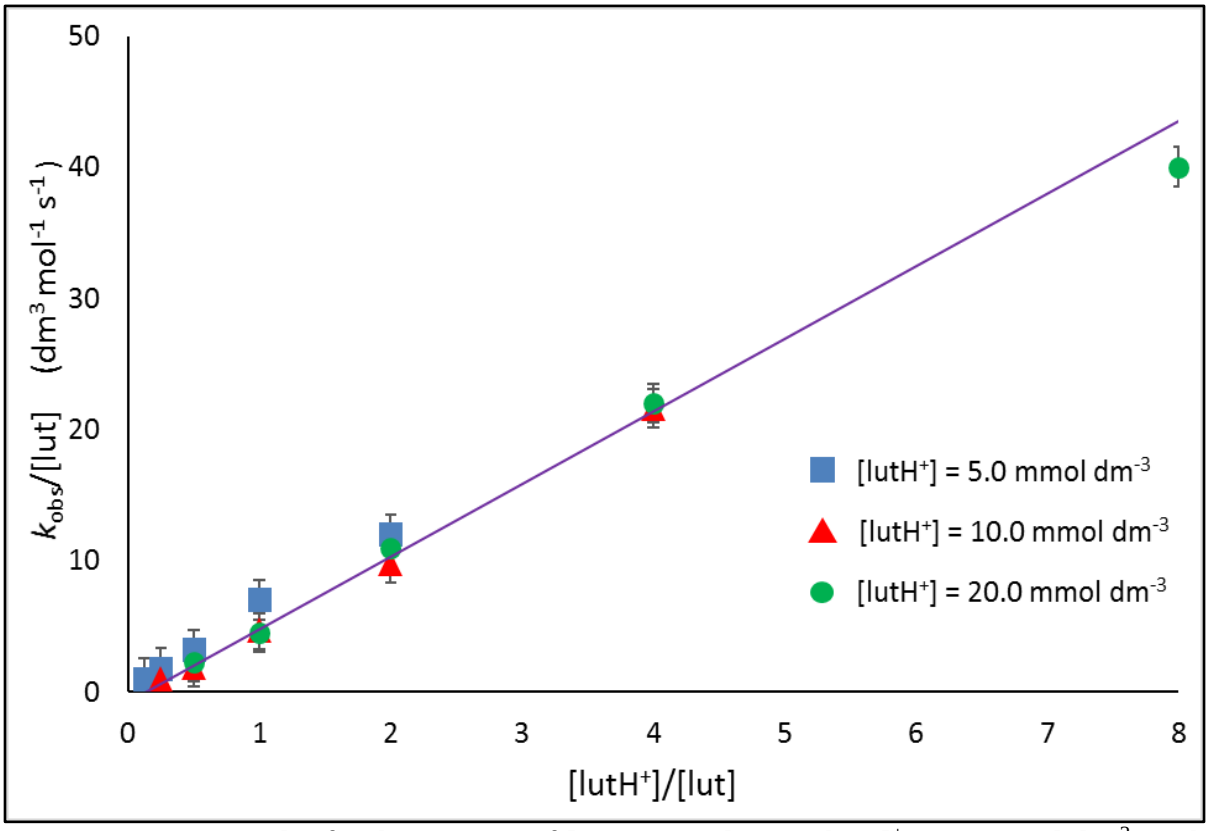

Figure 6.14. Kinetic plot for the reaction of [Ni(SC_6H_4Cl-2)(triphos)]$^+$ (0.50 mmol dm^{-3}) with mixtures of lutH$^+$ and lut in MeCN at 25.0 ºC. The line is defined by Equation (6.17).

The kinetic parameters for the reactions of [Ni(SC_6H_4R-2)(triphos)]$^+$ (R = Me, MeO, Cl) or [Ni($SC_6H_3Me_2$-2,6)(triphos)]$^+$ with mixtures of lutH$^+$ and lut, have been determined and presented in Table (6.11).

Table (6.11): Values of kinetic parameters for the reactions of [Ni(SC_6H_4R-2)(triphos)]$^+$ (R = Me, MeO or Cl) or [Ni($SC_6H_3Me_2$-2,6)(triphos)]$^+$ with mixtures of lutH$^+$ and lut in MeCN at 25.0 ºC.

R	**$(K_1^R)^{lut}$ (dm^3 mol^{-1})**	**$(k_2^R)^{lut}$ (s^{-1})**	**$(K_1^R k_2^R)^{lut}$ (dm^3 mol^{-1} s^{-1})**	**$(k_{-2}^R)^{lut}$ (dm^3 mol^{-1} s^{-1})**	**pK_a^{Ni}**
H	200	0.10	20.0	4.0	14.8
Me	500	0.03	16.5	0.2	16.0
MeO	628	0.06	36.3	0.5	16.0
Cl	≤ 10	≥ 0.5	5.3	0.1	15.8
Me_2	1200	0.03	33.6	0.2	16.3

The reactions of $lutH^+$ with all $[Ni(SC_6H_4R\text{-}2)(triphos)]^+$ and $[Ni(SC_6H_3Me_2\text{-}2,6)(triphos)]^+$ were performed using essentially the same concentration ranges of acid and base. Consequently, the different kinetic behaviour observed for the reaction of $[Ni(SC_6H_4Cl\text{-}2)(triphos)]^+$ with mixtures of $lutH^+$ and lut indicates that the association of $lutH^+$ with $[Ni(SC_6H_4Cl\text{-}2)(triphos)]^+$ is significantly weaker than with the other complexes.

6.6.2.3 Kinetics of protonation reactions with picH⁺ in the presence of pic.

Using the same procedure as described in (***section 6.6.2.2***), the kinetic reactions of $[Ni(SC_6H_4R\text{-}2)(triphos)]^+$ (R = H, Me, MeO, Cl) or $[Ni(SC_6H_3Me_2\text{-}2,6)(triphos)]^+$ with mixtures of $picH^+$ and pic have been investigated. Analysis of kinetics data indicates that the reaction occurs by the mechanism shown in Figure (6.15) and the rate law shown in Equations (6.18) and (6.19). (Where K_1^R = equilibrium constant for the protonation of complex, k_2^R = the rate constant for the protonation of complex, k_{-2}^R = the rate constant for the deprotonation of complex and R = H, Me, MeO or Cl).

$$\text{Rate} = \{\frac{(K_1^R k_2^R)^{pic}[picH^+]}{1 + (K_1^R)^{pic}[picH^+]} + (k_{-2}^R)^{pic}[pic]\}[Ni(SC_6H_4R-2)(triphos)^+] \qquad (6.18)$$

$$\text{Rate} = \{\frac{(K_1^{Me2} k_2^{Me2})^{pic}[picH^+]}{1 + (K_1^{Me2})^{pic}[picH^+]} + (k_{-2}^{Me2})^{pic}[pic]\}[Ni(SC_6H_3Me_2-2,6)(triphos)^+] \qquad (6.19)$$

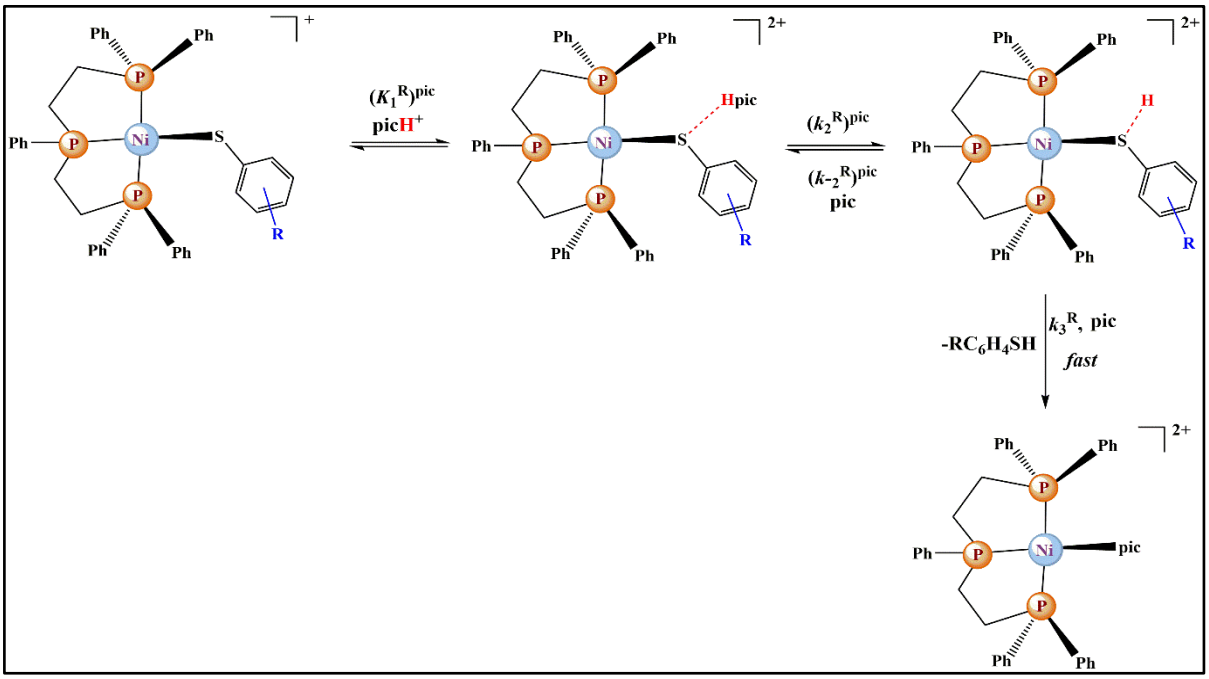

Figure 6.15. Mechanism of the reaction between $[Ni(SC_6H_4R)(triphos)]^+$ and mixtures of $picH^+$ and pic.

When monitored using stopped-flow spectrophotometry, the absorbance-time curves for the reactions of $[Ni(SC_6H_4R\text{-}2)(triphos)]^+$ or $[Ni(SC_6H_3Me_2\text{-}2,6)(triphos)]^+$ with mixtures of $picH^+$ and pic can be fitted to a single exponential curve, indicating that all these reactions exhibit a first order dependence on the concentration of complex. The dependence on the concentrations of $picH^+$ and pic were determined from plots of k_{obs}/[pic] versus [$picH^+$]/[pic]. The kinetics data and parameters have been determined and presented in Tables (6.12), (6.13), (6.14), (6.15), (6.16) and (6.17). In all cases the plots are straight lines provided the concentration of $picH^+$ is constant. Increasing the concentration of $picH^+$ gives a line with the same intercept but a smaller gradient. These kinetics provided $(k_{-2}^R)^{pic} > (k_3^R)^{pic}$, protonation of the complex $\{(k_2^R)^{pic}\}$ is rate-limiting.

For all cases, the plots shown in Figures (6.16), (6.17), (6.18), (6.19) and (6.20) are those defined by Equations (6.18) and (6.19). Moreover, the values of the equilibrium rate (K_1^R); the rate constant of protonation (k_2^R) and the rate constant of deprotonation (k_{-2}^R) are determined from these analyses and presented in Table (6.17).

Table (6.12): Kinetic data for the reaction of $[Ni(SC_6H_5)(triphos)]^+$ (0.25 mmol dm^{-3}) with mixtures of $picH^+$ and pic in MeCN at 25.0 °C. Data collected at λ = 350 nm.

$[picH^+]$ (mmol dm^{-3})	**[pic] (mmol dm^{-3})**	**$[picH^+]$ / [lut]**	**k_{obs} (s^{-1})**	**k_{obs} / [pic] ($mmol^{-1}$ dm^3 s^{-1})**	**ΔA**	**A_f**
2.5	2.5	1	0.65	260	0.124	0.2
	5	0.5	0.73	146	0.125	0.2
	10	0.25	0.94	94	0.126	0.2
	20	0.125	1.4	70	0.121	0.2
	40	0.0625	1.85	46.3	0.11	0.22
5	2.5	2	1.05	420	0.2	0.09
	5	1	1.09	218	0.21	0.09
	10	0.5	1.26	126	0.2	0.11
	20	0.25	1.67	83.5	0.19	0.14
	40	0.125	2	50	0.16	0.15
10	2.5	4	1.53	612	0.27	0.03
	5	2	1.82	364	0.27	0.03
	10	1	1.99	199	0.26	0.06
	20	0.5	2.38	119	0.24	0.08
	40	0.25	2.84	71	0.22	0.1

Table (6.13): Kinetic data for the reaction of $[Ni(SC_6H_4Me\text{-}2)(triphos)]^+$ (0.25 mmol dm^{-3}) with mixtures of $picH^+$ and pic in MeCN at 25.0 °C. Data collected at λ = 350 nm.

$[picH^+]$ (mmol dm^{-3})	**[pic] (mmol dm^{-3})**	**$[picH^+]$ / [lut]**	**k_{obs} (s^{-1})**	**k_{obs} / [pic] ($mmol^{-1}$ dm^3 s^{-1})**	**ΔA**	**A_f**
2.5	2.5	1	0.28	110	0.14	0.2
	5	0.5	0.3	60	0.14	0.2
	10	0.25	0.27	27	0.14	0.21
	20	0.125	0.31	15.5	0.14	0.21
	40	0.0625	0.58	14.5	0.14	0.21
5	2.5	2	0.37	148	0.22	0.1
	5	1	0.38	66	0.23	0.08
	10	0.5	0.39	39	0.22	0.11
	20	0.25	0.41	20.5	0.2	0.13
	40	0.125	0.58	13.5	0.2	0.17
10	2.5	4	0.5	200	0.24	0.004
	5	2	0.51	102	0.24	0.008
	10	1	0.55	55	0.24	0.012
	20	0.5	0.58	29	0.23	0.024
	40	0.25	0.58	14.5	0.22	0.037

Table (6.14): Kinetic data for the reaction of $[Ni(SC_6H_4OMe\text{-}2)(triphos)]^+$ (0.21 mmol dm^{-3}) with mixtures of $picH^+$ and pic in MeCN at 25.0 °C. Data collected at λ = 350 nm.

$[picH^+]$ (mmol dm^{-3})	**[pic] (mmol dm^{-3})**	**$[picH^+]$ / [lut]**	**k_{obs} (s^{-1})**	**k_{obs} / [pic] ($mmol^{-1}$ dm^3 s^{-1})**	**ΔA**	**A_f**
2.5	2.5	1	0.4	160	0.11	0.14
	5	0.5	0.43	85	0.11	0.14
	10	0.25	0.5	50	0.12	0.14
	20	0.125	0.72	36	0.1	0.16
	40	0.0625	1	24.8	0.1	0.16
5	2.5	2	0.49	196	0.16	0.08
	5	1	0.51	102	0.16	0.08
	10	0.5	0.52	52	0.15	0.09
	20	0.25	0.66	33	0.15	0.1
	40	0.125	0.77	19.3	0.14	0.11
10	2.5	4	0.54	216	0.23	0.02
	5	2	0.62	124	0.23	0.02
	10	1	0.72	72	0.23	0.02
	20	0.5	0.88	44	0.22	0.03
	40	0.25	1.09	27.3	0.2	0.05

Table (6.15): Kinetic data for the reaction of $[Ni(SC_6H_4Cl\text{-}2)(triphos)]^+$ (0.50 mmol dm^{-3}) with mixtures of $picH^+$ and pic in MeCN at 25.0 °C. Data collected at λ = 350 nm.

$[picH^+]$ (mmol dm^{-3})	**[pic] (mmol dm^{-3})**	**$[picH^+]$ / [lut]**	**k_{obs} (s^{-1})**	**k_{obs} / [pic] ($mmol^{-1}$ dm^3 s^{-1})**	**ΔA**	**A_f**
2.5	2.5	1	3.9	1544	0.08	0.3
	5	0.5	3.9	786	0.08	0.3
	10	0.25	4.5	453	0.08	0.3
	20	0.125	5	250	0.08	0.3
	40	0.0625	6.2	155	0.06	0.32
5	2.5	2	4	1600	0.13	0.34
	5	1	3.8	760	0.15	0.33
	10	0.5	4.1	410	0.14	0.35
	20	0.25	4.5	223	0.12	0.35
	40	0.125	6.5	163	0.1	0.38
10	2.5	4	4	1600	0.26	0.2
	5	2	4.3	850	0.26	0.21
	10	1	4	400	0.24	0.25
	20	0.5	5.4	270	0.21	0.29
	40	0.25	6.9	173	0.17	0.32

Table (6.16): Kinetic data for the reaction of $[Ni(SC_6H_3Me_2\text{-}2,6)(triphos)]^+$ (0.36 mmol dm^{-3}) with mixtures of $picH^+$ and pic in MeCN at 25.0 °C. Data collected at λ = 350 nm.

[picH$^+$] (mmol dm^{-3})	**[pic] (mmol dm^{-3})**	**[picH$^+$] / [lut]**	**k_{obs} (s^{-1})**	**k_{obs} / [pic] (mmol^{-1} dm^3 s^{-1})**	**ΔA**	**A_f**
2.5	2.5	1	0.018	7.3	0.13	0.32
	5	0.5	0.019	3.7	0.14	0.32
	10	0.25	0.019	1.93	0.14	0.32
	20	0.125	0.021	1.04	0.14	0.32
	40	0.0625	0.021	0.53	0.14	0.33
5	2.5	2	0.023	9.2	0.24	0.29
	5	1	0.023	4.6	0.25	0.28
	10	0.5	0.024	2.4	0.24	0.29
	20	0.25	0.024	1.2	0.25	0.28
	40	0.125	0.025	0.625	0.24	0.29
10	2.5	4	0.025	10	0.36	0.16
	5	2	0.024	4.8	0.36	0.16
	10	1	0.024	2.4	0.36	0.16
	20	0.5	0.024	1.2	0.36	0.16
	40	0.25	0.025	0.625	0.35	0.17

Table (6.17): Values of kinetic parameters for the reactions of $[Ni(SC_6H_4R\text{-}2)(triphos)]^+$ (R = H, Me, MeO or Cl) or $[Ni(SC_6H_3Me_2\text{-}2,6)(triphos)]^+$ with mixtures of $picH^+$ and pic in MeCN at 25.0 ^oC.

R	$(K_1^R)^{pic}$ **(dm^3 mol^{-1})**	$(k_2^R)^{pic}$ **(s^{-1})**	$(K_1^R k_2^R)^{pic}$ **(dm^3 mol^{-1} s^{-1})**	$(k_{-2}^R)^{pic}$ **(dm^3 mol^{-1} s^{-1})**	pK_a^{Ni}
H	100	3.0	300.8	35	15.4
Me	202	0.73	147.5	3.0	16.2
OMe	345	0.70	241.5	19	15.6
Cl	2600	4.0	1.0×10^4	100	16.5
Me_2	562	0.03	17.1	0.15	16.2

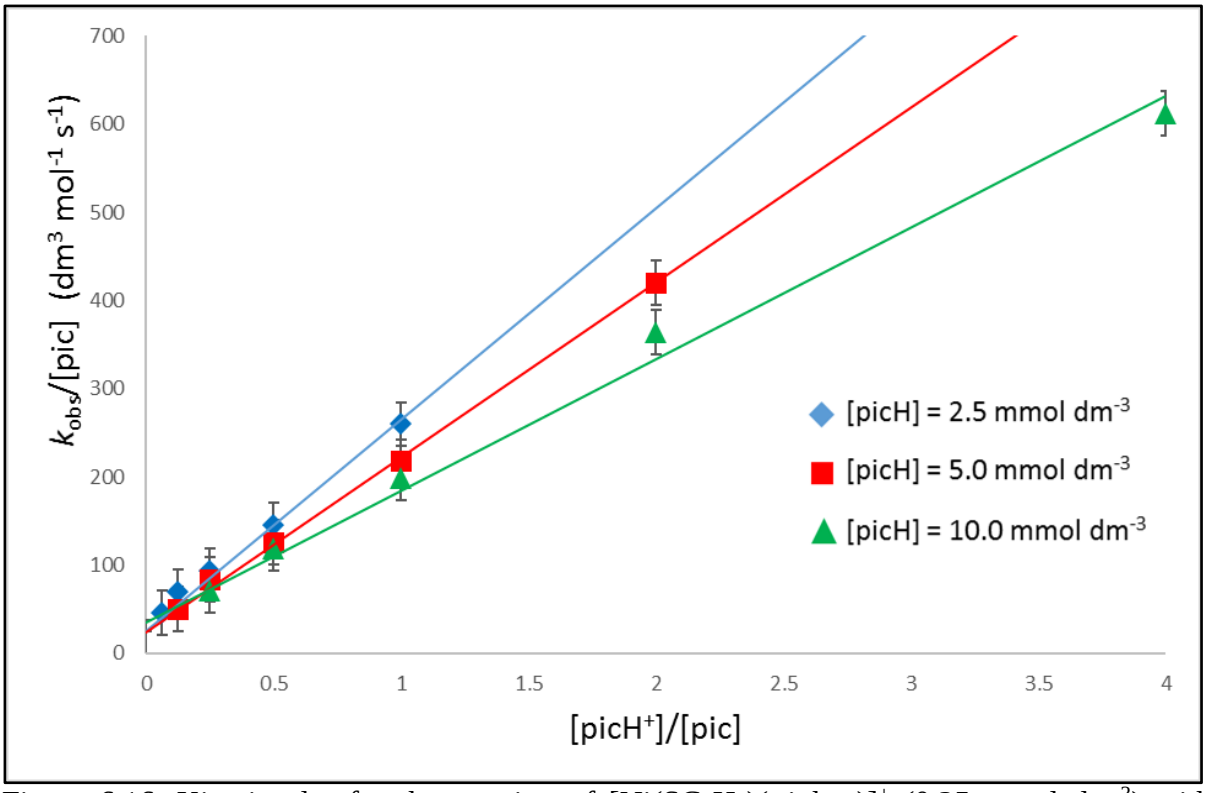

Figure 6.16. Kinetic plot for the reaction of $[Ni(SC_6H_5)(triphos)]^+$ (0.25 mmol dm^{-3}) with mixtures of picH$^+$ and pic in MeCN at 25.0 ^{o}C.The lines are defined by Equation (6.18).

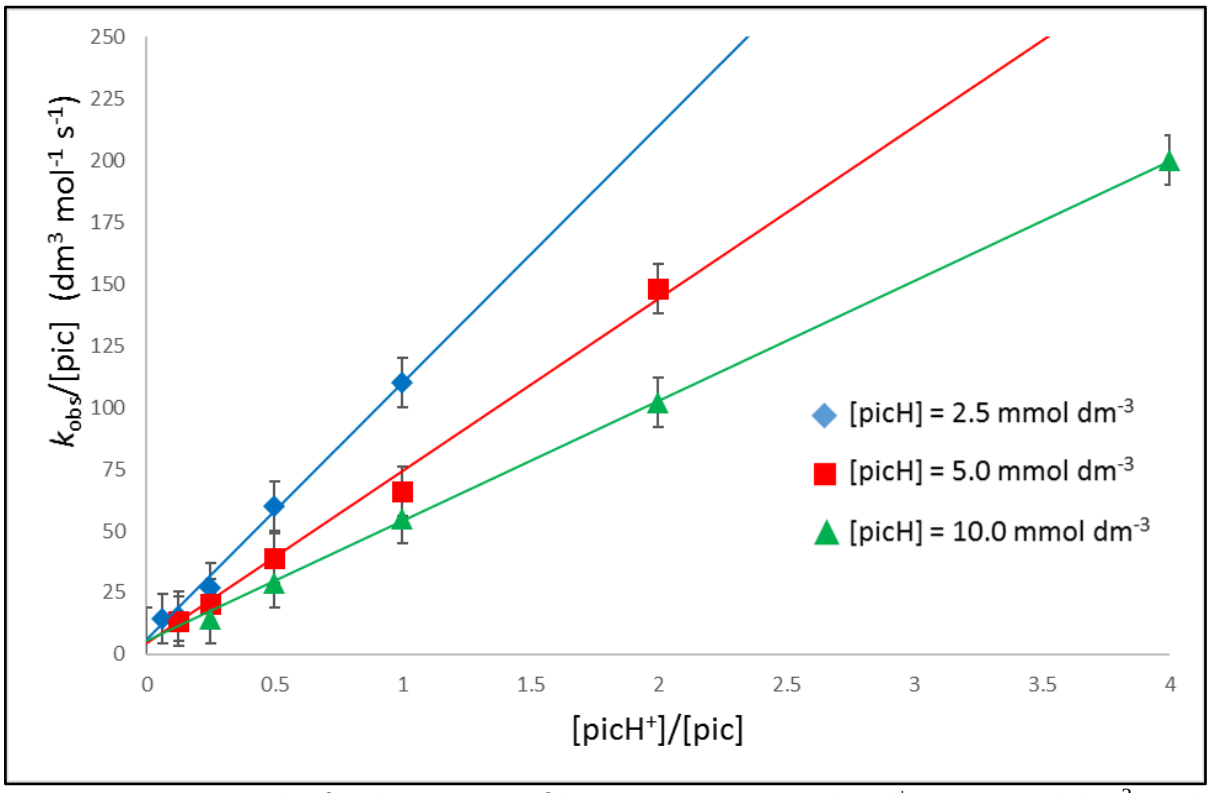

Figure 6.17. Kinetic plot for the reaction of $[Ni(SC_6H_4Me\text{-}2)(triphos)]^+$ (0.25 mmol dm^{-3}) with mixtures of picH$^+$ and pic in MeCN at 25.0 ^{o}C. The lines are defined by Equation (6.18).

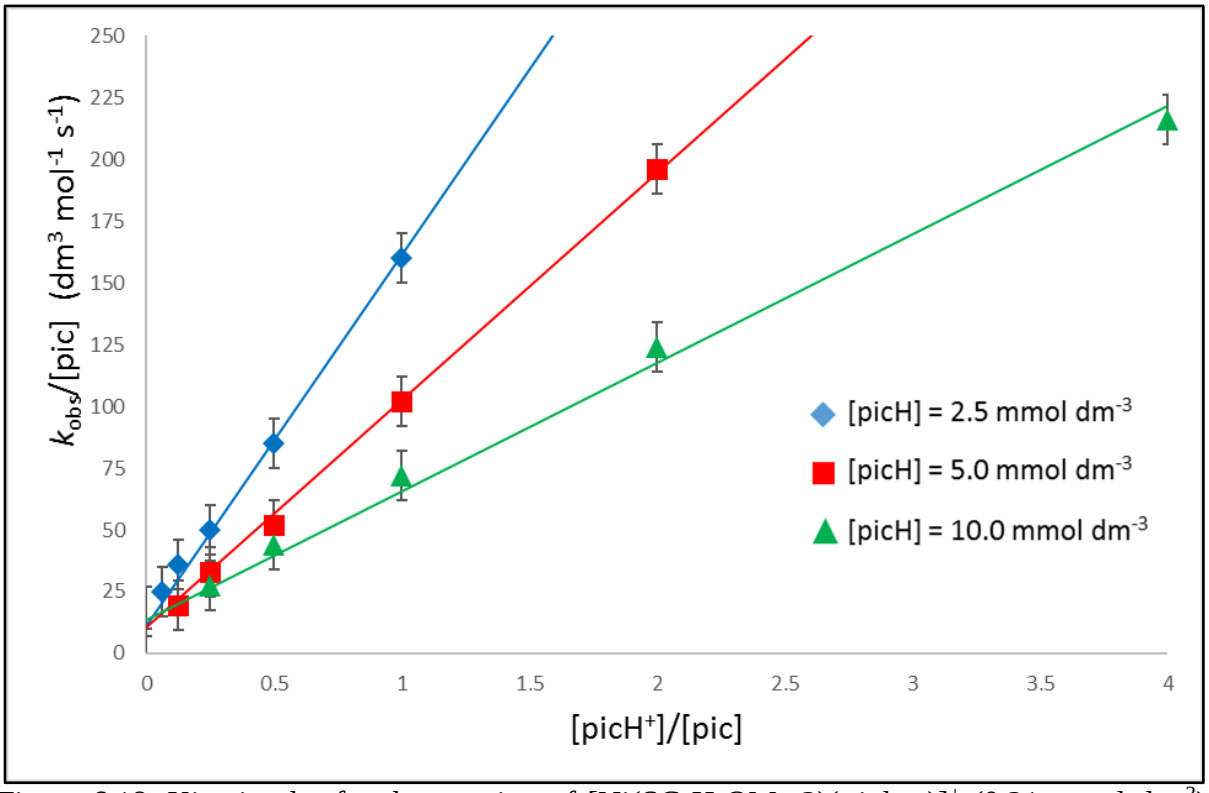

Figure 6.18. Kinetic plot for the reaction of [Ni(SC_6H_4OMe-2)(triphos)]$^+$ (0.21 mmol dm^{-3}) with mixtures of picH$^+$ and pic in MeCN at 25.0 ^{o}C. The lines are defined by Equation (6.18).

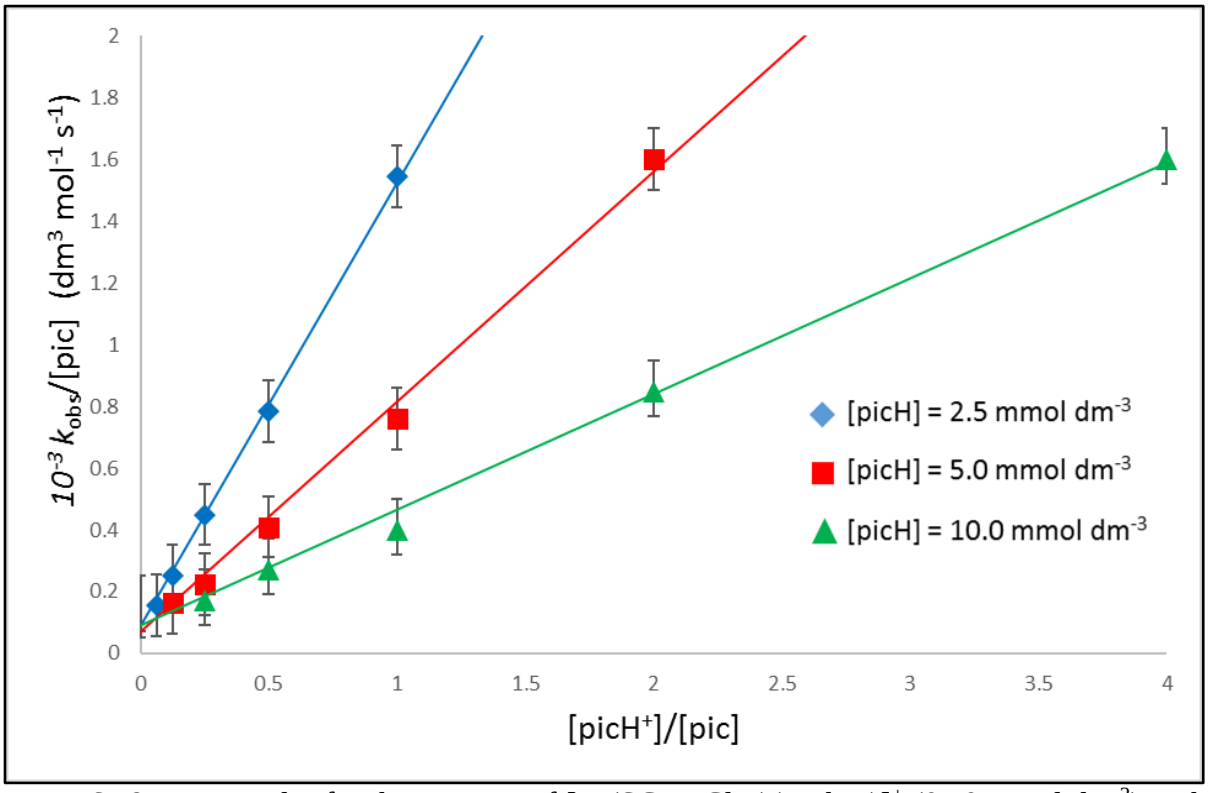

Figure 6.19. Kinetic plot for the reaction of [Ni(SC_6H_4Cl-2)(triphos)]$^+$ (0.50 mmol dm^{-3}) with mixtures of picH$^+$ and pic in MeCN at 25.0 ^{o}C. The lines are defined by Equation (6.18).

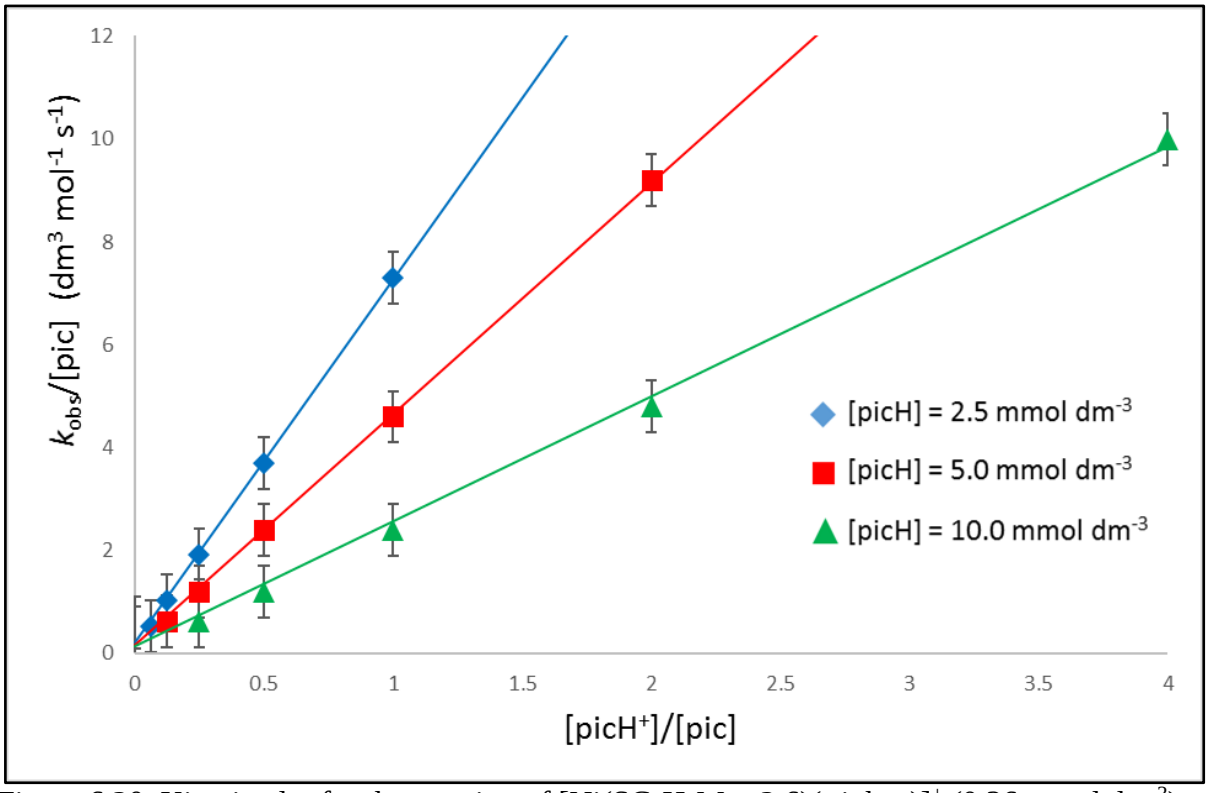

Figure 6.20. Kinetic plot for the reaction of [Ni($SC_6H_4Me_2$-2,6)(triphos)]$^+$ (0.36 mmol dm^{-3}) with mixtures of picH$^+$ and pic in MeCN at 25.0 ºC. The lines are defined by Equation (6.18).

6.6.2.4 Rates of proton transfer for the reactions of [Ni(thiolate)(triphos)]$^+$ with lutH$^+$ and picH$^+$.

The data in Tables (6.11) and (6.17) shows that for all the complexes, both the rates of protonation {$(K_1^R k_2^R)^{acid}$ = 300 – 5 dm^3 mol^{-1} s^{-1}} and deprotonation {$(k_{-2}^R)^{acid}$ = 100 – 0.15 dm^3 mol^{-1} s^{-1}} with either lutH$^+$ or picH$^+$ are significantly slower than the diffusion-controlled limit (k_{diff} = 3.7 x 10^{10} dm^3 mol^{-1} s^{-1} in MeCN)[6]. It has been known for some time that proton transfer reactions involving sulfur sites are slower than the diffusion limit but this is usually by a factor of only about 100[1, 25, 26]. It has been proposed that the much slower reactions observed in the reactions of [Ni(thiolate)(triphos)]$^+$ is a consequence of steric issues when the acid approaches the sulfur site which is effectively buried by the phenyl groups on triphos[10].

In this section, the kinetic data in Tables (6.11) and (6.17) will be discussed. A notable general feature is that, using the kinetic data in Tables (6.11) and (6.17), the pK_a^{Ni} of the coordinated thiols can be calculated from the relationship shown in Equation (6.20).

$$(K_1^R)^{acid} = K_a^{acid}/K_a^{Ni} \qquad (6.20)$$

For all complexes, there is good agreement between the pK_as calculated using $lutH^+$ and those using $picH^+$. This is consistent with both acids protonating the same site (*i.e.* sulfur) on $[Ni(thiolate)(triphos)]^+$.

Comparison of all the data in Tables (6.11) and (6.17) shows that the most prominent feature is that the rate of protonation of $[Ni(SC_6H_4Cl\text{-}2)(triphos)]^+$ is uniquely sensitive to the acid $\{(K_1^{Cl}k_2^{Cl})^{pic}/(K_1^{Cl}k_2^{Cl})^{lut} = 1.9 \times 10^3$; $(k_{-2}^{Cl})^{pic}/(k_{-2}^{Cl})^{lut} = 1 \times 10^3\}$. This exceptional increase in the proton transfer rates with this complex is principally due to a large difference in K_1^{Cl} $\{(K_1^{Cl})^{lut} < 10$ dm^3 mol^{-1}; $(K_1^{Cl})^{pic} = 2.6 \times 10^3$ dm^3 mol$^{-1}\}$, whilst the rates of intramolecular proton transfer are not too dissimilar $\{(k_2^{Cl})^{lut} \geq 0.5$ s^{-1}; $(k_2^{Cl})^{pic} = 4.0$ s$^{-1}\}$. The X-ray crystal structure of $[Ni(SC_6H_4Cl\text{-}2)(triphos)]^+$ shows that the 2-Cl-substituent interacts with the Ni. Although the Ni-Cl distance indicates that this is a relatively weak interaction (*vide supra*), it is possible that the Ni-Cl interaction is maintained throughout the proton transfer reaction, thus effectively locking the orientation of the thiolate and enforcing protonation to occur from the side of the square planar complex remote from the bound chloro-group (*i.e.* the closed face).

In principle, for $[Ni(thiolate)(triphos)]^+$, protonation of the sulfur can occur from either side of the square plane, provided the thiolate can undergo relatively unrestricted Ni-S rotation. Inspection of the X-ray crystal structures of $[Ni(SR')(triphos)]^+$ (R′ = Ph[18], $C_6H_4NO_2$-4[7], Bn[7], Et[12], Cy[12] and Bu^t[12], together with those for R = C_6H_4Me-2, C_6H_4OMe-2 and $C_6H_3Me_2$-2,6 reported in this chapter; Figures (6.6), (6.7) and (6.8) shows that, in all cases, the phenyl substituents on triphos impose different steric barriers on the two sides of the complex. This is a consequence of the conformations of the two chelate rings of triphos being mirror images of one another, Figure (6.21). Thus, the side of the square plane containing the phenyl group on P_2 (the open face) is less congested, with the distance between the phenyl groups of the two terminal phosphorus P_1 and P_3) being *ca* 5.0 Å. On the other side of the complex (the closed face), the distance between the phenyl groups on the two terminal phosphorus is only *ca* 3.0 Å. Earlier studies indicated that there is some flexibility in these dimensions depending on the configuration of the phenyl groups of triphos. The calculations assume that the phenyl groups can freely rotate about the P-C bond. The calculations use dimensions (bond lengths and angles) from X-ray crystal structure of $[Ni(SC_6H_5)(triphos)]BPh_4$. Thus, protonation *via* the closed face is sterically more challenging than protonation *via* the open face. The two acids used in these studies, $lutH^+$ and $picH^+$, have similar structures (based on pyridine), and similar pK_as[23, 24].

However, crucially, $lutH^+$ is sterically more demanding than $picH^+$ and thus differentiation between the two acids is most acute when protonation is enforced to occur from the closed face.

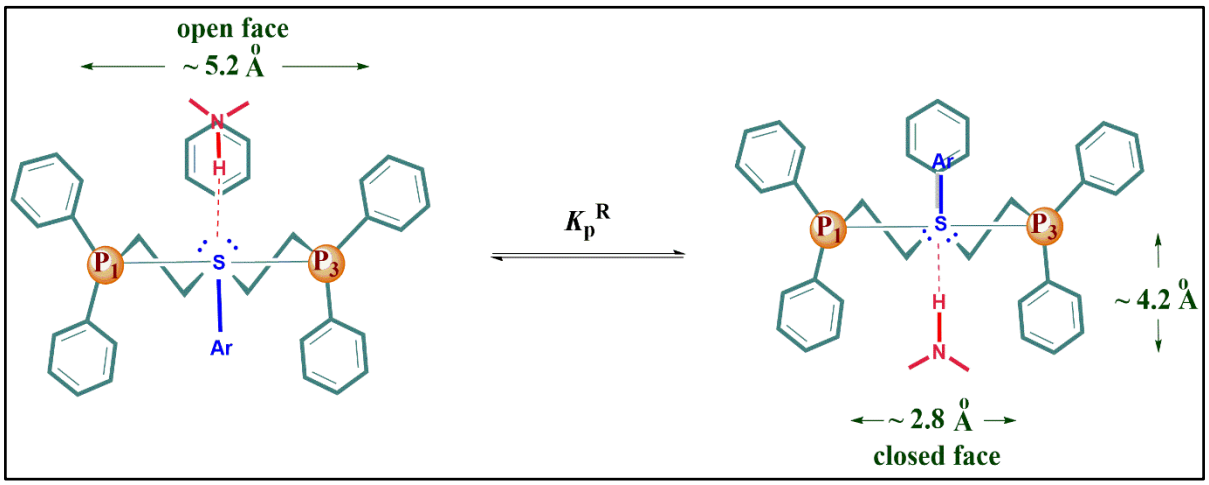

Figure 6.21. Representation of the different steric barriers on the two sides of the square plane of $[Ni(thiolate)(triphos)]^+$ and the different orientations of the thiolate necessary for protonation to occur from each face. The views are along the S-Ni-P_2 axis (from the S end). In this view the Ni and P_2 of the triphos are behind the S.

From the X-ray crystal structures, the depth of the cavity that the acid has to penetrate is *ca* 4.2 Å. Earlier theoretical studies indicated that (in preparation for proton transfer) the optimal NH…S hydrogen bond distance is *ca* 3.3 Å[27]. It is notable in the diagram shown in Figures (6.21) that the NH…S hydrogen bond distances are (*ca* 5.2 Å) for open face position and (*ca* 2.8 Å) for closed face position. Consequently, it can be suggested that either $lutH^+$ or $picH^+$ has to penetrate into the cavity by (*ca* 1 Å), which is the different steric barriers on the two sides of the square plane of $[Ni(thiolate)(triphos)]^+$. This is more difficult for $lutH^+$ than $picH^+$ because the width of $lutH^+$ is the Me…Me intranuclear distance which is *ca* 5.0 Å[28]. Consequently, $lutH^+$ will be held outside the cavity some distance from the sulfur, resulting in weak binding of $lutH^+$ to $[Ni(SC_6H_4Cl\text{-}2)(triphos)]^+$ and a non-optimal NH…S hydrogen bond distance, and hence slower proton transfer. Because $lutH^+$ cannot penetrate the phenyl substituents on the closed face, the precursor intermediate, $\{[Ni(SC_6H_4Cl\text{-}2)(triphos)]\ldots Hlut\}^{2+}$, is not stabilised by encapsulation, because the steric factor of bulky reactants will play an important role to restrict the approach of the $lutH^+$ towards the complex; and consequently does not accumulate, resulting in the rate law shown in Equation (6.17). In contrast, the smaller $picH^+$ (width = intramolecular $C_2\ldots C_6$ distance = *ca* 2.4 Å)[29] can more easily penetrate the cavity of the closed face, resulting in a stronger NH…S hydrogen bond and encapsulation of the acid stabilizes the hydrogen-bonded precursor intermediate $\{[Ni(SC_6H_4Cl\text{-}2)(triphos)]\ldots Hpic\}^{2+}$, resulting in the rate law of Equation (6.18).

For [Ni(SC_6H_4R-2)(triphos)]$^+$ (R = H, Me, MeO) and [Ni($SC_6H_3Me_2$-2,6)(triphos)]$^+$, there is only a modest difference in the rates of proton transfer with the two acids but, in all cases, the rates of proton transfer with picH$^+$ are about 10 times faster than the corresponding rates with lutH$^+$ {$(K_1^R k_2^R)^{pic}/(K_1^R k_2^R)^{lut}$ = 0.51 – 15.0; $(k_{-2}^R)^{pic}/(k_{-2}^R)^{lut}$ = 0.75 – 38.0}. This is not the trend anticipated from the pK_as of the two acids since, of the two acids, lutH$^+$ is slightly stronger. It seems likely that the observed trend is because lutH$^+$ is more sterically demanding than picH$^+$. The binding affinity of acid to [Ni(thiolate)(triphos)]$^+$ $(K_1^R)^{acid}$ to form the hydrogen-bonded precursor intermediate, {[Ni(thiolate)(triphos)]…acid}$^{2+}$, is, for all complexes, slightly smaller (about a factor of 2) with picH$^+$ than with lutH$^+$ {$(K_1^R)^{pic}/(K_1^R)^{lut}$ = 0.40 – 0.55}. This is consistent with the slightly larger pK_a of picH$^+$ which presumably results in a weaker NH…S hydrogen-bond. The rates of intramolecular proton transfer of {[Ni(thiolate)(triphos)]…acid}$^{2+}$ are faster with picH$^+$ {$(k_2^R)^{pic}/(k_2^R)^{lut}$ = 12 – 30} and deprotonation of [Ni(thiol)(triphos)]$^{2+}$ by pic is faster than with lut {$(k_{-2}^R)^{pic}/(k_{-2}^R)^{lut}$ = 9 – 38}. This is presumably because it is more difficult for the more sterically-demanding lutH$^+$ and lut to get sufficiently close to the sulfur for efficient proton transfer.

It seems reasonable that both electronic and steric effects from the 2-R-substituents on the thiolate will contribute to the rate. For the reactions with picH$^+$, the rates of protonation {$(K_1^R k_2^R)^{pic}$, R = H (300) > MeO (242) > Me (148) > Me_2 (17)} and deprotonation {$(k_{-2}^R)^{pic}$, R = H (35) > MeO (19) > Me (3) > Me_2 (0.15)} follow the same order. This order appears to indicate that: (i) introducing any group (larger than H) to the 2-position results in slower rates of protonation by picH$^+$ and (ii) although the data is limited, the order of reactivities of the R = MeO, Me and Me_2 derivative follows the electronic influence of the 2-R-substituent. For the reactions with lutH$^+$, the reactivity pattern is different to that observed with picH$^+$. Thus, the rates of protonation {$(K_1^R k_2^R)^{lut}$, R = MeO (36) ~ Me_2 (34) > H (20) > Me (17)} and deprotonation {$(k_{-2}^R)^{lut}$, R = H (4) > MeO (0.5) ~ Me (0.2) ~ Me_2 (0.2)} do not follow a common pattern. It seems likely that the reason for this is because, with these derivatives (unlike the 2-Cl complex), there is relatively unrestricted Ni-S bond rotation and consequently protonation with either acid can occur from the open or closed face.

The thermodynamic activation parameters for the intramolecular proton transfer in {[Ni(SC_6H_4R-2)(triphos)]…Hlut}$^{2+}$ (R = Me, MeO or Cl) and {[Ni($SC_6H_3Me_2$-2,6)(triphos)]…Hlut}$^{2+}$ have been investigated. The values of $\Delta H^{\ddagger}$, $\Delta S^{\ddagger}$ and $\Delta G^{\ddagger}$ are impacted by both the steric barrier and the electronic characteristics of R substituent.

DFT calculations were used to gauge the barrier to rotation of the Ni–S bond of the [Ni(thiolate)(triphos)]$^+$ complex. At the coordinated thiolate (R =Me, MeO or Me_2), if the rotation is easy then the protonation can occur from either the open or closed face. However, if there is a high barrier to rotation then the configuration of the thiolate will remain locked during protonation. Our calculations for [Ni(thiolate)(triphos)]$^+$ indicated that in all cases there is a very low barrier to rotation.

6.6.2.5 Temperature dependence of the reactions of [Ni(SC_6H_4R-2)(triphos)]$^+$ or [Ni($SC_6H_3Me_2$-2)(triphos)]$^+$ with lutH$^+$ in presence of lut.

The impact of temperature change on the rate of intramolecular proton transfer between [Ni(SC_6H_4R-2)(triphos)]$^+$ (R = Me, OMe or Cl) or [Ni($SC_6H_3Me_2$-2)(triphos)]$^+$ and [lutH$^+$] (k_2^R) have been investigated. The kinetic studies were performed by using constant concentrations of the complex and the acid [lutH$^+$] in presence of various concentrations of the base [lut] in acetonitrile (MeCN) at the range of temperatures 15.0-35.0°C. In all cases, the experiments were performed using a high concentration of lutH$^+$, so that K_1^R[lutH$^+$] > 1, and the rate laws in Equations (6.15) and (6.16) simplify to Equations (6.21) and (6.22) .

$$\text{Rate} = \{(k_2^{\text{R}})^{\text{lut}} + (k_{-2}^{\text{R}})^{\text{lut}}[\text{lut}]\}[\text{Ni}(\text{SC}_6\text{H}_4\text{R}-2)(\text{triphos})^+] \qquad (6.21)$$

$$\text{Rate} = \{(k_2^{\text{Me2}})^{\text{lut}} + (k_{-2}^{\text{Me2}})^{\text{lut}}[\text{lut}]\}[\text{Ni}(\text{SC}_6\text{H}_3\text{Me}_2-2,6)(\text{triphos})^+] \quad (6.22)$$

Under these conditions, in the graph of k_{obs}/[lut] against 1/[lut], the slope is $(k_2^R)^{lut}$. The kinetic results for the reactions of the [lutH$^+$] with [Ni(SC_6H_4R-2)(triphos)]$^+$ (R = Me, Cl) or [Ni($SC_6H_3Me_2$-2)(triphos)]$^+$ show that the intramolecular proton transfer step is affected by the change of temperatures. However, there is no significant effect for the temperatures change on the intramolecular proton transfer for the reaction of the [lutH$^+$] with [Ni(SC_6H_4OMe-2)(triphos)]$^+$. All experimental data are presented in Tables (6.18), (6.19) and (6.20); and Figures (6.22), (6.23) and (6.24).

Table (6.18): Experimental data for the reaction of $[Ni(SC_6H_4Me\text{-}2)(triphos)]^+$ (0.25 mmol dm^{-3}) with mixtures of $lutH^+$ (10.0 mmol dm^{-3}) and lut in MeCN at (15.0-35.0) ^oC.

T (K)	**[lut] (mmol dm^{-3})**	**1/[lut] (dm^3 $mmol^{-1}$)**	**k_{obs} (s^{-1})**	**k_{obs}/[lut]**
288	2.5	400	0.027	10.8
	5	200	0.029	5.8
	10	100	0.028	2.8
	20	50	0.027	1.35
	40	25	0.031	0.775
293	2.5	400	0.028	11.2
	5	200	0.03	6
	10	100	0.03	3
	20	50	0.029	1.45
	40	25	0.034	0.85
298	2.5	400	0.03	12
	5	200	0.033	6.6
	10	100	0.034	3.4
	20	50	0.033	1.65
	40	25	0.037	0.925
308	2.5	400	0.035	14
	5	200	0.04	8
	10	100	0.041	4.1
	20	50	0.04	2
	40	25	0.039	0.975

Table (6.19): Experimental data for the reaction of $[Ni(SC_6H_4Me_2\text{-}2,6)(triphos)]^+$ (0.25 mmol dm^{-3}) with mixtures of $lutH^+$ (10.0 mmol dm^{-3}) and lut in MeCN at (15.0-35.0) ^oC.

T (K)	**[lut] (mmol dm^{-3})**	**1/[lut] (dm^3 $mmol^{-1}$)**	**k_{obs} (s^{-1})**	**k_{obs}/[lut]**
288	2.5	400	0.015	6.0
	5	200	0.015	3.0
	10	100	0.019	1.9
	20	50	0.011	0.55
	40	25	0.012	0.3
293	2.5	400	0.02	8.0
	5	200	0.019	3.8
	10	100	0.021	2.1
	20	50	0.013	0.65
	40	25	0.014	0.35
298	2.5	400	0.026	10.4
	5	200	0.025	5.0
	10	100	0.026	2.6
	20	50	0.018	0.9
	40	25	0.02	0.5
308	2.5	400	0.032	12.8
	5	200	0.034	6.8
	10	100	0.035	3.5
	20	50	0.03	1.5
	40	25	0.026	0.65

Table (6.20): Experimental data for the reaction of $[Ni(SC_6H_4Cl\text{-}2)(triphos)]^+$ (0.25 mmol dm^{-3}) with mixtures of $lutH^+$ (10.0 mmol dm^{-3}) and lut in MeCN at (15.0-35.0) ^oC.

T (K)	**[lut] (mmol dm^{-3})**	**1/[lut] (dm^3 $mmol^{-1}$)**	**k_{obs} (s^{-1})**	**k_{obs}/[lut]**
288	2.5	400	0.068	27.2
	5	200	0.07	14
	10	100	0.07	7
	20	50	0.068	3.4
	40	25	0.072	1.8
293	2.5	400	0.08	32
	5	200	0.09	18
	10	100	0.091	9.1
	20	50	0.078	3.9
	40	25	0.084	2.1
298	2.5	400	0.1	40
	5	200	0.11	22
	10	100	0.11	11
	20	50	0.09	4.5
	40	25	0.092	2.3
308	2.5	400	0.135	54
	5	200	0.14	28
	10	100	0.14	14
	20	50	0.122	6.1
	40	25	0.128	3.2

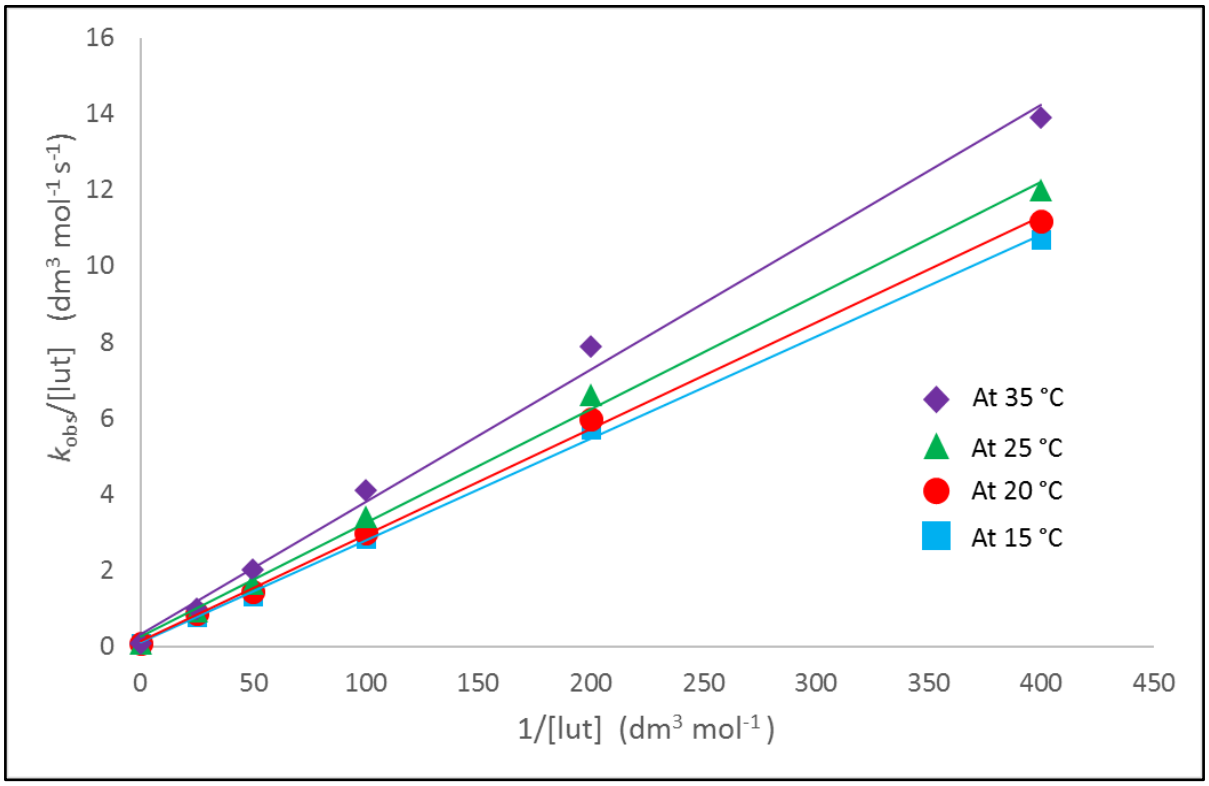

Figure 6.22. Plot of the rate change for the intramolecular proton transfer $(k_2^R)^{lut}$ between $[Ni(SC_6H_4Me\text{-}2)(triphos)]^+$ and $lutH^+$ in presence of lut, at (15-35) °C in MeCN.

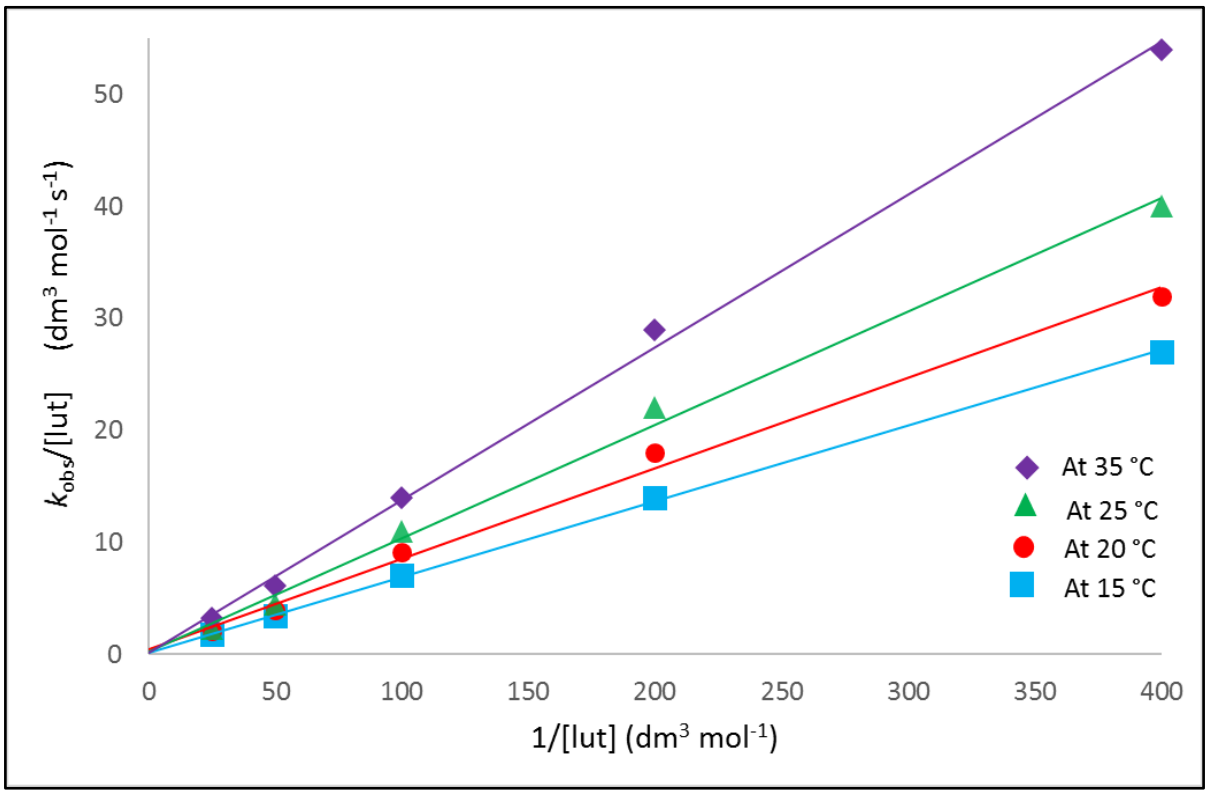

Figure 6.23. Plot of the rate change for the intramolecular proton transfer $(k_2^R)^{lut}$ between $[Ni(SC_6H_3Me_2\text{-}2,6)(triphos)]^+$ and $lutH^+$ in presence of lut, at (15-35) °C in MeCN.

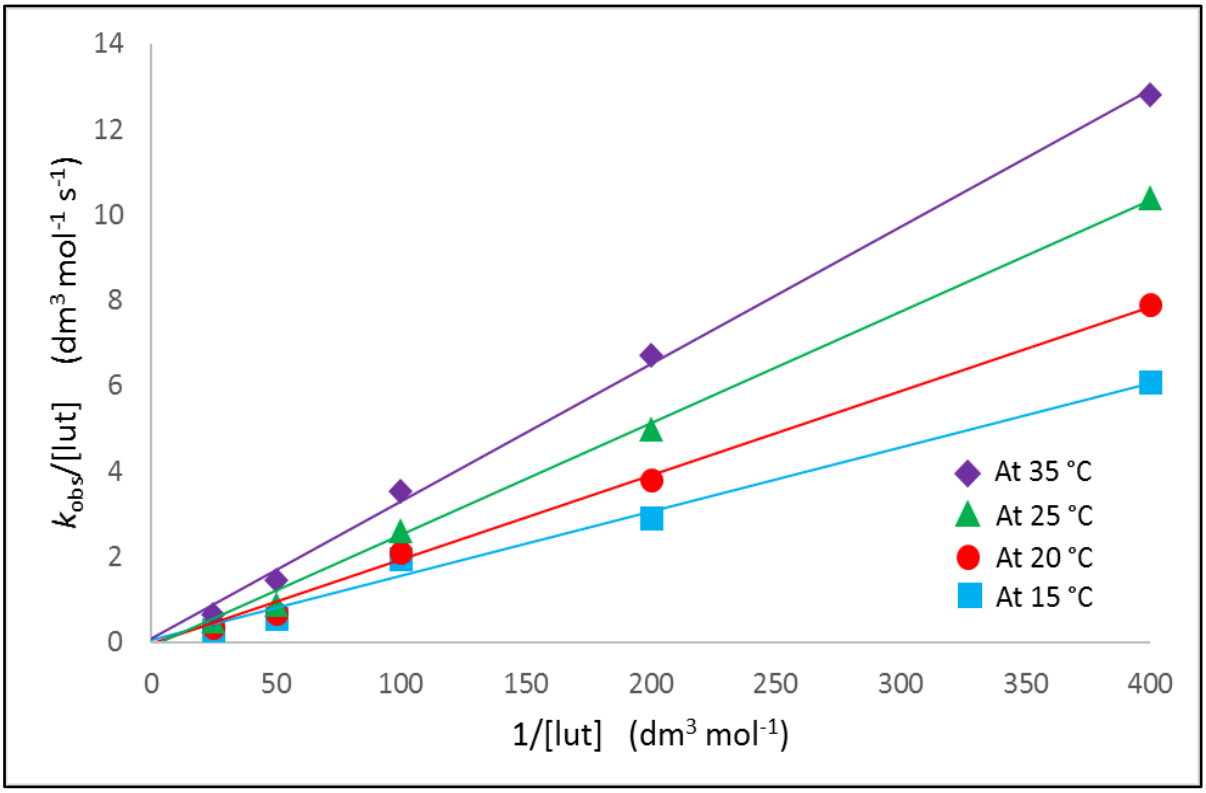

Figure 6.24. Plot of the rate change for the intramolecular proton transfer $(k_2^R)^{lut}$ between $[Ni(SC_6H_4Cl\text{-}2)(triphos)]^+$ and $lutH^+$ in presence of lut, at (15-35) °C in MeCN.

The thermodynamic parameters {the activation enthalpy ($\Delta H^{\ddagger}$) and the activation entropy ($\Delta S^{\ddagger}$)} for the reactions of $[Ni(thiolate)(triphos)]^+$ with mixtures of $lutH^+$ and lut have been determined by using Arrhenius and Eyring equation (6.23).

$$\ln\left(\frac{k}{T}\right) = -\frac{\Delta H^{\ddagger}}{R}\left(\frac{1}{T}\right) + \ln\frac{k_B}{h} + \frac{\Delta S^{\ddagger}}{R} \quad (6.23)$$

Or

$$\log_{10}\left(\frac{k}{T}\right) = -\frac{\Delta H^{\ddagger}}{R}\left(\frac{1}{T}\right) + \frac{\Delta S^{\ddagger}}{R} + 10.32$$

From the plots of $\log_{10}(k_2/T)$ against (1/T), the values of $\Delta H^{\ddagger}$ and $\Delta S^{\ddagger}$ were determined, when: slope $= -\frac{\Delta H^{\ddagger}}{R}$ and intercept $= \frac{\Delta S^{\ddagger}}{R} + 10.32$; and where {$k = k_2$ = rate constant for the intramolecular proton transfer $(k_2^R)^{lut}$, T = absolute temperature (K), R = gas constant (8.314 J mol^{-1} K^{-1} or 1.987 cal mol^{-1} K^{-1}), k_B = Boltzmann constant (1.381 x 10^{-23} J K^{-1}) and h = Planck constant (6.626 x 10^{-34} J s)}. In addition, the change in Gibbs free energy ($\Delta G^{\ddagger}$) at 298 K has been calculated using the relationship in Equation (6.24). `

$$\Delta G^{\ddagger} = \Delta H^{\ddagger} - T\Delta S^{\ddagger} \quad (6.24)$$

All kinetic and the thermodynamic data for the reactions between $[Ni(SC_6H_4R\text{-}2)(triphos)]^+$ or $[Ni(SC_6H_3Me_2\text{-}2)(triphos)]^+$ with $lutH^+$ in presence of lut are shown in Tables (6.21), (6.22), (6.23) and (6.24). Figure (6.25) shows the Eyring plots for all reactions at (15.0-35.0) °C in acetonitrile.

The activation parameters presented in Table (6.24) correspond to the product of two steps: (i) The binding of $lutH^+$ to complex (K_1^R); and (ii) subsequent proton transfer from $lutH^+$ to the thiolate ligand (k_2^R). The activation parameters, $\Delta H^{\ddagger}$ and $\Delta S^{\ddagger}$ will be affected by both the steric barrier and the electronic characteristics of R substituent.

Previous studies[7] on the temperature dependence of the reactions of $[Ni(SC_6H_4R\text{-}4)(triphos)]^+$ with $lutH^+$ indicated to the same effect for the electronic characteristics of R substituent and the values (R = OMe: $\Delta H^{\ddagger}$ = 4.1 kcal mol^{-1}, $\Delta S^{\ddagger}$ = -50.1 cal mol^{-1}; R = Cl: $\Delta H^{\ddagger}$ = 6.9 kcal mol^{-1}, $\Delta S^{\ddagger}$ = -41.2 cal mol^{-1} and R = NO_2: $\Delta H^{\ddagger}$ = 11.2 kcal mol^{-1}, $\Delta S^{\ddagger}$ = -16.4 cal mol^{-1}).

Table (6.21): Kinetics data of the reaction between $[Ni(SC_6H_4Me\text{-}2)(triphos)]^+$ and $lutH^+$ at (15.0-35.0) ^oC, in MeCN.

T (K)	**k_2 (s^{-1})**	**k_2/T (s^{-1} K^{-1})**	**1/T (K^{-1})**	**$\log_{10}$ (k_2/T)**
288	0.0239	8.29861 x 10^{-5}	0.003472	-4.08099
293	0.0273	9.31741 x 10^{-5}	0.003413	-4.0307
298	0.03	1.00671 x 10^{-4}	0.003356	-3.9971
308	0.0352	1.14286 x 10^{-4}	0.003247	-3.94201

Table (6.22): Kinetics data of the reaction between $[Ni(SC_6H_3Me_2\text{-}2,6)(triphos)]^+$ and $lutH^+$ at (15.0-35.0) ^oC, in MeCN.

T (K)	**k_2 (s^{-1})**	**k_2/T (s^{-1} K^{-1})**	**1/T (K^{-1})**	**$\log_{10}$ (k_2/T)**
288	0.0207	7.1875 x 10^{-5}	0.003472	-4.14342
293	0.025	8.53242 x 10^{-5}	0.003413	-4.06893
298	0.03	1.00671 x 10^{-4}	0.003356	-3.9971
308	0.0404	1.31169 x 10^{-4}	0.003247	-3.88217

Table (6.23): Kinetics data of the reaction between $[Ni(SC_6H_4Cl\text{-}2)(triphos)]^+$ and $lutH^+$ at (15.0-35.0) ^oC, in MeCN.

T (K)	k_2 **(s^{-1})**	k_2/T **(s^{-1} K^{-1})**	**1/T (K^{-1})**	$\log_{10}(k_2/T)$
288	0.162	5.63×10^{-4}	0.003472	-3.24988
293	0.275	9.39×10^{-4}	0.003413	-3.02753
298	0.402	1.349×10^{-3}	0.003356	-2.86999
308	0.626	2.032×10^{-3}	0.003247	-2.69198

Table (6.24): Thermodynamic activation parameters for the reactions between $[Ni(SC_6H_4R\text{-}2)(triphos)]^+$ or $[Ni(SC_6H_3Me_2\text{-}2)(triphos)]^+$ with $lutH^+$ and lut in MeCN.

Complex	$\Delta H^{\ddagger}$ **(kcal mol^{-1})**	$\Delta S^{\ddagger}$ **(cal deg^{-1} mol^{-1})**	$\Delta G^{\ddagger}_{298}$ **(kcal mol^{-1})**
$[Ni(SC_6H_4OMe\text{-}2)(triphos)]^+$	0.0	-55.0	16.4
$[Ni(SC_6H_4Me\text{-}2)(triphos)]^+$	1.2	-53.3	17.1
$[Ni(SC_6H_4Cl\text{-}2)(triphos)]^+$	4.8	-36.3	15.6
$[Ni(SC_6H_3Me_2\text{-}2)(triphos)]^+$	2.3	-50.2	17.3

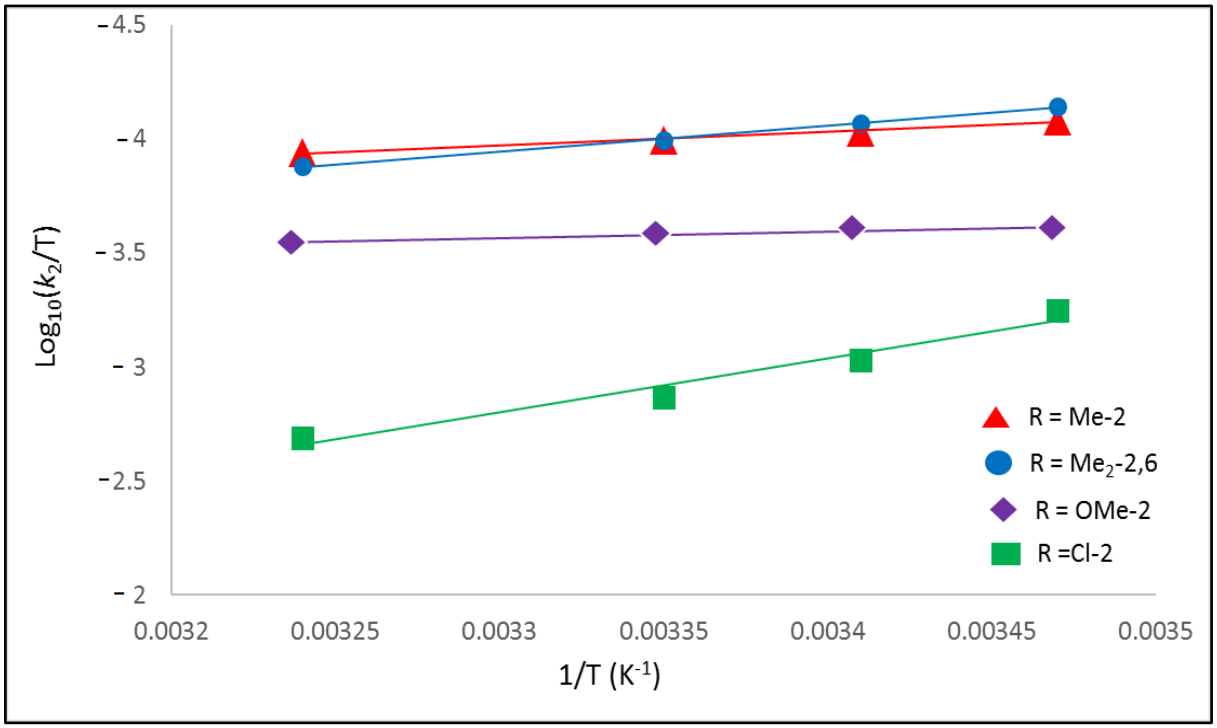

Figure 6.25. Eyring plots for the reactions between $[Ni(SC_6H_4R\text{-}2)(triphos)]^+$ or $[Ni(SC_6H_3Me_2\text{-}2)(triphos)]^+$ with $lutH^+$ and lut, at (15.0-35.0) ^oC in MeCN.

6.6.3 Computational studies for thiolate rotation and protonation from open and closed faces.

The X-ray crystallography for synthesised complexes shows that the geometrical structures of $[Ni(SC_6H_4OMe\text{-}2)(triphos)]^+$, $[Ni(SC_6H_4Me\text{-}2)(triphos)]^+$ and $[Ni(SC_6H_3Me_2\text{-}2,6)(triphos)]^+$ are square planar, whilst the geometrical structure for $[Ni(SC_6H_4Cl\text{-}2)(triphos)]^+$ is a square-based pyramid. The kinetic studies for the reactions between $[Ni(SC_6H_4R\text{-}2)(triphos)]^+$ (R = Me, OMe) or $[Ni(SC_6H_3Me_2\text{-}2)(triphos)]^+$ with $lutH^+$ and lut indicate that the protonation with acid can occur from either open or closed face.

DFT calculations (GAUSSIAN09 package)[20] have been used to explore the barriers to Ni-S bond rotation in $[Ni(SC_6H_4R\text{-}2)(triphos)]^+$ (R = H, Me or MeO) and $[Ni(SC_6H_3Me_2\text{-}2,6)(triphos)]^+$. For all complexes, the calculations indicate that complete rotation of the Ni-S bond can occur with relatively low barriers to rotation. As expected, the maximum barriers are evident when the S-aryl group passes each of the PPh_2 groups of the triphos, as shown in Figure (6.26).

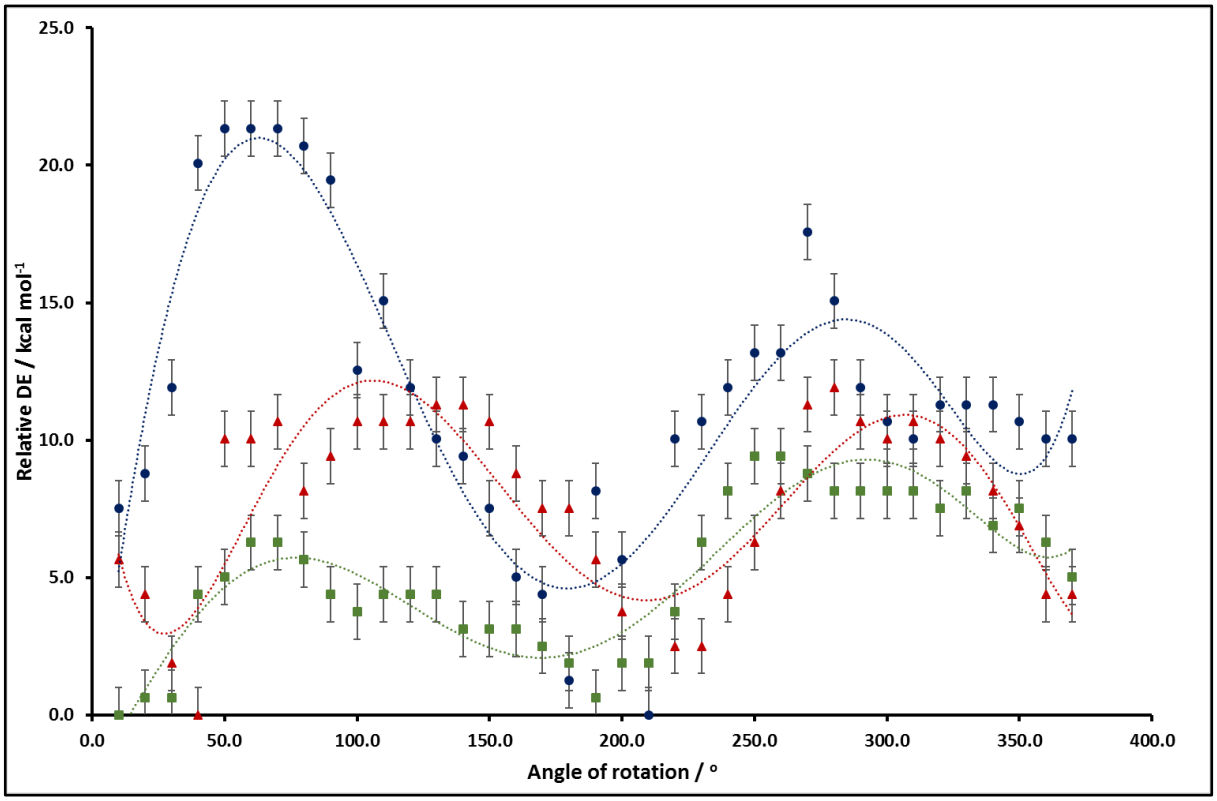

Figure 6.26. Diagrams of relative DE (kcal mol^{-1}) against angle of rotation (°) for the scan of optimisation calculations of $[Ni(SC_6H_4R\text{-}2)(triphos)]^+$ {R = OMe (●) ; Me (▲) and H (■)}.

The calculated barriers to rotation are: -0.63 kcal mol^{-1}, R = H; -1.63 kcal mol^{-1}, R = Me; -2.01 kcal mol^{-1}, R = MeO; -3.14 kcal mol^{-1}, R = Me_2. Revealingly, in calculations where the P_1-Ni-S angle is locked, rotation of the S-C_{ipso} bond has a prohibitively high energy (-0.6275 kcal mol^{-1}). This observation dictates that rotation about the Ni-S bond is effectively coupled to movement about the S-C_{ipso} bond, where the latter maintains the R-substituents in a constant direction as shown in Figure (6.26).

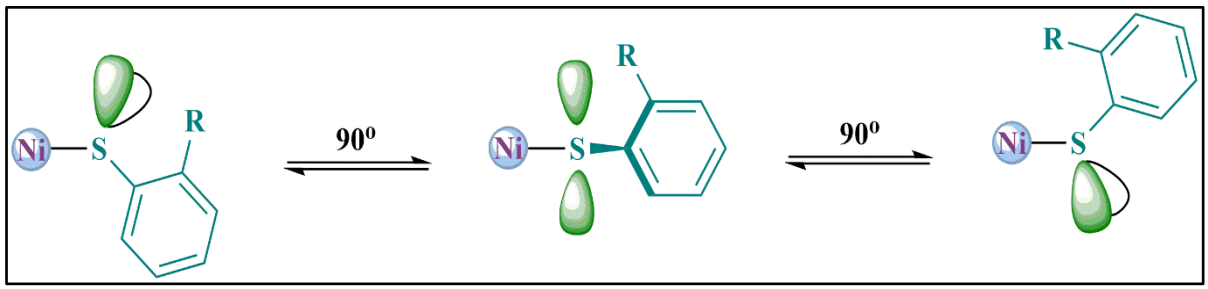

Figure 6.27. Orientation of the $SC_6H_4R\text{-}2$ ligand during Ni-S rotation with concomitant S-C_{ipso} rotation in $[Ni(SC_6H_4R\text{-}2)(triphos)]^+$. The triphos ligand is not shown (for clarity), but the two PPh_2 groups occupy.

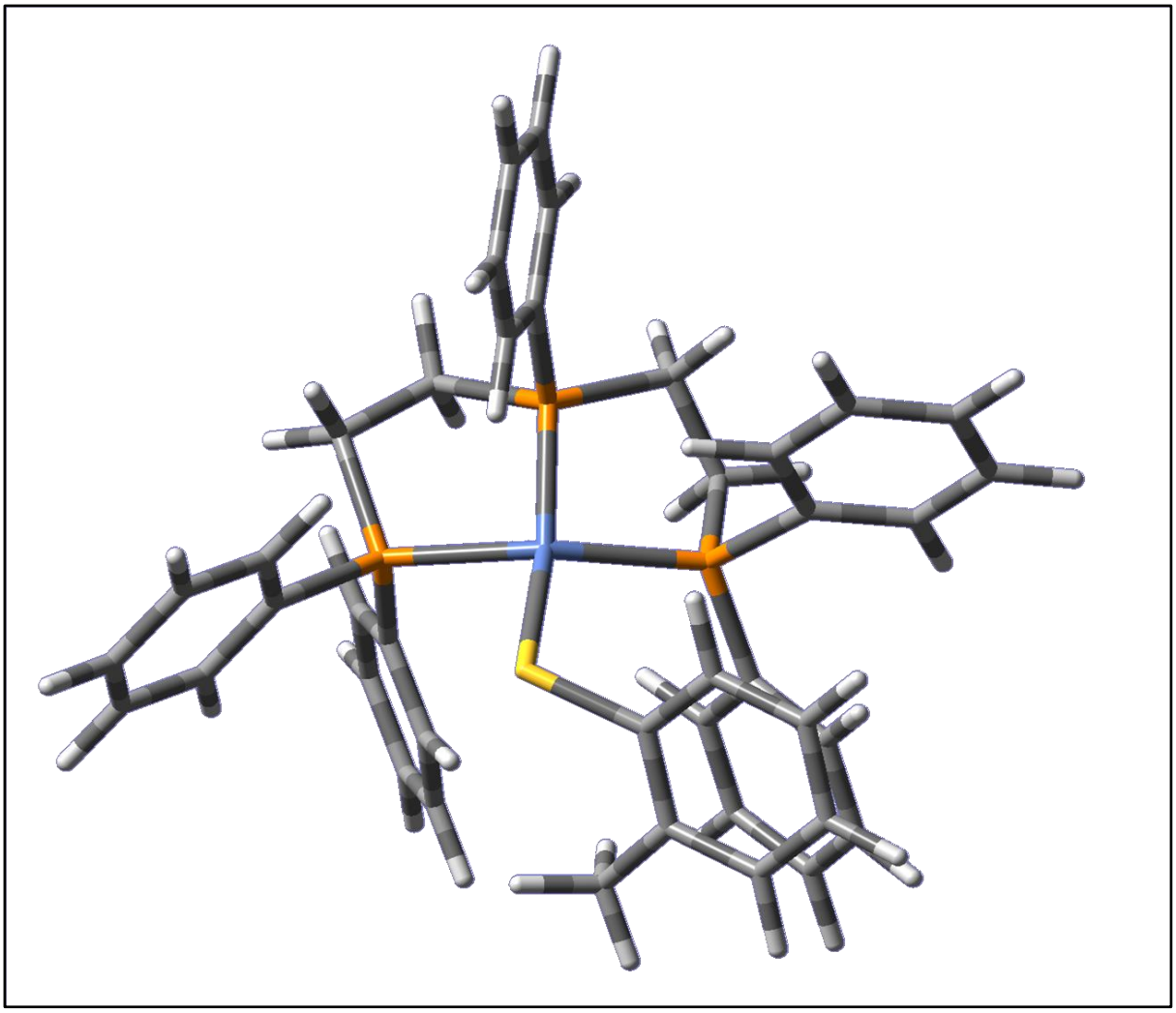

Figure 6.28. Picture of the optimised structure of $[Ni(SC_6H_4Me\text{-}2)(triphos)]^+$ showing barrier for the S-aryl group passes each of the PPh_2 groups of the triphos. Key: Ni = blue, P = orange, S = yellow, C = grey and H = white.

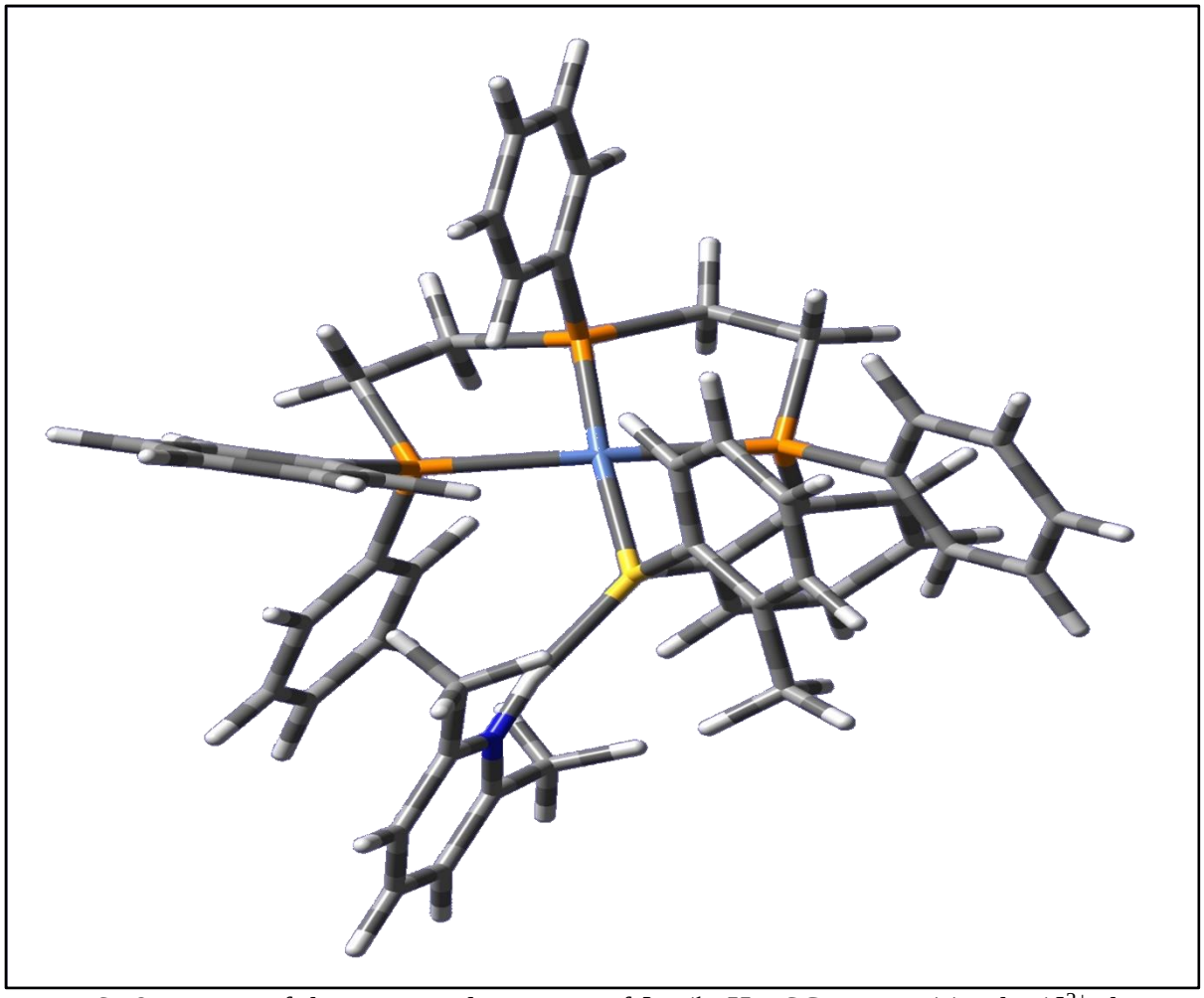

Figure 6.29. Picture of the optimised structure of [Ni(lutH…SC_6H_4Me-2)(triphos)]$^{2+}$ showing barrier for the S-aryl group passes each of the PPh_2 groups of the triphos. Key: Ni = blue, P = orange, S = yellow, N = dark blue, C = grey and H = white.

For [Ni(SC_6H_4R-2)(triphos)]$^+$ (R = H, Me) and [Ni($SC_6H_3Me_2$-2,6)(triphos)]$^+$ the bond lengths and angles at the Ni do not significantly distort from square planar geometry during the rotation of the thiolate. Thus, the bond lengths vary by less than 2% and the bond angles by less than 9%. Thus, there is no change in geometry at the Ni site during the rotation about the Ni-S bond, see Table (6.25).

Table (6.25): Variation in the calculated dimensions at the Ni during the calculated 360^{o} rotation of the Ni-S bond in [Ni(thiolate)(triphos)]$^{+}$.

Thiolate	**SC_6H_5**	**SC_6H_4Me-2**	**$SC_6H_3Me_2$-2,6**
bond lengths / Å			
Ni-S	2.104±0.024	2.120±0.055	2.136±0.045
Ni-P_1	2.160±0.032	2.133±0.031	2.130±0.021
Ni-P_2	2.078±0.032	2.059±0.019	2.066±0.016
Ni-P_3	2.150±0.024	2.135±0.027	2.143±0.022
bond angles / ^{o}			
P_1-Ni-S	103.15±10.67	100.12±6.99	100.19±6.58
P_2-Ni-S	148.42±9.36	149.84±8.89	155.21±13.65
P_3-Ni-S	107.67±10.57	101.15±6.72	99.32±7.48
P_1-Ni-P_2	89.03±2.72	87.68±1.66	87.60±1.02
P_1-Ni-P_3	145.49±7.86	149.78±7.94	150.39±7.81
P_2-Ni-P_3	86.87±0.70	88.19±1.47	87.61±1.38

6.7 Conclusions.

The kinetic studies for all [Ni(thiolate)(triphos)]$^+$ with lutH$^+$ and picH$^+$ show that the rates of proton transfer (k_2^R)^{acid} are markedly slower than the diffusion-controlled rate (k_{diff} = 3.7 x 10^{10} dm^3 mol^{-1} s^{-1}) in MeCN[6]. DFT calculations[10, 11] have shown that the steric factors for the phenyl groups of triphos play a significant role to exhibit this behaviour for the protonation reactions of [Ni(thiolate)(triphos)]$^+$ complexes. Previous studies[7-11] indicated that the slow proton transfer reactions associated with complexes of the type [Ni(thiolate)(triphos)]$^+$ are principally due to the bulky phenyl substituents on triphos impeding the approach of the acid in its trajectory towards the sulfur. Furthermore, the phenyl groups on triphos present different barriers to the two faces of the square plane (the open and closed faces); faces at which the acid must approach to gain access to the sulfur.

The studies on [Ni(SC$_6$H$_4$R-2)(triphos)]$^+$ (R = H, Me or MeO) and [Ni(SC$_6$H$_3$Me$_2$-2,6)(triphos)]$^+$ indicate that the substituents on the thiolate have little effect on the rates of proton transfer, and the rates with lutH$^+$ and picH$^+$ are little different. However, with [Ni(SC$_6$H$_4$Cl-2)(triphos)]$^+$ the rate of protonation with picH$^+$ is 2 x 10^3 times faster than with lutH$^+$. This is a consequence of the chloro-substituent being bound to the Ni which enforces the protonation to only occur from the more sterically challenging closed face of the complex.

In the light of the result with [Ni(SC$_6$H$_4$Cl-2)(triphos)]$^+$, it seems likely that the rates observed with [Ni(SC$_6$H$_4$R-2)(triphos)]$^+$ (R = H, Me or MeO) and [Ni(SC$_6$H$_3$Me$_2$-2,6)(triphos)]$^+$ represent contributions from protonation pathways in which the acid sits above the open face and the closed face. That is, there are two pathways for proton transfer and that (depending on the acid) the rates of the two pathways can be significantly different. This conclusion requires that we should reconsider the observed kinetics.

6.7.1 Re-evaluation of the kinetics.

The rate laws in Equations (6.15), (6.16), (6.18) and (6.19) are relatively simple and it is not immediately obvious that they are consistent with a mechanism where protonation occurs by more than a single pathway. If protonation can occur via either the open or closed faces then the derived general rate law for the reactions is Equation (6.25), where NH$^+$ = acid (lutH$^+$ or picH$^+$) and N = base (lut or pic), K_1^R is the equilibrium constant for association of NH$^+$ with the complex and k_2^R is the corresponding rate constant for intramolecular proton transfer within the hydrogen-bonded precursor intermediate {[Ni(thiolate)(triphos)]…HN}$^{2+}$, and $K_1'^R = K_1^R/(1 +$

K_p^R), where K_p^R is the equilibrium constant describing the orientation of the thiolate as shown in Figure (6.21).

$$\text{Rate} = \left\{\frac{\{K_p^R(K_1'^R k_2^R)^\circ + (K_1'^R k_2^R)^c\}[NH^+]}{1 + \{(K_1'^R)^c + K_p^R(K_1'^R)^\circ\}[NH^+]} + \{K_p^R(k_{-2}^R)^\circ + (k_{-2}^R)^c\}[N]\right\}[Ni] \quad (6.25)$$

Equation (6.25) is analogous to the rate laws shown in Equations (6.15), (6.16), (6.18) and (6.19) but describes two pathways for protonation: one involving the acid sitting over the open face and the other involving the acid siting over the closed face (superscript o and c, respectively). Clearly, if K_p^R is small (predominant orientation of $[Ni(SC_6H_4R\text{-}2)(triphos)]^+$ is that on right hand side of Figure (6.21), Equation (6.25) simplifies to Equation (6.26). Consequently, Equation (6.26) is the appropriate rate law for R = Cl. If K_p^R is large (predominant orientation is that on left hand side of Figure (6.21), Equation (6.25) simplifies to Equation (6.27). Equations (6.25), (6.26) and (6.27) are all the same mathematical form and analogous to the mathematical form of the experimental rate laws in Equations (6.15), (6.16), (6.18) and (6.19). It seems likely that for R = H, Me or MeO, K_p^R has an intermediate value and the experimental kinetics need to be interpreted using the full version of the rate law shown in Equation (6.25).

$$\text{Rate} = \left\{\frac{(K_1^R k_2^R)^c\}[NH^+]}{1 + (K_1^R)^c[NH^+]} + (k_{-2}^R)^c[N]\right\}[Ni] \quad (6.26)$$

$$\text{Rate} = \left\{\frac{K_p^R(K_1^R k_2^R)^\circ[NH^+]}{1 + K_p^R\{1 + (K_1^R)^\circ[NH^+]\}} + K_p^R(k_{-2}^R)^\circ[N]\right\}[Ni] \quad (6.27)$$

Appreciating that the rate laws of Equations (6.15), (6.16), (6.18) and (6.19) are deceptively simple and that they could correspond to more than one protonation pathway complicates the interpretation of the kinetic parameters shown in Tables (6.11) and (6.17). Comparison of elementary rate and equilibrium constants for reactions of different complexes may not be useful since the contribution from each pathway to the total rate is unknown. For example, the apparent binding constant of $picH^+$ to $[Ni(SC_6H_4Cl\text{-}2)(triphos)]^+$ is $(K_1^{Cl})^c$, but for binding of

picH$^+$ to [Ni(SC_6H_4OMe-2)(triphos)]$^+$ is {($K_1'^{MeO}$)^c + K_p^{MeO}($K_1'^{MeO}$)^o}. Meaningful comparison of rates between different complexes would require knowing ($K_1'^{R}$)^c, ($K_1'^{R}$)^o and K_p^{R} in each case. Only for complexes where the orientation of the thiolate is locked (as for [Ni(SC_6H_4Cl-2)(triphos)]$^+$) can the elementary rate and equilibrium constants be attributed to a single protonation pathway.

6.8 References.

1. M. Eigen, *Angew. Chem., Int. Ed. Engl.*, 1964, **3**, 1-19.

2. S. Hammes-Schiffer, *J. Am. Chem. Soc.*, 2015, **137**, 8860-8871.

3. J. J. Warren and J. M. Mayer, *Biochemistry*, 2015, **54**, 1863-1878.

4. P. S. Costa, D. P. Miller, J. D. Teeter, S. Beniwal, E. Zurek, A. Sinitskii, J. Hooper and A. Enders, *The Journal of Physical Chemistry C*, 2016, **120**, 5804-5809.

5. R. P. Bell, in *The Proton in Chemistry*, Chapman Hall, London, 2nd edn., 1973, p. 195.

6. F. Wilkinson, A. F. Olea, D. J. Mcgarvey and D. R. Worrall, *J. Braz.Chem. Soc.*, 1995, **6**, 211-220.

7. V. Autissier, P. M. Zarza, A. Petrou, R. A. Henderson, R. W. Harrington and W. C. Clegg, *Inorg. Chem.*, 2004, **43**, 3106-3115.

8. A. L. Petrou, A. D. Koutselos, H. S. Wahab, W. Clegg, R. W. Harrington and R. A. Henderson, *Inorg. Chem.*, 2011, **50**, 847-857.

9. R. A. Henderson, *BioInorg. React. Mech.* , 2012, **8**, 1-37.

10. A. Alwaaly and R. A. Henderson, *J. Chem. Soc.,Chem. Commun.*, 2014, **50**, 9669-9671.

11. A. Alwaaly, W. Clegg, R. A. Henderson, M. R. Probert and P. G. Waddell, *J. Chem. Soc., Dalton Trans.*, 2015, **44**, 3307-3317.

12. A. Alwaaly, W. Clegg, R. W. Harrington, A. L. Petrou and R. A. Henderson, *J. Chem. Soc., Dalton Trans.*, 2015, **44**, 11977-11983.

13. CrysAlisPro, *Virsion 1.171.35*, Oxford diffraction, 2010.

14. O. V. Dolomanov, L. J. Bourhis, R. J. Gildea, J. A. K. Howard and H. Puschmann, *J. Appl. Cryst.*, 2009, **42**, 339-341.

15. G. M. Sheldrick, *Acta Cryst.*, 2015, **71**, 3-8.

16. G. M. Sheldrick, *Acta Cryst.*, 2008, **64**, 112-122.

17. K. S. Hagen and R. H. Holm, *Inorg. Chem.*, 1984, **23**, 418-427.

18. W. Clegg and R. A. Henderson, *Inorg. Chem.*, 2002, **41**, 1128-1135.

19. K. L. C. Gronberg, R. A. Henderson and K. E. Oglieve, *J. Chem. Soc., Dalton Trans.*, 1998, 3093-3104.

20. M. J. Frisch, G. W. Trucks, H. B. Schlegel, G. E. Scuseria, M. A. Robb, J. R. Cheeseman, G. Scalmani, V. Barone, B. Mennucci, G. A. Petersson, H. Nakatsuji, M. Caricato, X. Li, H. P. Hratchian, A. F. Izmaylov, J. Bloino, G. Zheng, J. L. Sonnenberg, M. Hada, M. Ehara, K. Toyota, R. Fukuda, J. Hasegawa, M. Ishida, T. Nakajima, Y. Honda, O. Kitao, H. Nakai, T. Vreven, J. A. Montgomery, Jr., J. E. Peralta, F. Ogliaro,

M. Bearpark, J. J. Heyd, E. Brothers, K. N. Kudin, V. N. Staroverov, R. Kobayashi, J. Normand, K. Raghavachari, A. Rendell, J. C. Burant, S. S. Iyengar, J. Tomasi, M. Cossi, N. Rega, J. M. Millam, M. Klene, J. E. Knox, J. B. Cross, V. Bakken, C. Adamo, J. Jaramillo, R. Gomperts, R. E. Stratmann, O. Yazyev, A. J. Austin, R. Cammi, C. Pomelli, J. W. Ochterski, R. L. Martin, K. Morokuma, V. G. Zakrzewski, G. A. Voth, P. Salvador, J. J. Dannenberg, S. Dapprich, A. D. Daniels, Ö. Farkas, J. B. Foresman, J. V. Ortiz, J. Cioslowski and D. J. Fox, *Gaussian 09*, Revision D.01, Gaussian, Inc., Wallingford, CT, 2004.

21. A. W. Addison, T. N. Rao, J. Reedijk, J. van Rijn and G. C. Verschoor, *J. Chem. Soc., Dalton Trans.*, 1984, 1349-1356.

22. V. Autissier, E. Brockman, W. Clegg, R. W. Harrington and R. A. Henderson, *Journal of Organometallic Chemistry*, 2005, **690**, 1763-1771.

23. G. Cauquis, A. Deronzier, D. Serve and E. Vieil, *J. Elect-Anal. Chem.*, 1975, **60**, 205-215.

24. B. G. Cox, *Acids and Bases Solvent Effects on Acid-Base Strength*, Oxford University Press, UK, 2013.

25. C. F. Bernasco, *Acc. Chem. Res.*, 1978, **11**, 147-152.

26. M. R. Crampton and B. Gibson, *J.C.S. Perkin II*, 1981, 533-539.

27. S. Scheiner, *Acc. Chem. Res.*, 1985, **18**, 174-180.

28. J. D. Lee and S. C. Wallwork, *Acta Cryst.*, 1965, **19**, 311-313.

29. P. C. Rerat, *Acta Cryst.*, 1962, **15**, 427-433.

APPENDIX A: The Derivation of Rate Laws

A. 1. Chapter 1: The rate law for substitution reaction of $[Fe_4S_4(SEt)_4]^{2-}$ with PhS^- in the presence of $NHEt_3^+$ and NEt_3, Equation (1.2).

From the mechanism shown in Figure (1.9), when the substitution steps are rate-limiting for both the uncatalyzed (k_0) and acid-catalyzed (k_2):

$$\frac{-\mathrm{d}[\mathrm{Fe_4S_4(SEt)_4^{2-}}]}{\mathrm{dt}} = k_0[\mathrm{Fe_4S_4(SEt)_4^{2-}}]_e + k_2[\mathrm{Fe_4S_3HS(SEt)_4^-}]_e \quad (\mathrm{A.\,1.1})$$

(where the subscript e indicates to the concentration formed at equilibrium)

The equilibrium constant for protonation step can be defined as:

$$K_1 = \frac{[\mathrm{Fe_4S_3HS(SEt)_4^-}]_e[\mathrm{NEt_3}]}{[\mathrm{Fe_4S_4(SEt)_4^{2-}}]_e[\mathrm{NHEt_3^+}]} \quad (\mathrm{A.\,1.2})$$

$$[\mathrm{Fe_4S_3HS(SEt)_4^-}]_e = K_1[\mathrm{Fe_4S_4(SEt)_4^{2-}}]_e([\mathrm{NHEt_3^+}]/[\mathrm{NEt_3}]) \quad (\mathrm{A.\,1.3})$$

$$[\mathrm{Fe_4S_4(SEt)_4^{2-}}]_\mathrm{T} = [\mathrm{Fe_4S_4(SEt)_4^{2-}}]_e + [\mathrm{Fe_4S_3HS(SEt)_4^-}]_e \quad (\mathrm{A.\,1.4})$$

(where the subscript T indicates to the total concentration at initial of the reaction)

Substitution Equation (A. 1.3) into Equation (A. 1.4):

$$[\mathrm{Fe_4S_4(SEt)_4^{2-}}]_\mathrm{T} = [\mathrm{Fe_4S_4(SEt)_4^{2-}}]_e + K_1[\mathrm{Fe_4S_4(SEt)_4^{2-}}]_e([\mathrm{NHEt_3^+}]/[\mathrm{NEt_3}]) \quad (\mathrm{A.\,1.5})$$

$$[\mathrm{Fe_4S_4(SEt)_4^{2-}}]_\mathrm{T} = \{1 + K_1([\mathrm{NHEt_3^+}]/[\mathrm{NEt_3}])\}[\mathrm{Fe_4S_4(SEt)_4^{2-}}]_e \quad (\mathrm{A.\,1.6})$$

$$[\mathrm{Fe_4S_4(SEt)_4^{2-}}]_e = \frac{[\mathrm{Fe_4S_4(SEt)_4^{2-}}]_\mathrm{T}}{1 + K_1([\mathrm{NHEt_3^+}]/[\mathrm{NEt_3}])} \quad (\mathrm{A.\,1.7})$$

Substitution Equations (A. 1.3) and (A. 1.7) into Equation (A. 1.1) results:

$$\frac{-\mathrm{d}[\mathrm{Fe_4S_4(SEt)_4^{2-}}]}{\mathrm{dt}} = \frac{(k_0 + K_1k_2[\mathrm{NHEt_3^+}]/[\mathrm{NEt_3}])[\mathrm{Fe_4S_4(SEt)_4^{2-}}]_\mathrm{T}}{1 + K_1[\mathrm{NHEt_3^+}]/[\mathrm{NEt_3}]} \quad (\mathrm{A.\,1.8})$$

To apply Equation (A. 1.8) on general system, it can be used Equation (A. 1.8):

$$\frac{-\mathrm{d}[\mathrm{cluster}]}{\mathrm{dt}} = \frac{(k_0 + K_1k_2[\mathrm{NHEt_3^+}]/[\mathrm{NEt_3}])[\mathrm{cluster}]}{1 + K_1[\mathrm{NHEt_3^+}]/[\mathrm{NEt_3}]} \quad (\mathrm{A.\,1.8})$$

A. 2. Chapter 5: the rate law for the reaction between [Ni(4-RC_6H_4S)(triphos)]$^+$ complex and lutH$^+$ in presence of lut, Equation (5.15).

From the mechanism shown in Figure (5.11) it can be derived the rate law as following:

(we can consider that [lutH$^+$] and [lut] are constants and [C$^+$] = [Ni(SC_6H_4R-4)(triphos)$^+$])

When the intramolecular proton transfer is the rate-limiting for the reaction.

$$\text{Rate} = k_d\{[\text{C} \dots \text{Hlut}^{2+}]_F - [\text{C} \dots \text{Hlut}^{2+}]_e\} - k_{-d}\{[\text{C} \dots \text{H}^{2+}]_F - [\text{C} \dots \text{H}^{2+}]_e\}[\text{lut}] \quad (A.2.1)$$

Where the subscript F indicates to the concentration of a species at final equilibrium and e indicates to deviation of equilibrium. Thus, Equation (A. 2.1) considers the concentration at any time of the reaction.

When the equilibrium of intramolecular proton transfer step is attained:

$$k_d[\text{C} \dots \text{Hlut}^{2+}]_F = k_{-d}\{[\text{C} \dots \text{H}^{2+}]_F[\text{lut}] \quad (A.2.2)$$

Thus, substituting the cases for Equation (A. 2.2) into Equation (A. 2.1) results:

$$\text{Rate} = -k_d[\text{C} \dots \text{Hlut}^{2+}]_e + k_{-d}[\text{C} \dots \text{H}^{2+}]_e[\text{lut}] \quad (A.2.3)$$

The first equilibrium is rapid, so it can be considered that at any time:

$$k_{-c}\{[\text{C} \dots \text{Hlut}^{2+}]_F - [\text{C} \dots \text{Hlut}^{2+}]_e\} = k_c\{[\text{C}^+]_F - [\text{C}^+]_e\}[\text{lutH}^+] \quad (A.2.4)$$

At the equilibrium:

$$k_{-c}[\text{C} \dots \text{Hlut}^{2+}]_F = k_c[\text{C}^+]_F[\text{lutH}^+] \quad (A.2.5)$$

Substitution Equation (A. 2.4) into (A. 2.5) resulted:

$$k_{-c}[\text{C} \dots \text{Hlut}^{2+}]_e = k_c[\text{C}^+]_e[\text{lutH}^+] \quad (A.2.6)$$

$$[\text{C}^+]_e = -\{[\text{C} \dots \text{Hlut}^{2+}]_e + [\text{C} \dots \text{H}^{2+}]_e\} \quad (A.2.7)$$

And then introducing Equation (A. 2.7) into (A. 2.6) and the rearrangement gives:

$$[\text{C} \dots \text{Hlut}^{2+}]_e = -\frac{K_c[\text{lutH}^+]}{1 + K_c[\text{lutH}^+]}[\text{C} \dots \text{H}^{2+}]_e \quad (A.2.8)$$

Substitution Equation (A. 2.8) into (A.2.3) and rearrangement gives:

$$\text{Rate} = \{\frac{K_c k_d[\text{lutH}^+]}{1 + K_c[\text{lutH}^+]} + k_{-d}[\text{lut}]\}[\text{C}^+]_F \quad (\text{A. 2.9})$$

The mechanism yields then the generic rate law, Equation (A. 2.10).

$$\text{Rate} = \{\frac{K_c k_d[\text{lutH}^+]}{1 + K_c[\text{lutH}^+]} + k_{-d}[\text{lut}]\}[\text{Ni}(\text{SC}_6\text{H}_4\text{R} - 4)(\text{triphos})^+] \quad (\text{A. 2.10})$$

With k_{obs}:

$$k_{obs} = \frac{K_c k_d[\text{lutH}^+]}{1 + K_c[\text{lutH}^+]} + k_{-d}[\text{lut}] \quad (\text{A. 2.11})$$

Finally, Equation (A. 2.11) is the rate law defined in Chapter 5 by Equation (5.15).

APPENDIX B: Characterisations of [Ni(SC_6H_4R-2)(triphos)]$^+$ (R = Me, OMe, Cl or H) and [Ni($SC_6H_3Me_2$-2,6)(triphos)]$^+$ by Spectroscopy

B.1. FTIR Spectra.

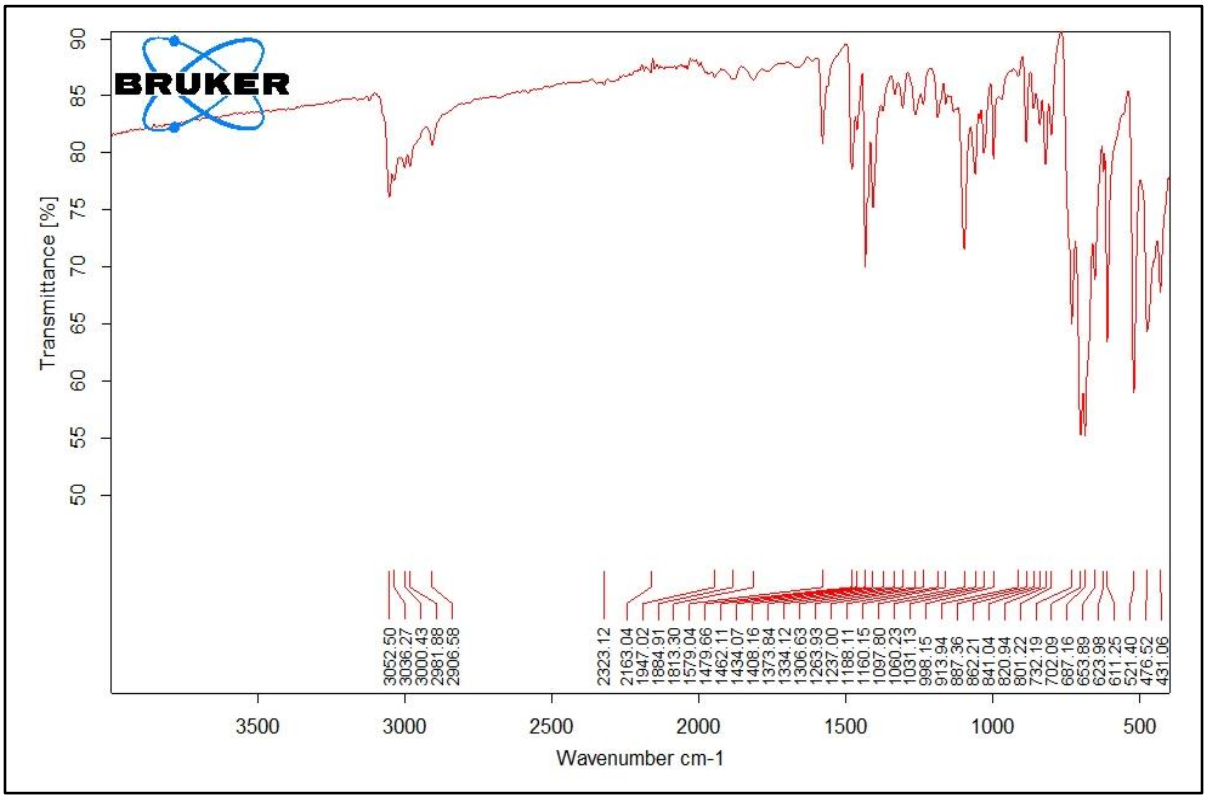

Figure B.1.1. FTIR–Spectrum for [Ni(SC_6H_4Me-2)(triphos)]BPh_4 complex.

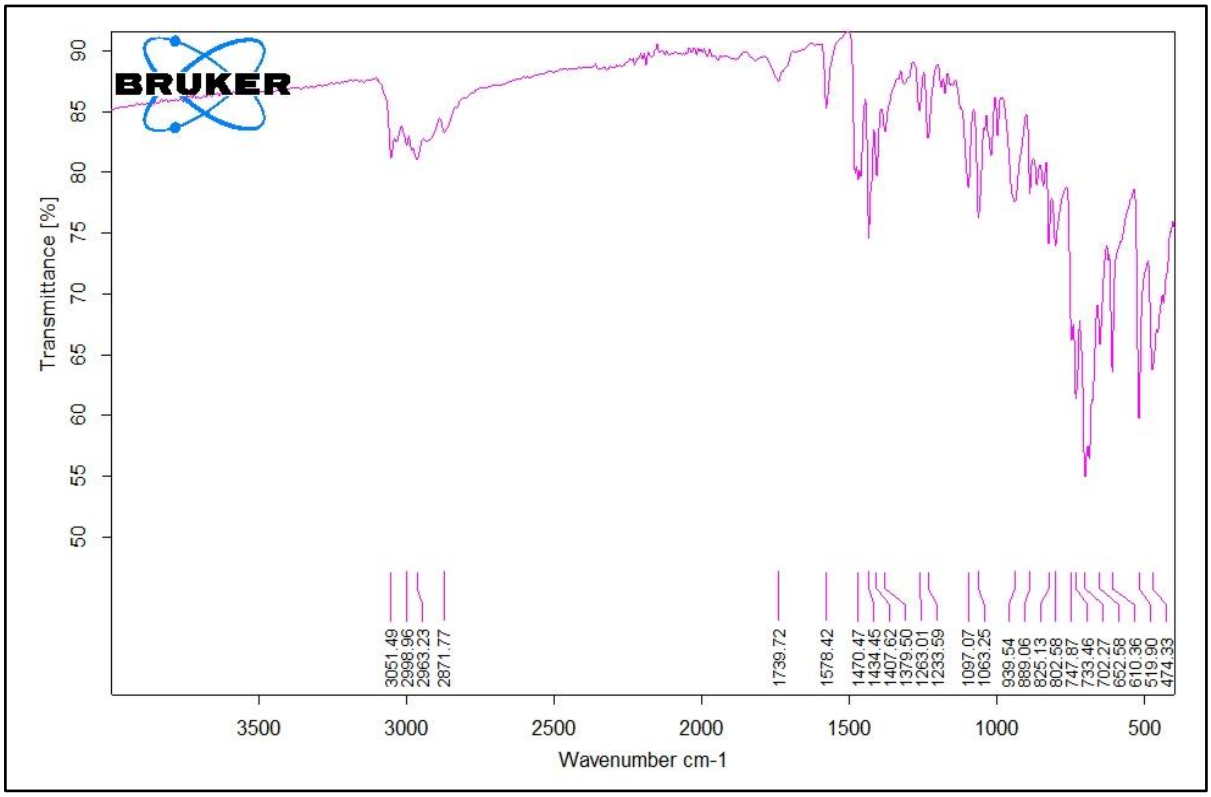

Figure B.1.2. FTIR–Spectrum for [Ni(SC_6H_4OMe-2)(triphos)]BPh_4 complex.

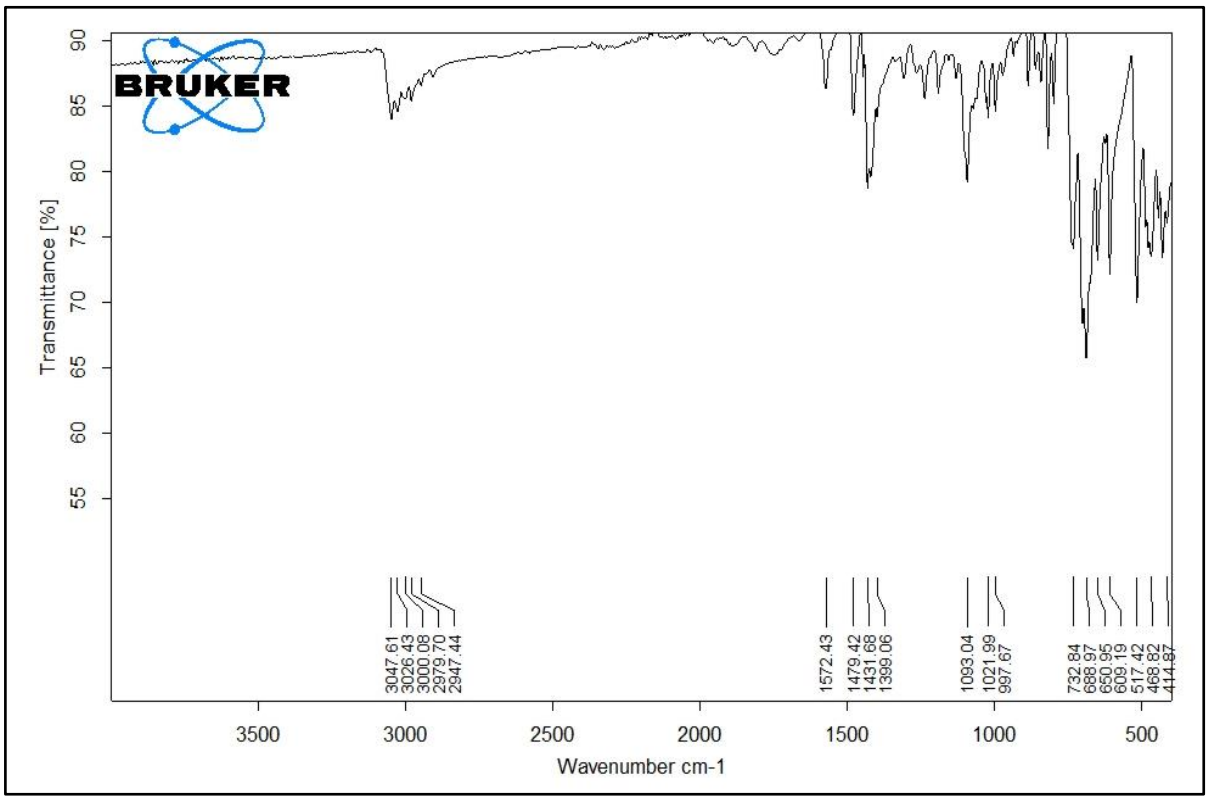

Figure B.1.3. FTIR–Spectrum for [Ni(SC_6H_4Cl-2)(triphos)]BPh_4 complex.

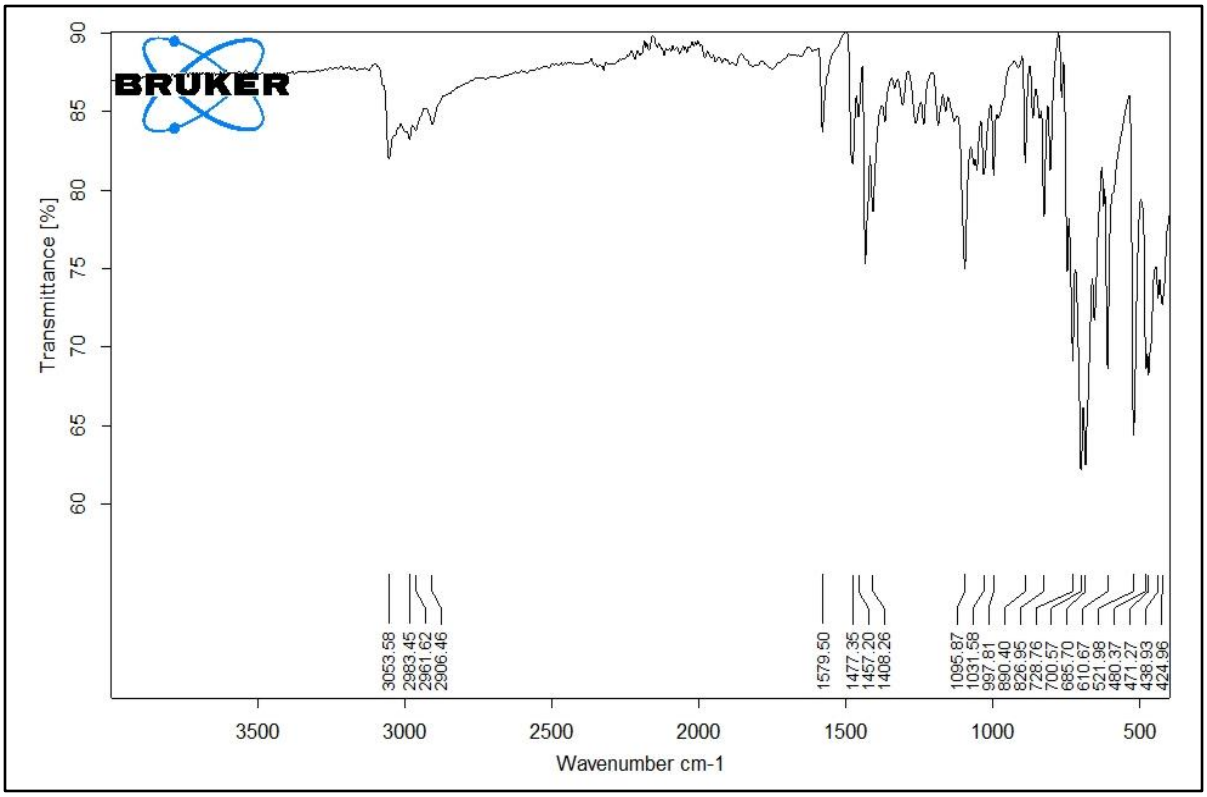

Figure B.1.4. FTIR–Spectrum for [Ni($SC_6H_3Me_2$-2,6)(triphos)]BPh_4 complex.

B.2. ^{1}H NMR Spectra.

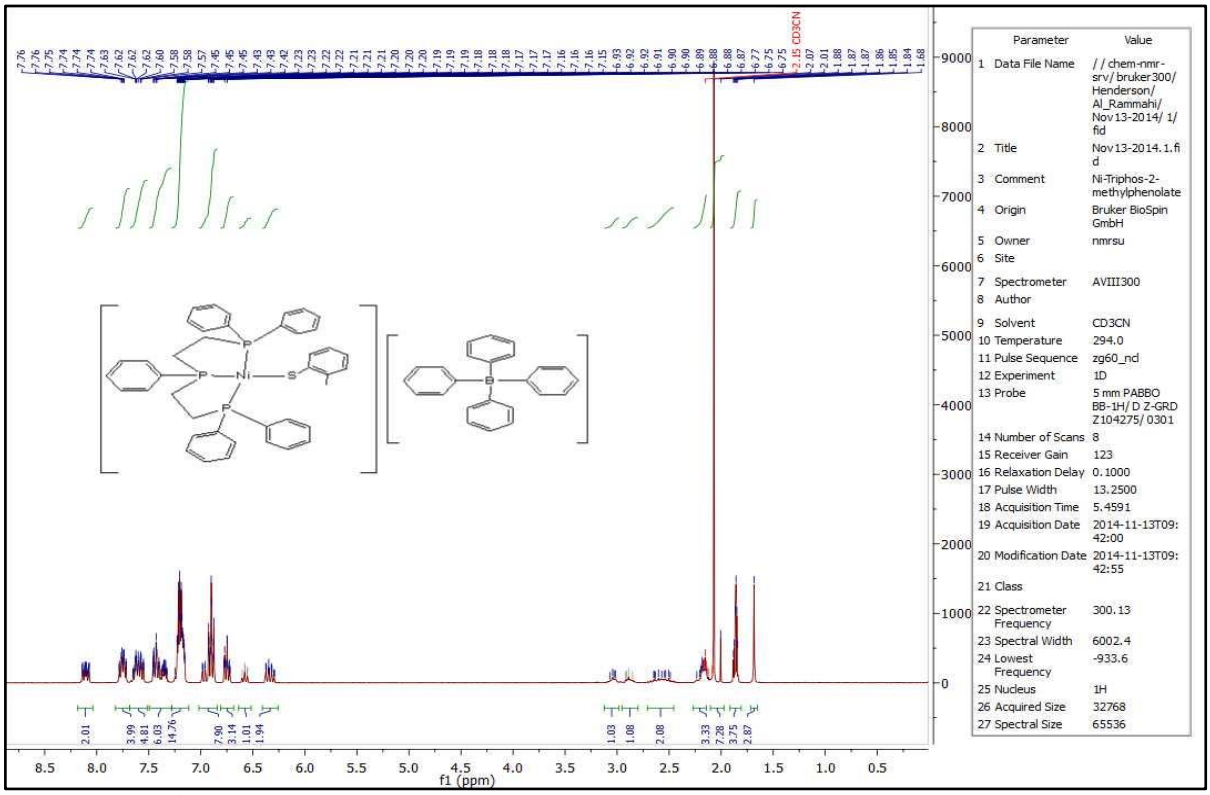

Figure B.2.1. ^{1}H NMR–Spectrum for [Ni(SC_6H_4Me-2)(triphos)]BPh_4 complex in CD_3CN.

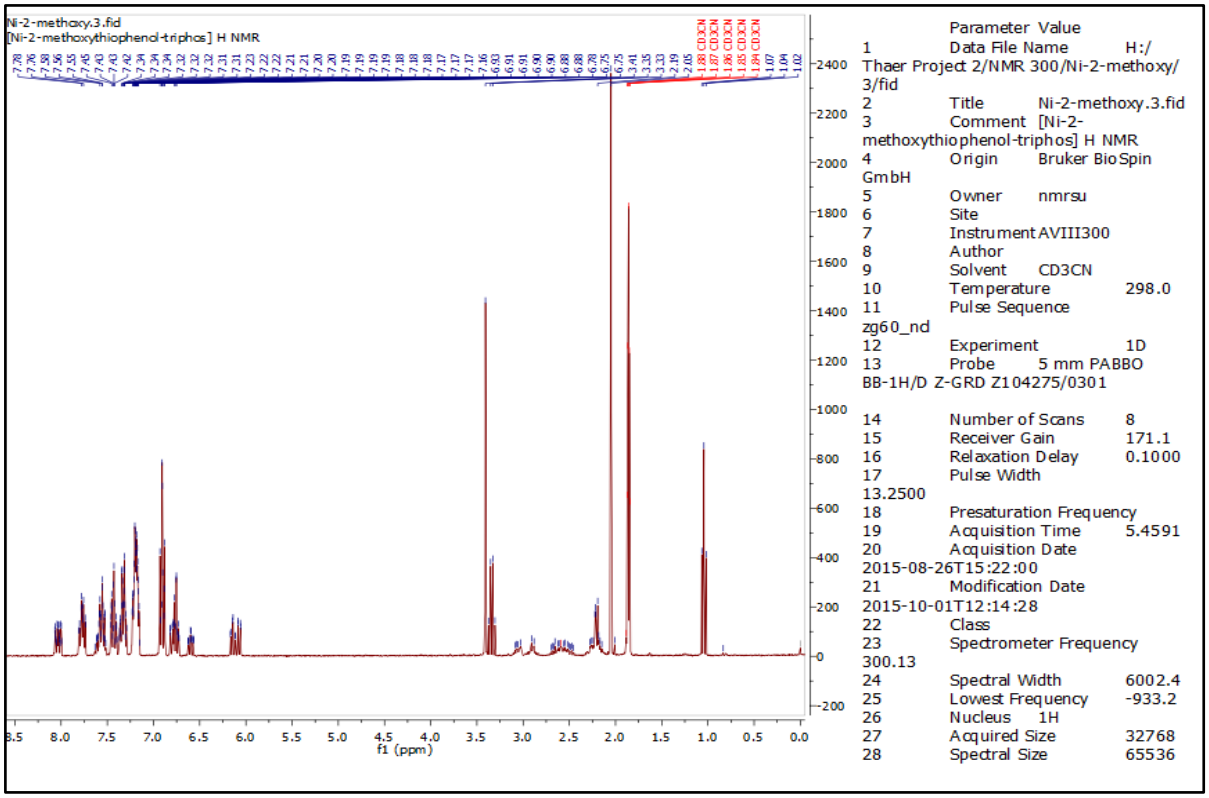

Figure B.2.2. ^{1}H NMR–Spectrum for [Ni(SC_6H_4OMe-2)(triphos)]BPh_4 complex in CD_3CN.

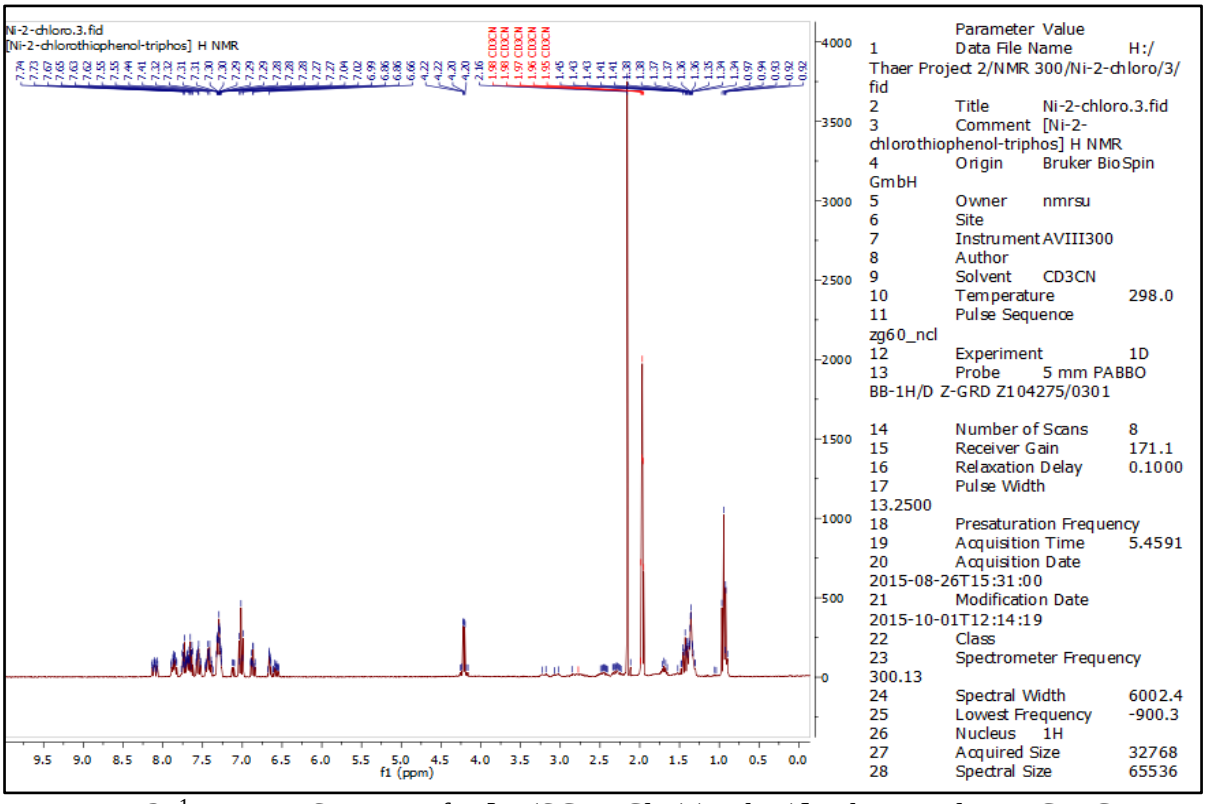

Figure B.2.3. ^{1}H NMR–Spectrum for [Ni(SC_6H_4Cl-2)(triphos)]BPh_4 complex in CD_3CN.

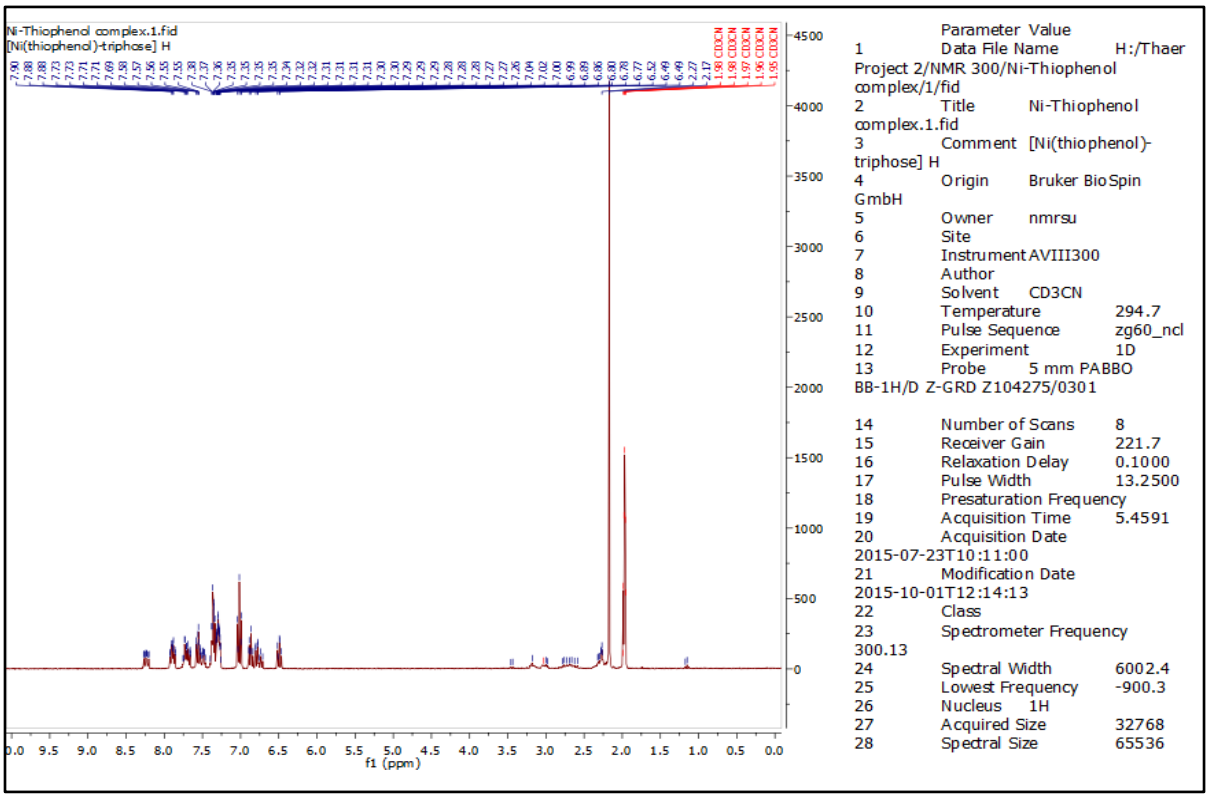

Figure B.2.4. ^{1}H NMR–Spectrum for [Ni(SC_6H_5)(triphos)]BPh_4 complex in CD_3CN.

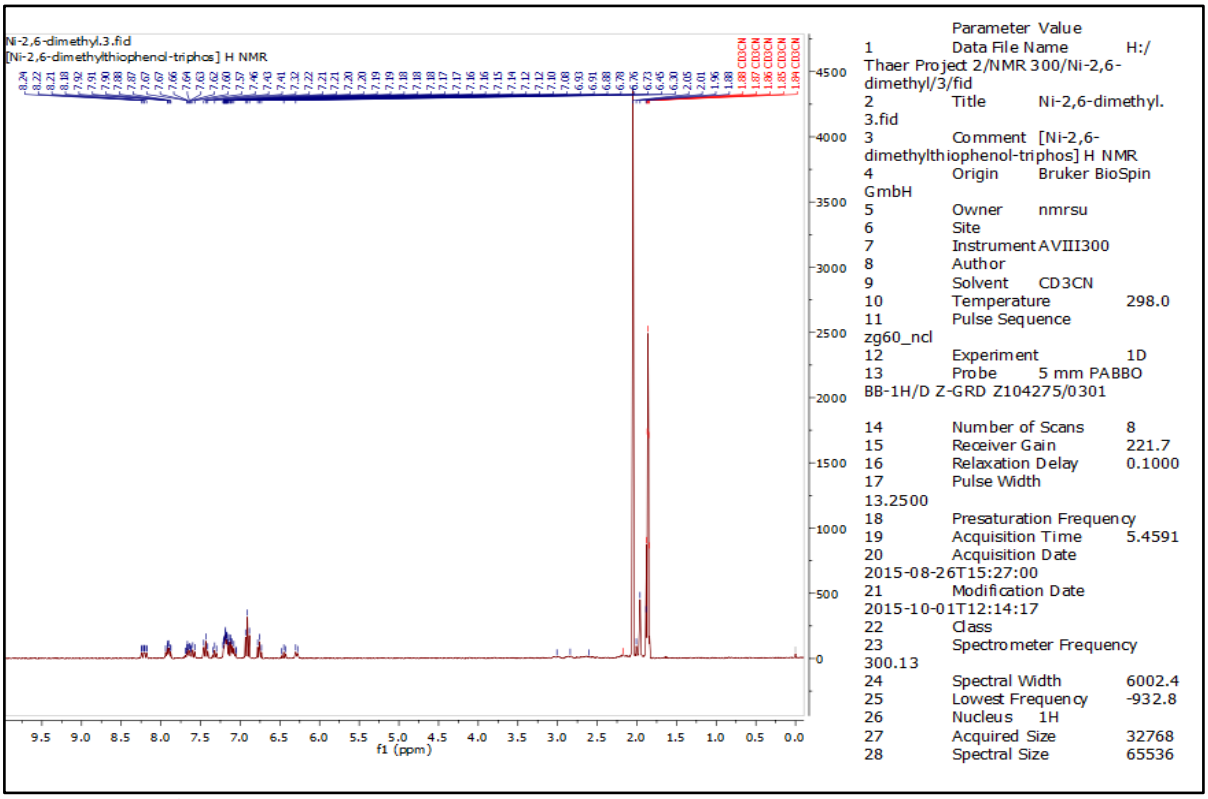

Figure B.2.5. ^{1}H NMR–Spectrum for $[Ni(SC_6H_3Me_2\text{-}2,6)(triphos)]BPh_4$ complex in CD_3CN.

B. 3. ^{31}P $\{^{1}H\}$ NMR Spectra.

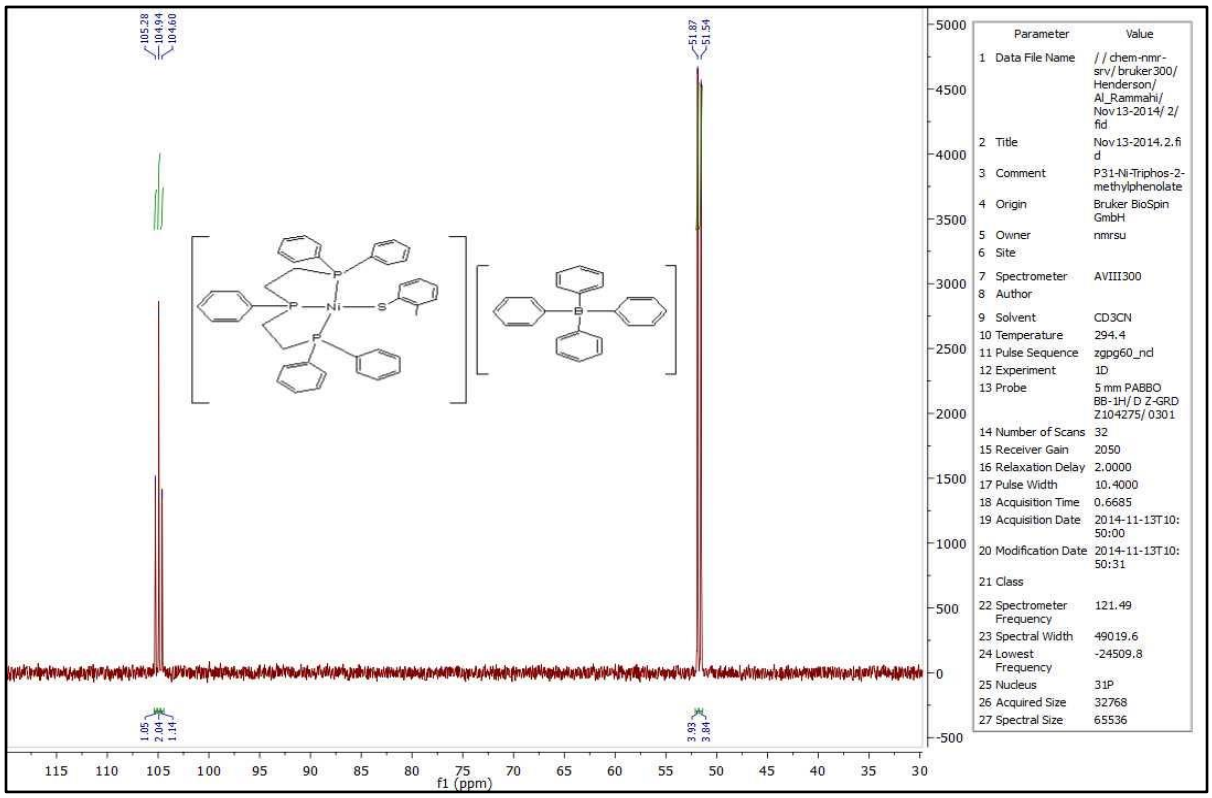

Figure B.3.1. ^{31}P $\{^{1}H\}$ NMR–Spectrum for $[Ni(SC_6H_4Me\text{-}2)(triphos)]BPh_4$ complex in CD_3CN.

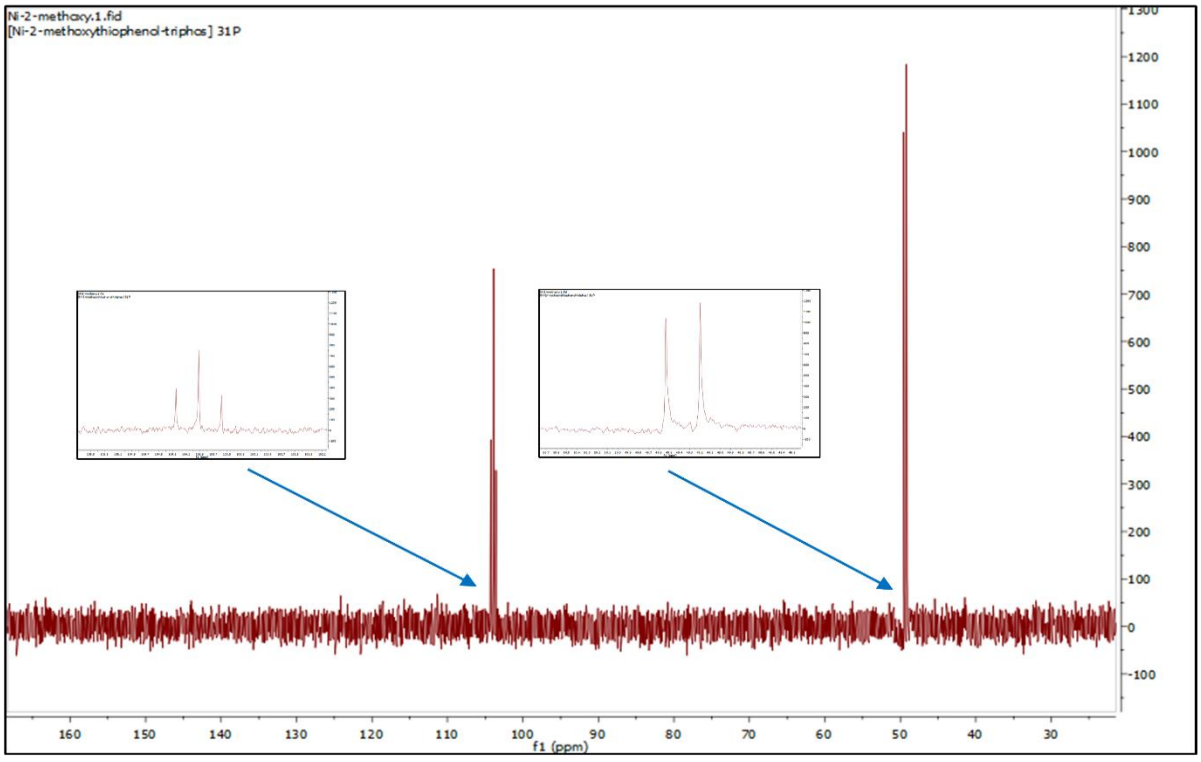

Figure B.3.2. ^{31}P $\{^{1}H\}$ NMR–Spectrum for $[Ni(SC_6H_4OMe\text{-}2)(triphos)]BPh_4$ complex in CD_3CN.

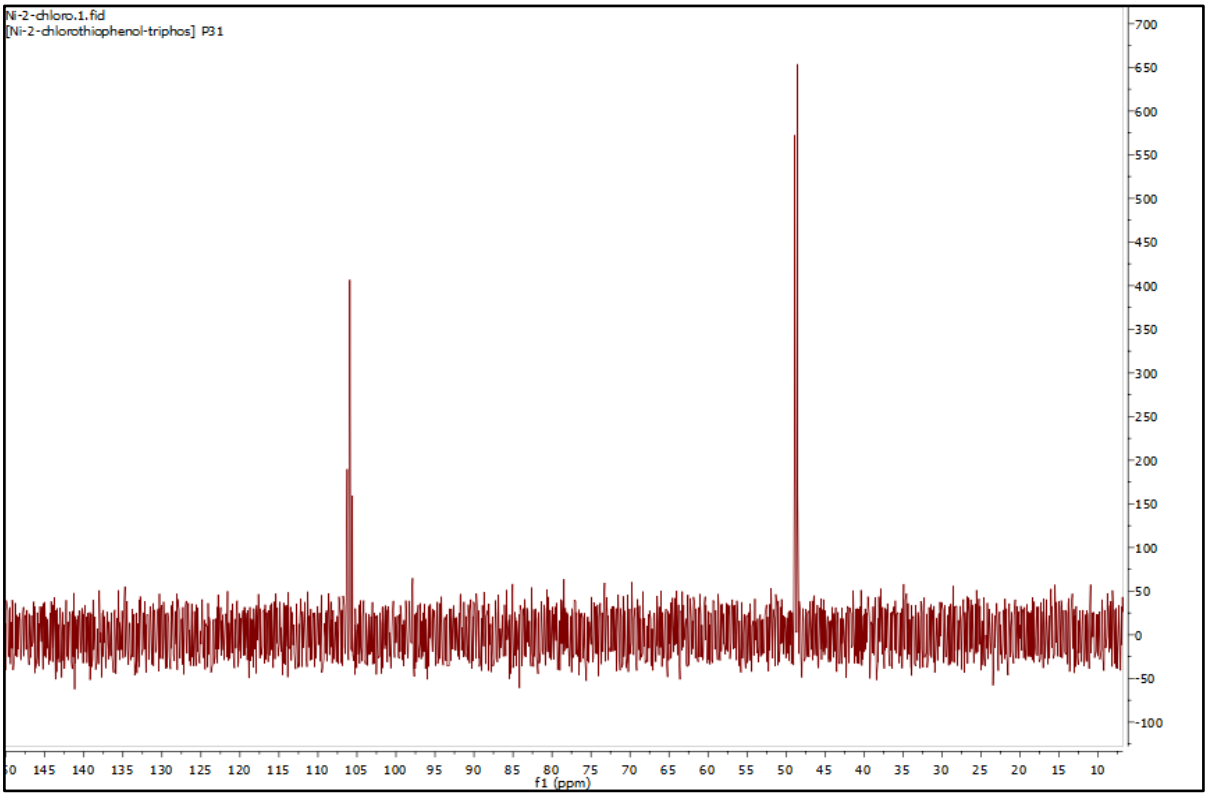

Figure B.3.3. ^{31}P $\{^{1}H\}$ NMR–Spectrum for $[Ni(SC_6H_4Cl\text{-}2)(triphos)]BPh_4$ complex in CD_3CN.

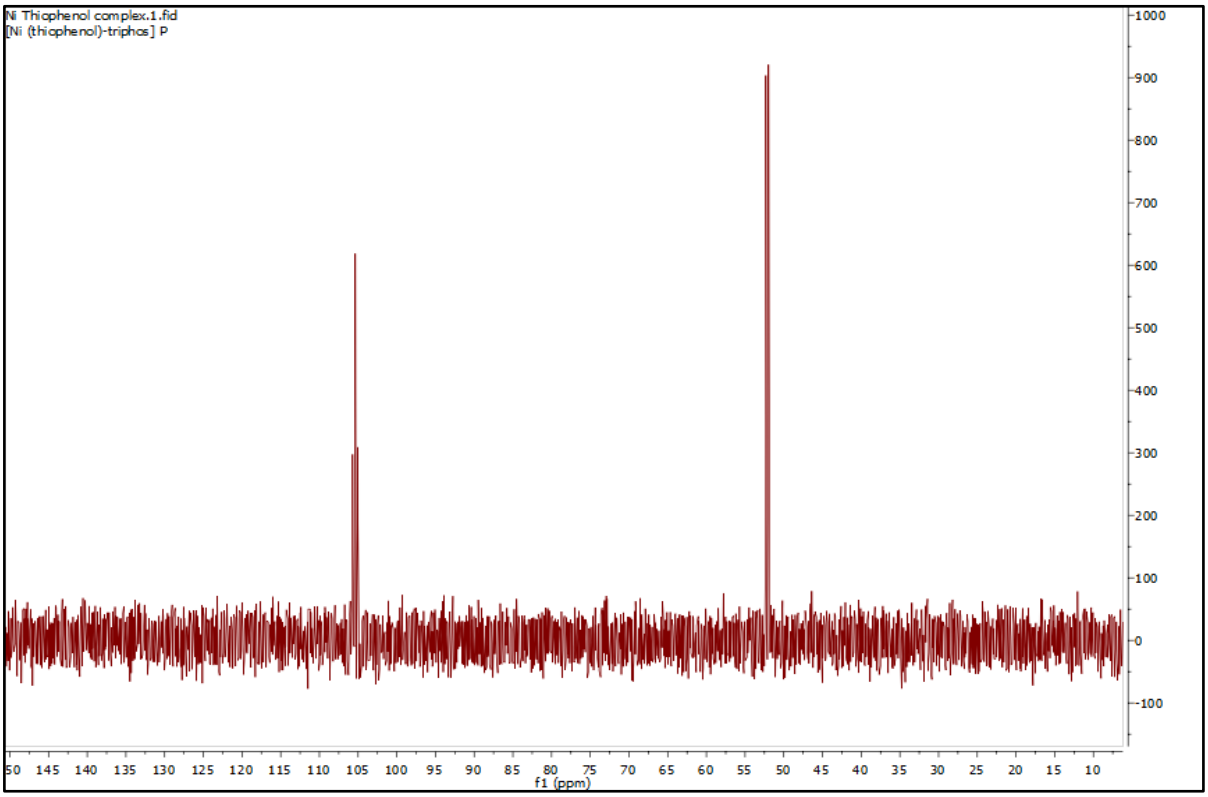

Figure B.3.4. ^{31}P $\{^{1}H\}$ NMR–Spectrum for $[Ni(SC_6H_5)(triphos)]BPh_4$ complex in CD_3CN.

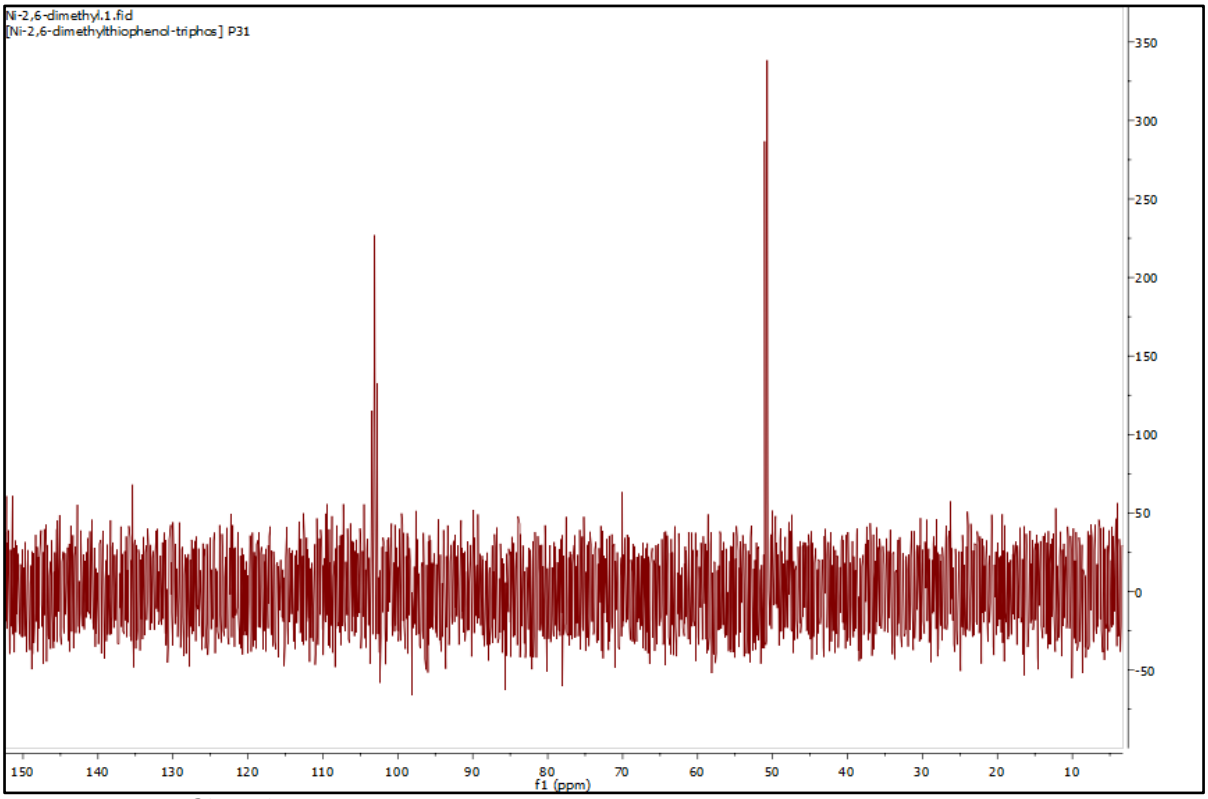

Figure B.3.5. ^{31}P $\{^{1}H\}$ NMR–Spectrum for $[Ni(SC_6H_3Me_2\text{-}2,6)(triphos)]BPh_4$ complex in CD_3CN.

B. 4. Observation of the formation of $[Ni(pic)(triphos)]^{2+}$ complex by $^{31}P\ \{^{1}H\}$ NMR spectroscopy.

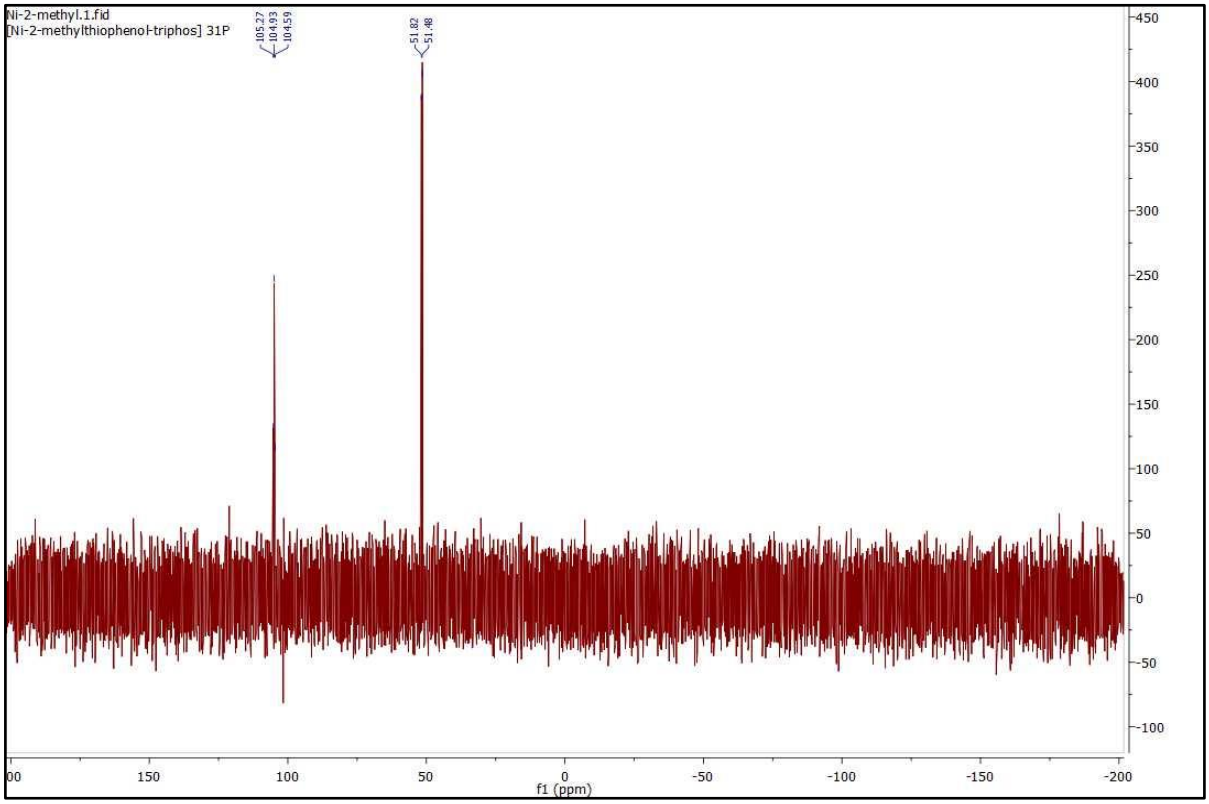

Figure B.4.1. $^{31}P\ \{^{1}H\}$ NMR–Spectrum for the reaction between the solution of $[Ni(SC_6H_4Me\text{-}2)(triphos)]BPh_4$ and 20-fold concentration of $[picH^+]$ in CD_3CN.

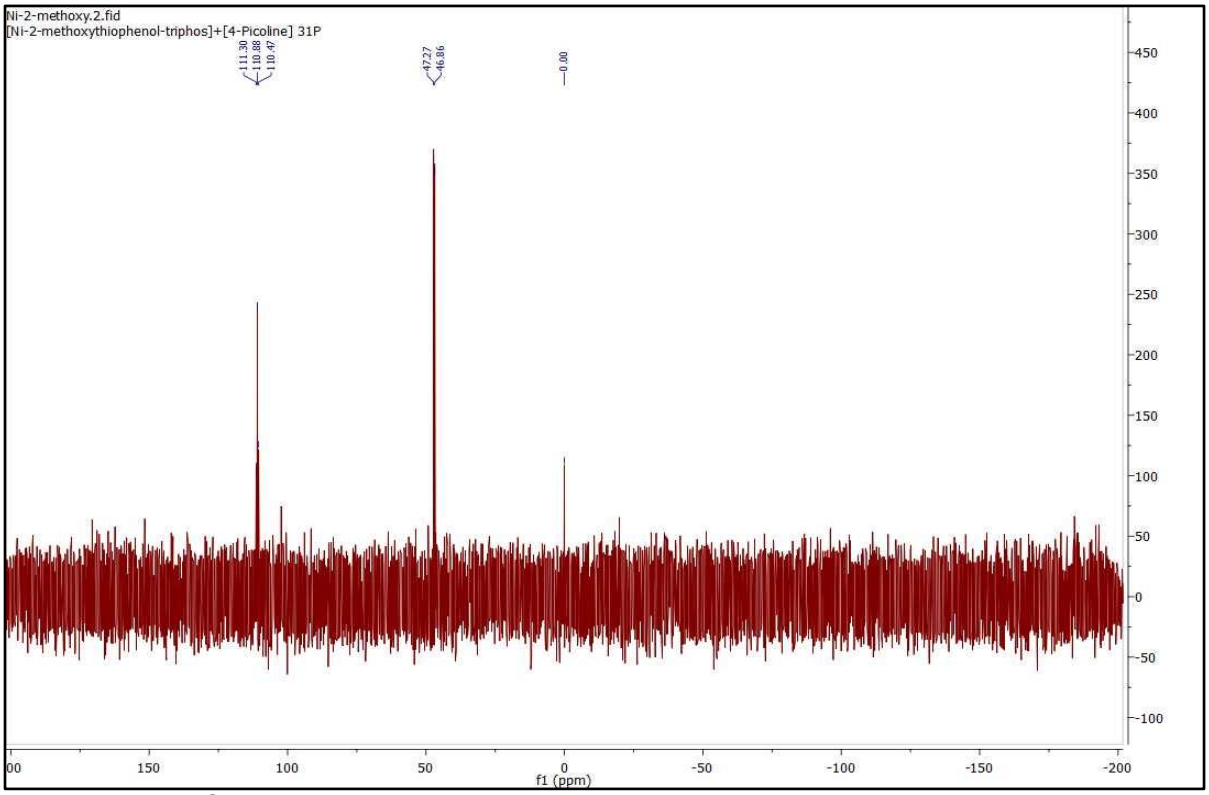

Figure B.4.2. ^{31}P $\{^{1}H\}$ NMR–Spectrum for the reaction between the solution of $[Ni(SC_6H_4OMe\text{-}2)(triphos)]BPh_4$ and 20-fold concentration of $[picH^+]$ in CD_3CN.

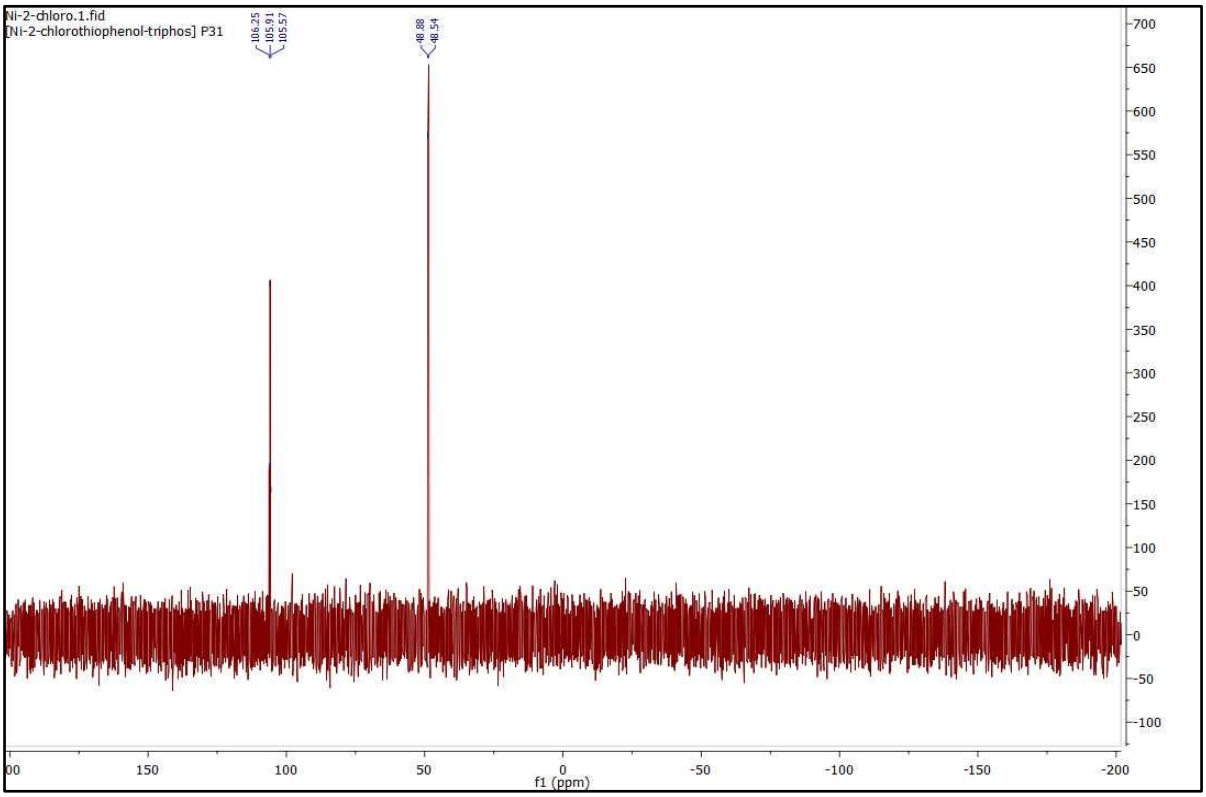

Figure B.4.3. ^{31}P $\{^{1}H\}$ NMR–Spectrum for the reaction between the solution of $[Ni(SC_6H_4Cl\text{-}2)(triphos)]BPh_4$ and 20-fold concentration of $[picH^+]$ in CD_3CN.

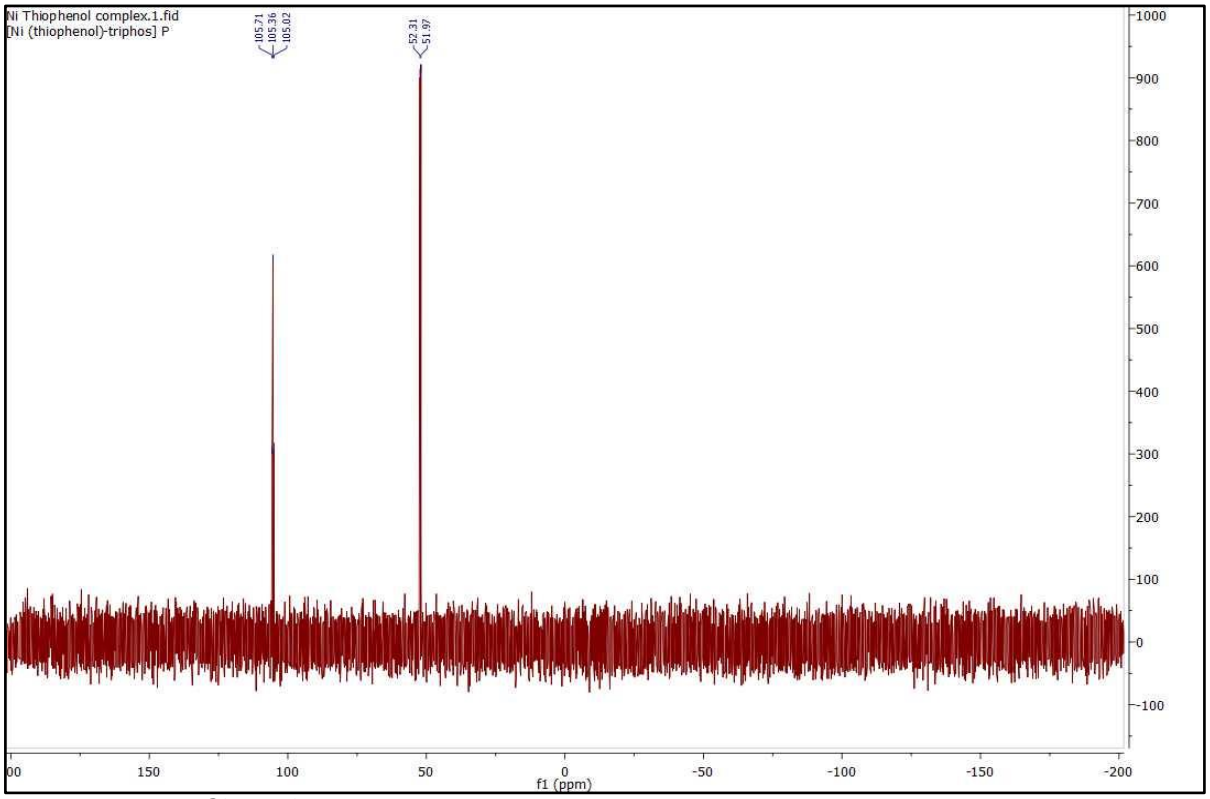

Figure B.4.4. ^{31}P $\{^{1}H\}$ NMR–Spectrum for the reaction between the solution of $[Ni(SC_6H_5)(triphos)]BPh_4$ and 20-fold concentration of $[picH^+]$ in CD_3CN.

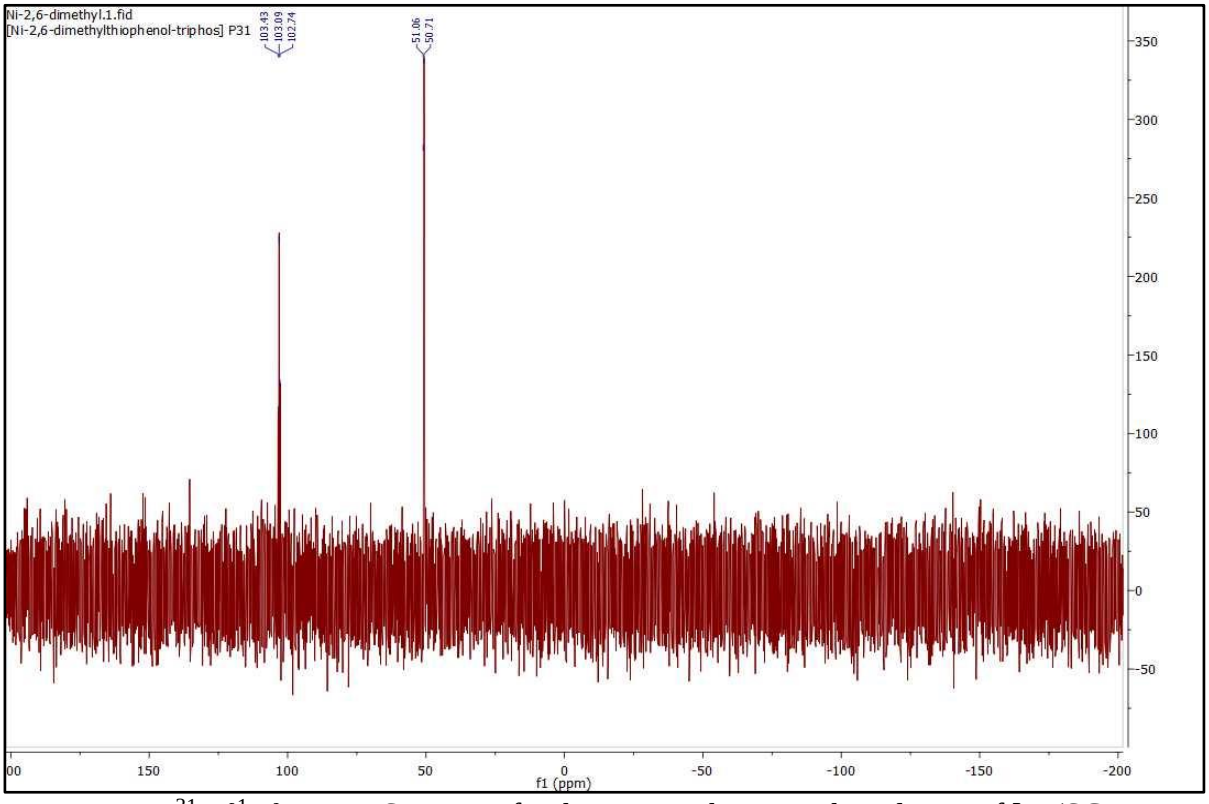

Figure B.4.5. ^{31}P $\{^{1}H\}$ NMR–Spectrum for the reaction between the solution of $[Ni(SC_6H_3Me_2\text{-}2,6)(triphos)]BPh_4$ and 20-fold concentration of $[picH^+]$ in CD_3CN.

APPENDIX C: DFT Calculations

C.1. Scan for the orientation of Ni–S (360°) for [Ni(thiolate)(triphos)]$^+$ complexes.

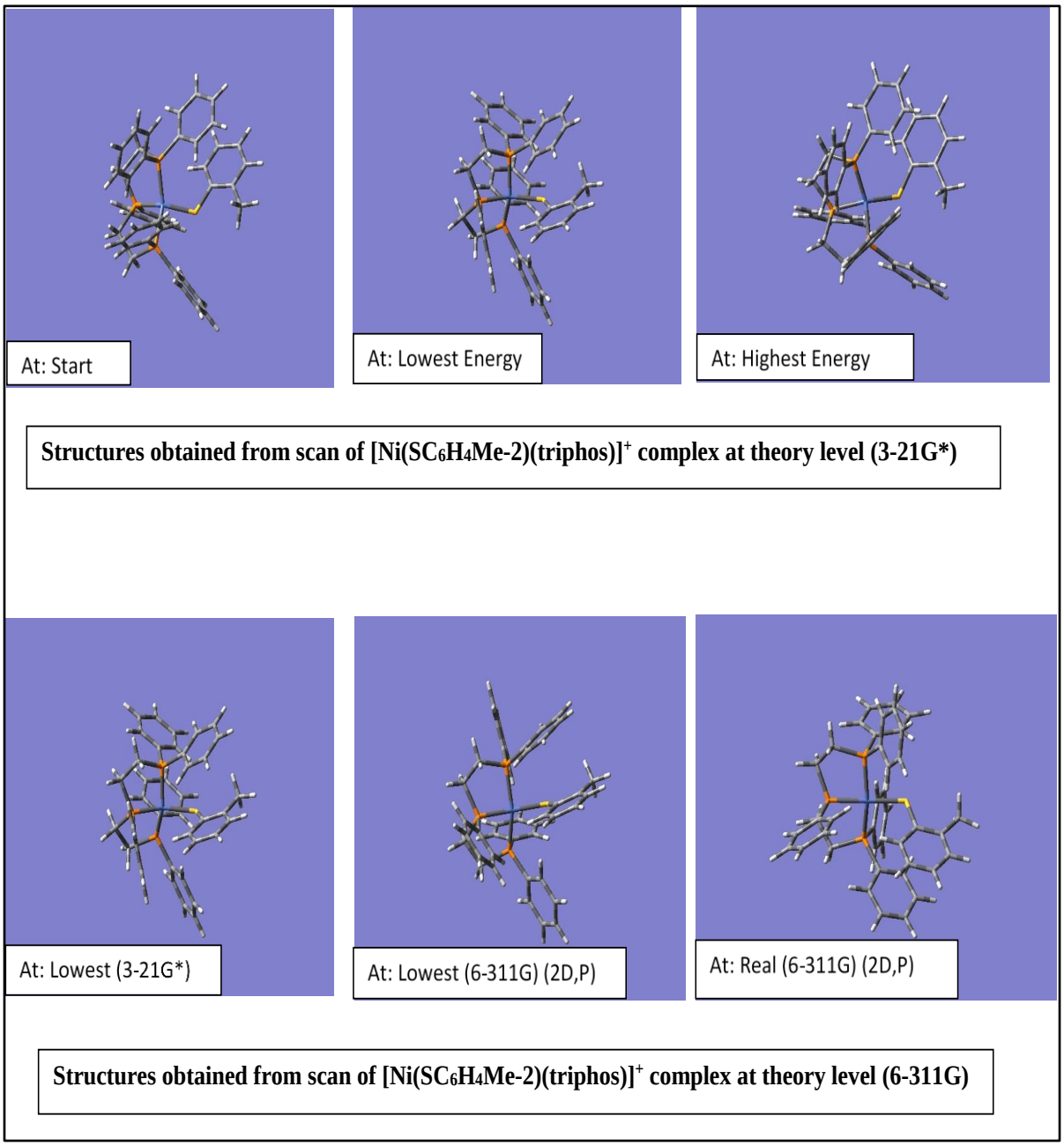

Figure C.1.1. Structures obtained from the scan of [Ni(SC$_6$H$_4$Me-2)(triphos)]$^+$ complex at two theoretical levels (3-21G*) and (6-311). Key: Key: Ni = blue, P = orange, S = yellow, C = grey and H = white.

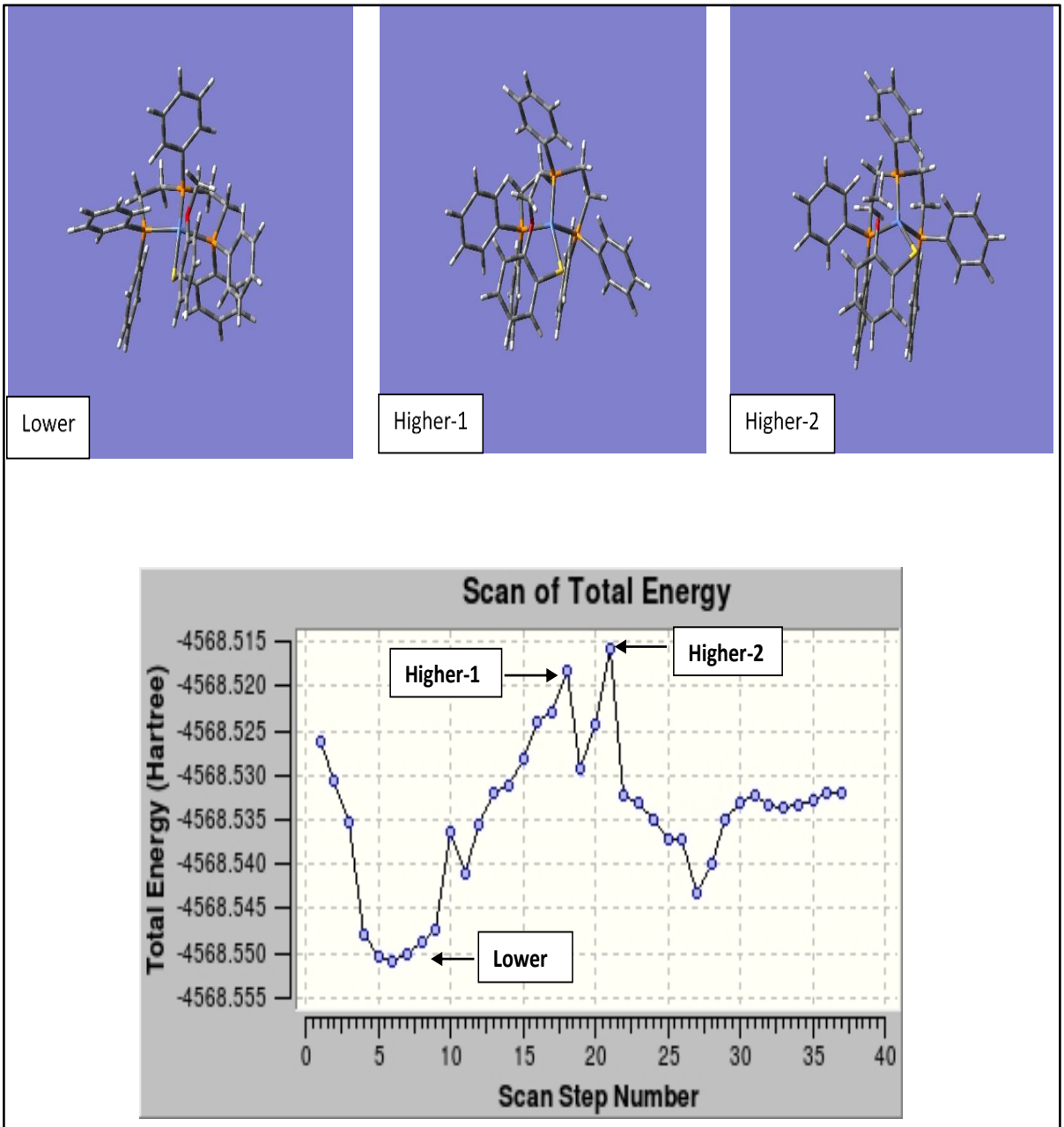

Structures obtained from scan of $[Ni(SC_6H_4OMe\text{-}2)(triphos)]^+$ complex at theory level (3-21G*)

Figure C.1.2. Structures obtained from the scan of $[Ni(SC_6H_4OMe\text{-}2)(triphos)]^+$ complex at theoretical level (3-21G*). Key: Key: Ni = blue, P = orange, S = yellow, C = grey and H = white.

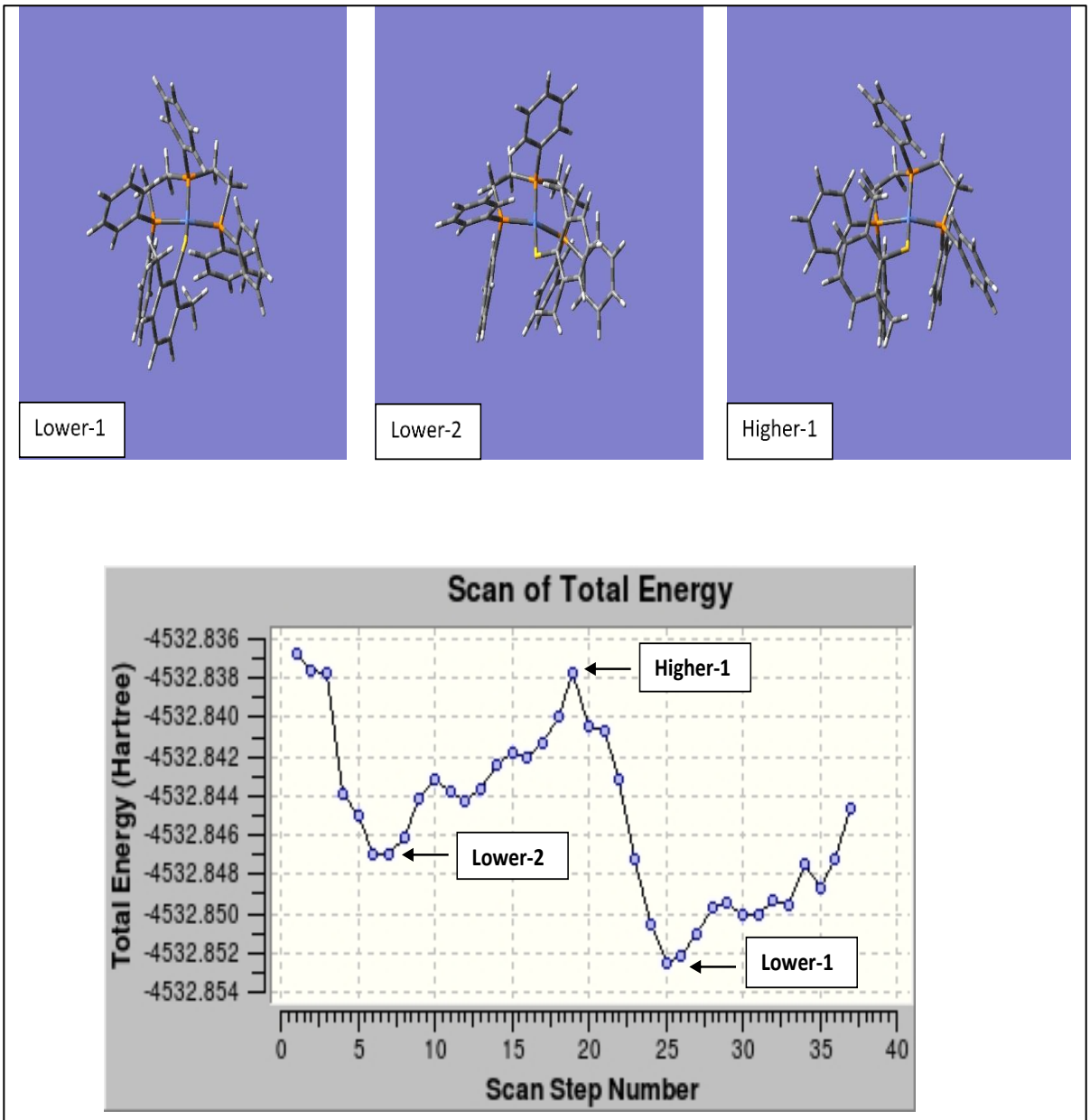

Structures obtained from scan of [Ni($SC_6H_3Me_2$-2,6)(triphos)]$^+$ complex at theory level (3-21G*)

Figure C.1.3. Structures obtained from the scan of [Ni($SC_6H_3Me_2$-2,6)(triphos)]$^+$ complex at theoretical level (3-21G*). Key: Key: Ni = blue, P = orange, S = yellow, C = grey and H = white.

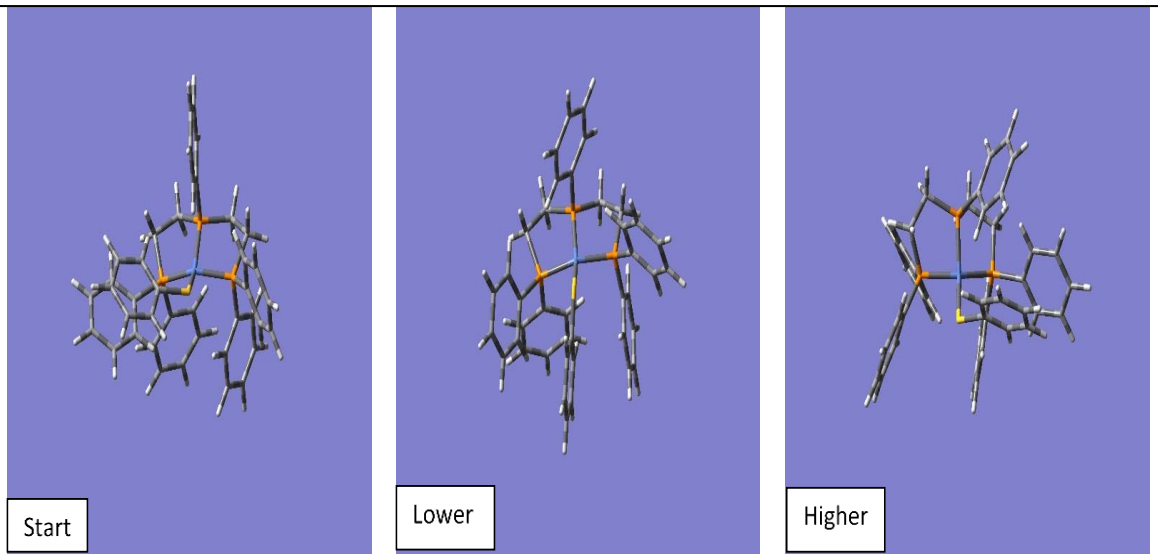

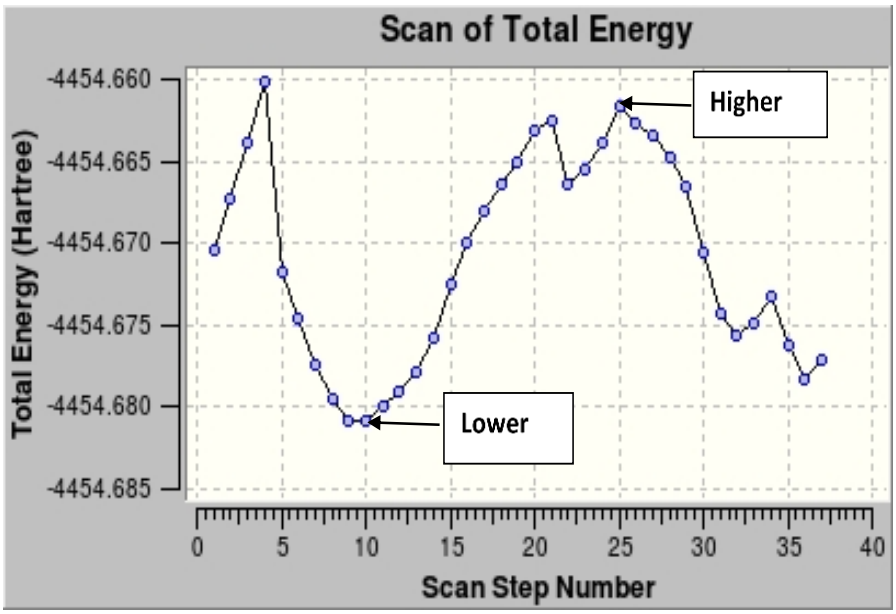

Structures obtained from scan of $[Ni(SC_6H_5)(triphos)]^+$ complex at theory level (3-21G*)

Figure C.1.4. Structures obtained from the scan of $[Ni(SC_6H_5)(triphos)]^+$ complex at theoretical level (3-21G*). Key: Key: Ni = blue, P = orange, S = yellow, C = grey and H = white.

C.2.1. COMPLEX = [Ni(SC$_6$H$_4$Me-2)(triphos)]$^+$

Angle	Bond Lengths (Å)				Bond Angles (°)						
	Ni-S	Ni-P_1	Ni-P_2	Ni-P_3	Ni-S-C	P_1-Ni-S	P_2-Ni-S	P_3-Ni-S	P_1-Ni-P_2	P_1-Ni-P_3	P_1-Ni-P_2
10	2.13110	2.12947	2.06774	2.15688	116.773	93.133	146.058	107.864	87.557	148.762	87.406
50	2.09824	2.16381	2.06281	2.14269	122.646	96.787	141.286	104.942	86.02	152.586	87.291
90	2.0973	2.16219	2.05317	2.14041	126.778	99.631	142.572	99.888	86.462	155.775	86.721
130	2.09745	2.15040	2.05047	2.14814	119.237	96.205	143.732	101.405	86.756	157.719	87.056
170	2.0654	2.12913	2.06734	2.13206	121.298	102.143	140.944	103.494	88.554	144.565	86.743
210	2.11219	2.16403	2.07700	2.11983	115.053	107.106	145.344	94.425	87.665	146.793	88.555
250	2.13389	2.13779	2.05668	2.10794	110.185	100.332	149.231	99.286	88.131	146.367	88.801
290	2.17379	2.11081	2.04036	2.11124	107.341	99.881	158.731	98.830	89.344	148.725	88.984
330	2.15926	2.10774	2.04204	2.11863	107.913	99.504	156.047	95.838	89.02	144.631	89.667
370	2.12243	2.10192	2.06247	2.16169	115.446	96.682	151.632	105.036	88.046	141.843	88.046
Xtal	**2.1689**	**2.2013**	**2.1360**	**2.1948**	**118.24**	**106.38**	**163.41**	**87.574**	**84.809**	**158.22**	**85.48**

C.2.2. COMPLEX = $[Ni(SC_6H_5)(triphos)]^+$

Angle	Bond Lengths (Å)				Bond Angles (°)						
	Ni-S	Ni-P_1	Ni-P_2	Ni-P_3	Ni-S-C	P_1-Ni-S	P_2-Ni-S	P_3-Ni-S	P_1-Ni-P_2	P_1-Ni-P_3	P_1-Ni-P_2
10	2.12370	2.12825	2.06907	2.15956	115.717	93.822	144.67	108.194	87.814	147.437	87.567
50	2.11767	2.14377	2.07060	2.16981	114.581	93.47	147.168	100.361	86.633	163.342	86.728
90	2.10324	2.14058	2.05129	2.14082	113.759	98.866	147.402	98.765	87.037	155.102	87.524
130	2.09230	2.13936	2.04627	2.15300	113.818	100.236	143.819	99.899	88.572	151.124	87.281
170	2.08436	2.13359	2.06506	2.17303	122.147	102.722	141.51	97.10	88.434	153.387	86.953
210	2.08011	2.14154	2.07008	2.15492	120.348	105.228	139.054	99.01	88.873	146.627	87.571
250	2.12682	2.19247	2.07178	2.12730	110.105	113.812	143.03	93.576	86.307	141.895	86.676
290	2.11299	2.16609	2.10346	2.12626	91.173	107.496	153.351	97.756	86.852	135.625	86.17
330	2.11941	2.14157	2.11010	2.15967	67.847	96.975	157.782	106.647	90.054	122.248	86.921
370	2.20024	2.13112	2.10965	2.22659	63.314	92.477	151.919	118.244	91.754	107.629	86.662
Xtal	**2.2456**	**2.2101**	**2.1506**	**2.1858**	**99.20**	**99.03**	**173.89**	**89.76**	**86.41**	**161.50**	**85.82**

C.2.3. COMPLEX = $[Ni(SC_6H_4Me_2\text{-}2,6)(triphos)]^+$

Angle	Bond Lengths (Å)				Bond Angles (°)						
	Ni-S	Ni-P_1	Ni-P_2	Ni-P_3	Ni-S-C	P_1-Ni-S	P_2-Ni-S	P_3-Ni-S	P_1-Ni-P_2	P_1-Ni-P_3	P_1-Ni-P_2
10	2.13065	2.15007	2.08167	2.14626	120.214	106.774	149.807	91.841	86.752	152.141	87.103
50	2.15756	2.13704	2.05959	2.12437	117.732	100.916	160.308	92.759	88.072	149.815	87.781
90	2.18122	2.11648	2.05444	2.12315	117.389	93.606	168.86	95.641	88.622	147.666	88.198
130	2.18785	2.12263	2.05932	2.12073	113.781	98.494	165.994	92.269	88.434	144.511	88.992
170	2.16208	2.10929	2.06219	2.13972	117.175	95.187	157.778	101.952	88.092	142.588	88.227
210	2.09056	2.13575	2.06643	2.15542	121.148	98.339	135.487	106.794	87.825	147.894	88.007
250	2.10047	2.15016	2.05217	2.14603	118.446	100.445	144.295	96.901	86.577	158.20	86.992
290	2.09533	2.13434	2.05004	2.15853	125.606	98.95	142.415	99.459	86.827	157.466	86.485
330	2.09186	2.13975	2.06364	2.15755	122.602	104.761	141.559	97.372	86.902	152.031	86.233
370	2.11322	2.14927	2.07232	2.16400	118.986	106.372	146.206	92.057	88.361	153.126	86.699
Xtal	**2.7136**	**2.2076**	**2.1425**	**2.2127**	**119.07**	**107.029**	**163.07**	**88.187**	**84.53**	**157.20**	**84.875**

C.3.1. Frequency and Thermochemical Analysis of Energies at 298.15 K by DFT Calculations

Compound	SCF *E* (Kcal/mole)	*E* (Electronic + ZPE) (Kcal/mole)	*E* (Electronic + Thermal) (Kcal/mole)	*H* (Electronic + Thermal) (Kcal/mole)	*G* (Electronic + Thermal) (Kcal/mole)	*S* (Kcal/mole)
[Ni(SC_6H_5)(triphos)]$^+$	-2809540.14	-2809131.693	-2809104.734	-2809104.141	-2809181.889	-260.768
[Ni(SC_6H_4Me-2)(triphos)]$^+$	-2834394.99	-2833969.791	-2833941.953	-2833941.361	-2834020.373	-265.008
[Ni(SC_6H_4OMe-2)(triphos)]$^+$	-2881392.77	-2880963.505	-2880935.272	-2880934.679	-2881013.461	-264.236
[Ni($SC_6H_3Me_2$-2,6)(triphos)]$^+$	-2858865.94	-2858423.069	-2858394.374	-2858393.781	-2858474.385	-270.345